UNIVERSITY OF CALIFORNIA, MERCED

Assessment of the physiochemical properties associated with charge transfer and colloidal assembly in organic, organometallic, and inorganic systems through thermodynamic and kinetic proxies.

By:

Ryan Patrick Brisbin

A dissertation submitted in partial satisfaction of the requirements for the degree

Doctor of Philosophy

In

Chemistry and Chemical Biology

Committee in charge:

Professor Erik Menke (Chair)

Professor Sayantani Ghosh

Professor Yue (Jessica) Wang

Professor Ryan Baxter (Advisor)

UNIVERSITY OF CALIFORNIA, MERCED

Assessment of the physiochemical properties associated with charge transfer and colloidal assembly in organic, organometallic, and inorganic systems through thermodynamic and kinetic proxies.

By:

Ryan Patrick Brisbin

A dissertation submitted in partial satisfaction of the requirements for the degree

Doctor of Philosophy

In

Chemistry and Chemical Biology

Committee in charge:
Professor Erik Menke (Chair)
Professor Sayantani Ghosh
Professor Yue (Jessica) Wang
Professor Ryan Baxter (Advisor)

The Dissertation of Ryan Brisbin is approved, and it is acceptable in quality and form for publication on microfilm and electronically:

Professor Erik Menke (Chair)

Professor Sayantani Ghosh

Professor Yue (Jessica) Wang

Professor Ryan Baxter (Advisor)

University of California, Merced 2020

Dedication:

This work is dedicated to my parents, Colleen and Tim Brisbin who encouraged me to wonder about the impossible and instilled in me the tenacity of its pursuit. By architecture or chance, you have gifted me the indomitable will to pursue my goals, undeterred by notions of difficulty or failure. I would neither be where I am nor as capable, if not for all I have learned from you. Rest in paradise ‘Pops’.

Table of Contents

List of Abbreviations

DA- donor acceptor

BIP- bis(imino)pyridine

PhMe- toluene

CV- cyclic voltammetry

Ag- silver

AgCl- silver chloride

Ia – peak anodic current

Ic- peak cathodic current

mV- millivolt

NIO- natural ionization orbitals

CdSe/ZnS- cadmium selenide zinc sulfate

ODA- octadecyl amine

ITO- indium tin oxide

ZnO- zinc oxide

eV- electron volt

QD-quantum dots

τ – lifetime

FRET- Forster resonant energy transfer

PL- photoluminescence spectroscopy

TEM- transmission electron microscopy

PDF- pair distribution function

Nm-nanometer

HOMO- highest occupied molecular orbital

LUMO- lowest unoccupied molecular orbital

FWHM- full width half max

LC- Liquid crystal

NP-nanoparticles

SL- super lattices

5CB- 4-Cyano-4'-pentylbiphenyl

SEM- scanning electron microscopy

DLS- differential light scattering

^{o}C- degrees Celsius

$CHCl_3$- chloroform

iPr- isopropyl

Me-methyl

DMEM- Dulbecco’s modified eagle medium

FBS- fetal bovine serum

CO_2- carbon dioxide

GFs- growth factors

TiO2- titanium dioxide

UV- ultraviolet

MO- methyl orange

Al- aluminum

FEM- finite element metho

XRD- x-ray diffraction

DI- deionized

RET- resonant energy transfer

OLED- organic light emitting diodes

NARFS- non-aqueous redox flow batteries

EPR- electro-paramagnetic resonance

ΔG- free energy

hrs- hours

$AgNO_3$- silver nitrate

K_2HSO_4- sulfuric acid

K_2SO_8 - potassium persulfate

THF- tetrahydro furan

$Pd(OAc)_{2-}$ palladium acetate

4OMe- 4 methoxy acetophenone

4F- 4-fluro acetophenone

SeO_2- selenium dioxide

SF- select flur

BPH- benzoyl pyrazine

BPF 4-fluro benzoyl pyrazine

BPOMe- 4- methoxy benzoyl pyrazine

MeCN- acetonitrile

EtOAc- ethyl acetate

BPH-BF_4- benzoyl pyrizinium tetrafluoro borate

AIE- aggregated induce emission

AIQ- aggregated induced quenching

BPL-1- benzoyl pyrizinium tetrafluoro borate

BPL-2- 4-fluro benzoyl pyrizinium tetrafluoro borate

BPL-3- 4-methoxy benzoyl pyrizinium tetrafluoro borate

DMSO- dimethyl sulfoxide

TICT- twisted intramolecular charge transfer

DOSY- Diffusion oriented spectroscopy

NMR- nuclear magnetic resonance

CT- charge transfer

List of Figures

Chapter 1

Chapter 2

Acknowledgements

I would like to take this time to acknowledge my committee: Dr. Erik Menke, Dr. Sayantani Ghosh, and Dr. Yue Wang. The members of my committee have all taken a personal interest in my development as a young scientist, to the extent of supporting endeavors into various disciplines from organic electro chemistry to photo physics. They have taken the time to ensure I have the tools to be self-sufficient regardless of what I was undertaking that day, and I will be forever grateful. I would also like to say thank you to my advisor Dr. Baxter, you granted me an unprecedented amount of freedom to explore anything I was curious about and supported me through all the second guessing and confusion. Without that freedom and support I would not be the scientist I am today, thank you.

I would like to thank all my group members—current and former—and the various grad students I have had the pleasure to interact with for acting as idea sound boards, their enlightening discussions, and the many fun times we had.

I would like to thank my sister Sarah and mother Colleen: as well as my uncles Cole and Jim and aunts Sherri and Kathy, and cousins: Nick, Jarad, Britany, and Kodie. Their support through both this process and the difficulties presented were crucial for my success.

Carl, Susan, Evan, and Brandon Neese, you have been an irreplaceable support system for me, and words cannot express my gratitude.

I would also like to extend a special thanks to three mentors: Dr. David Hirschberg, Dr. Stan Langevin, and Dr. Allan Chang. Without your guidance and willingness to take a chance on an odd ball, graduate school would not have been an option, nor would I have had the opportunities and experiences that I have had. Thank you

Lastly, I would like to thank my beautiful wife, Katie. This has been an arduous journey. From the years of long distance and losing my father, to planning a wedding only to have a global pandemic lead to canceling the event. With all that has transpired for us, your support and love through this process remains the light that brought me through.

Vita

Ryan P. Brisbin

3276 Denver Avenue Apartment 4A • Merced, California 95340 • rbrisbin@ucmerced.edu • (253) 686-5375

Education

University of California, Merced

Merced, CA

PhD Candidate, Chemistry and Chemical Biology

August 2016 January 2022 (Expected graduation date)

Adviser: Prof. Ryan Baxter

Thesis Title: Assessment of the physiochemical properties associated with charge transfer in organic, organometallic, and inorganic systems through thermodynamic and kinetic proxies.

University of Washington, Tacoma

Tacoma, WA

BA in Criminal Justice

September 2011- June 2015

Publications and Patents

Brisbin, R.; Bartolo, M.; Gopinathan, A.; Leville, M.; Ghosh, S*.; Baxter, R*. Modulating self-assembly processes in mesogenic guided systems through perturbation of isotropic to nematic phase transition using non-mesogenic ligands. (**Accepted**)

Brisbin, R.*; Harb, H.; Debow, J.; Fettinger, J.; Hrant, H.; Baxter, R.; The effect of torsional angle on Donnor-Acceptor Stability using bis(imino)pyridines as a proxy. (**in preparation**)

Brisbin, R.: Zhou, J.; Bond, T.; Voss, L.; Simon, A.; Baxter, R. Chang, A*. Plasmonics-Enhanced UV Photocatalytic Water Purification. *The Journal of Physical Chemistry C 2021, https://doi.org/10.1021/acs.jpcc.1c00613*

Bartolo, D, M.; **Brisbin, P, R**.; Fettinger, J.; Ghosh, S.; Baxter, D, R*. Impact of Bis(imino)pyridine Ligands on Mesoscale Properties of CdSe/ZnS Quantum Dots. *The Journal of Physical Chemistry C 2020, 124, 41, 22677-22683*

Sun, F.; Gangull, A.; Nguyen, J.; **Brisbin, R**.; Shanmugam, K.; Hirschberg, D.; Wheeler, M.; Bashir, R.; Nash, D.; Cunningham, B*.; Smartphone-based

multiplex 30-minute nucleic acid test of live virus from nasal swab extract. *Lab Chip, 2020, 20, 1621-1627*

Chang, A.; **Brisbin, R**.; Zhou, J.; Bond, T.; Simon, A.; Voss, L.; U. S. Provisional patent application Serial No. 62/883,550. Filed on 08/06/2019

Chen, W.; Yu, H.; Sun, F.; Ornob, A.; **Brisbin, R**.; Ganguli, A.; Vemuri, V.; Strzebonski, P.; Cui,G.; Allen, K.; Desai, S.; Lin, W.; Nash, D.; Hirschberg, D.; Brooks, I.; Bashir, R.; Cunningham, B*. Mobile Platform for Multiplexed Detection and Differentiation of Disease-Specific Nucleic Acid Sequences, Using Microfluidic Loop-Mediated Isothermal Amplification and Smartphone Detection. *Anal. Chem. 2017, 89, 21, 11219–11226*

Bauman, J*.; Adamson, J.; **Brisbin, R**. Cline, E.; Keiffer, C.H.; Soil Metals and Ectomycorrhizal Fungi Associated with American Chestnut Hybrids as Reclamation Trees on Formerly Coal Mined Land*. International Journal of Agronomy. 2017, 2017, Article ID 9731212*

Finke, J*.; Ayers, K.; **Brisbin, R**.; Hill, H.; Wing, E.; Banks, W.; Antibody blood-brain barrier efflux is modulated by glycan modification. *Biochimica et Biophysica Acta (BBA) - General Subjects Volume 1861, Issue 9, September 2017, Pages 2228-2239*

Bauman, J*.; **Brisbin, R**.; Adamson, J.; Cline, E. Metals in Soil and American Chestnut Tissue In Experimental Soil Treatments Plots On A Coal Mine Reclamation Site*. The Journal of American Society of Mining and Reclamation 5: 1-18.*

ABSTRACT OF THE DISSERTATION

Assessment of the physiochemical properties associated with charge transfer and colloidal assembly in organic, organometallic, and inorganic systems through thermodynamic and kinetic proxies.

By:

Ryan Patrick Brisbin

Doctor of Philosophy in Organic Chemistry University of California, Merced, 2020

Professor Erik Menke, Chair

Professor Ryan Baxter, Advisor

The following dissertation discusses the assessment of the physiochemical properties associated with charge transfer and self-assembling systems. Initially, a series of studies (chapter 1-2) focus on understanding the physical effects of bis(imino)pyridines on charge transfer both independently and when chelated to nanoparticles through use of cyclic voltammetry and photo lumisicent spectroscopy. Following the assessment of the charge transfer properties of the bis(imino)pyridines, their application in mesoscale assemblies (chapter 3) is explored using a series of DLS/microscopy/and enthalpic measurements.

Chapter 4 is an assessment of a novel plasmonicaly enhanced photocatalyst for a redox based water purification process. Plasmonic enhancement is confirmed through kinetic assessment of rates of decomposition of an environmental pollutant using UV-Vis spectroscopy.

Chapter 5 depicts the development of a novel synthetic method leading to a highly modular material that has applications in both energy storage light emitting technology.

Chapter 2 Is an adapted an adapted reprint of J. Phys. Chem. C 2020, 124, 41, 22677–22683

Chapter 3 is an adapted article accepted by Scientific Reports as of 12/06/2021

Chapter 4 is an adapted reprint of J. Phys. Chem. C 2021, 125, 18, 9730–9735

Chapter 1

The Effect of Torsional Angle on Reversible Electron Transfer in Donor-Acceptor Frameworks Using Bis(imino)pyridines as a Proxy.

Introduction

Donor-Acceptor (DA) frameworks are crucial parts of any technology requiring charge transport. This type of behavior is ubiquitous across technologies from semi-conductors to solar panels. Currently, most DA systems involve metallic components, but progressive research is being pursued to design fully organic DA systems to be used as both organic semi-conductors and light emit-ting diodes. These systems are currently comprised of conductive polymers and salts. However, little is known about the effect of various physical aspects (size, torsional angle, electron density) have on the act of reversible charge transfer. Herein, the effect of torsional angle on reductive stability in bis(imino)pyridines is analyzed using a combination of single crystal analysis and electro-chemical peak current ratios from cyclic voltammetry. The computed free energies of reduction and electron attachment points were also investigated through density functional theory calculations to gain greater understanding of the global effect torsional angles have on electron transfer in bis(imino)pyridines. Findings indicate that torsional angles are a multi-variable parameter affected by both local steric constraints and resonant electronic contributions. Local steric impacted torsional angles demonstrated a negligible effect on electrochemical

reversibility, while resonant affected torsional angles were observed to significantly alter the electrochemical reversibility.

Electron transfer is the base of all redox processes, from energy generation to photosynthesis.[1–3] Within this type of process there are molecules known as “Donor-Acceptor” (DA) molecules. These molecules are capable of facilitating the movement of charge carriers (electrons/holes).[4,5] Recently, DA molecules have garnered significant attention for their applications in numerous technologies, including bio-sensing, energy generation/storage, and light emitting diodes.[6–8]. Advancements in the field of organic chemistry has allowed for a shift to either small molecules or highly defined oligomers .[7,8] This shift corresponds to a greater level of control over the tuning of energy levels, allowing for more efficient charge movement. [9–12]

Costly and toxic rare metals have dominated the technological sector associated with semiconductors and are the principal reason the scientific community is pushing for a greater understanding of organic DA molecules. Organic DA molecules provide alternatives to metal-based semiconductors and a potential route to ultimately replacing metal based semi-conductors Development of technology employing DA molecules have led to attempts at understanding the relationship between molecular structure and DA behavior. Relations between DA behavior and structure *are limited*. Current studies focus on relations between electronic structure and DA behavior (usually a chromatic behavior) .[13–17] Recently, Antoni *et al*. showed that bond distortion can impact a molecules electron transfer ability.[18] With bond distortion showing a significant effect on DA

behavior, planarity in polyaromatic DA systems is a significant question. In this study, we examine the electronic structures and molecular properties of a class of DA molecules to develop better insight into the physical and chemical properties of a class of molecules that have shown to present themselves as potential candidates for a range of applications.

To investigate the effect of planarity on DA behavior, a bis(imino)pyridine scaffold (BIP) was chosen. (**Figure 1A**) BIPs have been observed to act as both

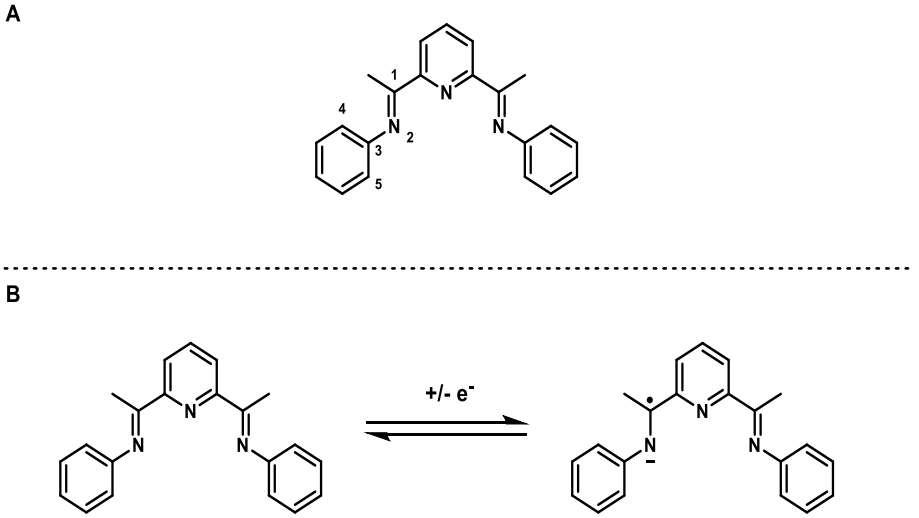

Figure 1) *A) Bis(imino)pyridine scaffold. B) Computationally derived electronic structure of the bis(imino)pyridine scaffold with radical character on imine carbon.*

a donor and an acceptor when chelated to various metals.[19,20,21,22] BIP scaffolds are synthetically simple and highly modular. This facilitates the inspection of the torsional angle and electronics independently. Extensive theoretical and experimental work has elucidated the change in electronic structure between the neutral and reduced BIP.[23–26] This characterization has shown that the largest probability density of the radical anion of the BIP scaffold when chelated to a metal is present at the imine carbon.[25,27] (**Figure 1B**) The certainty in the location of the radical anion of the metalated species allows for the unique ability

to investigate the torsional angle effect of the condescended *N-aryl* groups on the stability of the DA behavior of the non-metalated molecule independent from the electronic structure.

Experimental and Analysis

Multiple iterations of BIPs were synthesized through refluxing 4,5 diacetyl

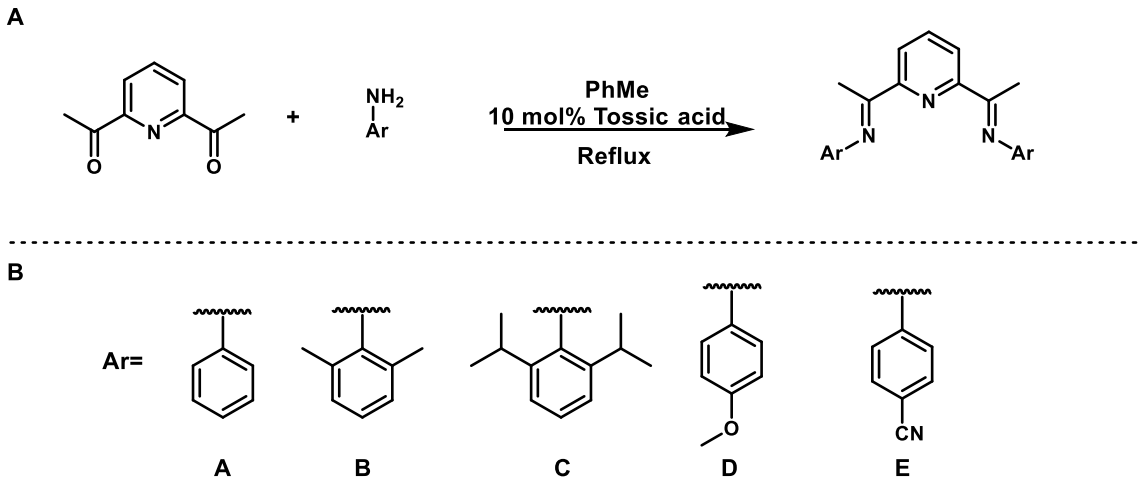

Scheme 1 *A) Synthetic scheme for generation of bis(imino)pyridines. B) different aniline derivatives used for bis(imino)pyridine scaffolds.*

pyridine with its corresponding aniline derivative in excess with catalytic *p*-toluenesulfonic acid (**Scheme 1A)**.[28] A Dean-Stark apparatus for azeotropic distillation was employed for increased yields of bis products. BIPs were designed in two fashions: 1) alkyl substitution in the 4,5 positions to constrain the torsional angle of the condensed imine bond through iterative increase in steric bulk, **A-C** 2) substitution in the para position of the condensed *N*–aryl groups that principally change the electronic structure of the nitrogen carbon bond in the imine, **D-E.** (**Scheme 1B**.)

Single crystals of **A-E** were grown by dissolving in hot methanol and cooled to room temperature for 24 hours, then cooled further to -20°C for another

24 hours. X-ray crystallography was performed and analyzed at the University of California Davis, Center for Crystallography. (see supporting information for

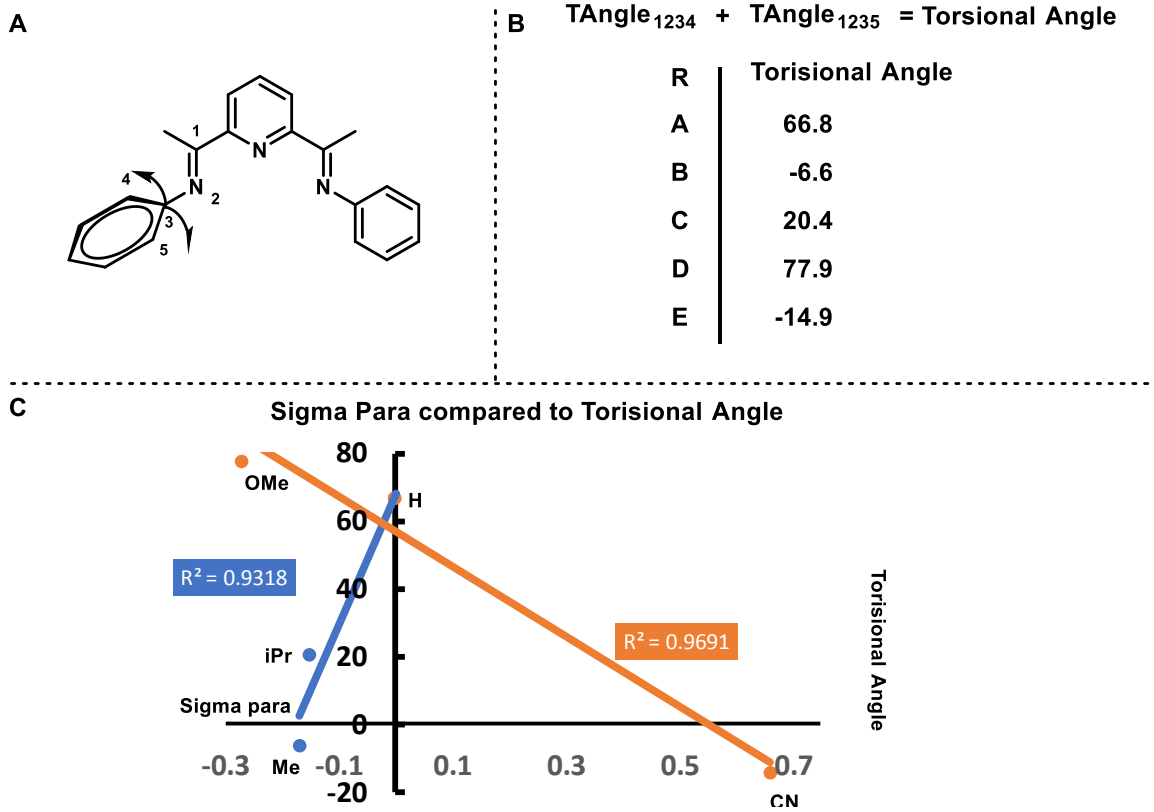

Figure 2. *A) Torsional angles from crystal structure used for the summation. B) Formulaic summation of the torsional angles. C) Comparison of sigma para values of substituents to the torsional angle separated by sterics(blue) electronics (orange). * Me, iPr, CN were anisotropic, but summation was kept consistent.*

crystal structures) Torsional angles were summed as depicted in **Figure 2A** and **Figure 2B**. Summed torsional angles were compared with sigma para values, and line arity was observed between substitution in the 2,6 position of increasing ster ic bulk and electronic modulation in the para position observed in **Figure 2C** [29,30] While linearity is observed in reference to the summed torsional angles across both alkyl substituents (increasing steric bulk) and electronic modulating substituents, the electronic structure of both the ground state and radical anion

differs drastically across the studied scaffold. While structures **A-C** show significant impact on the imine bond torsional angle through steric effect, contribution to electronic structure through inductive donation is negligible. Conversely, structures **D-E** have no steric influence over the imine torsional angle but have significant impact on the electron density through resonant donation and withdrawing effects. This observation initiate that torsional angle in conjugate systems is a multivariable issue, and can be perturbed either through local steric effects (A-C) or distal electronic effects (D-E) Although both electronic donation/withdrawing effects were observed to significantly impact imine torsional angles in **Figure 2C**, delineation between electronic contributions and steric constraints enables comparison of isolated torsional angle on electron acceptor stability independently from electron density.

Stability of DA behavior was explored using cyclic voltammetry (CV). All cyclic voltammetry measurements were performed using Ika ElectraSyn 2.0 cyclic voltammetry kit. CVs were conducted in a three-electrode cell consisting of: a platinum counter, 3mm glassy carbon working electrode, and an aqueous Ag/AgCl reference electrode stored in 3.0 M KCl. A 1.0 mM BIP solution in 0.1M

tetra butyl ammonium tetrafluoroborate was used to obtain peak current ratios at 80 mV shown in **Figure 3**. (* **D** was conducted at 70 mV/s due to instrumental

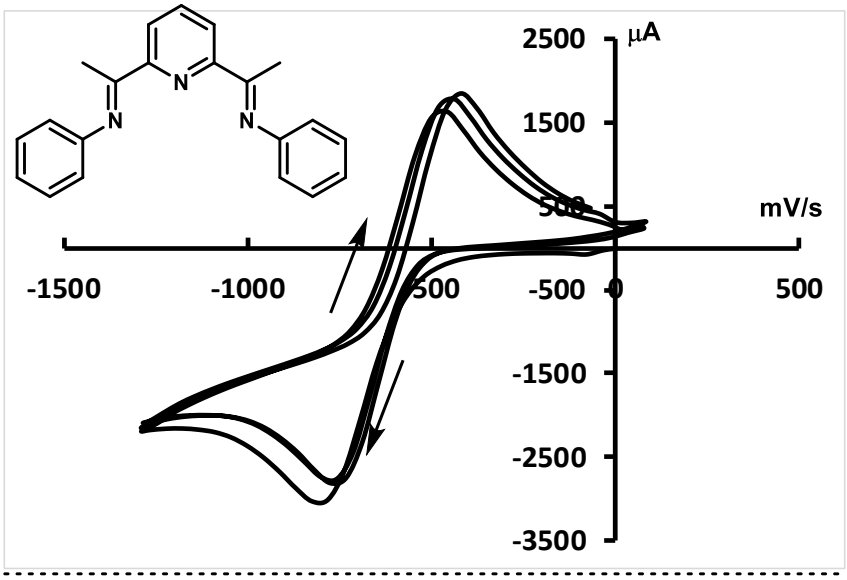

Peak Anodic (μA, I_A)	Peak Cathodic (μA,I_C)	I_A/I_c
1641	3029	0.5418
1794	2759	0.6502
1861	2811	0.6620

Figure 3) *Cyclic Voltammogram of 1mM A in 0.1M TBABF4 with peak currents outlined and chosen sweep rate (2).*

difficulties. Differences between 70 and 80 mV/s was determined to be negligible.) Peak current ratios were taken by absolute values of the peak anodic (Ia) and peak cathodic (Ic) ratio of the second sweep, and standard deviations were calculated using all sweeps for analytical comparison using all sweep.[31] A negligible effect on the peak current ratio was observed between structures **A-C**, despite decreasing torsional angles (**Figure 4 Top).** This indicates that, in situations of increasing imine torsional strain, little to no loss of coplanarity of the

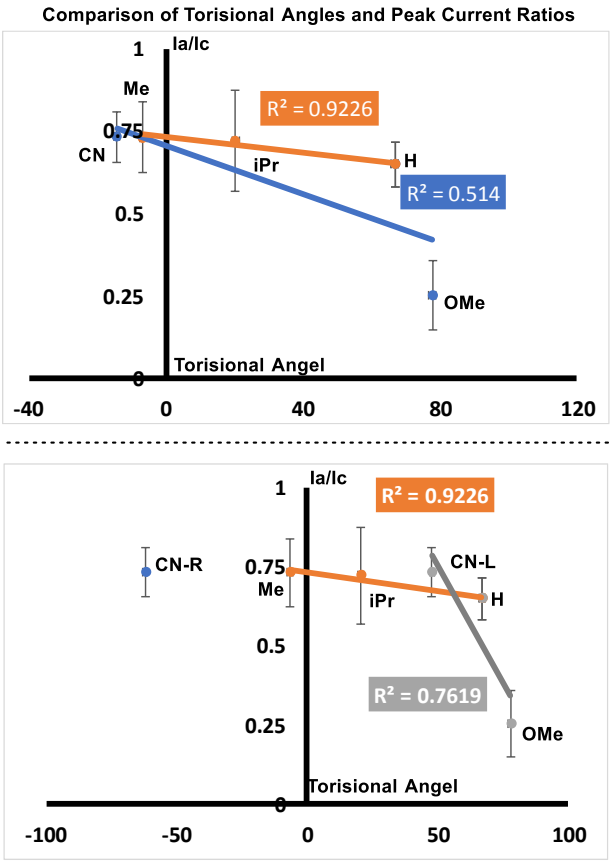

Figure 4 *Top) Comparison of the torsional angles versus peak current ratio (Ia/Ic). with summed torsional angles. Bottom) Comparison of torsional angle and peak current ratio with E separated into left and right side.*

conjugate pi-system is lost. Alternately, electronic perturbation of the imine bond resulted in significant effect of both imine torsional angle and peak current ratios observed in **Figure 2C** and **Figure 4 Bottom**. This highlights the relationship between electron density and torsional angle, and electron density and reversibility. When electron rich **D** has a torsional angle of 77.9 angstroms it has a reversibility of approximately 25% compared to the electron deficient **E** with a torsional angle of 14.9 angstroms and a reversibility of 75%. This affirms the earlier assertion that in conjugate systems torsional angle is a multi-variable parameter. However, the effect of electronic perturbations significantly impacts

the stability of the electron acceptor behavior while sterics present a negligible impact.

Further investigation of the crystal structure of **E** revealed the torsional angles between right and left side was more significant than other anisotropic ligands (**B**, **C** < 10% compared to **E** ≈ 78%). The torsional angle anisotropy of **E** allowed a new comparison to be made between the torsional angles of the left side and the torsional angle of the right side with a much stronger trend (R^2 =0.57 vs. R^2=0.76, respectively) in **Figure 4B**. This potentially indicates that the “left side” (more planar side) of **E** is the principal acceptor, whereas the right side is either non-participatory or possibly a donor.[32] While it is relatively common to have a molecule comprised of both a donor and an acceptor, further optical excitation experiments (pulse radiolysis, photoluminescence, etc.)are needed to confirm the DA behavior of the left and right side of **E.**

Computational Results

To more fully characterize the nature of the relationship between torsional angle and DA behavior, geometry optimizations were performed using local

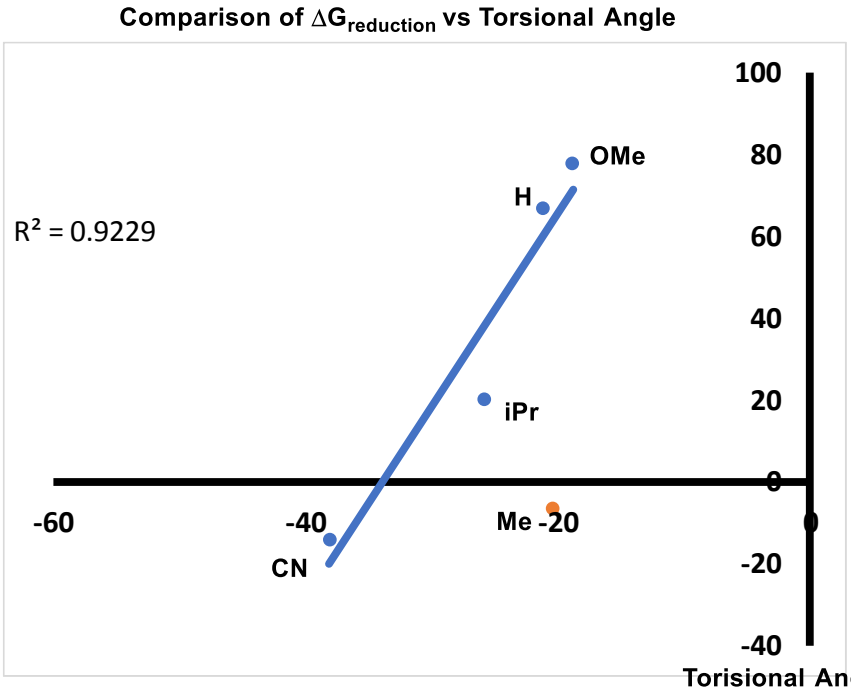

Figure 5) *Comparison of computationally derived dG vs torsional angle. R^2 with omitted methyl point.*

development version of Gaussian program to calculate the free energy of reduction ($\Delta G_{reduction}$) of structures **A-E**.[33] Calculations were performed using the hybrid B3LYP functional and 6-311G(d) basis set.[34,35] To account for dispersion, Grimme's D3 empirical dispersions were implemented.[36] A high degree of linearity was observed between the torsional angle of the crystal structures of **A-E** and the computed free energy of reduction. However, **B** was an anomaly with a lower torsional angle (-6.6 Å). Currently, the reduced torsional angle of **B** is believed to be caused by a more energetically favorable packing conformation in the solid-state crystal lattice. The volume of the crystal lattices of the 4,5

substituted BIPs is shown to scale proportionally with the size of the alkyl substituent.[22] The volume increase in the lattice requires different molecular packing in order to maximize the global entropy, which is believed to be the cause of the lower torsional angles in **B.**[37,38] The relationship becomes increasing strong when B is omitted generating an R^2 of 0.92 shown in **Figure 5**. The observed relationship of increasingly positive computed free energies of reduction as torsional angles increase are not surprising, and are attributed to ring strain.[39,40] As torsional strain increases, the molecules occupy a higher energy ground state resulting in an increased $\Delta G_{reduction}$. In this system $\Delta G_{reduction}$ is influenced independently from the stability of charge transfer (peak current ratios).

To examine the site of electron attachment/detachment, the natural ionization orbital (NIO) model was implemented.[41] The NIO model provides us with a compact and simplified orbital description on the site of ionization. With the provided orbital description of the attachment/detachment process, one can essentially determine the region that is more directly involved with the ionization process. **(Figure 6)** In our cases, all attachments/detachments of structures **A-E** distinctly show that the orbital involved in reduction is a predominantly π orbital localized on one side of the ligand. **Figure 6** shows the lowest unoccupied molecular orbital (LUMO) of structure **E** (top) and the NIO that corresponds to the

reduction of **E** (bottom). At first, one notices that the LUMO of **E** is more localized on one side of the molecule, while the NIO depicts more delocalization over the entire molecule. However, NIO analysis also shows that the NIO corresponding to the reduction of **E** is mostly the LUMO of the neutral structure of **E** as its major contributor (81%), and the slight delocalization observed in **Figure 6** (bottom) are smaller contributions from higher unoccupied orbitals of **E**. *This supports the*

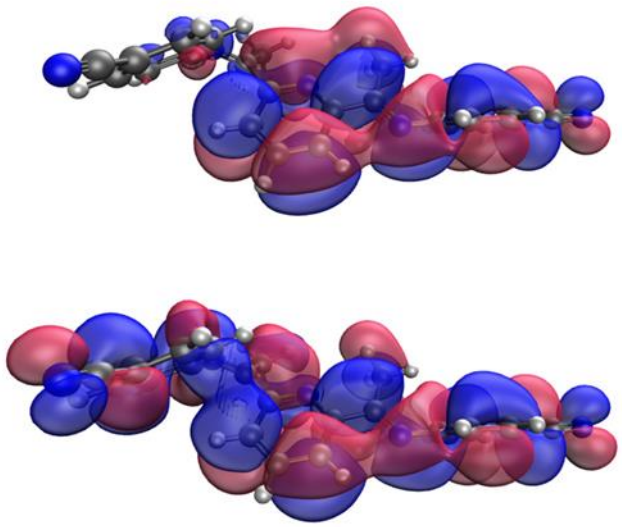

Figure 6) *Lowest unoccupied molecular orbital of E (top) and Natural ionization orbital for the ionization of E (bottom).*

*notion of **E** having only one side participate in the electron transfer.* The angular momentum of the relevant NIOs was inspected using Mulliken population analysis, which confirmed the predominantly p-character of the sites of electron attachment and detachment.[42] All relevant NIOs showed %p character of 92%-93%, which further supports the predominant π nature of the orbitals involved in the attachment/detachment processes. It is also worth noting that no relationship was observed between %p character and torsional angles, confirming that that

torsional angle did not impact the orbital overlap of the π system within the BIPs. All relevant NIOs and %p characters are presented in the supporting information.

Conclusion

With DA behavior becoming a critical area of investigation with broad scale applications, understanding the physical characteristics that lead to stable DA molecule is essential. Here we provide evidence demonstrating the effect of sterically influenced torsional angle on stability of DA behavior is *minimal*. However, electronic structure of the ionized molecule is critical and can impact torsional angle. This is demonstrated by structures **C** having a negligible difference on the degree of electrochemical reversibility compared to **D** and **E** electronic modulation of the radical anion bearing moiety. When the atom(s) and bonds with the highest probability density of a radical are electron rich, stability drops (**D**), opposed to electron deficient (**E**) where stability increased substantially (X=50%). While the effect that the torsional angle has on reversibility seems negligible, it does seem to play a role on the thermodynamic reduction energy. Currently further attempts are being made to explore the effect of electronically modulated torsional angles on DA stability in both organic and organometallic structures.

This work was performed with the assistance of: Hassan Harb, Justin Debow, James Fettinger, Hrant P. Hratchian, Ryan Baxter

REFERENCES

1. Foyer, C. H. Reactive oxygen species, oxidative signaling and the regulation of photosynthesis. *Environ. Exp. Bot.* **154**, 134–142 (2018).

2. Wang, Q. & Domen, K. Particulate Photocatalysts for Light-Driven Water Splitting: Mechanisms, Challenges, and Design Strategies. *Chem. Rev.* **120**, 919–985 (2020).

3. Hussain, F., Rahman, M. Z. & Nair, A. *Chapter 6 - Energy storage technologies*. *Energy for Sustainable Development* (Elsevier Inc., 2020). doi:10.1016/B978-0-12-814645-3.00006-7.

4. Wan, X., Li, C., Zhang, M. & Chen, Y. Acceptor-donor-acceptor type molecules for high performance organic photovoltaics - chemistry and mechanism. *Chem. Soc. Rev.* **49**, 2828–2842 (2020).

5. Urieta-Mora, J., García-Benito, I., Molina-Ontoria, A. & Martín, N. Hole transporting materials for perovskite solar cells: a chemical approach. *Chem. Soc. Rev.* **47**, 8541–8571 (2018).

6. Geng, Y., Tang, A., Tajima, K., Zeng, Q. & Zhou, E. Conjugated materials containing dithieno[3,2-: B:2′,3′- d] pyrrole and its derivatives for organic and hybrid solar cell applications. *J. Mater. Chem. A* **7**, 64–96 (2019).

7. Zampetti, A., Minotto, A. & Cacialli, F. Near-Infrared (NIR) Organic Light-Emitting Diodes (OLEDs): Challenges and Opportunities. *Adv. Funct. Mater.* **29**, 1–22 (2019).

8. Ma, X. *et al.* Highly efficient quaternary organic photovoltaics by optimizing photogenerated exciton distribution and active layer morphology. *Nano Energy* **70**, 104496 (2020).

9. Zhang, F., Dai, X., Zhu, W., Chung, H. & Diao, Y. Large Modulation of Charge Carrier Mobility in Doped Nanoporous Organic Transistors. *Adv. Mater.* (2017) doi:10.1002/adma.201700411.

10. Shen, Z. *et al.* Twisted donor–acceptor molecules for efficient deep blue electroluminescence with CIE y ∼ 0.06 . *J. Mater. Chem. C* (2020) doi:10.1039/d0tc01705a.

11. Zatsikha, Y. V. *et al.* Tuning Electronic Structure, Redox, and Photophysical Properties in Asymmetric NIR-Absorbing Organometallic BODIPYs. *Inorg. Chem.* **54**, 7915–7928 (2015).

12. Bredas, J. L. Mind the gap! *Mater. Horizons* **1**, 17–19 (2014).

13. Park, J. M., Jung, C. Y., Jang, W. D. & Jaung, J. Y. Effect of donor-π-acceptor structure on photochromism of dithienylethene-based dyes. *Dye. Pigment.* **177**, 108315 (2020).

14. Leith, G. A. *et al.* A Dual Threat: Redox-Activity and Electronic Structures of Well-Defined Donor–Acceptor Fulleretic Covalent-Organic Materials. *Angew. Chemie - Int. Ed.* **59**, 6000–6006 (2020).

15. Medjanik, K. *et al.* Electronic structure of large disc-type donors and acceptors. *Phys. Chem. Chem. Phys.* **12**, 7184–7193 (2010).

16. Kulkarni, A. P., Zhu, Y., Babel, A., Wu, P. T. & Jenekhe, S. A. New ambipolar organic semiconductors. 2. Effects of electron acceptor strength on intramolecular charge transfer photophysics, highly efficient electroluminescence, and field-effect charge transport of phenoxazine-based donor-acceptor materials. *Chem. Mater.* **20**, 4212–4223 (2008).

17. Ozkilinc, O. & Kayi, H. Effect of chalcogen atoms on the electronic band gaps of donor-acceptor-donor type semiconducting polymers: a systematic DFT investigation. *J. Mol. Model.* **25**, (2019).

18. Antoni, P. W., Bruckhoff, T. & Hansmann, M. M. Organic Redox Systems Based on Pyridinium-Carbene Hybrids. *J. Am. Chem. Soc.* **141**, 9701–9711 (2019).

19. Kaim, W. The shrinking world of innocent ligands: Conventionaland non-conventional redox-active ligands. *Eur. J. Inorg. Chem.* 343–348 (2012) doi:10.1002/ejic.201101359.

20. Lyaskovskyy, V. & de Bruin, B. Redox Non-Innocent Ligands: Versatile New Tools to Control Catalytic Reactions. *ACS Catal.* **2**, 270–279 (2012).

21. Kaim, W. Manifestations of noninnocent ligand behavior. *Inorg. Chem.* **50**, 9752–9765 (2011).

22. Bartolo, M. D., Brisbin, R. P., Ghosh, S. & Baxter, R. D. Impact of Bis (imino) pyridine Ligands on Mesoscale Properties of CdSe / ZnS Quantum Dots. (2020) doi:10.1021/acs.jpcc.0c06335.

23. Chirik, P. J. & Wieghardt, K. Radical ligands confer nobility on base-metal catalysts. *Science (80-.).* **327**, 794–795 (2010).

24. Chirik, P. J. Carbon–Carbon Bond Formation in a Weak Ligand Field: Leveraging Open-Shell First-Row Transition-Metal Catalysts. *Angew. Chemie - Int. Ed.* **56**, 5170–5181 (2017).

25. Bart, S. C., Lobkovsky, E. & Chirik, P. J. Preparation and Molecular and Electronic Structures of Iron(0) Dinitrogen and Silane Complexes and Their Application to Catalytic Hydrogenation and Hydrosilation. *J. Am. Chem. Soc.* **126**, 13794–13807 (2004).

26. Chirik, P. J. Iron- and Cobalt-Catalyzed Alkene Hydrogenation: Catalysis with Both Redox-Active and Strong Field Ligands. *Acc. Chem. Res.* **48**, 1687–1695 (2015).

27. Bowman, A. C., Tondreau, A. M., Lobkovsky, E., Margulieux, G. W. & Chirik, P. J. Synthesis and Electronic Structure Diversity of Pyridine(diimine)iron Tetrazene Complexes. *Inorg. Chem.* **57**, 9634–9643 (2018).

28. Small, B. L., Brookhart, M. & Bennett, A. M. A. Highly Active Iron and Cobalt Catalysts for the Polymerization of Ethylene. *J. Am. Chem. Soc.* **120**, 4049–4050 (1998).

29. Hammett, L. P. & Hammett, B. L. P. The Effect of Structure upon the Reactions of Organic Compounds . Benzene Derivatives Reactivity. **125**, 96–103 (1936).

30. Hammett, P. Vol. 50. **50**, 2666–2673 (1933).

31. Elgrishi, N. *et al.* A Practical Beginner's Guide to Cyclic Voltammetry. *J. Chem. Educ.* **95**, 197–206 (2018).

32. Miller, J. R., Calcaterra, L. T. & Closs, G. L. Intramolecular long-distance electron transfer in radical anions. The effects of free energy and solvent on the reaction rates. *J. Am. Chem. Soc.* **106**, 3047–3049 (1984).

33. Frisch, M. J. *et al.* G16_C01. Gaussian 16, Revision C.01, Gaussian, Inc., Wallin (2016).

34. Becke, A. D. Density-functional thermochemistry. III. The role of exact exchange. *J. Chem. Phys.* **98**, 5648–5652 (1993).

35. Krishnan, R., Binkley, J. S., Seeger, R. & Pople, J. A. Self-consistent molecular orbital methods. XX. A basis set for correlated wave functions. *J. Chem. Phys.* **72**, 650–654 (1980).

36. Grimme, S., Antony, J., Ehrlich, S. & Krieg, H. A consistent and accurate ab initio parametrization of density functional dispersion correction (DFT-D) for the 94 elements H-Pu. *J. Chem. Phys.* **132**, (2010).

37. Pauling, L. The Structure and Entropy of Ice and of Other Crystals with Some Randomness of Atomic Arrangement. *J. Am. Chem. Soc.* **57**, 2680–2684 (1935).

38. Savage, J. R. *et al.* Entropy-driven crystal formation on highly strained substrates. *Proc. Natl. Acad. Sci.* **110**, 9301–9304 (2013).

39. Khoury, P. R., Goddard, J. D. & Tam, W. Ring strain energies: Substituted rings, norbornanes, norbornenes and norbornadienes. *Tetrahedron* **60**, 8103–8112 (2004).

40. Turkowska, J., Durka, J. & Gryko, D. Strain release - an old tool for new transformations. *Chem. Commun.* **56**, 5718–5734 (2020).

41. Thompson, L. M., Harb, H. & Hratchian, H. P. Natural ionization orbitals for interpreting electron detachment processes. *J. Chem. Phys.* **144**, (2016).

42. Mulliken, R. S. Electronic population analysis on LCAO-MO molecular wave functions. I. *J. Chem. Phys.* **23**, 1833–1840 (1955).

Chapter 2
Impact of Bis(imino)pyridine Ligands on Mesoscale Properties of CdSe/ZnS Quantum Dots

Introduction

We investigate the effect of surface modification of CdSe/ZnS quantum dots (QDs) with bis(imino)pyridine (BIP) ligands. BIPs are a class of redox non-innocent ligands known to facilitate charge transfer in base metals on the molecular scale, but their behavior in nano- to meso-scale systems has been largely unexplored. Using electron microscopy, crystallography and ultrafast spectroscopy, we reveal that structure specific π-π stacking of the BIP molecules alters in-ter-dot separation in QD films, thereby leading to changes in optical and electronic properties. The three variations used are unsubstituted (BIP-H), dimethyl (BIP-Me) and diisopropyl (BIP-Ipr) bis(imino)pyridine, and when compared with the native octadecylamine (ODA) ligand, we find that both energy and charge transfer efficiencies between QDs are increased post-ligand exchange, the highest achieved through BIP-Ipr, despite its larger unit cell volume. We further investigate charge transfer from QD films to conducting (indium tin oxide, ITO) and semiconducting (zinc oxide, ZnO) substrates using time-resolved spectroscopy, and determine that the influence of the ligands is QD band gap dependent. In QDs with large band gap (2.3 eV) the BIP ligands facilitate charge transfer to both ITO and ZnO substrates, but in dots with small band gap (1.9 eV) they pose a hindrance when ZnO is used, resulting in reduced recombination rates. These results highlight the importance of investigating multiple avenues in order to optimize surface

modification of QDs based on the end goal. Finally, we verify that BIP ligands hasten the rate of QD photo brightening under continuous illumination, allowing the ensemble to achieve stable emission faster than in their native configuration. Our study sets the stage for novel charge transfer systems in the meso and nanoscale, yielding a diverse selection of new surface ligands for applications such as conductive materials and energy production/storage devices employing QDs.

Semiconducting quantum dots (QDs) are widely implemented in a variety of applications that leverage their size-tunable optical and electronic properties[1–3]. These include opto-electronic devices, such as, photodetectors[4–6], light-emitting diodes[7], and photovoltaics[8] among others, as well as devices for biomedical sensing[9,10] and diagnostics[11,12]. In order to optimize performance in these platforms, the treatment of QD surfaces is of critical importance, given the dots' large surface-to-volume ratios, and the one effective approach to surface passivation is *via* the use of organic ligands[13–15]. The most common among these are long chain aliphatic hydrocarbons, which have proven very successful in passivating surface defect-related trap states, thereby suppressing non-radiative recombination and stabilizing the QD core from photo-induced degradation, such as photo-darkening and photo-oxidation[16–19]. However, as they insulating molecules they hinder transport of charge carriers within QD films, reducing the conductivity, and substrates, but in dots with small band gap (1.9 eV) they pose a hindrance when ZnO is used, resulting in reduced recombination rates. Surface states also play a significant role in the photo-stability of colloidal QDs[30,31]. Photo-induced changes include photo brightening, photo darkening and photo-oxidation,

all of which result in changes in spectral emission intensity and wavelength over time. These shorten the shelf-life of QD samples and affect performance. The presence of ligands passivates the surface states and arrest these processes to varying degrees[18,32,33], and therefore, it is important to investigate this aspect following a ligand exchange. We verify that BIP ligands hasten the rate of QD photo brightening under continuous illumination, allowing the ensemble to achieve stable emission faster than in their native configuration.

Experimental and Analysis

To investigate intermolecular packing and size properties of QDs bound with organic BIP ligands, single crystal x-ray analyses were performed on each un-bound ligand shown in **Figure 1**. Substitution at the 2- and 6-position of the aniline sub-units produced solid-state molecular geometries that minimize steric interaction between the aniline and central pyridine units, causing an out of plane tilt of aromatic rings that increases with substituent size (molecular geometries shown in **1B**, *i*-Pr > CH_3 > H for degree of out of plane aromatic tilt). These results are consistent with previous reports of BIP ligands when chelated to a central metal in a Lewis basic fashion.[34] Although the geometric configuration of an single BIP ligand may be unsurprising, analysis of unit-cell packing is likely more informative for considering the bulk properties of numerous ligands creating a surface layer on the exterior of QDs. Due to the size disparity between QDs and BIP ligands, direct binding of the central pyridine to the QD surface is unlikely. Alternatively, induced dipole interactions between BIP □-systems and the QD surface could provide electrostatic attraction to promote an alternative mode of binding. Subsequent

layers of BIP ligands extending from the QD surface would depend on intermolecular forces between BIP ligands to determine the overall size of the BIP-ligated QDs.

As shown in **Figure 1C**, the unsubstituted BIP-H ligand interacts primarily through the pre-existing dipole of the

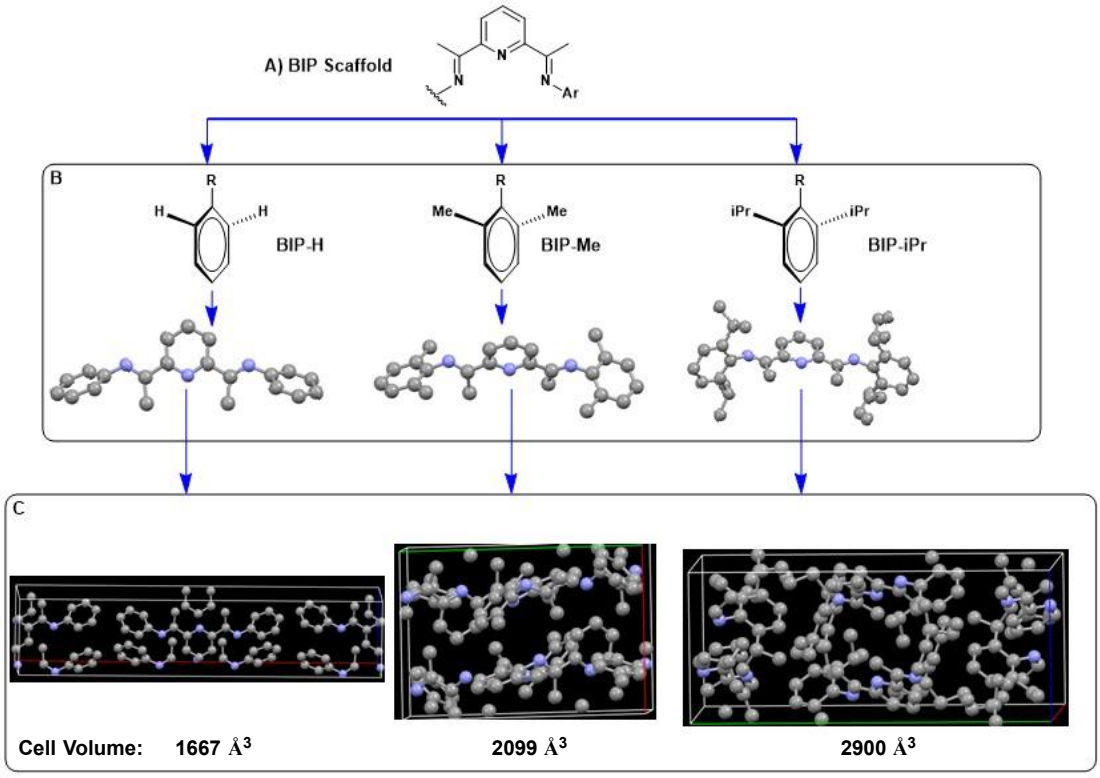

Figure 1. *(A) The basic BIP scaffold (B) The three modular units used to design the ligands: BIP-H (unsubstituted BIP), BIP-Me (Dimethyl BIP), and BIP-Ipr (Diisopropyl BIP) (C) Unit cell structures formed by the ligands on crystallization.*

central pyridine unit, resulting in a tightly packed unit cell with the smallest observed volume and less than 3-angstroms between repeating pyridine units. The reduced steric size of BIP-H renders it the only ligand studied that packed in this fashion. Unit cells for the remaining ligands showed primarily □-□ interactions between aniline subunits on neighboring ligand molecules, resulting in larger

values for distance of inter-ligand spacing and overall unit cell volume for BIP-Me (3.7 Å spacing, 2099 $Å^3$ volume) and BIP-Ipr (4.5 Å spacing and 2900 $Å^3$ volume) ligands. Such difference in packing and inter-ligand distance affects the physical and electronic properties of QDs ligated with the different BIP ligands, resulting in unique structure-activity relationships for the QDs depending on their environment (*vide infra*).

We summarize the basic spectroscopic characterization of QDs post ligand-exchange in **Figure 2**, along

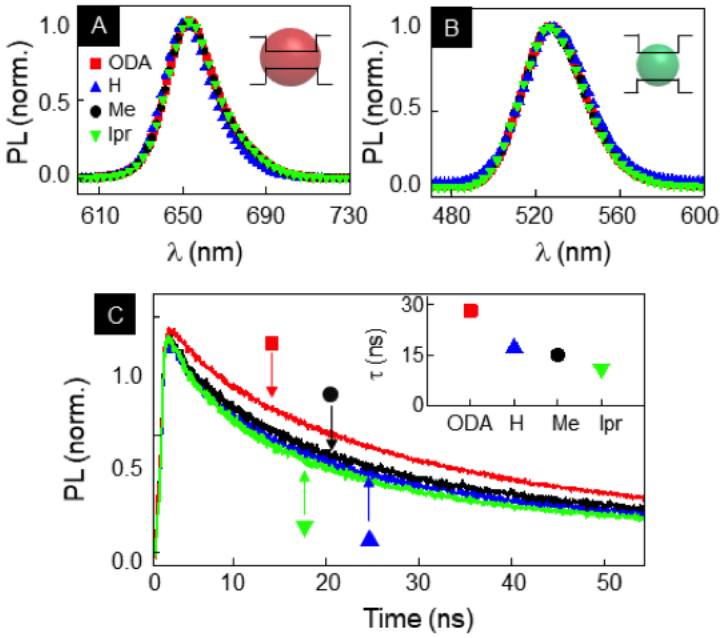

***Figure 2**. PL emission of (A) CZ640 and (B) CZ500 CdSe/ZnS QDs functionalized with ODA and the three BIP variations. (C) Time-resolved PL for all four populations of QD films.*

with results of the ODA-ligated control dots for comparison. This is an important check because surface functionalization can cause changes in quantum confinement, which result in an emission red-shift, or proliferation of surface defects, which may accelerate core photo-oxidation and darkening.

Photoluminescence (PL) of CZ640 and CZ500 nm QDs dispersed in solution shown in **Figure 2A** and **2B** confirm that there are no significant changes to any aspect of the emission spectra after the ODA ligands are exchanged by the three variations of BIP. Time-resolved PL measurements of the QDs in solution further reveal no distinction between dots functionalized with ODA, BIP-H, BIP-Me and BIP-Ipr, with the recombination time for all four populations being 40 ±3 ns. **Figure 2C** plots the time-resolved PL curves for QD films deposited on a glass substrate, and the charge recombination lifetimes are calculated by first using a bi-exponential fit $I_{PL} = A_1 e^{-t/\tau_1} + A_2 e^{-t/\tau_2}$ and then using the results to extract the average lifetime $\tau = (A_1\tau_1^2 + A_2\tau_2^2)/(A_1\tau_1 + A_2\tau_2)$. These values are plotted in the inset and show a clear variation between the native ODA and the BIP ligands, where τ decreases from 30 ns for ODA-QDs to 11 ns for BIP-Ipr. Faster lifetimes are the norm when comparing QDs in films versus isolated QDs in solutions, as inter-dot interactions allow additional routes of charge recombination. The most common mechanism is Forster resonant energy transfer (FRET), a dipole-dipole coupling where the efficiency $\varepsilon \sim 1/r^6$, *r* being the inter-dot separation[35]. This data would therefore suggest that the distance between QDs in the films, on average, decreases in ODA, BIP-H, BIP-Me and BIP-Ipr functionalized QDs.

In an ensemble, FRET occurs as a result of the size inhomogeneity of the QDs, and the roles of donors and acceptors are satisfied by the smaller and larger dots in the population. As a result, the extent of FRET varies with the wavelength of the

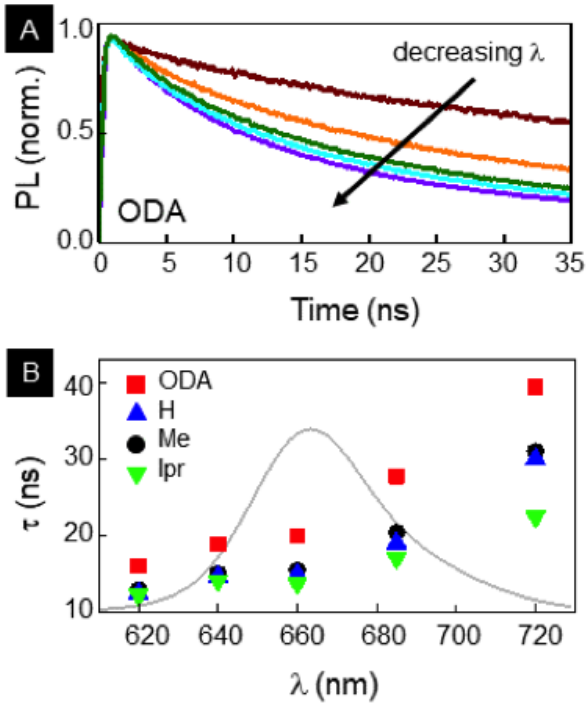

***Figure 3**. (A) Time-resolved PL curves at different spectral bands of the emission curve for ODA functionalized QD film. Lifetimes decrease with decreasing emission wavelength. (B) Spectrally resolved recombination times for all four QD films superposed on the corresponding spectral region over which they are evaluated.*

the emission wavelength at which the data is taken decrease. We verify this in **Figure 3**. Time-resolved PL curves for ODA-QDs with spectral resolution are plotted in **Figure 3A**, and the recombination can be seen to get faster as **Figure 3B** shows the extracted τ across the emission spectrum for all four differently ligated QDs. For ODA-QDs, we notice the expected variation of τ with wavelength, as well as the fact that at the long wavelength end τ approaches the lifetime measured in solution. For the BIP-functionalized QDs the trend is the same, but

the shorter lifetimes even at the reddest end of the spectrum imply that the recombination is much faster than the solution values. This would indicate that there is some other route in addition to FRET, and the nature of aromatic ligands would suggest that to be charge transfer.

There remains the possibility that some of the difference in recombination between the ODA-QDs and the BIP-QDs may be due to differences in inter-dot separation. To investigate that, we analyze transmission electron microscopy (TEM) images of close-packed QD films, such as those shown in **Figure 4A** and **4B**, for ODA and BIP-H functionalized QDs, respectively. For each type of QD, we generate a pair-distribution function (PDF) of its TEM image, as shown in **Figure 4C**, which plots the probability of finding a QD at a separation *r* from another QD. The first peak of this PDF is the average nearest-neighbor distance between the dots, and from this main figure which shows the PDF of ODA functionalized QDs, that distance is 8.3 nm. Similar analyses of the other QDs return varying QD separations and are plotted in the inset as a function of volume of the ligand unit cells. The inverse inverse relation provides an interesting insight into the packing efficiency of the different ways the three BIP ligands stack, as shown in **Figure 1C**. But it also implies there is a variation in FRET efficiency based on the ligand on the QDs. We return to the averaged lifetimes of the QD films in the inset of **Figure 2C** and using τ of ODA-QDs in film and solution, calculate an efficiency $\varepsilon_{Total} = 1 - \tau_{film}/\tau_{solution}$. As ODA is insulating, it is reasonable that energy transfer is the only inter-dot interaction among these QDs, and given that, we extract the FRET

constant R_o using $\varepsilon_{Total} = \varepsilon_{FRET} = 1/1 + ({}^{r}/_{R_o})^6$. R_o is defined as the separation where $\varepsilon_{FRET=50\%}$ and is theoretically calculated using the overlap integral of the donor emission spectrum with the acceptor absorption spectrum and their mutual molecular orientation. Here, we evaluate it by equating the two expressions of ε_{FRET} and estimate R_o= 7nm, which is very close to the rigorously calculated value of ~ 6.8nm.

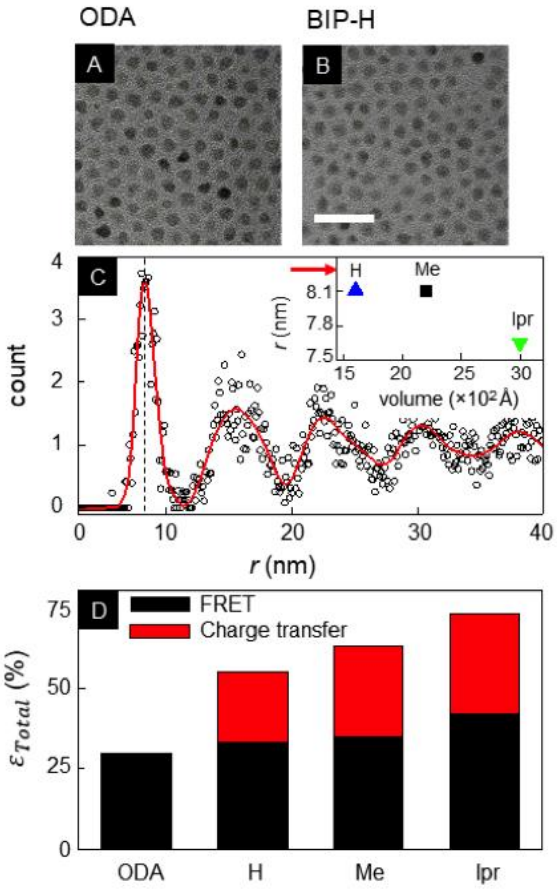

Figure 4. *TEM images of drop-cast QD films with (A) ODA and (B) BIP-H ligands. Scale bar: 50 nm. (C) Radial distribution of inter-dot separation r obtained from TEM images and (inset) r values of the BIP variations plotted with unit cell volume. Arrow indicates r for ODA functionalized QDs. (D) Energy and charge transfer efficiencies for the four QD populations.*

Then, we calculate ε_{FRET} for the QDs ligated with the BIP ligands using this distance dependent relation and the same R_o, and when plotted in **Figure 4D** it highlights that FRET does increase in case of the BIP-functionalized QDs. However, when we calculate ε_{Total} for the BIP-QDs using the formulation involving recombination times, those values are significantly greater than what is accounted for by FRET. For example, $\varepsilon_{Total} = 54\%$ for BIP-H QDs but $\varepsilon_{FRET} = 33\%$. We attribute this difference to charge transfer and calculate that efficiency $\varepsilon_{Total} -$

$\varepsilon_{FRET} = \eta$ to be 21% (BIP-H), 28% (BIP-Me) and 30% (BIP-Ipr) functionalized QDs. The increase of η between the different BIP ligands follows the trend of ε_{FRET} in them, both getting larger as inter-dot separation decreases in the QD films. distribution of inter-dot separation *r* obtained from TEM images and (*inset*) *r* values of the BIP variations plotted with unit cell volume. Arrow indicates *r* for ODA functionalized QDs. (D) Energy and charge transfer efficiencies for the four QD populations.

The confirmation of increased charge transport between QDs post-functionalization with the aromatic BIP ligands in the films is encouraging, but for optimal device performance, efficient and fast charge extraction at electrodes or other interfaces is also a necessity. With this inthe same (12.6 and 13 ns) on ITO and ZnO. When functionalized with BIP variations, recombination does get faster for both substrates, and this can be attributed to the charged delocalization of the aromatic rings. The schematics in **Figure 5C** demonstrates the relative band alignments of ITO and ZnO with the QD. The positional advantage of the QD conduction band makes electron transfer to either substrate energetically favorable when functionalized with ODA (**Figure 5C**, *left*). The BIP ligands are hole-accepting as their highest occupied molecular orbital (HOMO) aligns above the QD valence band (**Figure 5C**, *right*). This allows both the electrons and holes to be transferred away from the QD core, resulting in the observation of faster recombination in the BIP-QDs.

The same measurements for CZ640 QDs, which are larger and therefore have a smaller bandgap, have different results. For ODA, τ is again very similar on ITO and ZnO (14.7 and 15.3 ns, respectively). As the left schematic in **Figure 5D** shows, electron transfer to ITO is clearly favorable. Although the conduction band of ZnO ~ 0.1 eV above that of the QD, stochastic electron transfer is allowed. BIP-QDs show minor increase in electron transfer to ITO, driven again by the delocalized charges of the ligands. However, the change in recombination rate when mind, we investigate the recombination dynamics of the QD films when deposited on metallic and semiconducting substrates. The four differently ligated QDs are spin coated onto indium tin oxide (ITO) coated glass and on optically polished *n*-type zinc oxide (*n*-ZnO) single crystalline sample. The recombination time τ for both sized QDs on the two substrates are shown in **Figure 5A** and **5B**.

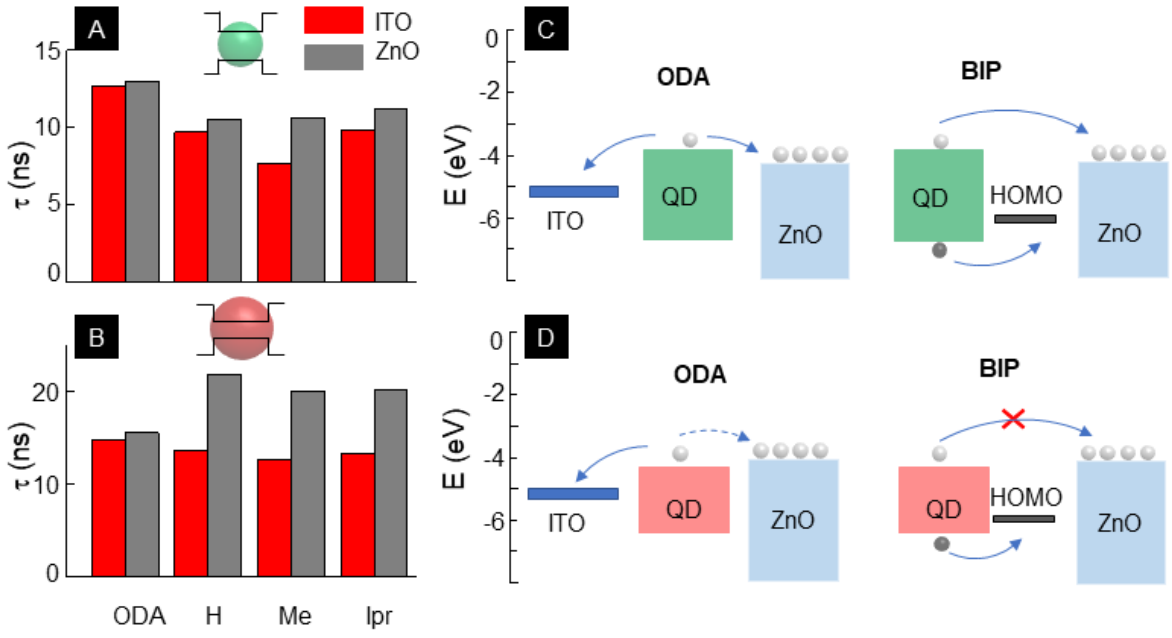

Figure 5*. Recombination times for (A) CZ500 and (B) CZ640 QD films functionalized with ODA and the BIP ligands, when deposited on conducting indium tin oxide (ITO) and semiconducting n-ZnO substrates. (C, D) Schematics sketching the charge transfer routes for the differently sized QDs.*

For CZ500 (the smaller QDs with the larger bandgap) charge recombination times when ligated with ODA, while expectedly shorter than on glass, are nearly BIP-QDs are deposited on ZnO is both significant and unexpected. Recombination lifetimes of BIP-QDs are approximately 30% longer than that of ODA-QDs, indicating that functionalization by the BIP ligands, while facilitating hole transfer, somehow prevents electron transfer from the QD. As the excitation energy used in our studies is smaller than the wide bandgap of ZnO, the presence of oxygen vacancies makes as-grown ZnO highly *n*-doped. Therefore, a possibility is that the delocalized electron cloud of the BIP ligands not only interacts with the photogenerated electrons in the QD core, but also with those in the conduction

band of ZnO. This has no consequence for the smaller QDs, where the difference between the energy levels of the QD core and ZnO drives electrons from the former to the latter. The near alignment of conduction bands in the case of the larger QDs and ZnO removes the advantage of this driving potential and concludes with the BIP ligands preventing electron extraction, while still allowing hole transfer. As a result, the recombination rate drops.

This modulation of charge carrier transfer based on band alignment between the QDs and the substrates mediated by the BIP ligands is an interesting find, as it opens up the possibility of tailoring functionalization based on specific needs of an application. But as mentioned earlier, the influence of ligands extends beyond that of transient charge transfer. Modification of QD surfaces may adversely affect long term photo stability of the QDs, and in **Figure 6** we compare how functionalization with BIP ligands alter photo induced effects.

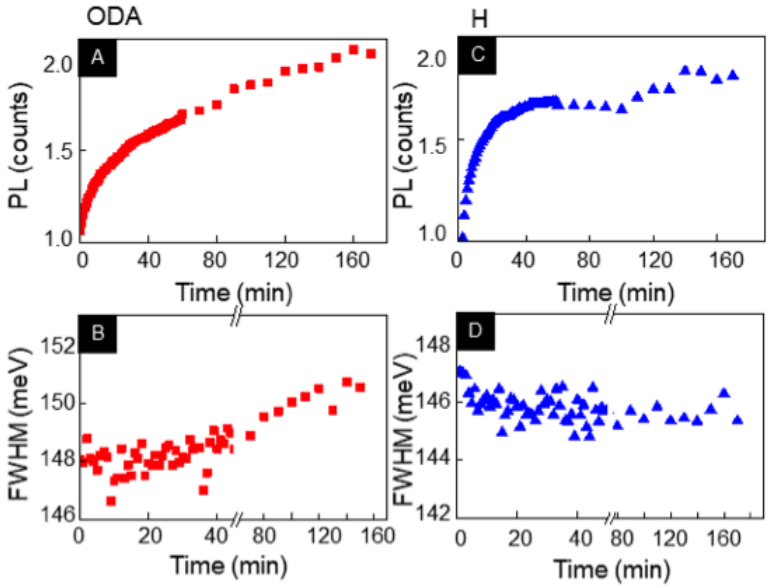

Figure 6. *(A) Spectrally integrated PL intensity and (B) FWHM of emission spectra for ODA-functionalized QDs un-der constant photoexcitation as functions of illumination time. (C) Spectrally integrated PL intensity and (B) FWHM of emission spectra for BIP-H-functionalized QDs measured under the same conditions.*

Figure 6A plots the spectrally integrated PL intensity for ODA-QDs over time under continuous photo excitation. It increases rapidly for the first 20 min and then continues to rise at a slower rate. This photo-brightening is a sign that there exist trap states within the bandgap of the core, most likely at the core-shell interface. Photo-generated carriers saturate these states, effectively de-activating non-radiative recombination centers, resulting in increasing PL. But over the same time frame, the FWHM of the QD ensemble increases, which, coupled with a small blue-shift of the emission wavelength, suggests there is photo-oxidation of the QD core. As this reduces the core diameter, the size inhomogeneity of the ensemble is

worsened, and the spectral width enhanced. In contrast, the photo-brightening of BIP-H QDs stabilize much faster and there is no observable increase in the emission FWHM over time. It is known that hole-accepting ligands can passivate QD surfaces more effectively than insulating ones[36], and our results confirm that here. It is also an important result as it demonstrates there are no detrimental long-term stability effects because of the BIP ligands.

Conclusions

Heterogenous charge transfer has continued to be a critical area of advancement in science due to the increase in demand of society on technology that predicates itself off interfacial charge movement. The role of heterogenous charge transfer in modern conveniences such as smart phones to energy infrastructure *cannot be underrepresented*. This importance on understanding heterogenous charge transfer has set the stage for this work and has shown both a novel and nuanced approach in which to modulate the kinetics of meso-scale heterogenous charge transfer. This was accomplished through the functionalizing semi-conducting quantum dots with redox non-innocent (RNI) ligands as hole acceptors. Through non-standard application of these RNI ligands, *controlled modulation* of the charge transfer dynamics has been achieved on meso-scale material. Moreover, this study has *illuminated* an intriguing band gap dependence on the photoluminescent recombination lifetimes, which can be observed across both deposited substrates of ITO and ZnO. While interesting, further work is needed in terms of characterizing the complex charge transfer dynamics as well as the effect of other RNI type ligands through tuning of the band gap.

Methods

Representative Ligand Synthesis: Bis(imino)pyridine ligands were synthesized through azeotropic distillation of 2,6-diacetylpyridine in toluene with the corresponding aniline. 2,6-diacetylpyridine (3 mmols), the aniline derivative (12 mmol), and *p*-toluenesulfonic acid (0.3 mmol) were added to a flame-dried 250ml round bottom flask. Dry toluene (100 ml) was added and the resulting mixture was refluxed using a Dean-Stark apparatus for 24 hours. The reaction mixture was cooled to room temperature and aqueous saturated sodium bicarbonate (100 ml) was added. This mixture was transferred to a separatory funnel the organic layer was extracted. The aqueous layer was washed 3-4 times with dichloromethane and the organic layers were combined, dried with sodium sulfate, and concentrated. The resulting concentrate was dissolved in 15-20 ml of methanol and placed at –20 Celsius for approximately 12 hours. The resulting yellow solid was vacuum filtered and washed with cold methanol. ^{1}H-NMR was used to assess purity and recrystallization in cold methanol was performed if impurities were detected. Single crystals were grown through solvation in hot methanol and allowed to cool over night at room temperature.

Ligand Exchange: ODA-capped CdSe/ZnS QDs CZ640 (bandgap 1.91 eV) and CZ500 (bandgap 2.3 eV) were purchased from NN-Labs. CZ640 QDs have a core diameter of 4.8 nm (5-10% size inhomogeneity) and CZ500, a 2.0 nm core diameter (10-15% size inhomogeneity). Their surfaces were modified using BIP-H, BIP-Me, and BIP-Ipr. Surface exchange was carried out under inert conditions by adding the QDs to a hexane solution containing an excess of the modifying

ligands relative to the native ODA. This solution is incubated for at least 5 minutes and then purified with acetonitrile (MeCN) and chloroform ($CHCl_3$). The QDs are then separated by centrifugation and dispersed in hexanes for optical measurements.

Sample preparation: For analysis in solution, the QDs were housed in 2.5 mL glass vials. For measurements of QD films, the dots were spin-coated onto glass, ITO (indium tin oxide), and *n*-ZnO (zinc oxide) substrates at 4500 rpm for 15 s, followed by annealing in an oven for 50^{o} C for 30 minutes.

Spectral characterization: For static spectroscopy we use a Princeton Instruments SP2300i spectrometer coupled to a thermo-electrically cooled deep depletion and low noise charge coupled detector, with a spectral resolution of 0.18 nm. An NKT Photonics Super-K laser tuned to 430 nm is used for excitation. For time-resolved measurements, the Super-K is set to a repetition rate of 26 MHz and the collected signal is first dispersed by the spectrometer, and then directed onto a single photon avalanche diode (SPAD) coupled to a PicoHarp 300 time-correlated single photon counting system (TCSPC) with an instrument response function of 28 ps.

Transmission Electron Microscopy (TEM): QD solutions were pipetted onto Pure C on 300 mesh Cu grids and left to dry overnight in an oven at 50^{o}C, then imaged in Thermo Fisher's Talos F200C G2 TEM.

This work was performed in collaboration with Mark D. Bartolo, James C. Fettinger, Sayantani Ghosh, and Ryan D. Baxter*

REFERENCES

1. Moreels, I. *et al.* Size-tunable, bright, and stable PbS quantum dots: A surface chemistry study. *ACS Nano* **5**, 2004–2012 (2011).

2. Wei, G. *et al.* Size-tunable Lateral Confinement in Monolayer Semiconductors. *Sci. Rep.* **7**, 1–8 (2017).

3. Fan, Q. *et al.* Lead-Free Halide Perovskite Nanocrystals: Crystal Structures, Synthesis, Stabilities, and Optical Properties. *Angew. Chemie - Int. Ed.* **59**, 1030–1046 (2020).

4. Grotevent, M. J. *et al.* Nanoprinted Quantum Dot–Graphene Photodetectors. *Adv. Opt. Mater.* **7**, 3–9 (2019).

5. Livache, C. *et al.* A colloidal quantum dot infrared photodetector and its use for intraband detection. *Nat. Commun.* **10**, 1–10 (2019).

6. Sukhovatkin, V., Hinds, S., Brzozowski, L. & Sargent, E. H. Colloidal quantum-dot photodetectors exploiting multiexciton generation. *Science (80-.).* **324**, 1542–1544 (2009).

7. Yu, S. *et al.* Enhanced optical and thermal performance of white light-emitting diodes with horizontally layered quantum dots phosphor nanocomposites. *Photonics Res.* **6**, 90 (2018).

8. Cho, C., Song, J. H., Kim, C., Jeong, S. & Lee, J. Y. Broadband light trapping strategies for quantum-dot photovoltaic cells (>10%) and their issues with the measurement of photovoltaic characteristics. *Sci. Rep.* **7**, 1–9 (2017).

9. Khan, S. A., Smith, G. T., Seo, F. & Ellerbee, A. K. Label-free and non-contact optical biosensing of glucose with quantum dots. *Biosens. Bioelectron.* **64**, 30–35 (2015).

10. Tajarrod, N., Rofouei, M. K., Masteri-Farahani, M. & Zadmard, R. A quantum dot-based fluorescence sensor for sensitive and enzymeless detection of creatinine. *Anal. Methods* **8**, 5911–5920 (2016).

11. Brazhnik, K. *et al.* Quantum dot-based lab-on-a-bead system for multiplexed detection of free and total prostate-specific antigens in clinical human serum samples. *Nanomedicine Nanotechnology, Biol. Med.* **11**, 1065–1075 (2015).

12. Sukhanova, A. *et al.* Oriented conjugates of single-domain antibodies and quantum dots: Toward a new generation of ultrasmall diagnostic nanoprobes. *Nanomedicine Nanotechnology, Biol. Med.* **8**, 516–525 (2012).

13. Yang, X. *et al.* Hydroiodic Acid Additive Enhanced the Performance and Stability of PbS-QDs Solar Cells via Suppressing Hydroxyl Ligand. *Nano-Micro Lett.* **12**, 1–12 (2020).

14. Chuang, C. H. M., Brown, P. R., Bulović, V. & Bawendi, M. G. Improved performance and stability in quantum dot solar cells through band alignment engineering. *Nat. Mater.* **13**, 796–801 (2014).

15. Choi, M. J. *et al.* Cascade surface modification of colloidal quantum dot inks enables efficient bulk homojunction photovoltaics. *Nat. Commun.* **11**, 1–9 (2020).

16. Krivenkov, V. *et al.* Ligand-Mediated Photobrightening and Photodarkening of CdSe/ZnS Quantum Dot Ensembles. *J. Phys. Chem. C* **122**, 15761–15771 (2018).

17. Zhang, Y. & Clapp, A. Overview of stabilizing ligands for biocompatible quantum dot nanocrystals. *Sensors* **11**, 11036–11055 (2011).

18. Cao, Y., Stavrinadis, A., Lasanta, T., So, D. & Konstantatos, G. The role of surface passivation for efficient and photostable PbS quantum dot solar cells. *Nat. Energy* **1**, 1–6 (2016).

19. Hines, D. A. & Kamat, P. V. Quantum dot surface chemistry: Ligand effects and electron transfer reactions. *J. Phys. Chem. C* **117**, 14418–14426 (2013).

20. Seker, F., Meeker, K., Kuech, T. F. & Ellis, A. B. Surface chemistry of prototypical bulk II-VI and III-V semiconductors and implications for chemical sensing. *Chem. Rev.* **100**, 2505–2536 (2000).

21. Yoshihara, T., Druzhinin, S. I. & Zachariasse, K. A. Fast intramolecular charge transfer with a planar rigidized electron donor/acceptor molecule. *J. Am. Chem. Soc.* **126**, 8535–8539 (2004).

22. Slama-Schwok, A., Blanchard-Desce, M. & Lehn, J. M. Intramolecular charge transfer in donor-acceptor molecules. *J. Phys. Chem.* **94**, 3894–3902 (1990).

23. Tamai, K. *et al.* Visible-Light Selective Photooxidation of Aromatic Hydrocarbons via Ligand-to-Metal Charge Transfer Transition on Nb2O5. *J. Phys. Chem. C* **121**, 22854–22861 (2017).

24. Sevov, C. S. *et al.* Physical Organic Approach to Persistent, Cyclable, Low-Potential Electrolytes for Flow Battery Applications. *J. Am. Chem. Soc.* (2017) doi:10.1021/jacs.7b00147.

25. Chirik, P. J. & Wieghardt, K. Radical ligands confer nobility on base-metal catalysts. *Science* (2010) doi:10.1126/science.1183281.

26. Kaim, W. Manifestations of noninnocent ligand behavior. *Inorganic Chemistry* (2011) doi:10.1021/ic2003832.

27. Small, B. L., Brookhart, M. & Bennett, A. M. A. Highly active iron and cobalt catalysts for the polymerization of ethylene [18]. *Journal of the American Chemical Society* (1998) doi:10.1021/ja9802100.

28. Lyaskovskyy, V. & De Bruin, B. Redox non-innocent ligands: Versatile new tools to control catalytic reactions. *ACS Catalysis* (2012) doi:10.1021/cs200660v.

29. Docherty, J. H., Peng, J., Dominey, A. P. & Thomas, S. P. Activation and discovery of earth-abundant metal catalysts using sodium tert-butoxide. *Nat. Chem.* (2017) doi:10.1038/nchem.2697.

30. Bol, A. A. & Meijerink, A. Luminescence quantum efficiency of nanocrystalline ZnS:Mn2+: 2. Enhancement by UV irradiation. *J. Phys. Chem. B* **105**, 10203–10209 (2001).

31. Xu, L., Chen, K., El-Khair, H. M., Li, M. & Huang, X. Enhancement of band-edge luminescence and photo-stability in colloidal CdSe quantum dots by various surface passivation technologies. *Appl. Surf. Sci.* **172**, 84–88 (2001).

32. Yoo, D. *et al.* Origin of the Stability and Transition from Anionic to Cationic Surface Ligand Passivation of All-Inorganic Cesium Lead Halide Perovskite Nanocrystals. *J. Phys. Chem. Lett.* **11**, 652–658 (2020).

33. Frederick, M. T. & Weiss, E. A. Relaxation of exciton confinement in CdSe quantum dots by modification with a conjugated dithiocarbamate ligand. *ACS Nano* **4**, 3195–3200 (2010).

34. Bart, S. C., Lobkovsky, E. & Chirik, P. J. Preparation and molecular and electronic structures of iron(0) dinitrogen and silane complexes and their application to catalytic hydrogenation and hydrosilation. *J. Am. Chem. Soc.* (2004) doi:10.1021/ja046753t.

35. Crooker, S. A., Hollingsworth, J. A., Tretiak, S. & Klimov, V. I. Spectrally Resolved Dynamics of Energy Transfer in Quantum-Dot Assemblies: Towards Engineered Energy Flows in Artificial Materials. *Phys. Rev. Lett.* **89**, 186802 (2002).

36. Tan, Y., Jin, S. & Hamers, R. J. Influence of hole-sequestering ligands on the photostability of CdSe quantum dots. *J. Phys. Chem. C* **117**, 313–320 (2013).

Chapter 3

Tuning three-dimensional nano-assembly in the mesoscale *via* bis(imino)pyridine molecular functionalization

Introduction

We investigate the effect of bis(imino)pyridine (BIP) ligands in guiding self-assembly of semiconducting CdSe/ZnS quantum dots (QDs) into three-dimensional multi-layered shells with diameters spanning the entire mesoscopic range, from 200 nm – 2 μm. The assembly process is directed by guest-host interactions between the BIP ligands and a thermotropic liquid crystal (LC), with the latter's phase transition driving the process. Characterization of the shell structures, through scanning electron microscopy and dynamic light scattering, demonstrates that the average shell diameter depends on the BIP structure, and that changing one functional group in the chemical scaffold allows systematic tuning of shell sizes across the entire range. Differential scanning calorimetry confirms a relationship between shell sizes and the thermodynamic perturbation of the BIP molecules to the LC phase transition temperature, allowing analytical modeling of shell assembly energetics. This novel mechanism to controllably tune shell sizes over the entire mesoscale *via* one standard protocol is a significant development for research on *in situ* cargo/drug delivery platforms using nano-assembled structures.

Advances in synthesis and assembly of nano-scale materials have offered routes towards meeting the increasing demands of precision engineering on progressively smaller length scales.[1,2] Many critical technologies, including computer circuitry, and medical and energy devices rely on specialized nano-scale materials for optimum performance. Strategies for assembling meso-scale constructs from nanoparticles (NPs) generally fall into two categories: ‘top down’ or ‘bottom up’. The former offers high precision and spatial order,[3,4] leading to the fabrication of ‘superlattices’ (SLs), but these are geometrically constrained and not easily scalable. ‘Bottom-up’ methods are driven by colloidal techniques and SLs developed to date include some that are on the microscale, are three-dimensional and compositionally heterogeneous, comprising up to three different types of NPs as building blocks.[5-12]

An intriguing subset of bottom-up self-assembly techniques is one guided by host-guest interactions of NPs (guests) with suitable functionalized surfaces dispersed in solvents (hosts).[13-18] These resultant assemblies are usually amorphous, possessing short-range order. However, the potential for modularity leading to structurally diverse and non-planar assemblies represents distinct advantages over SLs.[19-21] The host, when exposed to an appropriate set of conditions, directs the NPs to assemble into complex structures. The most common host materials are polymers and liquid crystals (LCs), and the assembly is driven by a phase transition, where the NPs are segregated at interfaces between the phases, leading to the formation of the superstructures. We have pioneered an LC-driven nano-assembly process,[22] where the NPs were

functionalized with mesogenic (LC-like) ligands and dispersed in 4-Cyano-4'-pentylbiphenyl, a common LC, known as 5CB. As the LC host is cooled, it transitions from an isotropic (disordered) phase to a nematic (ordered) phase. During the transition, the dispersed NPs are pushed together at the phase boundary, where they form three-dimensional shell structures, with walls consisting of multiple layers of NPs. We further demonstrated that these nano-assembled shells were capable of encapsulating and retaining cargo over a period of months.[13] These structures showed tremendous potential for cargo delivery in biomedical and bioengineering applications,[23-25] as they could be optically activated to rupture within seconds by photothermally disrupting the shell integrity. But this approach, though a novel and versatile form of nano-assembly, has practical hindrances. One is that the mesogenic ligand used in driving the assembly are highly cytotoxic; the other is the lack of control in tuning shell sizes, leading to structures too large to be suitable for *in vitro* applications.[26,27] In this work, we move away from mesogenic ligands and focus on bis(imino)pyridine (BIP) family of ligands,[28] which, in addition to being biocompatible, allow structural modularity and offer a route to fundamentally understand, and thereby, manipulate the assembly process to controllably tune the shell sizes. Using Cdse/ZnS core/shell quantum dots (QDs) functionalized with BIP molecules and dispersed in 5CB, we demonstrate that subtle changes to the BIP structure results in a tunable assembly process, yielding shells of predictable sizes. Dimethyl BIP, unsubstituted BIP and diisopropyl BIP create shells with average diameters of 200 nm, 400 nm and 900 nm, respectively,

confirmed using scanning electron microscopy (SEM) and dynamic light scattering (DLS). We further determine both the essential chemical structure needed for the assembly process using a series of control ligands, and the thermodynamic parameters associated with the isotropic-nematic phase transition of 5CB that allows size tunability. Data from differential scanning calorimetry (DSC) of LC-BIP mixtures agree with our analytical model of how shell radius is predicated by the free energy balance of BIP-functionalized QDs in the host at the interface of the two. And finally, cell toxicity studies confirm that the dimethyl- and isopropyl-BIP ligands are non-toxic even at high concentrations, thereby making practical applications for controlled delivery of growth factors into developing tissues a possibility.

Shell assembly

The shell assembly process begins with QD surface functionalization. Octadeclyamine (ODA)-capped CdSe/ZnS QDs (NN-Labs) with a core diameter of 4.8 nm (5–10% size inhomogeneity) undergo ligand exchange under inert conditions. The QDs are added to a hexane solution containing an excess of the modifying ligands relative to the native ODA. This solution is incubated for 5 min, and then purified with acetonitrile and chloroform. The QDs are then separated by centrifugation and redispersed in toluene. Following surface modification, a 1.5 mL microcentrifuge tube (mct) is filled with 20 µL of 5CB (Sigma Aldrich) in isotropic phase and mixed with 20 µL of functionalized QDs diluted to 0.5 mg/mL in toluene. The QD-LC mixture is heated to 50^{o}C in a sonication bath for a minimum of 5 hours to obtain complete QD dispersion within the isotropic LC.

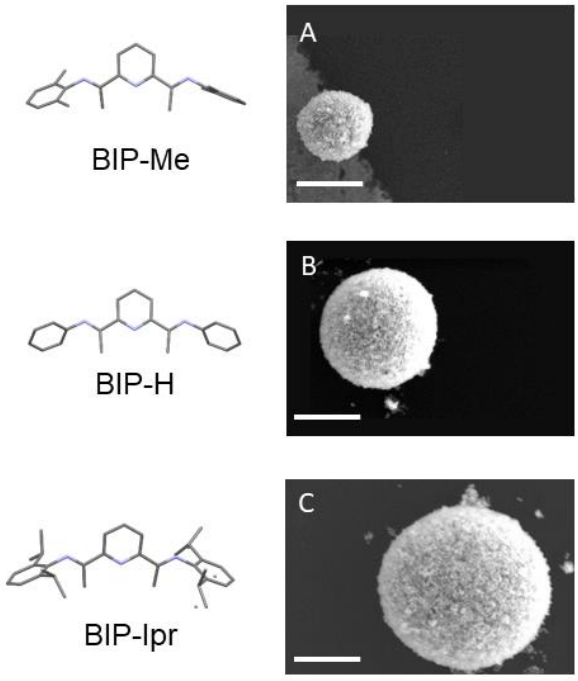

Figure 1 *(A – C) SEM images of QD shells formed using BIP-Me, BIP-H and BIP-IPr, respectively. Ligand structures are shown to the left. All scale bars are 200 nm.*

Then the mct is cooled to 25°C, during which, as the LC is driven through its isotropic-nematic transition temperature of 34.4°C, the QDs are expelled from the ordered regions to minimize free energy and as they are confined in shrinking volumes within the host, π-π interactions between the ligands drive self-

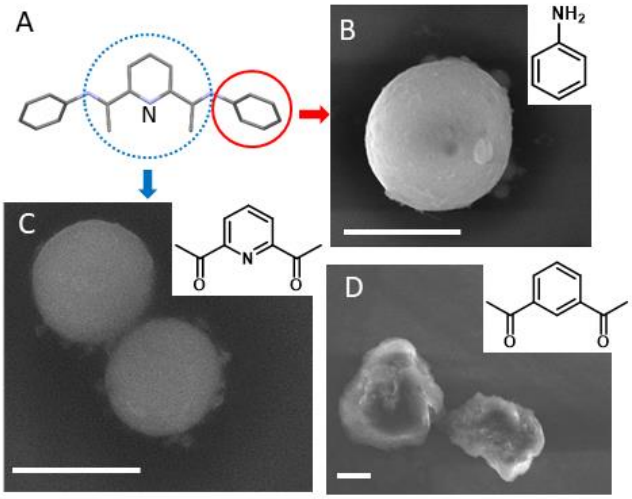

Figure 2 *(A) Schematic outlining the components of BIP used as control. Dashed and solid circles highlight the aromatic/nonaromatic lewis basic nitrogens (DAP/aniline). SEM images of QD shells formed using (B) Aniline, (C) 2,6-DAP and (D) 1,3-DAB. All scale bars are 1 μm. Chemical structures of the component molecules are shown as accompanying insets.*

assembly to form shells.

Three variations of BIP ligands are examined: dimethyl-BIP (BIP-Me), unsubstituted-BIP (BIP-H) and diisopropyl-BIP (BIP-IPr). The results, following the ligand exchange and shell assembly protocols, are summarized in **Figure 1**. Figure 1A – 1C are SEM images of shells assembled with BIP-Me, BIP-H and BIP-IPr, respectively, and show clear variation in shell diameter. Before delving deeper into the physiochemical relationships that govern shell sizes, in order to further pinpoint which chemical component in the BIP structure drives the π-π

interactions between the ligands to facilitate shell assembly, we isolated the structural components of the BIPs, as shown in **Figure 2A**, and attempt shell formation with aniline, 2,6-DAP (Diacetylpyridine) and 1,3-DAB (Diacetyl benzene). Figure 2B – 2C are the corresponding SEM images of shells formed by QDs functionalized these. We find that aniline (Figure 2B) and 2,6-DAP (Figure 2C) functionalized QDs do form shells, with diameters in the range 800 nm – 2 μm. However, QDs functionalized with 1,3-DAB (Figure 2D) do not form shells, instead forming large (> 2 μm) and irregular clusters. Such clusters are typically observed when QD surfaces are functionalized with long organic chains, such as ODA. This set of results demonstrates that in addition to aromaticity, the presence of nitrogen is critical to shell formation.

In **Figure 3** we turn to accurately recording the size inhomogeneity of the shells, inherent in any colloidally processed ensemble. Figure 3A and 3B are SEM images of shells produced in one synthesis process using BIP-IPr functionalized QDs, and clearly demonstrate significant size variation. We

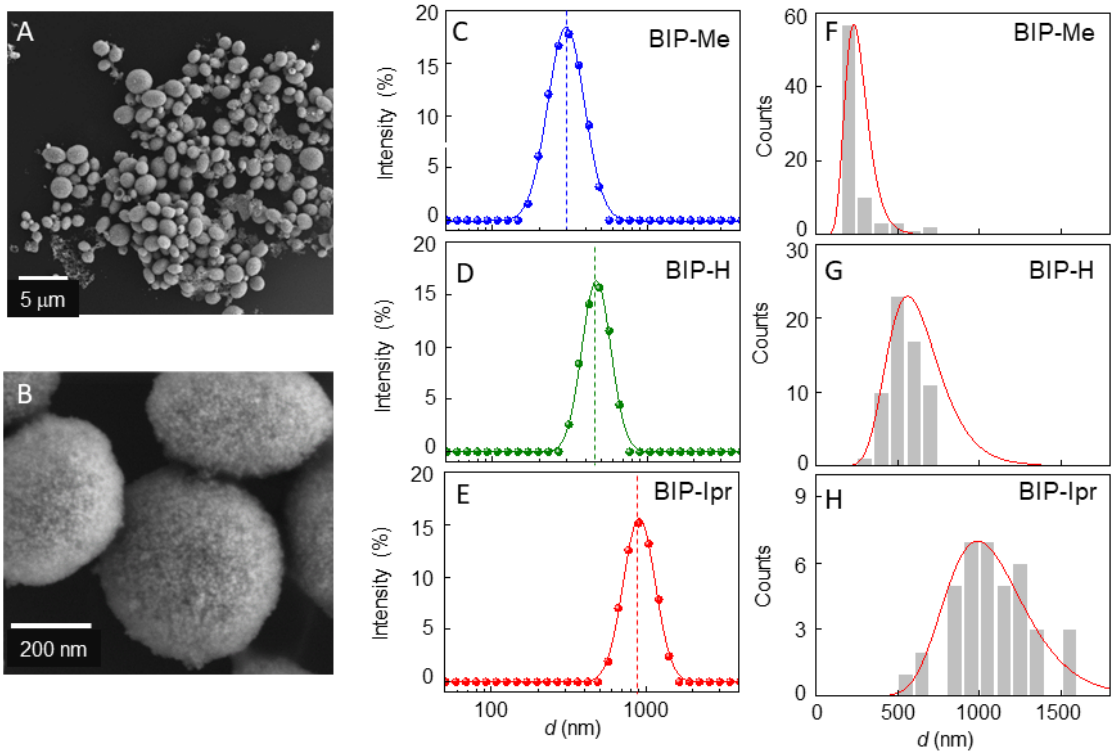

Figure 3 *(A, B) SEM images of shell ensembles in a typical synthesis (C – E) DLS data of ensembles of shells for each of the BIP ligands. (F – H) Shell size distribution obtained from image analysis of multiple samples of each kind for the three different BIP ligands.*

characterize this inhomogeneity in two ways. First, using dynamic light scattering (DLS) measurements, where samples of each type of BIP-QD shells are mixed with 40 µL of chloroform ($CHCl_3$) and centrifuged for 10 minutes at 6000 rpm. The aliquot is removed, redispersed in $CHCl_3$ for a second centrifugation, and redispersed in 250 µL of toluene by sonication. A Malvern Zetasizer Pro is used

to conduct DLS at 40 ^{o}C, and the results are shown in Figure 3C – 3E. These confirm the trends observed in SEM images of single shells, i.e., BIP-Me functionalized QDs form the smallest shells, with a mean diameter of 300 nm and a variance of 100 nm. For BIP-H and BIP-IPr, the mean shell diameters (variances) are 460 nm (125 nm) and 900 nm (300 nm), respectively. To obtain a better estimate of shell sizes and distributions, we additionally performed a more thorough global statistical analysis of the BIP-functionalized shells *via* image processing of SEM data of all synthesis attempts, a total of 232. The results are plotted in Figure 3F – 3H and the results further substantiate the prior observations. However, while the correlation between BIP variants and shell

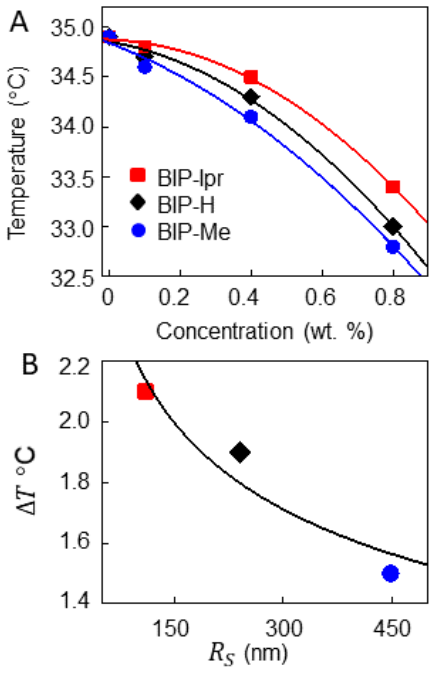

Figure 4 *(A) DSC results summarized for the three BIP ligands, plotting the 5CB isotropic-nematic transition temperature with increasing ligand concentration. (B) Average shell radius R_S varying with the change in the transition temperature ΔT for each ligand. The fit is explained in the text.*

sizes is reassuring, investigating the mechanism by which the sizes are tuned is of greater fundamental importance, as that would provide the means for establishing this assembly technique as a standard protocol capable of rational design.

First, we sought to ascertain whether the steric ligand parameters affect the mean shell size. Unit cell structures of the BIP ligands, obtained from crystallization data,[28] reveal that BIP-H has the smallest volume, while BIP-IPr the largest, which does not correlate to shell size, since BIP-Me functionalized QDs lead to the smallest shells. Packing density of QDs in the shell walls was next suspected to determine shell size, but with BIP- IPr QDs having the smallest inter-dot separation, this physical property was also not in agreement with observed shell size variation.[28] This lack of a relationship to any physiochemical property (lattice dimensions, torsional angles, sterics, lattice volumes) prompted an investigation of the thermodynamic effect of the ligands on the host 5CB using differential scanning calorimetry (DSC) in **Figure 4**. The isotropic-nematic phase transition in LCs is weakly first order, and in scanning calorimetry measurements demonstrate peaks at the transition temperatures.[29] For 5CB alone, we observe the transition at 34.8°C. When the measurements are repeated with the ligands added to it, the transition temperature decreases to different extents for the three variants, shown in Figure 4A. Incorporation of additives lead to suppression of the LC transition temperature as the added materials act like an impurity.[30-32] Therefore, the increased suppression with increasing ligand concentration is logical. When the radius of the shell R_S is plotted against the change in transition

temperature ΔT in Figure 4B we notice a monotonically decreasing relation. A simple power law fit of $\Delta T \propto {R_S}^{-\alpha}$ returns $\alpha = 0.22$. In addition, we can also assess the wall thickness of ruptured shells using SEM imaging. **Figure 5A** and **5B** show a BIP-Me shell with a wall thickness t_S of 114 nm, and a BIP-iPr shell of t_S 29 nm, respectively. Correlating thickness t_S to shell radius R_S (**Figure 5C**) seems to suggest shell walls get thinner with increasing shell diameter. Given the small population of shells that rupture, the error bars in this plot are significant and we therefore do not draw any quantitative conclusion from it.

Physics of Shell formation

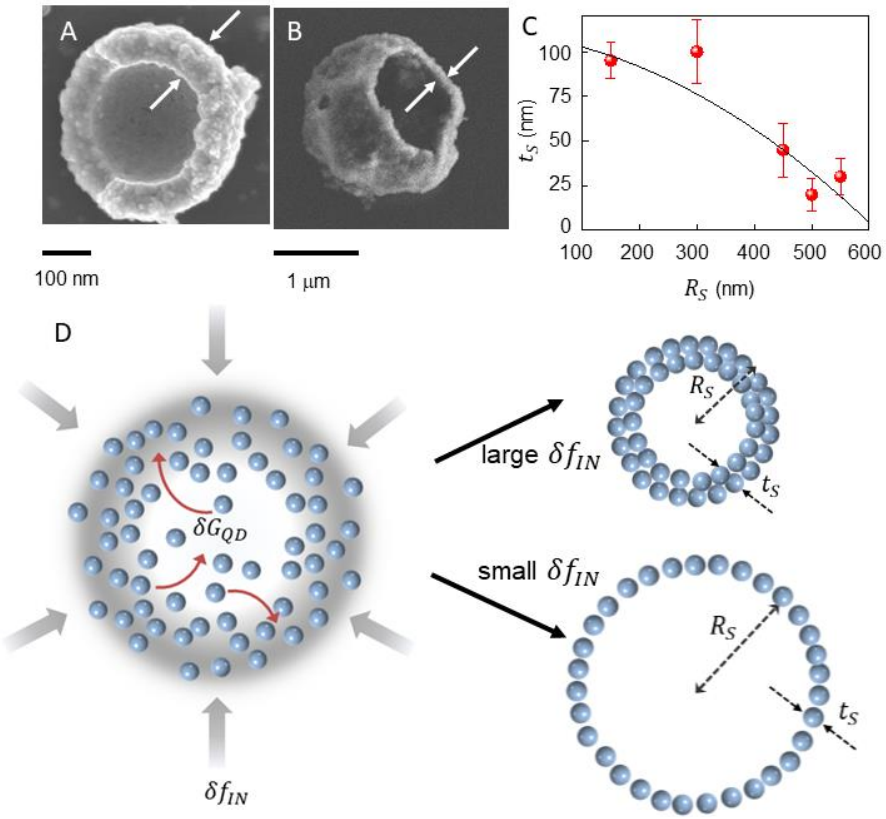

Figure 5 *Ruptured shells of (A) BIP-Me functionalized and (B) BIP-IPr functionalized QDs showing different wall thicknesses. (C) Plot of t_s as function of R_s (D Schematic depicting the formation. R_s: shell radius; t_s: shell wall thickness; R_s: shell radius; P_{IN}: Pressure from nematic phase boundary; δf_{IN}: free energy density change during transition.*

To understand why the small changes to BIP scaffolds result in such significant variation in shell size, we develop a simple model of the assembly mechanism, shown in **Figure 5D**. During the shell formation process, the shell wall is a boundary between the nematic (N) phase outside and the isotropic phase (I) inside. This boundary, or front, has an effective pressure differential P_{IN} associated with it that serves as the initial driving force, which in turn varies

linearly[33] with the free energy change δf_{IN} per unit volume between the two homogenous phases, leading to:

$$P_{IN} = \delta f_{IN} \quad (1)$$

The effective pressure differential creates a compressive stress γ in the shell, which can be expressed using the Young-Laplace relation as:

$$\gamma = R_S P_{IN}/2 \quad (2)$$

where R_S is the shell radius. As long as the compressive stress exceeds the free energy gain per unit area increase of the shell over its thickness by QD insertion, the shell will continue to shrink. The process stops when the stress becomes equal to this free energy gain, which can be expressed in terms of the free energy gain δG_P per unit volume of QD inserted into the shell as:

$$\delta G_P t_S = \gamma \quad (3)$$

where t_S is the shell thickness. Combining these equations, the shell radius is:

$$R_S = 2t_S \left({}^{\delta G_P}/_{\delta f_{IN}} \right) \quad (4)$$

The energy cost δG_P is dominated by the QD properties, rather than the ligands, but δf_{IN}, defined as the change in free energy between the N and I phases, is directly proportional to T_{IN}, the thermotropic transition temperature.[34] Therefore, the lower the value of T_{IN} (the larger the change ΔT) the larger the value of R_S where the shell structure will stabilize. The inverse relation of R_S and ΔT in Figure 4B would suggest our data agrees with this, but eq. (4) contains the term t_S, which, as Figure 5A – 5C shows, is not constant with shell size. A logical assumption would allow us the following framework: when the phase transition

begins, the isolated QDs are dispersed in the LC and the thermodynamic effect of the ligands is minimal. Therefore, the number of QDs swept into the initial bubble is independent of the BIP variant, which would imply $R_S^2 t_S \approx$ constant. This implies $t_S \propto R_S^{-2}$ and incorporating this in eq. (4) implies $\delta f_{IN} \sim \Delta T \propto R_S^{-1/3}$, close to the 0.22 obtained. The discrepancy could be attributed to the fact that we have assumed δG_{QD} is unchanged with R_S.

Cytotoxicity studies

Apart from being able to controllably tune the shell sizes, the biocompatibility of the ligands is an additional parameter than needs evaluation. We examined the cell toxicity for the three ligands, BIP-Me, BIP-H, and BIP-IPr,

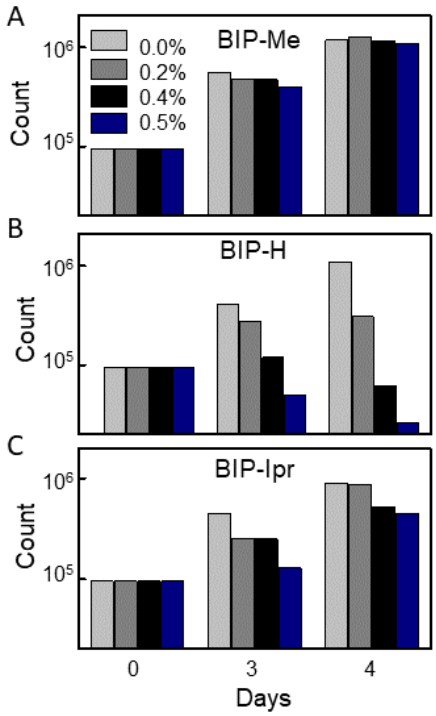

Figure 6 *Cells counted over time show cytotoxicity results for (A) BIP-Me (B) BIP-H and (C) BIP-IPr ligands taken over several days for different ligand concentrations by weight.*

shown in **Figure 6**. C2C12 skeletal myoblasts (ATCC) were plated into 12 well-plates at a density of 10,000 cells/ cm^2, fed cell culture medium containing Dulbecco's Modified Eagle Medium (DMEM), 10% fetal bovine serum (FBS), 2mM glutamine, and $1x10^{-4}$M nonessential amino acids, and cultured at 37℃ under 5% CO_2. After 1 day, the media was replaced with 1 mL of new medium with the ligands added to the wells over a range of concentrations and cultured over time. Viability assays were performed with trypsin exclusion and counted on a using a hemocytometer. Figure 6A – 6C plot counts over Days 0 – 4 for cells with varying concentrations of ligands added to the cell culture medium. For every ligand concentration, six plates were used. BIP-Me and BIP-IPr appear to be tolerated well, even up to 0.5% ligand by weight, but BIP-H hinders cell growth above 0.2%. This moderately positive outcome is encouraging, indicating that when this versatile assembly process is performed with non-toxic QDs or metallic nanoparticles as the constituents,

Conclusions

We have demonstrated that nanoshell self-assembly can be tuned in a liquid crystalline environment using non-mesogenic organic ligands to alter the enthalpy associated with the isotropic to nematic phase change. Differential scanning calorimetry confirms that shell size distributions are directly influenced by the non-mesogenic organic ligands. The influence of these ligands is predicated on their ability to iteratively depress the isotropic to nematic phase change temperature (T_{IN}) of the liquid crystal host (5CB). This depression of T_{IN} on shell size is observed using both SEM and DLS to significantly influence the

center of the size distribution of self-assembled structures. While further investigation of the host-guest interaction of liquid crystal facilitated self-assembly systems are being pursued, this work stands as one of the first examples of utilizing ligands to influence the thermodynamics of the host-guest interaction for directed assembly in a manner that controllably tunes the size of the assembled structures across the entire mesoscale. Further, the fact that the ligands are biocompatible to a significant extent open up possibilities of application in novel areas, such as in the field of tissue engineering, where the incorporation of nanomaterials is a relatively new effort. Nano-assembled capsules such as these could provide a platform for improved delivery of biological materials *in vitro*, for example, growth factors (GFs), which are proteins that direct cell growth and differentiation.[35] The standard approaches of either mixing the GFs into the extracellular matrix[36] or allowing them to be absorbed on surfaces of interest,[37] suffer from a lack of control in terms of time of release, as well as inefficient retention. While some nano-assembled carriers[38-42] have been devised, none have optimized the requirements of high loading efficiency, stability, and well-defined and predictable release profile. The size-tunable shells described here could resolve many of these issues, and combined with the success of earlier works,[13] may prove to be a model platform for *in vitro* cargo delivery in 3D tissue engineering applications.

This work was performed in collaboration with Mark Bartolo, Michael Leville, Arya K. Rajan, Basharat Jahan, Kara E. McCloskey, Ajay Gopinathan, Sayantani Ghosh, Ryan Baxter

---

References

1. Chuanhui Huang, Xiangyu Chen, Zhenjie Xue, Tie Wang, *Sci. Adv*. **2020**, 6, 1.
2. Jose V. Rival, et. al., *Small* **2021**, 2005718, 1.
3. S. Zhang, et al., *Nanoscale* **2016**, 8, 9118.
4. A. Maier, R. Löffler, M. Scheele, *Nanotechnology* **2020**, 31, 405302.
5. E. Josten, E. Wetterskog, A. Glavic, P. Boesecke, A. Feoktystov, E. Brauweiler-Reuters, U. Rücker, G. Salazar-Alvarez, T. Brückel, L. Bergstrm, *Sci. Rep.* **2017**, 7, 1.
6. A. Dong, J. Chen, P. M. Vora, J. M. Kikkawa, C. B. Murray, *Nature* **2010**, 466, 474.
7. A. E. Saunders, et al., *Nano Lett.* **2004** 4, 1943.
8. B. Yoon, et al., *Nat. Mater*. **2014**, 13 807.
9. D. Wang, A. Yang, A. J. Hryn, G. C. Schatz, T. W. Odom, *ACS Photonics* **2015**, 2, 1789.
10. A. Dong, X. Ye, J. Chen, C. B. Murray, *Nano Lett.* **2011**, 11, 1804.
11. X. Huang, J. Zhu, B. Ge, F. Gerdes, C. Klinke, Z. Wang, *J. Am. Chem. Soc.* **2021**, 143, 4234.
12. R. Schreiber, et. al., *Nat*. *Nanotechnol*. **2014**, 9, 74.
13. M. T. Quint, et. al., *Sci. Rep.* **2017**, *7*, 1.
14. S. C. Manna, S. Mistri, A. D. Jana, *CrystEngComm* **2012**, *14*, 7415.
15. M. Xiao, Y. Xian, F. Shi, *Angew. Chemie* **2015**, *127*, 9080.
16. Y. Zheng, Z. Yu, R. M. Parker, Y. Wu, C. Abell, O. A. Scherman, *Nat. Commun.* **2014**, *5*, 1.

17. W. I. Park, Y. Kim, J. W. Jeong, K. Kim, J. K. Yoo, Y. H. Hur, J. M. Kim, E. L. Thomas, A. Alexander-Katz, Y. S. Jung, *Sci. Rep.* **2013**, *3*, 1.
18. S. Shi and T. P. Russell, *Adv.Mater.***2018**, 30, 1800714.
19. Yingqing Lu, Jiaping Lin, Liquan Wang, Liangshun Zhang, and Chunhua Cai, *Chemical Reviews* **2020** 120, 4111.
20. Guofen Song, et. al., *Small* **2019**, 15, 1805308.
21. Hao Yao, Yin Ning, Craig P. Jesson, Jia He, Renhua Deng, Wei Tian, and Steven P. Armes, *ACS Macro Letters* **2017** 6 1379.
22. A. L. Rodarte, R. J. Pandolfi, S. Ghosh, L. S. Hirst, *J. Mater. Chem. C* **2013**, *1*, 5527.
23. I. Wheeldon, A. Farhadi, A. G. Bick, E. Jabbari, A. Khademhosseini, *Nanotechnology* **2011**, 22, 212001.
24. Aida Llauró, et. al., *Nanoscale*, **2016**, 8, 9328
25. Raj Kumar, Sameer V. Dalvi, and Prem Felix Siril, *ACS Applied Nano Materials* **2020** 3 4944.
26. Saurabh S Mogre et al 2020 Phys. Biol.17 061003
27. A. Sen Gupta, *WIREs Nanomed Nanobiotechnol,* **2016** 8 2550.
28. Mark D. Bartolo, Ryan P. Brisbin, Sayantani Ghosh, and Ryan D. Baxter, *J. Phys. Chem. C* **2020**, 124, 22677.
29. Katleen Denolf, Bert Van Roie, Christ Glorieux, and Jan Thoen, *Phys. Rev. Lett.,* **2006**, 97,107801.

30. Karen Kolya Vardanyan, Adam Thiel, Bryce Fickas and Alexander Daykin, *Liquid Crystals*, **2015**, 42, 445.
31. Prabir K. Mukherjee, *Liquid Crystals*, **1997**, 22, 239.
32. Saswati Chakraborty & Anuradha Mukhopadhyay, *Phase Transitions*, **2009**, 82, 115.
33. Alejandro D. Rey and E. E. Herrera-Valencia, *Soft Matter*, **2014**, 10, 1611.
34. Vlad Popa-Nita, Ivan Gerlic, and Samo Kralj, *Int. J. Mol. Sci*. **2009**, 10, 3971.
35. Y. H. Hsu, M. L. Moya, C. C. Hughes, S. C. George, A. P. Lee, *Lab on a chip* **2013**, 13, 2990.
36. K. Sakaguchi, T. Shimizu, S. Horaguchi, H. Sekine, M. Yamato, M, Umezu, T. Okano, *Sci Rep* **2013**, 3, 1316.
37. V. Vickerman, J. Blundo, S. Chung, R. Kamm, *Lab on a chip* **2008**, 8, 1468.
38. M.-A. Lauzon, A. Daviau, B. Marcos, N. Faucheux, *Journal of Controlled Release* **2015**, 206, 187.
39. K. Nagpal, S. K. Singh, D. N. Mishra, *International Journal of Biological Macromolecules* **2013**, 59, 72-83.
40. S. Wohlfart, A. S. Khalansky, S. Gelperina, D. Begley, J. Kreuter, *Journal of Controlled Release* **2011**, 154, 103.
41. L. R. Hanson, et. al., *Drug Delivery* **2012**, 19 149.
42. Z. Wang, Z, Wang, W. W. Lu, W. Zhen, D. Yang, S. Peng, *Npg Asia Materials* **2017**, 9, e435.

Chapter 4

Plasmonics-Enhanced UV Photocatalytic Water Purification

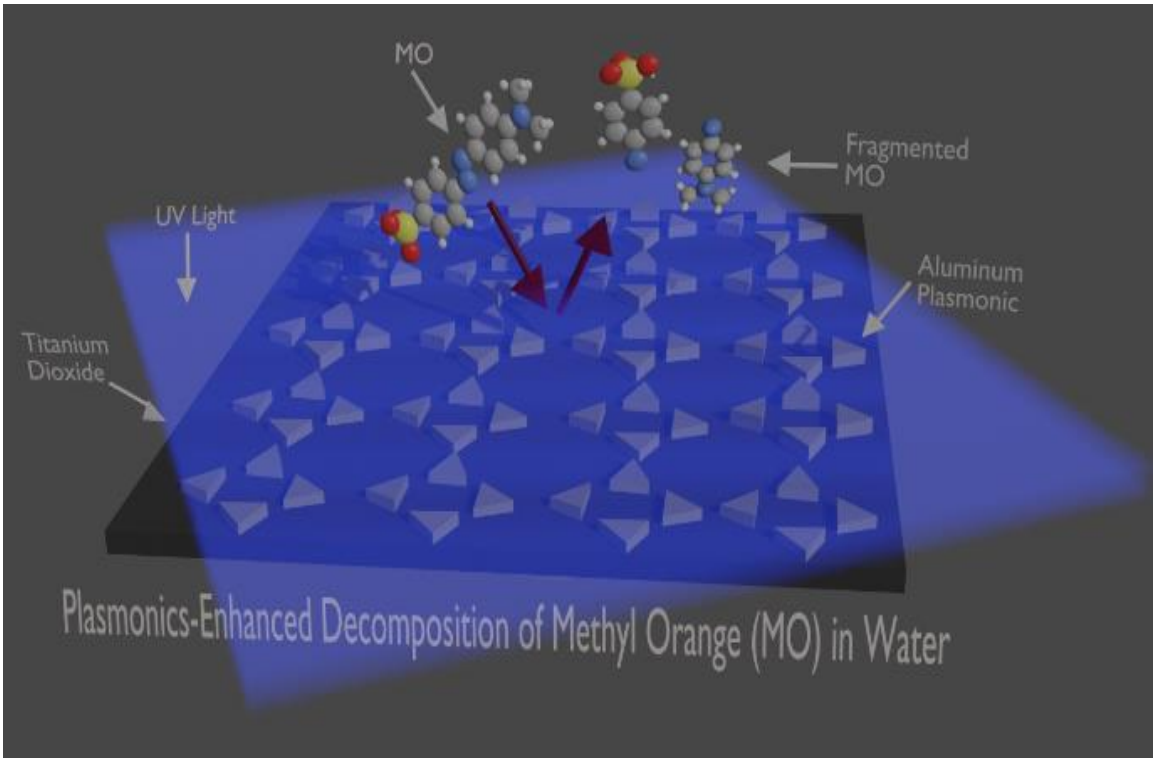

Graphical depiction of plasmonic nanostructures for the catalyst enhancement.

Introduction

Titanium dioxide (TiO_2) is commonly used for photocatalytic decomposition of organic contaminants for the purpose of water purification. One promising method to enhance TiO_2 photocatalysis is the incorporation of surface plasmon resonance on its surface where photocatalytic reactions take place. Herein a novel methodology using plasmonically tuned aluminum nanostructures to enhance the rate of photo decomposition of aqueous methyl orange is demonstrated. These nanostructures are tuned to the TiO_2 bandgap in the UV regime and patterned on TiO_2-coated substrates using nanosphere lithography. Compared to blank TiO_2 film, the plasmonics is found to enhance the initial TiO_2 photocatalytic rate by up to 10 times, and further enhancement is possible upon refinement of the plasmonic technology

Access to clean water is of critical importance to humanity, and increases in both industrialization and population has generated the need for less costly and faster methods of water purification of industrial contaminants.[1,2] The additive production in sectors of industry that necessitate the use of dyestuffs (textiles, paper mills, etc.) has led to an increase in the amount of colored wastewater.[3] Due to coloring being a principle indicator of (bad) water quality new ways to either remove the dyes or decolor the water are paramount.[4] A primary component of most colored water waste streams is methyl orange (MO), an aromatic azo dye**.** Due to its prevalence in textile waste streams, the scientific community has adopted MO as a proxy for evaluating water purification systems

using titanium dioxide as a photocatalyst. In order to maximize the amount of purification and minimize both the necessary components (excess reactants, costly materials, etc.) photocatalytic decomposition has been an area of significant investigation.

Photocatalysis using TiO_2 has seen a tremendous amount of development over the past 40 years.[5,6] The use of TiO_2 was pioneered in the early 1970s using a photoelectrochemical cell from the semi-conducting material for the tandem photo-electrochemical splitting of water.[7] Following the advent of the initial discovery, the use of TiO_2 for photocatalytic redox processes expanded significantly, and have been expanded to broader applications such as sensing.[8–13] impacting also the area of water purification.[14–17]

Through the continued progress in such area , the technology relying on TiO_2 photocatalyst has been readily adapted for treatment of MO. [18–24] With the current successes of using TiO_2 to decompose MO, innovation is constantly sought out in order to improve upon the existing standards of efficiency and rates. Current approaches to improve the baseline catalytic activity of TiO_2 has been directed towards two primary routes: 1) additives, such as iron, tin, and carbon nanoparticles (np) and 2) nanostructures, such as carbon nano-tubes or porous surfaces.[25–30]

Recently, there has been another approach to enhance photocatalysis through the combination of the photoexcitation of TiO_2 and surface plasmon.[31] The coupling of TiO_2 with surface plasmon, usually on gold, has shown the ability

to enhance the redox capability and activity in systems using TiO_2.[32–36] While examples of this enhancement with gold are very prevalent in the literature, gold is effective only in the visible spectral range, where efficiency of TiO_2 photocatalysis is low. More recently, alternative plasmonic materials such as aluminum (Al) have been explored. Al is more cost effective and can have UV plasmonic response that overlaps with the bandgap of TiO_2.[37,38] Herein a novel method using Al nanostructures for the purpose of increasing photo absorptivity and providing a catalytic rate enhancement in the decomposition process of MO through the activation of the Al surface plasmon is demonstrated. This system represents the first time this methodology has been used in a patterned substrate which allows for precise tuning of the plasmonic response.

Results and Discussion Simulation

To guide the design of our Al nanostructures, 3D finite-element-method (FEM) simulation was carried out using commercial COMSOL program. Plane wave is incident upon an Al equilateral nano-triangle (which models the shape of nanostructure patterned by our methodology as outlined below) sitting on top of a layer of TiO_2. An absorbing boundary condition was used. The geometry of the nano-triangle was varied to obtain resonance in the desired UV regime. This in turn guides our fabrication process parameters. For resonance at wavelength of 350nm, which corresponds to the band-edge of TiO_2, the side length of the equilateral nano-triangle is found to be 95 nm, and thickness 30 nm. **(Figure 1)**

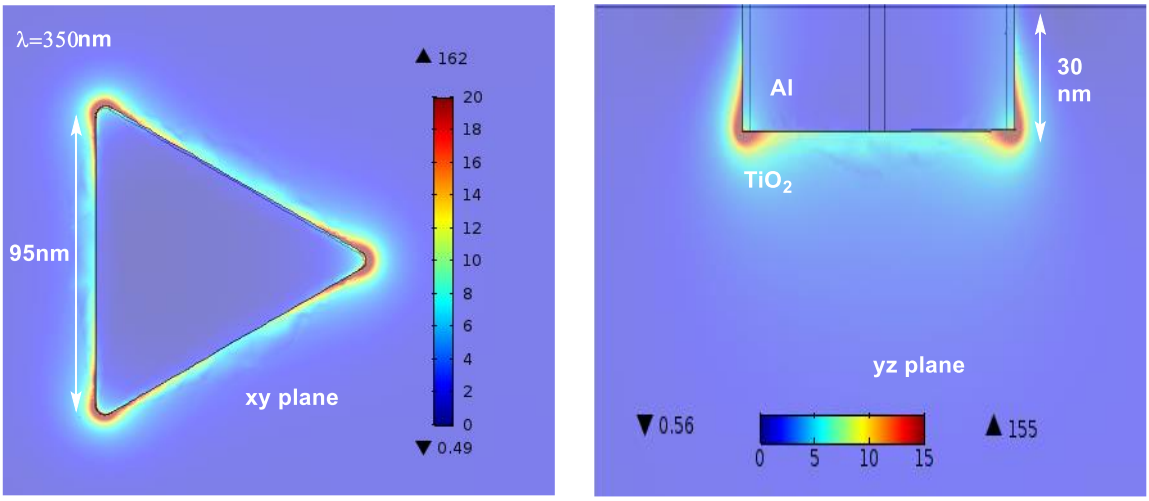

Figure 1. *COMSOL simulation results showing the field enhancement of Al nano-triangle at photon energy above TiO2 bandgap*.

Substrate Fabrication

The nano-triangles modeled by COMSOL were fabricated by nanosphere lithography. The five major steps in substrate fabrication are: (1) TiO_2 film deposition, (2) self-assembly of polystyrene beads via spin-coating, (4) nanosphere tuning by plasma etching (3) Al film deposition, and (4) lift-off. Fused silica-wafers with thickness of 500μm were used for substrate fabrication. The wafers were soaked in an 80ºC aqueous solution of deionized water, ammonia hydroxide, and hydrogen peroxide (5:1:1 volume ratio) for 30 minutes to remove any organic residues. This was followed by a thorough rinse with deionized water (DI) and dried using nitrogen. Afterwards, a 100nm layer of TiO_2 was deposited by electron beam evaporation onto the wafer surface and further annealed at 500°C for 1 hour in ambient air to obtain TiO_2 anatase-phase.[39,40] Catalytically active anatase phase was confirmed through XRD analysis shown in **Figure 2**

and compared to reference pattern from JCPDS card no. 21-1272 for anatase TiO_2.[41,42] The confirmation of anatase was critical due to its higher photocatalytic activity compared to the rutile crystal structure. [43]

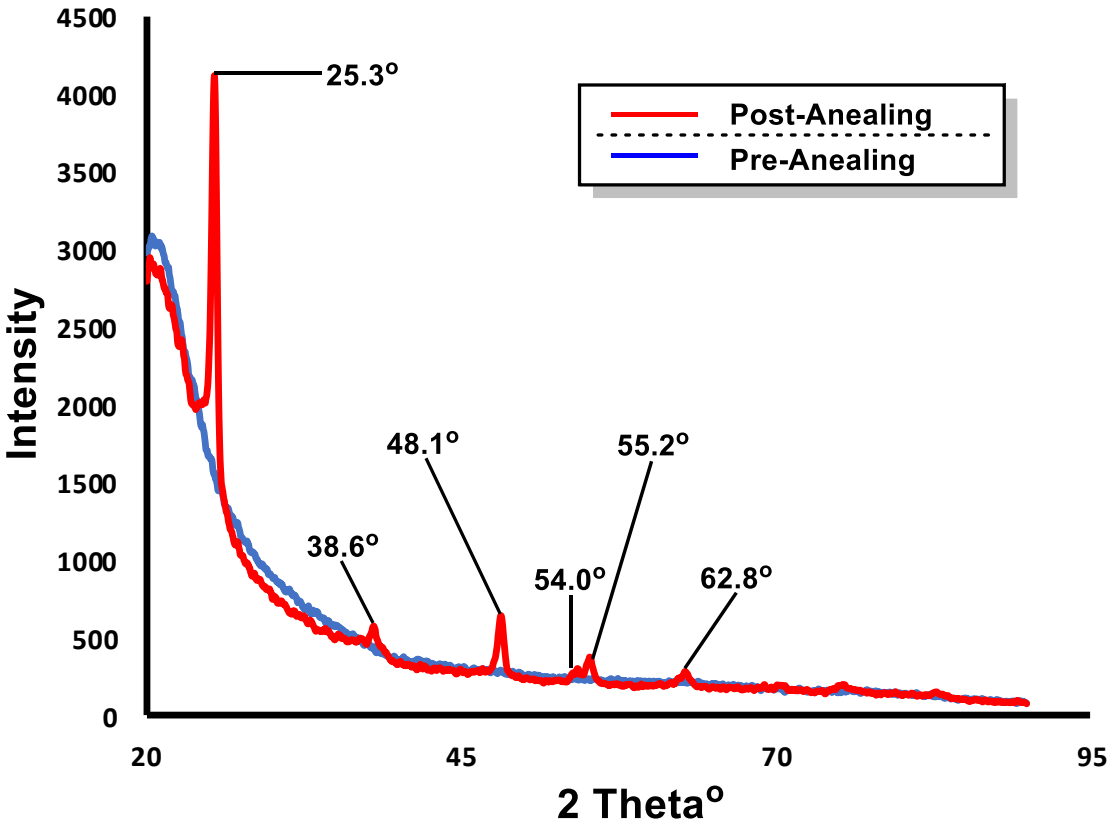

Figure 2. *XRD patterns of TiO2 thin film before and after annealing at 500°C. Peaks present after anneal process refer to peaks specific to anatase phase.*

The wafers were cleaved into smaller substrates and cleaned in acetone and isopropyl alcohol and rinsed with DI water. Next, during nano-sphere lithography, either 300nm or 460nm diameter polystyrene beads (Sigma Aldrich, St. Louis, MO) were spun onto the substrates using a commercial spin-coater where the attractive forces of the beads lead to formation of a hexagonal-close packed monolayer (**Figure 3A**).[41,42,44–46] A total of 3 spin steps allow for (1) improved

surface coverage, (2) monolayer generation, and (3) removal of nanospheres from edges. The 3 spin steps are as follows: (1) 1940 rpm for 10 seconds at a ramp rate of 308 rpm/sec, (2) 2300 rom for 10 seconds at a ramp rate of 1001 rpm/sec, (3) 6000 rpm for 15 seconds at a ramp rate of 1001 rpm/sec.

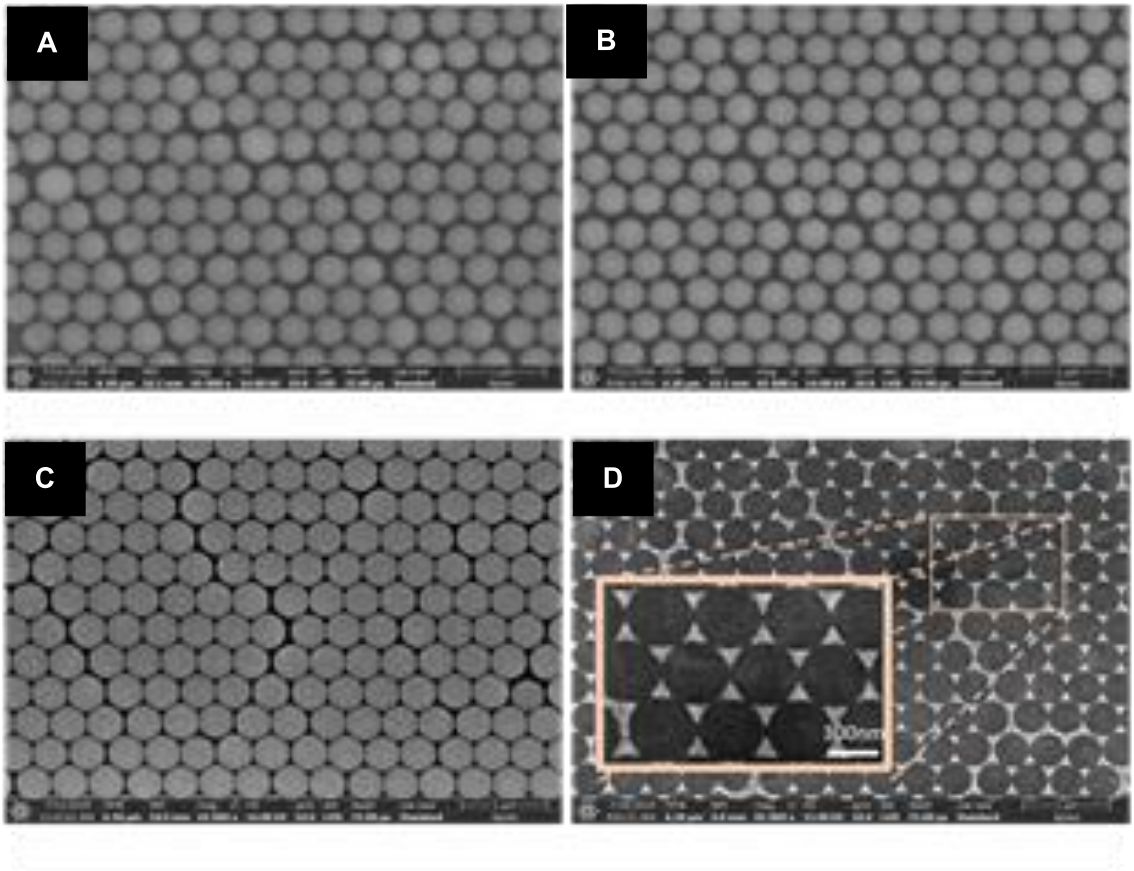

Figure 3. *SEM images of TiO_2 + Al plasmonic substrate microfabrication process. (3A) Monolayer of nanospheres on top of anatase-phase TiO2 film after nanosphere lithography. (3B) Plasma etched nanospheres. (3C) E-beam deposition of Al on top of nanospheres. (3D) Post nano-sphere lift off in toluene.*

The size of the polystyrene beads coated on the TiO_2 surface were tuned with plasma[37] to achieve the desired size using a parallel plate reactive ion etcher with radio frequency power of 100W, flow rate of 10 sccm O_2 and 36 sccm CF_4 for 75 seconds. (**Figure 3B**) Next, 50nm layer of Al was electron beam deposited on top of the tuned polystyrene beads filling the gaps in between the beads.

(**Figure 3C**) Finally, the majority of the beads were removed with tape and the remaining beads were sonicated in toluene for 30 seconds to dissolve the polystyrene beads and remove the excess Al leaving behind the Al patterns defined by the nanospheres on the TiO_2 surface. (**Figure 3D**)

After substrate manufacturing and tuning of the Al nanostructures, surface plasma resonance (SPR) activity was characterized via UV-Vis spectrophotometer (Perkin Elmer lambda 950) with an attached 60mm integrating sphere. *An important note is that the size of polystyrene beads had a direct and significant effect on the Al feature size*, where the feature size refers to the side of the triangular Al pattern. The 300 nm polystyrene beads yield an average feature size of ≈ 90 nm while the 460 nm polystyrene beads yield average feature size of ≈ 120 nm. Along with change of Al feature size, red shifts were observed via increasing the size of the patterned Al nanostructures, with the 300nm spheres yielding a higher degree of energy overlap between the Al nanostructure and TiO_2 thin film. (**Figure 4)** The experimental absorptions of the Al features were compared with COMSOL predicted absorptions of blank TiO_2 and a 90nm Al triangle, in which similar absorptions are observed seen in **Figure 4.** The different feature sizes obtained by using two different sizes of polystyrene

beads allowed a deeper investigation into the effect of activation of the Al plasmon on catalysis

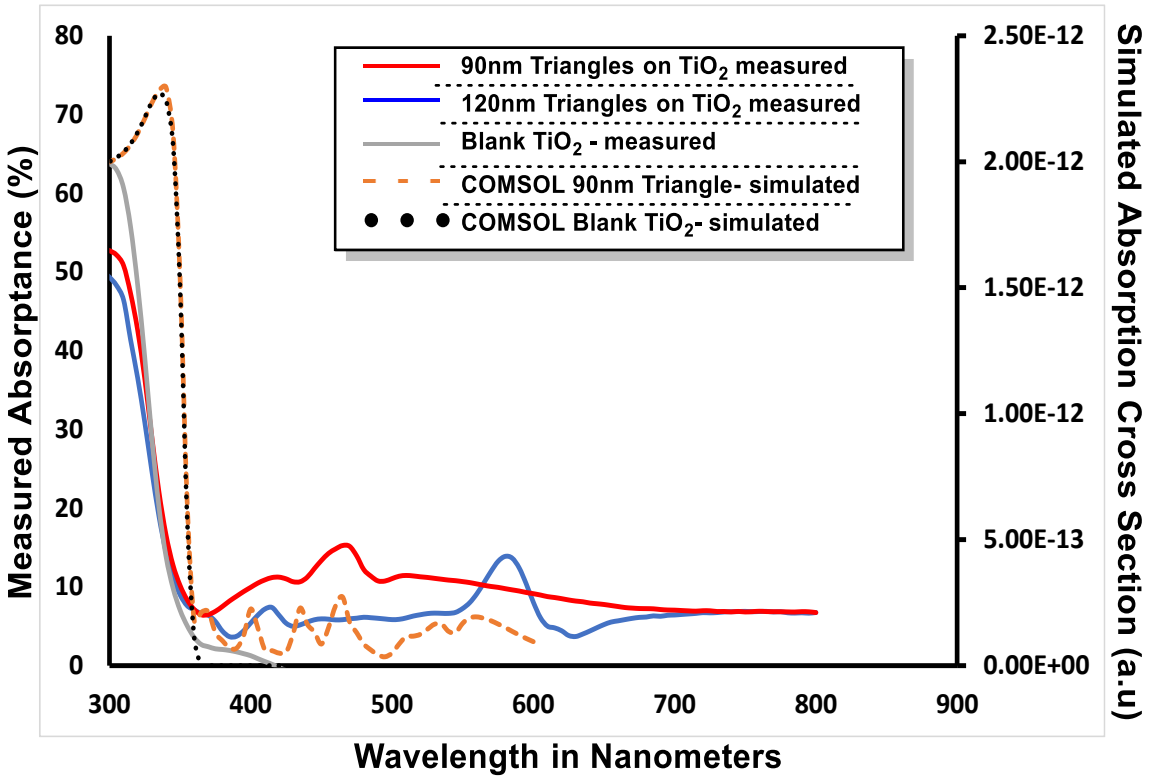

***Figure 4**. Measured UV-Vis absorption of two different sized Al structures on TiO2 90nm triangles (red) 120nm triangles(blue). Also plotted are COMSOL simulated absorption cross-section of 90nm Al nanotriangles patterned on TiO2 thin-film (dashed orange) and plain TiO2 thin-film (dotted black).*

MO Decomposition

All reactions were conducted in a 6" diameter boro-silicate petri dish and irradiated using an IntelliRay-600 UV shutter flood light set to 35% power with no temperature input. Methyl Orange (1%W:V) was purchased from Sigma Aldrich. A Perkin Elmer lambda 950 UV-Vis spectrophotometer with attached 60mm

integrating sphere was used for all measurements for: 1) (pre-reaction) catalyst characterization, 2) MO concentration determination (via MO absorption peak at 469nm), and 3) post reaction catalyst characterization. All experiments were conducted with a 15mL aliquot of a batch solution with a 1:15 dilution of MO in DI water from the MO stock. Each time point was a self-contained and independent reaction, using the same catalyst. (X time points = between 3-6 reactions).

All reactions were conducted on a 6 cm^2 substrate. The substrate was placed in a 6” borosilicate petri dish and covered with 15mL (measured via volumetric flask) of dilute MO bulk solution. The substrate was equilibrated in solution for 10 minutes while the vessel was capped and wrapped in tin foil. The reaction vessel was placed in the UV flood light system and irradiated for incremental time periods. Post exposure, reaction was transferred into a clean and dry 15mL volumetric flask and volume was restored to 15mL to account for evaporative loss due to catalysis, followed by inversion (4x). Following volume normalization and homogenization, a 1:100 dilution of the bulk sample was prepared in a plastic UV-Vis cuvette for analysis and the results were compared to a MO control spectrum to determine MO concentration loss (see SI)

Control reactions of MO with no catalyst system yielded negligible change in concentration through the entire exposure time. Both substrates (larger and smaller Al features) were tested for catalytic enhancement (is this the first step of catalytic characterization?). The substrate with a larger Al nanotriangle feature size (≈ 120 nm) demonstrated a more red-shifted absorption spectra than the

smaller feature size (≈ 90 nm) in the pre-reaction characterization. These off-tuned substrates showed a decrease in concentration over the 10-minute irradiation period but was not significantly different from the thin film TiO_2 control experiment. The lack of plasmonic enhancement by the larger Al-feature sizes is believed to be caused by the lack of overlap between the of Al plasmon and TiO_2.[47] Further refinement of the Al plasmonic feature by reducing the polystyrene nanospheres size to 300nm effectively decreased the feature size from 120nm to 90nm, which increased the spectral overlap of the plasmonic Al nanostructure and TiO_2 (≈ 365 nm). As a result of the increase in spectral overlap, the 90nm Al feature size yielded a significant rate enhancement over the course of the 10-minute exposure as demonstrated in **Figure 5A**.

The observed rate enhancement with the smaller Al nano-features was attributed to the to the successful transfer of energy from the localized SPR leading to

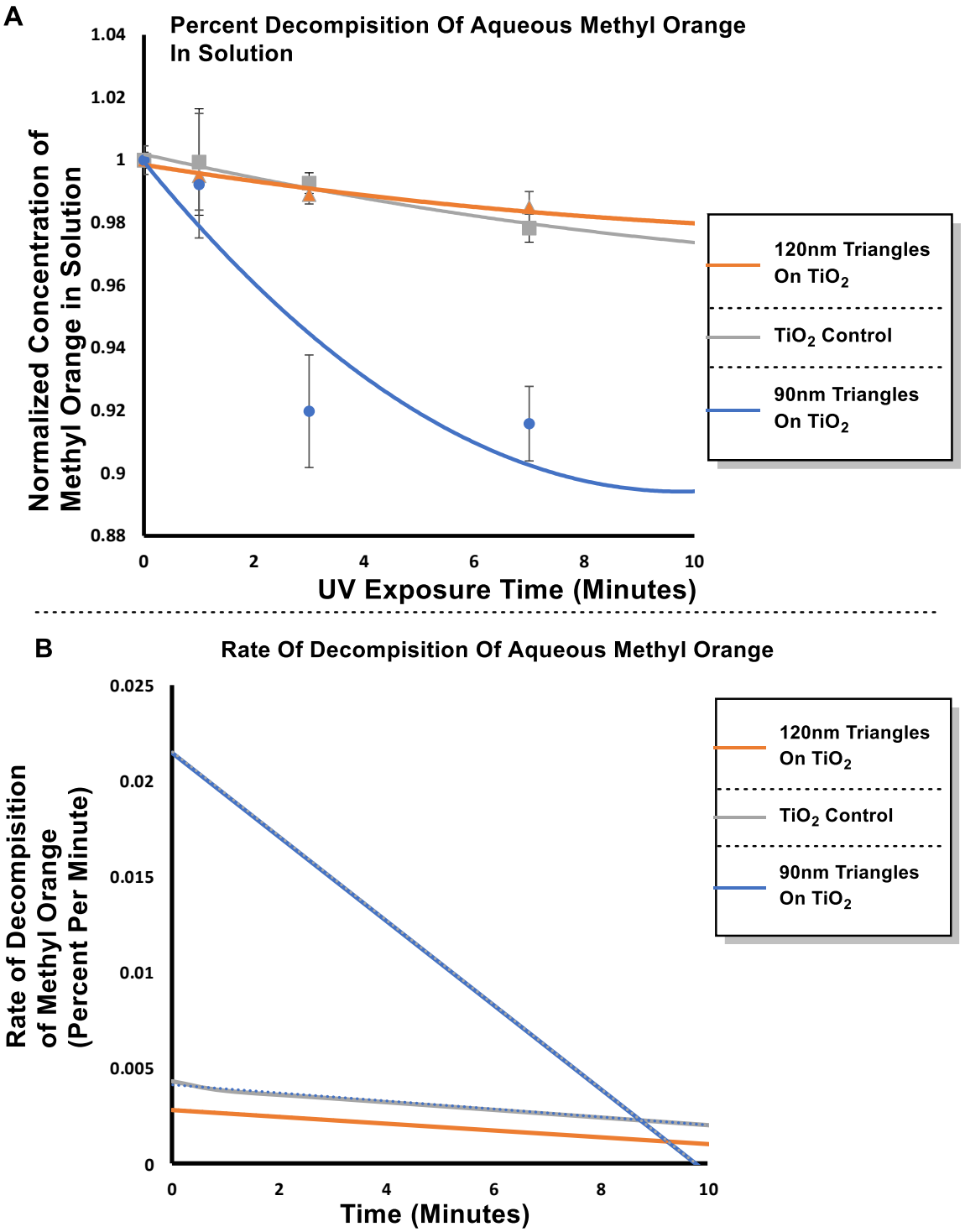

Figure 5. *A) Reaction kinetics plots of methyl orange photodecomposition. Titanium Dioxide Control (gray), off tuned Al (orange), Tuned Al nanostructure (blue). B) Plot of the first derivative of the Methyl orange decomposition over time all substrates*.

photoexcitation of TiO_2. While the mechanism of energy transfer from the activation of SPR to a semiconducting metal is still an area of active research, it is currently believed that the energy transfer between the Al surface plasmon and TiO_2 catalyst film occurs via two possible processes. The primary suspected energy transfer mechanism is resonant energy transfer (RET).[48,49] The lack of coherence between the theoretical and observed absorption spectra could be due to various mitigating variables that are currently not accounted for in the simulations (sample inhomogeneity, Al structure spacing etc). Due to the lack of coherence between our simulations and observed data possible explanation of the increased catalytic activity can be explained through a non-photonic route such as Landau damping effect and accompanied electron scattering. [48,50–52] This system, however, needs further exploration to understand the intricacies of the energy transfer mechanism between the Al plasmon and the TiO_2. It is evident from our measurements that, the average rate of enhancement with Al plasmonic is significant.

Initial rates of MO decomposition were observed for 10 minutes across all substrates and MO concentration was determined via integration of UV-Vis MO absorption peak. MO decomposition over time was plotted and fitted to second order polynomial functions. The first derivative of the fitted polynomial functions were calculated and plotted to analyze the rate (**Figure 5B**).[53] Negligible differences were observed between the rate of decomposition of MO between both larger Al-features and TiO_2 control. The smaller Al features yielded a significant rate enhancement (0.022% decomposition /minute) *an increase ~ 10x*

over the TiO_2 control substrate is observed. While a significant enhancement, the potential for further enhancement exists with refinement of plasmonic technology.

While a significant increase in the initial rate is observed in the smaller Al feature sizes compared to both the TiO_2 control and the larger Al feature sizes, it is short lived. The observed catalytic enhancement of the smaller Al feature sizes only exists for the first seven minutes of UV exposure. Also, it was noted that the COMSOL simulations showed significant plasmonic absorption peaks near the band edge of TiO_2, but these peaks were not observed in UV-Vis measurements. This could be explained by inhomogeneities of the plasmonic-enhanced surface.

Al plasmonics tend to be altered in the presence of both hydroxyl radicals and broad-spectrum UV light.[54] **Figure 6** displays uv-vis spectroscopic characterization of a deactivated (UV-exposed in MO solution) catalyst compared to active catalysts. While differences in absolute percentages are observed in the Al patterned TiO_2, line shape across reflectance, transmission, and absorption are nearly identical indicating no distinct photophysical reason for catalyst deactivation. SEM imaging of catalysts post deactivation shows significant corrosion of the catalysts (see supporting information) of the Al nano-structures

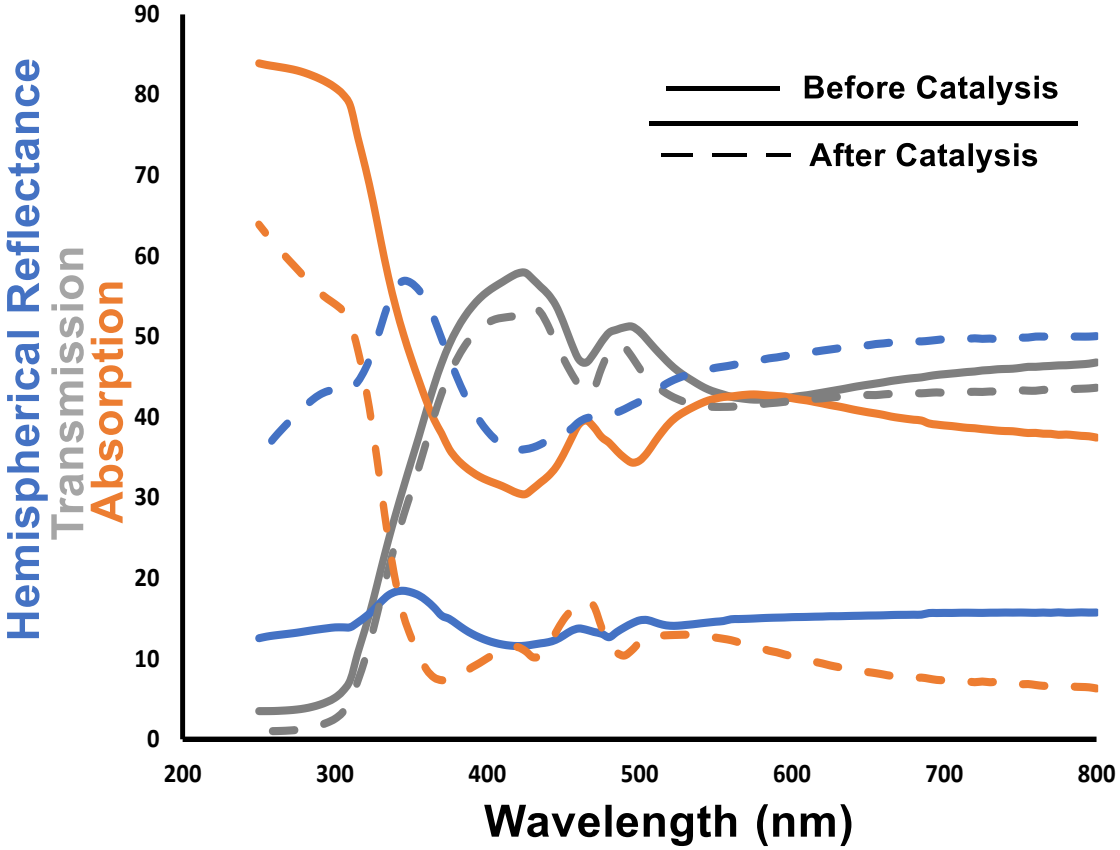

***Figure 6**. Uv-vis spectroscopic characterization of 90 nm plasmonic catalyst post reaction. Solid lines indicate measurements before catalysis and dotted lines after catalysis. Blue is measured hemispherical reflectance (R), Gray is measured transmission (T), and orange is absorption (A) given by A = 1- R -T.*

which could have caused the observed catalyst deactivation. Due to the observed corrosion it is believed that this deactivation pathway could be mitigated through coating the Al nano-structures with protective oxide layer, however further experimentation is needed to confirm this hypothesis.

Current efforts are being devoted to both the complex transfer of energy between the active Al plasmon and the TiO_2 surface and adapting this technology to a colloidal system in order to maximize surface area of the heterogenous process. The energy transfer step between the active SPR and the TiO_2 is a critical step in

advancing not only this technology, but the interface of all fields employing plasmonics for energy transfer. Transferring this system from a patterned substrate-based system to a colloidal system would increases the applicability of this technology to industrial areas needing faster and improved water treatment technologies.

Conclusion

Herein we have successfully shown that aluminum nano structures closely tuned to the band gap of TiO_2 when placed on a surface constituting a catalytically active layer of TiO_2 can provide a significant rate enhancement (~ 10x) of the photochemical decomposition of MO. While further work is needed to characterize the exact pathway of catalyst passivation and energy transfer, this is a step forward in developing methods for plasmonicaly enhancing UV driven processes.

This work was completed with the combined effort of Ryan Brisbin, Jenny Zhou, Tiziana Bond, Lars Voss, Aaron Simon, Ryan Baxter, and Allan S.P. Chang

---

REFERENCES

(1) Gong, R.; Ye, J.; Dai, W.; Yan, X.; Hu, J.; Hu, X.; Li, S.; Huang, H. Adsorptive Removal of Methyl Orange and Methylene Blue from Aqueous Solution with Finger-Citron-Residue-Based Activated Carbon. Ind. Eng. Chem. Res. 2013, 52 (39), 14297–14303..

(2) CRINI, G. Non-Conventional Low-Cost Adsorbents for Dye Removal: A Review. Bioresour. Technol. 2006, 97 (9), 1061–1085.

(3) Hou, W.; Liu, Z.; Pavaskar, P.; Hung, W. H.; Cronin, S. B. Plasmonic Enhancement of Photocatalytic Decomposition of Methyl Orange under Visible Light. J. Catal. 2011, 277 (2), 149–153.

(4) Banat, I. M.; Nigam, P.; Singh, D.; Marchant, R. Microbial Decolorization of Textile-Dye-Containing Effluents: A Review. Bioresour. Technol. 1996, 58 (3), 217–227.

(5) Nakata, K.; Fujishima, A. TiO 2 Photocatalysis: Design and Applications. J. Photochem. Photobiol. C Photochem. Rev. 2012, 13 (3), 169–189.

(6) Paramasivam, I.; Jha, H.; Liu, N.; Schmuki, P. A Review of Photocatalysis Using Self-Organized TiO 2 Nanotubes and Other Ordered Oxide Nanostructures. Small 2012, 8 (20), 3073–3103.

(7) Finegold, L.; Cude, J. L. Electrochemical Photolysis of Water at a Semiconductor Electrode. Nature 1972, 238 (5358), 38–40.

(8) Fujishima, A.; Zhang, X.; Tryk, D. A. TiO2 Photocatalysis and Related Surface Phenomena. Surf. Sci. Rep. 2008, 63 (12), 515–582.

(9) Fujishima, A.; Rao, T. N.; Tryk, D. A. TiO2 Photocatalysts and Diamond Electrodes. Electrochim. Acta 2000, 45 (28), 4683–4690.

(10) Su, L.; Tong, P.; Zhang, L.; Luo, Z.; Fu, C.; Tang, D.; Zhang, Y. Photoelectrochemical Immunoassay of Aflatoxin B 1 in Foodstuff Based on Amorphous TiO 2 and CsPbBr 3 Perovskite Nanocrystals. Analyst 2019, 144 (16), 4880–4886.

(11) Hill, I. G.; Kahn, A.; Soos, Z. G.; Pascal, R. A. Charge-Separation Energy in Films of π -Conjugated Organic Molecules. Chem. Phys. Lett. 2000, 327 (3–4), 181–188.

(12) Cai, G.; Yu, Z.; Tang, D. Actuating Photoelectrochemical Sensing Sensitivity Coupling Core-Core-Shell Fe3O4@C@TiO2 with Molecularly Imprinted Polypyrrole. Talanta 2020, 219 (June), 121341.

(13) Cai, G.; Yu, Z.; Ren, R.; Tang, D. Exciton–Plasmon Interaction between AuNPs/Graphene Nanohybrids and CdS Quantum Dots/TiO 2 for Photoelectrochemical Aptasensing of Prostate-Specific Antigen. ACS Sensors 2018, 3 (3), 632–639.

(14) Brezová, V.; Jankovičová, M.; Soldán, M.; Blažková, A.; Reháková, M.; Šurina, I.; Čeppan, M.; Havlínová, B. Photocatalytic Degradation of P-Toluenesulphonic Acid in Aqueous Systems Containing Powdered and Immobilized Titanium Dioxide. J. Photochem. Photobiol. A Chem. 1994, 83 (1), 69–75.

(15) Matthews, R. W. Kinetics of Photocatalytic Oxidation of Organic Solutes over Titanium Dioxide. J. Catal. 1988, 111 (2), 264–272.

(16) Faust, B. C.; Hoffmann, M. R. Photoinduced Reductive Dissolution of α-Fe2O3 by Bisulfite. Environ. Sci. Technol. 1986, 20 (9), 943–948.

(17) Rosenberg, I.; Brock, J. R.; Heller, A. Collection Optics of TiO2 Photocatalyst on Hollow Glass Microbeads Floating on Oil Slicks. J. Phys. Chem. 1992, 96 (8), 3423–3428.

(18) Gomes da Silva, C.; Faria, J. L. Photochemical and Photocatalytic Degradation of an Azo Dye in Aqueous Solution by UV Irradiation. J. Photochem. Photobiol. A Chem. 2003, 155 (1–3), 133–143.

(19) Lee, S. Y.; Park, S. J. TiO2 Photocatalyst for Water Treatment Applications. J. Ind. Eng. Chem. 2013, 19 (6), 1761–1769.

(20) Dai, K.; Chen, H.; Peng, T.; Ke, D.; Yi, H. Photocatalytic Degradation of Methyl Orange in Aqueous Suspension of Mesoporous Titania Nanoparticles. Chemosphere 2007, 69 (9), 1361–1367.

(21) Liu, S.; Yang, J. H.; Choy, J. H. Microporous SiO2-TiO2 Nanosols Pillared Montmorillonite for Photocatalytic Decomposition of Methyl Orange. J. Photochem. Photobiol. A Chem. 2006, 179 (1–2), 75–80.

(22) Liao, D. L.; Badour, C. A.; Liao, B. Q. Preparation of Nanosized TiO2/ZnO Composite Catalyst and Its Photocatalytic Activity for Degradation of Methyl Orange. J. Photochem. Photobiol. A Chem. 2008, 194 (1), 11–19.

(23) Wang, J.; Guo, B.; Zhang, X.; Zhang, Z.; Han, J.; Wu, J. Sonocatalytic Degradation of Methyl Orange in the Presence of TiO 2 Catalysts and Catalytic Activity Comparison of Rutile and Anatase. Ultrason. Sonochem. 2005, 12 (5), 331–337.

(24) Tong, T.; Zhang, J.; Tian, B.; Chen, F.; He, D. Preparation of Fe3+-Doped TiO2 Catalysts by Controlled Hydrolysis of Titanium Alkoxide and Study on Their Photocatalytic Activity for Methyl Orange Degradation. J. Hazard. Mater. 2008, 155 (3), 572–579.

(25) Wang, X. H.; Li, J. G.; Kamiyama, H.; Moriyoshi, Y.; Ishigaki, T. Wavelength-Sensitive Photocatalytic Degradation of Methyl Orange in Aqueous Suspension over Iron(III)-Doped TiO2 Nanopowders under UV and Visible Light Irradiation. J. Phys. Chem. B 2006, 110 (13), 6804–6809.

(26) Tasaki, T.; Wada, T.; Fujimoto, K.; Kai, S.; Ohe, K.; Oshima, T.; Baba, Y.; Kukizaki, M. Degradation of Methyl Orange Using Short-Wavelength UV Irradiation with Oxygen Microbubbles. J. Hazard. Mater. 2009, 162 (2–3), 1103–1110.

(27) Vinodgopal, K.; Kamat, P. V. Enhanced Rates of Photocatalytic Degradation of an Azo Dye Using SnO2/TiO2 Coupled Semiconductor Thin Films. Environ. Sci. Technol. 1995, 29 (3), 841–845.

(28) Li, Y.; Li, X.; Li, J.; Yin, J. Photocatalytic Degradation of Methyl Orange by TiO2-Coated Activated Carbon and Kinetic Study. Water Res. 2006, 40 (6), 1119–1126.

(29) Prado, A. G. S.; Costa, L. L. Photocatalytic Decouloration of Malachite Green Dye by Application of TiO2 Nanotubes. J. Hazard. Mater. 2009, 169 (1–3), 297–301.

(30) Guo, W.; Zhang, F.; Lin, C.; Wang, Z. L. Direct Growth of TiO2 Nanosheet Arrays on Carbon Fibers for Highly Efficient Photocatalytic Degradation of Methyl Orange. Adv. Mater. 2012, 24 (35), 4761–4764.

(31) Nie, J.; Patrocinio, A. O. T.; Hamid, S.; Sieland, F.; Sann, J.; Xia, S.; Bahnemann, D. W.; Schneider, J. New Insights into the Plasmonic Enhancement for Photocatalytic H2 Production by Cu-TiO2 upon Visible Light Illumination. Phys. Chem. Chem. Phys. 2018, 20 (7), 5264–5273.

(32) Jani, N. A.; Haw, C. Y.; Chiu, W. S.; Rahman, S. A.; Lim, Y. C.; Khiew, P. S.; Yaghoubi, A. Understanding the Effect of Plasmonic Enhancement on Photocatalytic Activity of TiO2 Nanotube Arrays. Mater. Charact. 2017, 128 (November 2016), 134–141.

(33) Zhang, H.; Chen, Y.; Wang, H.; Hu, S.; Xia, K.; Xiong, X.; Huang, W.; Lu, H.; Yu, J.; Guan, H.; He, M.; Liu, W.; Zhang, J.; Luo, Y.; Xie, Z.; Chen, Z. Titanium Dioxide Nanoparticle Modified Plasmonic Interface for Enhanced Refractometric and Biomolecular Sensing. Opt. Express 2018, 26 (25), 33226.

(34) Shu, J.; Qiu, Z.; Lv, S.; Zhang, K.; Tang, D. Plasmonic Enhancement Coupling with Defect-Engineered TiO2-x: A Mode for Sensitive Photoelectrochemical Biosensing. Anal. Chem. 2018, 90 (4), 2425–2429.

(35) Asapu, R.; Claes, N.; Ciocarlan, R. G.; Minjauw, M.; Detavernier, C.; Cool, P.; Bals, S.; Verbruggen, S. W. Electron Transfer and Near-Field Mechanisms in Plasmonic Gold-

Nanoparticle-Modified TiO2 Photocatalytic Systems. ACS Appl. Nano Mater. 2019, 2 (7), 4067–4074.

(36) Khatun, F.; Abd Aziz, A.; Sim, L. C.; Monir, M. U. Plasmonic Enhanced Au Decorated TiO2 Nanotube Arrays as a Visible Light Active Catalyst towards Photocatalytic CO2 Conversion to CH4. J. Environ. Chem. Eng. 2019, 7 (6), 103233.

(37) Hao, Q.; Wang, C.; Huang, H.; Li, W.; Du, D.; Han, D.; Qiu, T.; Chu, P. K. Aluminum Plasmonic Photocatalysis. Sci. Rep. 2015, 5, 1–7.

(38) Honda, M.; Kumamoto, Y.; Taguchi, A.; Saito, Y.; Kawata, S. Efficient UV Photocatalysis Assisted by Densely Distributed Aluminum Nanoparticles. J. Phys. D. Appl. Phys. 2015, 48 (18), 184006.

(39) Taherniya, A.; Raoufi, D. The Annealing Temperature Dependence of Anatase TiO2 Thin Films Prepared by the Electron-Beam Evaporation Method. Semicond. Sci. Technol. 2016, 31 (12).

(40) Bakri, A. S.; Sahdan, M. Z.; Adriyanto, F.; Raship, N. A.; Said, N. D. M.; Abdullah, S. A.; Rahim, M. S. Effect of Annealing Temperature of Titanium Dioxide Thin Films on Structural and Electrical Properties. AIP Conf. Proc. 2017, 1788 (January).

(41) Cheung, C. L.; Nikolić, R. J.; Reinhardt, C. E.; Wang, T. F. Fabrication of Nanopillars by Nanosphere Lithography. Nanotechnology 2006, 17 (5), 1339–1343.

(42) Chen, J.; Dong, P.; Di, D.; Wang, C.; Wang, H.; Wang, J.; Wu, X. Controllable Fabrication of 2D Colloidal-Crystal Films with Polystyrene Nanospheres of Various Diameters by Spin-Coating. Appl. Surf. Sci. 2013, 270, 6–15.

(43) Linsebigler, A. L.; Lu, G.; Yates, J. T. Photocatalysis on TiO2 Surfaces: Principles, Mechanisms, and Selected Results. Chem. Rev. 1995, 95 (3), 735–758.

(44) John, C. H.; Richard, P. V. D. Nanosphere Lithography: A Materials General Fabrication Process for Periodic Particle Array Surfaces. J. Vac. Sci. Technol. A Vacuum, Surfaces, Film. 1995, 13 (3), 1553–1558.

(45) Wang, Q. D.; Ye, L.; Wang, L.; Li, P. Y.; Cao, Y.; Li, Y. Rapid Nanopatterning Technique Based on Monolayer Silica Nanosphere Close-Packing by Spin Coating. Sci. China Technol. Sci. 2016, 59 (10), 1573–1580.

(46) Zhang, C.; Cvetanovic, S.; Pearce, J. M. Fabricating Ordered 2-D Nano-Structured Arrays Using Nanosphere Lithography. MethodsX 2017, 4, 229–242.

(47) Scholes, G. D. Long-Range Resonance Energy Transfer in Molecular Systems. Annu. Rev. Phys. Chem. 2003, 54 (18), 57–87.

(48) Ma, X. C.; Dai, Y.; Yu, L.; Huang, B. B. Energy Transfer in Plasmonic Photocatalytic Composites. Light Sci. Appl. 2016, 5 (April 2015).

(49) Cushing, S. K.; Li, J.; Meng, F.; Senty, T. R.; Suri, S.; Zhi, M.; Li, M.; Bristow, A. D.; Wu, N. Photocatalytic Activity Enhanced by Plasmonic Resonant Energy Transfer from Metal to Semiconductor. J. Am. Chem. Soc. 2012, 134 (36), 15033–15041.

(50) Gellé, A.; Jin, T.; de la Garza, L.; Price, G. D.; Besteiro, L. V.; Moores, A. Applications of Plasmon-Enhanced Nanocatalysis to Organic Transformations. Chem. Rev. 2020, 120 (2), 986–1041.

(51) Luo, Q.; Zhang, C.; Deng, X.; Zhu, H.; Li, Z.; Wang, Z.; Chen, X.; Huang, S. Plasmonic Effects of Metallic Nanoparticles on Enhancing Performance of Perovskite Solar Cells. ACS Appl. Mater. Interfaces 2017, 9 (40), 34821–34832.

(52) Schuller, J. A.; Barnard, E. S.; Cai, W.; Jun, Y. C.; White, J. S.; Brongersma, M. L. Plasmonics for Extreme Light Concentration and Manipulation. Nat. Mater. 2010, 9 (3), 193–204.

(53) Blackmond, D. G. Reaction Progress Kinetic Analysis: A Powerful Methodology for Mechanistic Studies of Complex Catalytic Reactions. Angew. Chemie - Int. Ed. 2005, 44 (28), 4302–4320.

(54) Barulin, A.; Claude, J. B.; Patra, S.; Moreau, A.; Lumeau, J.; Wenger, J. Preventing Aluminum Photocorrosion for Ultraviolet Plasmonics. J. Phys. Chem. Lett. 2019, 10 (19), 5700–5707.

Chapter 5
Benzoyl Pyraziniums: A novel molecular structure with applications in energy storage and luminescent materials.

Advancement of science and technology relies on the ability to understand and apply the topic of electron transfer in various materials and processes. This concept while deceptively narrow, is broad in both scope and nature. It threads itself through varied disciplines from: biology (signaling/monitoring/metabolic pathways/ etc.), industrial processes, and energy storage and transfer.[1–6] While most of these systems employ a metal component, sustainability issues have driven the development of organic based systems shown in **Figure 1** (organic semiconductors/electrolytes/light emitting diodes [OLED]), with the hope of replacing, or limiting the use of metal components.[7–10]

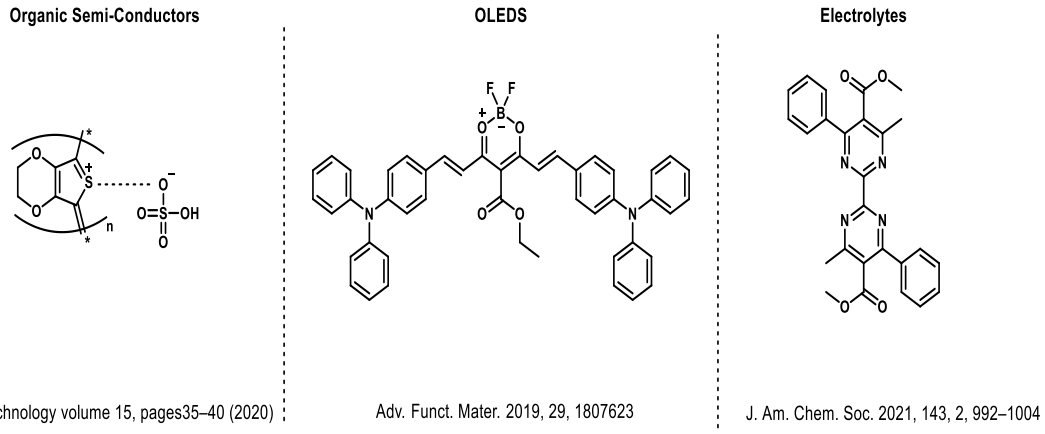

Figure 1. *Depiction of current state of the art technologies for organic semi-conductors, OLEDs and electrolytes*

These technologies have various purposes from energy storage to light emission, however their components can be distilled into two main concepts: 1) radical stability, and 2) mobility through an organic scaffold. Radical stability encompasses several structural relationships. These relationships involve everything from the orbital framework (localized vs delocalized) as shown in **Figure 2** to the local steric and electronic environment and solvation affects.[11–15]

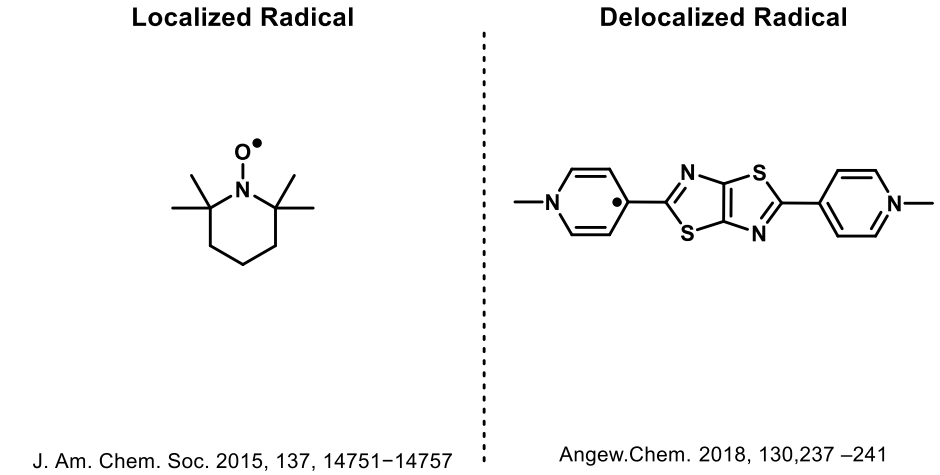

Figure 2. *Examples of stable localized and delocalized radicals.*

While radical stability can be boiled down to primarily structural trends, electron/hole pair mobility is a function of excitonic diffusion.[16–18] Excitonic diffusion has multiple aspects, but it can be understood in this context as the materials propensity to freely disassociate to charge carriers (organic semiconductors) or recombination events of electron/hole pairs (OLEDs). The primary component associated with excitonic diffusion in the determination of the system bias for charge carrier propagation or recombination events is the exciton binding energy, which is a direct reflection of the dielectric permittivity of the material.[19,20] Various methodologies have been employed to tune the excitonic

binding energy associated with organic materials, but the standard approach is to increase the polarizability of the molecule or polymer through the addition of electron donating substituents juxtaposed to electron withdrawing substituents.[21] Excitonic binding energy has significant applications in the area of energy, including: storage, generation, and propagation due to the importance of excitonic binding energy to electron transfer.

With all the varied fields electron transfer impacts, we decided to focus in on the area of energy storage. More specifically the application of non-aqueous redox flow batteries (NARFS) for grid scale energy storage. NARFs are a unique type of battery depicted in **Figure 3**. What makes NARF systems beneficial is

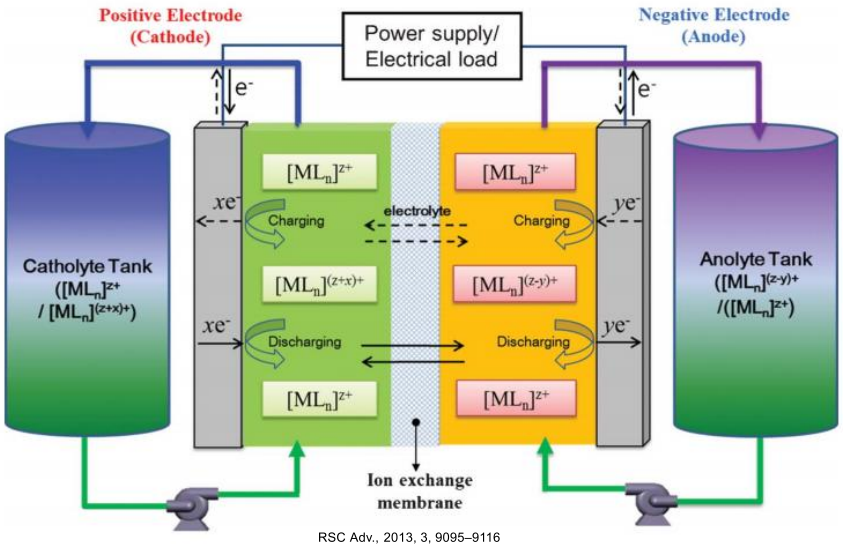

Figure 3. *Depiction of a redox flow battery system taken from source listed in citation.*

fourfold: 1) they possess the most direct scaling, 2) they allow for the decoupling of power and work through mechanical perturbation by way of hydraulic pumps, 3) limits irreversible discharge due to extreme temperatures by employing

temperature controlled electrolyte housing, 4) larger potential window over their aqueous counterparts. [22–24] This area has seen numerous advancements over the past decade including the application of super electron donors as organic anolytes and development of highly varied organic and organometallic anolytes and catholytes.[25–28] These redox systems employ several trends; flat, conjugated, aromatic, positively charged nitrogen.

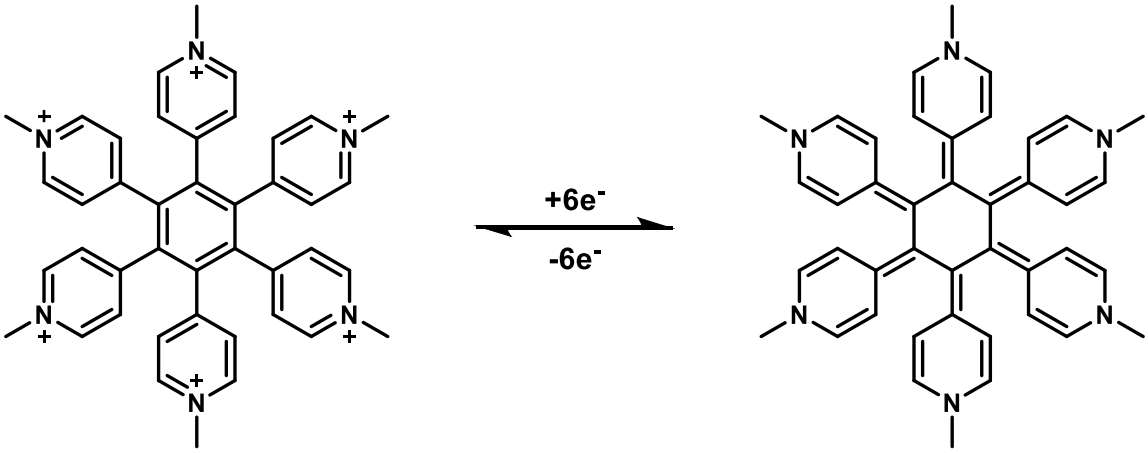

Figure 4. *Six electron reversible redox couple developed polycyclic, conjugated, positively charged nitrogen.*

In almost all cases the amount of electrons in which a system can tolerate seems to scale proportionally to the number of aromatic systems as shown in **Figure 4.** [29]

However, a current limiting factor for this technology is the limited amount of anolytes vs catholyte material**. Figure 5** showcases the material differential between anolytes and while these materials are operative at various redox

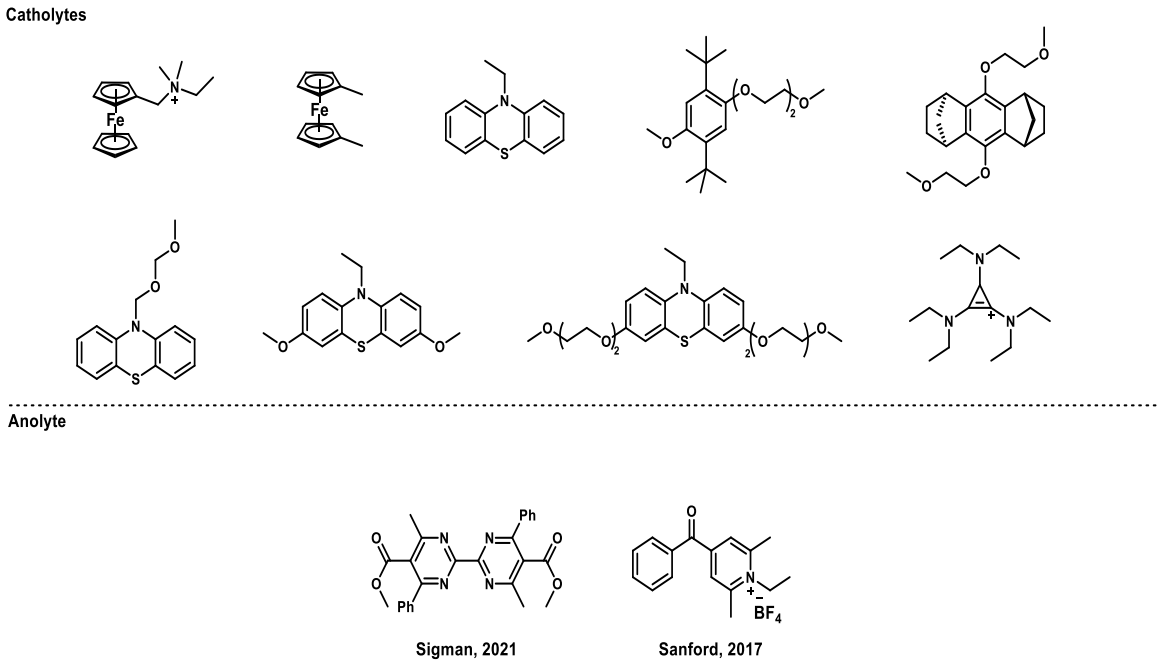

J. Am. Chem. Soc. 2021, 143, 992-1004, ACS Energy Lett. 2019, 4, 2220-2240, J. Am. Chem. Soc. 2017, 139, 2924-2927,J. Phys. Chem. C 2017, 121, 24376-24380

Figure 5. *Current anolyte (Fall, 2021) and catholyte materials for NARF systems. catholytes currently as of 2021 for NARF systems with only two organic anolytes available.*

potentials, they are also limited by the previous stated limitation of the number of electrons being proportional to the number of aromatic systems.

This limited amount of anolyte materials has served as our focal point for the goal of developing a novel scaffold that could potentially provide increased charge storage and a high degree of stability. This target led to an in-depth search for new heterocycle core that offered unique benefits. Pyrazine (shown in **Figure 6A** was selected for two primary reasons. The first reason being the di-cationic pyrizinium (**Figure 6B**) was shown in 1965 to exist as over 100 different radical states simultaneously in solution through EPR. This unique example provided evidence that a cationic pyrizinium scaffold would be able to act as a stable radical, a critical component for an organic anolyte.[30] The second reason comes from a result in2017 in which the zwitterion of quinoxaline(benzopyrazine)

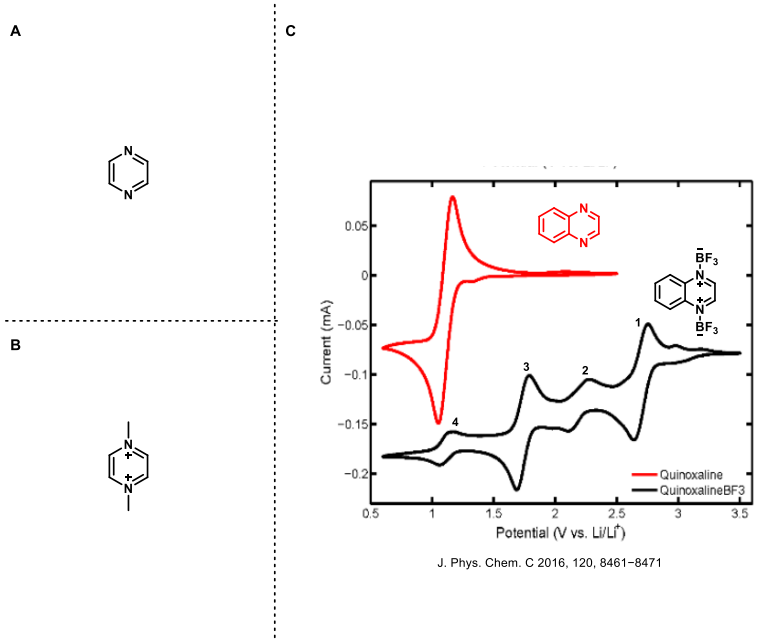

Figure 6. *A) Pyrazine. B) Di-cation of pyrazine that demonstrated over 100 radical states. C) Zwitterion of pyrazine derivative showing 4 reversible electron movements.*

reported 4 discrete reversible electron movements through cyclic voltammetry (**Figure 6C**),

indicating that pyrazine as a base for a battery would have a strong chance of success. These precedents involving pyrazine, coupled with modern relationships developed by Melanie Sanford and Matt Sigmans groups lead to the design of our base anolyte structure of a benzoylated pyrizinium (**Figure 7**).[14,31]

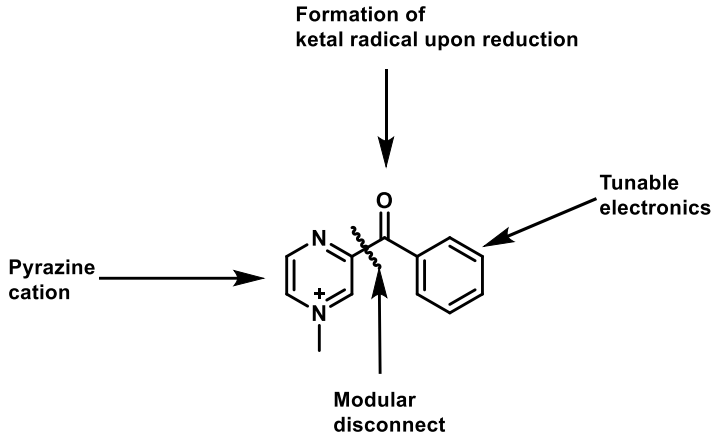

Figure 7*. Benzoylated pyrizinium salt, with respective design elements.*

Due to the innate difficulty associated with synthesizing and characterizing novel molecules validation of this concept was pursued using computational methodology developed by Argonne National Labs under their "electrolyte genome project".[32] First a

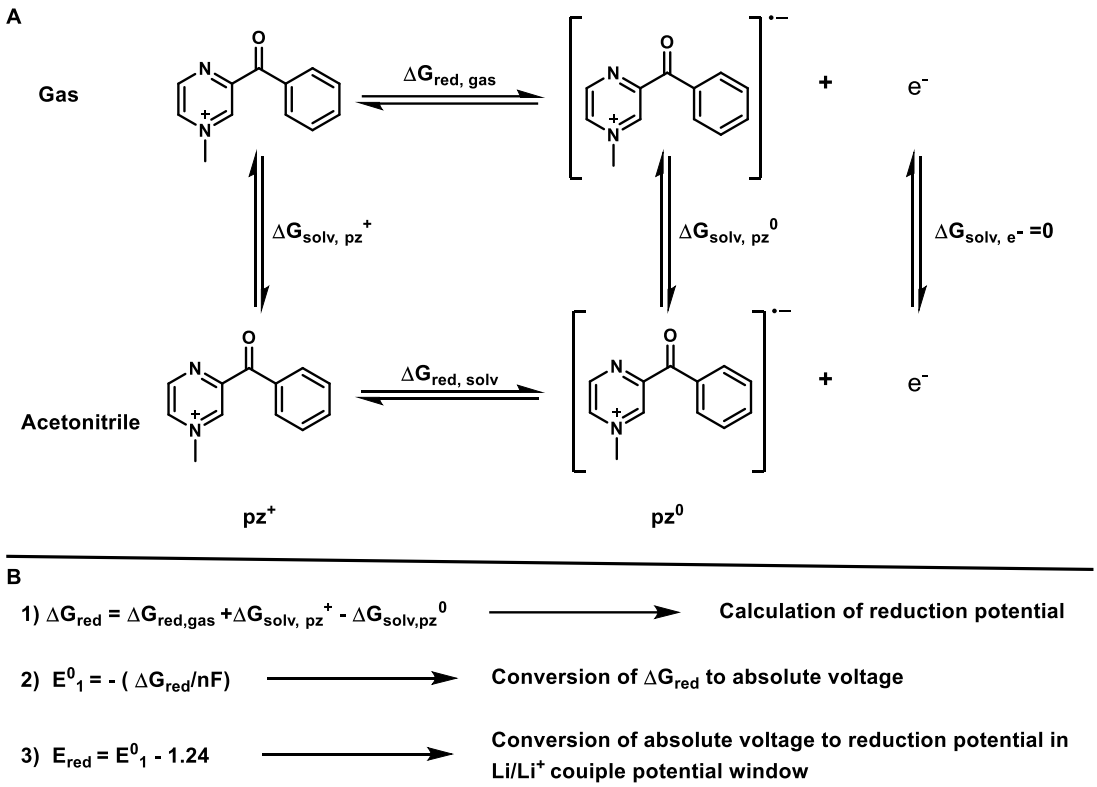

Figure 8. *A) Thermodynamic cycle associated used for determining redox potentials and solubility. B) Formulation used for determining redox potentials*.

Thermodynamic cycle was constructed as depicted in **Figure 8A** which allows for the formulations shown in **Figure 8B** to be used for the determination of the free energies. This cycle allowed extrapolations redox potentials and the determination of substituent affects through application of various linear free energy relationships.[33–35]

Computational Results

All computational results were obtained using density functional theory (DFT) at the B3LYP level using a basis set of 6-31+G(2d,p), and using a solvation model of SMD in acetonitrile.[36] **Figure 9** shows the relationship between the steric component of the using Charton values of N-alkyl substituent and redox potential.[37,38]

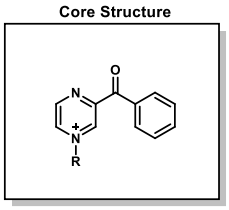

R	E_c^0 vs Li/Li^+
H	7.18
Me	6.82
Ethyl	6.88
iPr	6.45
Tbutyl	6.33
Bn	6.22

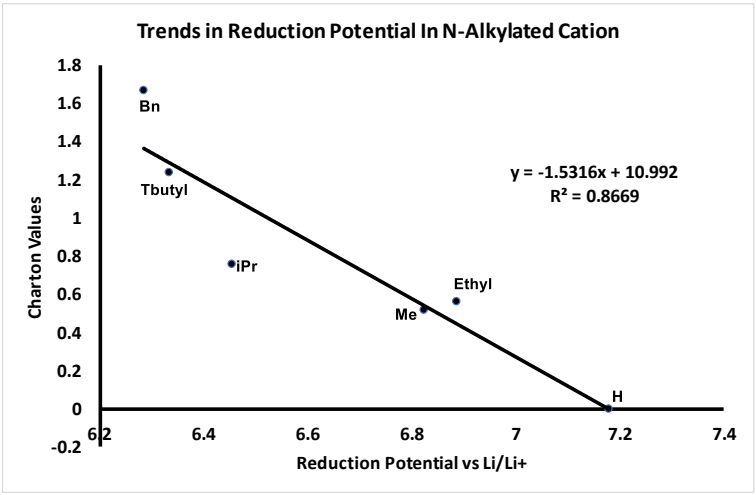

Figure 9. *Linear free energy relationship establishing the sensitivity of the redox potential of benzoyl pyrazine based on the sterics of the N-alkyl group.*

A correlation was observed between the steric bulk of the N-alkyl group and the redox potentials. The computed redox potentials showed that for the purpose of energy storage it would be beneficial to have larger substituents connected to the

pyrazine nitrogen in order to store a higher energy electron. While reduction potential is a critical element for energy storage in NARF systems, as the energy density directly correlates to the amount of electroactive material that remains solubilized, solubility is also a critical component. Due to the importance of solubility for NARF systems a way to determine solubilities in our target solvent (MeCN) was necessary. Computationally ascertaining quantitative solubilities of compounds is incredibly difficult, requiring high- level molecular dynamics or quantum mechanical molecular dynamics, but the free energies of solvation obtained through the thermodynamic cycle shown above can provide relative solubilities within the group using free energy as a proxy.[39] Applying this computational methodology **Figure 10** shows a strong trend opposite of the computationally generated reduction potentials trend from **Figure 9.** The free energies of solvation (ΔG_{solv})

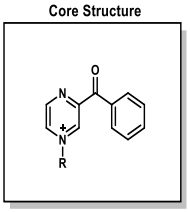

R	ΔG_{solv}
H	-68.60
Me	-65.19
Ethyl	-63.56
iPr	-62.00
Tbutyl	-60.92
Bn	-64.20

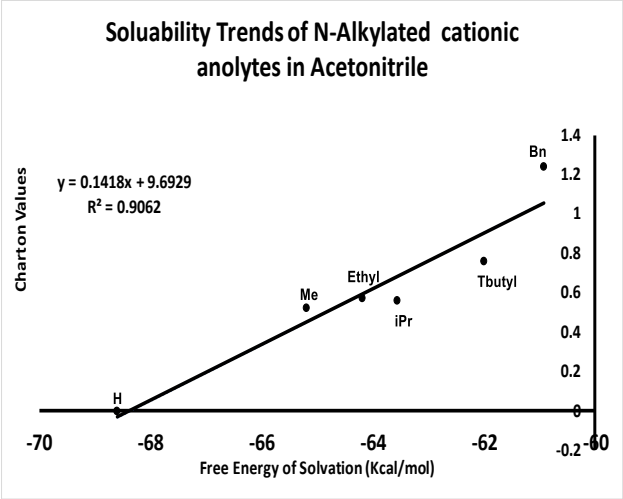

Figure 10. *Free energy of solvation related to steric bulk of N-alkyl substituents.*

increased as a steric size increased. These antithetical trends illustrate the balancing act of designing molecules of this nature, while one modification

increases its benefit with respect to redox potential it is simultaneously is detrimental to its solubility. However, with this computational data validating the design synthetic routes could now be pursued.

Synthesis and Isolation

Benzoylation of heterocycles is a difficult process to design a scalable route for the production bulk materials. **Figure 11 A, B, C** show the two main routes to install a benzoyl group onto a heterocycle.[40–42] **Figure 11A** employs a palladium catalyzed cross coupling reaction to install the benzoyl group. While moderate yields and a high degree of modularity are observed in this reaction due to the high variety of aryl boronic acids, purification of recovery of palladium does not lend itself well to a scalable synthesis,

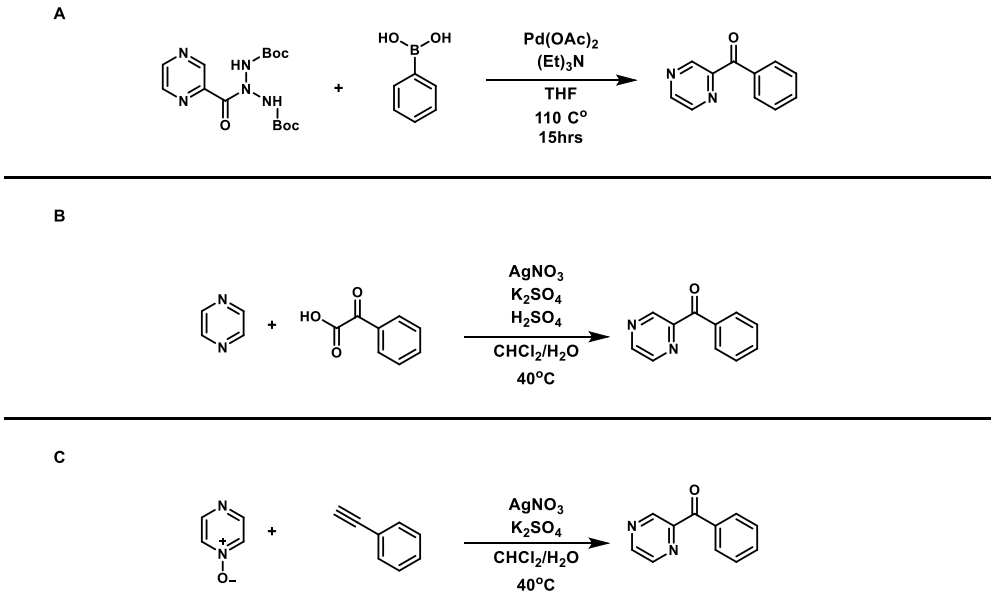

Figure 11*. A) Suzuki cross coupling approach to achieve benzoylation of pyrazine. B) Minisci reaction using aryl-alpha keto acids for benzoylation of pyrazine. C) Generation of benzoyl pyrazinium from N-oxyl pyrazinium and phenyl-acetylene.*

Figure 11B is a classic Minisci reaction, which employs stochiometric acid and a radical decarboxylation. While a classic Minisci reaction does work well, there is a lack of modularity in the synthetic approach due to the necessary aryl alpha-keto acids as the necessary nucleophilic synthon for the installation of the benzoyl group. **Figure 11 C** demonstrates a unique approach for the generation of benzoylated heterocycles taking advantage of the N-oxyl heterocycle species to generate an electrophile similar to the protonated heterocycle in the Minisci reaction, then coupling it with an phenyl-acetylene. While this method does use a unique approach from potentially scalable materials, the

sub 50% isolated yields significantly limit any scalable application of this synthetic approach. The lack of scalable chemistry from cheap commodity chemicals generated the need to develop a new approach for the generation of a benzoylated heterocycle.

Due to our groups high level of expertise in Minisci chemistry and the absence of rare earth metals (Pd/Rh/Pt etc), this approach seemed ideal. However, the limitation of modularity of the aryl alpha keto acid coupling partners became readily apparent. The lack of modular aryl alpha keto acids, lead to the search for a synthetic equivalent that could be employed in the Minisci conditions developed by our lab.[43,44] It was discovered that aryl glyoxal

compounds shown in **Figure 12**, while reactive could be converted to its geminal diol equivalent through recrystallization in water.

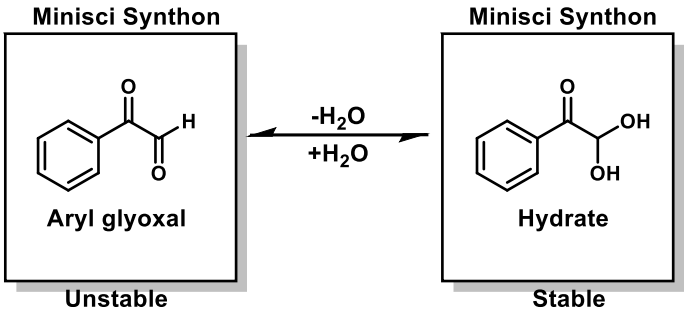

Figure 12. *Equilibrium dynamics between aryl glyoxal and its geminal diol/ hydrate.*

Aryl glyoxal compounds can be accessed through a highly scalable synthetic pathway using cheap commodity chemicals, acetophenone and selenium (IV) dioxide through the application of a reaction known as the riley oxidation. [45] This reaction shown in **Figure 13** allows for the oxidation of a methyl alpha to a ketone to an aldehyde, in the case of acetophenone and its derivatives that aldehyde can be readily converted to its geminal diol counterpart through a brief reflux in water followed by refrigeration. Upon refrigeration the geminal diol crystalizes out of the aqueous solution and remains bench stable, although depending on storage slow reversion from the geminal diol to the glyoxal will occur. Conversely, for long term storage (yearly time scale) the glyoxal compound can be polymerized using a rotary evaporation and a heated water bath. This polymer can be easily converted back to the geminal diol through recrystallization from water.

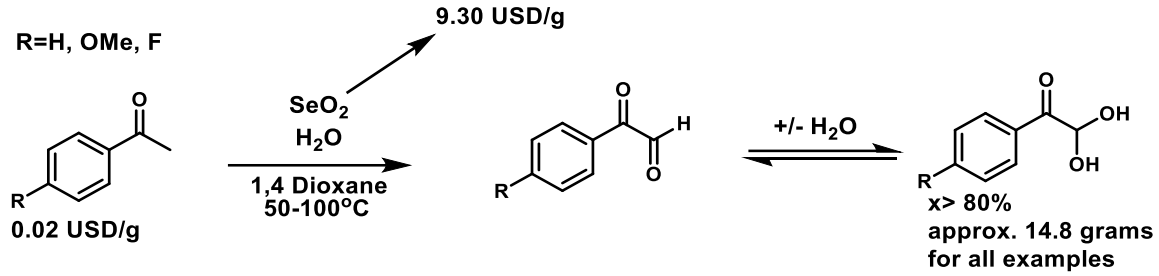

Figure 13. *Riley Oxidation of acetophenone to its corresponding aryl glyoxal compound followed by the equilibrium dynamics of the aryl glyoxal with its hydrate form*.

Once the process of synthesizing the geminal diols from acetophenone was established two other acetophenone derivatives were attempted: 4-methoxy acetophenone (4OMe) and 4-fluroacetaphenone (4F). Both electron rich and deficient substrates yielded greater than 80% isolated geminal diol. Further refinement of this procedure allowed for the elimination of column chromatography through successive filtrations through celite to remove various selenium allotrope impurities (insoluble- black selenium / insoluble in water-red selenium). This synthetic process allowed for a highly scalable and streamlined process for the subsequent Minisci reaction for the generation of the benzoyl pyrazines.

With an established pipeline for the generation of geminal diols from acetophenone (and its derivatives) validation needed to be obtained for their application as radical precursors for the use in the Minisci reactions. A Minisci reaction was conducted as shown in **Figure 14** using conditions developed

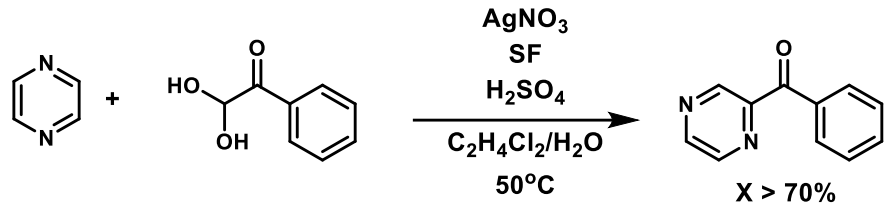

Figure 14. *Minisci reaction using the geminal diol as a radical precursor.*

by Baxter et al.[43] This reaction successfully produced the desired monosubstituted benzoyl pyrazine in excellent yields of 70% or greater. While this result was not entirely surprising, what was unexpected was that the product was obtained upon pure (>93%) upon extraction with no observable by products. While further work needs to be done in order to fully develop this methodology, some mechanistic insight can be drawn from the observed reactions of the 4F and 4OMe geminal diols compared to the unsubstituted geminal diol. Both 4F and 4OMe generated mixtures of mono and bis products as expected from Minisci chemistry leading to the qualitative assertion that both the equilibrium and rate the equilibrium is established between the geminal diol and its glyoxal counterpart play a critical role in rate of radical generation.

With three derivatives of benzoylated pyrazines synthesized and characterized by both 1- and 2-dimensional nuclear magnetic resonance (NMR) shown in **Figure 15**, alkylation reactions were attempted using methyl iodide. Due to the deactivation of

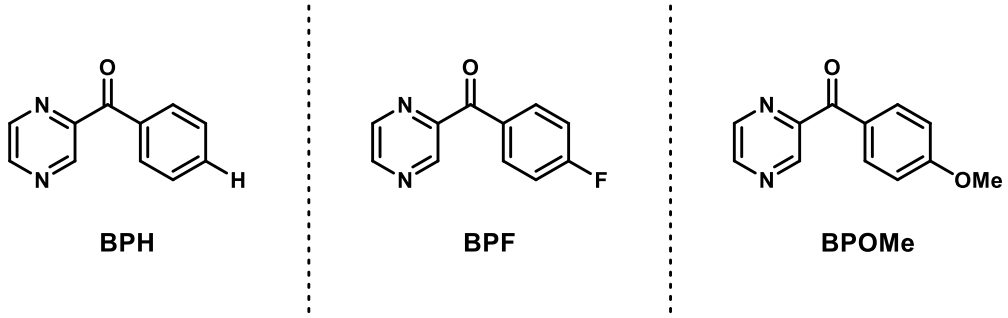

Figure 15 *Benzoyl pyrazine derivatives successfully synthesized.*

benzoyl moiety a cosolvent system consisting of 1:1 acetonitrile and methanol was used in order to facilitate an SN1 style substitution allowing for the alkylation of the pyrazine nitrogen and the formation of a quaternary nitrogen salt (**Figure 16**). All alkylation's progressed reasonably well leading to yields between 50-95% isolated yield however, initial difficulty presented itself in the form of purification of the benzoyl pyrazinium as standard silica column chromatography did not work. This was overcome by ascertaining the solubilities in various solvents of the iodine salts. It was discovered that while the iodine salts were soluble in dichloromethane and acetonitrile, they were insoluble in ethyl acetate allowed purification from MeCN with EtOAc.

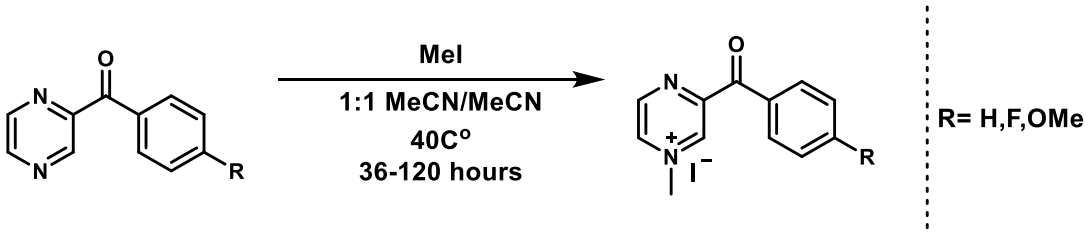

Figure 16. *Alkylation reaction conditions for benzoyl pyrazinium*

With the successfully synthesized and purified iodine salts all that was left was an ion exchange using $AgBF_4$ to swap the iodine for tetrafluoro borate. All ion exchanges were quantitative yields.

Preliminary Electrochemical Results

With the goal of validating the use of these novel molecules as anolytes for the cyclic voltammetry (CV) using Ika ElectraSyn 2.0 was employed. A 3mm glassy carbon working electrode, electroplated platinum counter, and an Ag/AgCl aqueous reference electrode were used in anhydrous MeCN. Initial CV data shown **Figure 17** of the BPH-BF_4 salt demonstrated a single irreversible reduction with an extremely high current response given the concentration of the anolyte. The cell was taken apart to check for

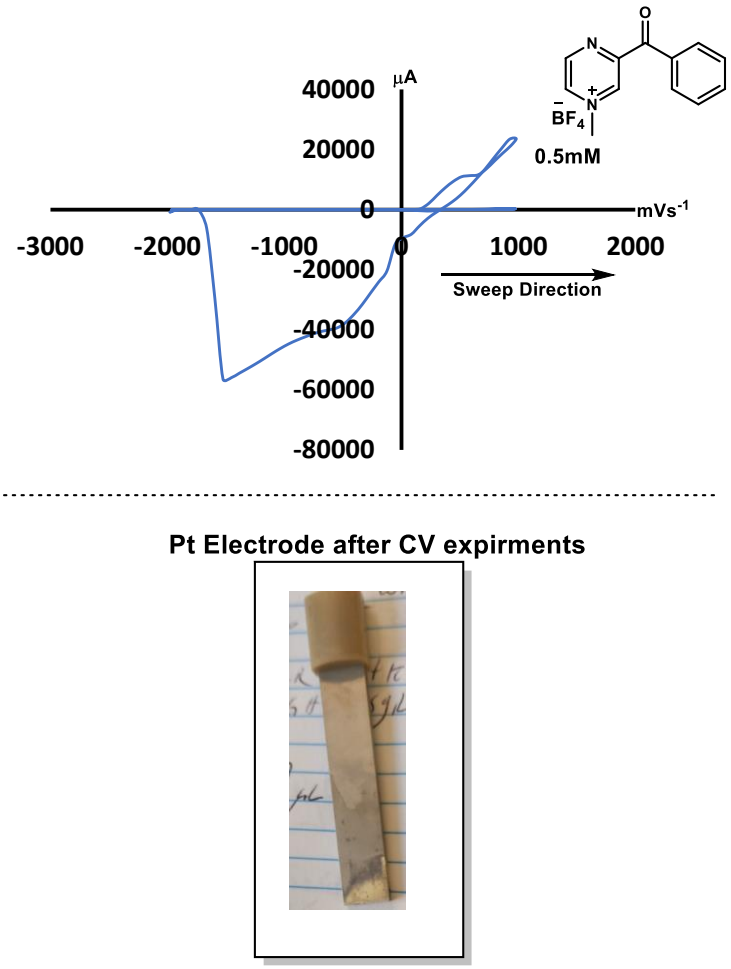

Figure 17. *Irreversible reduction of BPH-BF_4 salt and stripped platinum counter electrode*

instrument malfunctions and it was discovered that the platinum counter electrode had been stripped. Further data was obtained of the BPOMe BF_4 salt and while multiple electron movements (4) were obtained as shown in **Figure 18** they were not reversible. While the multiple electron movements of **Figure 18** demonstrate the promise of this design for energy storage applications, due in part to its irreproducibility of further refinement of the structural design elements as well as the decomposition products needs to be pursued before the potential of this novel salt can be realized. While initial results are promising for BPL compounds to serve applications in energy storage, the design principles of stabilizing a radical anion and the unique electronic structure of pyrazine (strange EPR data) BPL photo physical properties were investigated.

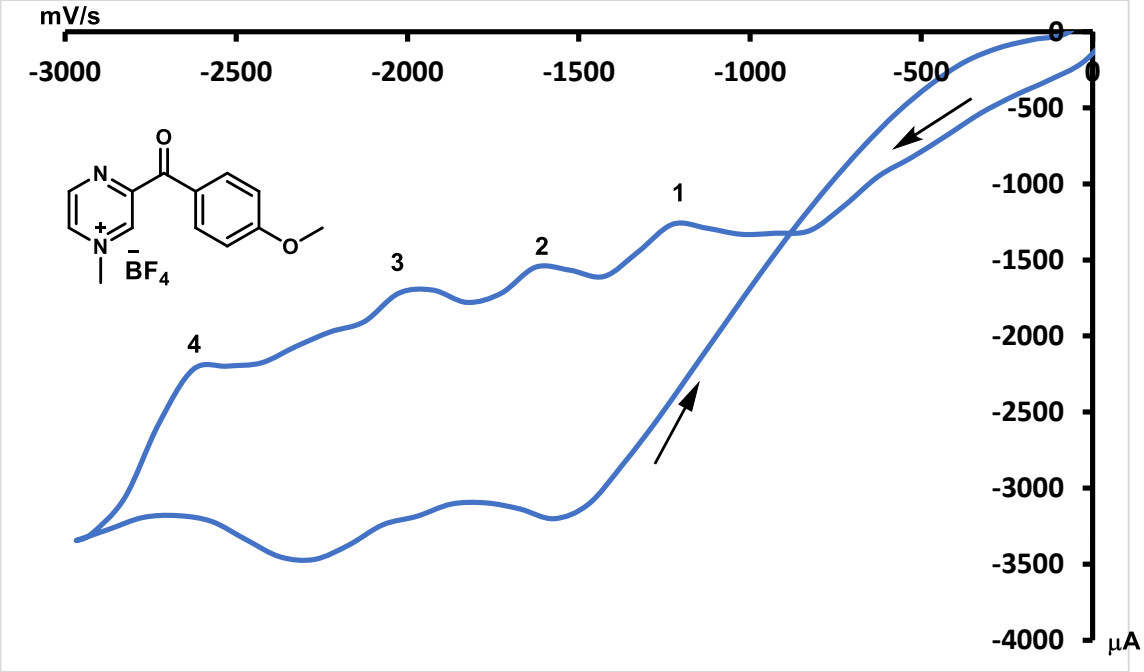

***Figure 18**. Four electron reductions of BPOME BF_4 salt. Concentration 0.5mM in MeCN.*

Applications and Development of Photophysical Properties of Benzoyl Pyraziniums

Aggregate induced emission (AIE) is a photophysical property introduced in 2001 by Luo and coworkers, in which the paradigm of aggregation induced quenching of fluorescence was challenge and the term AIE was coined (**Figure 19**).[46] Since the coinage of the term

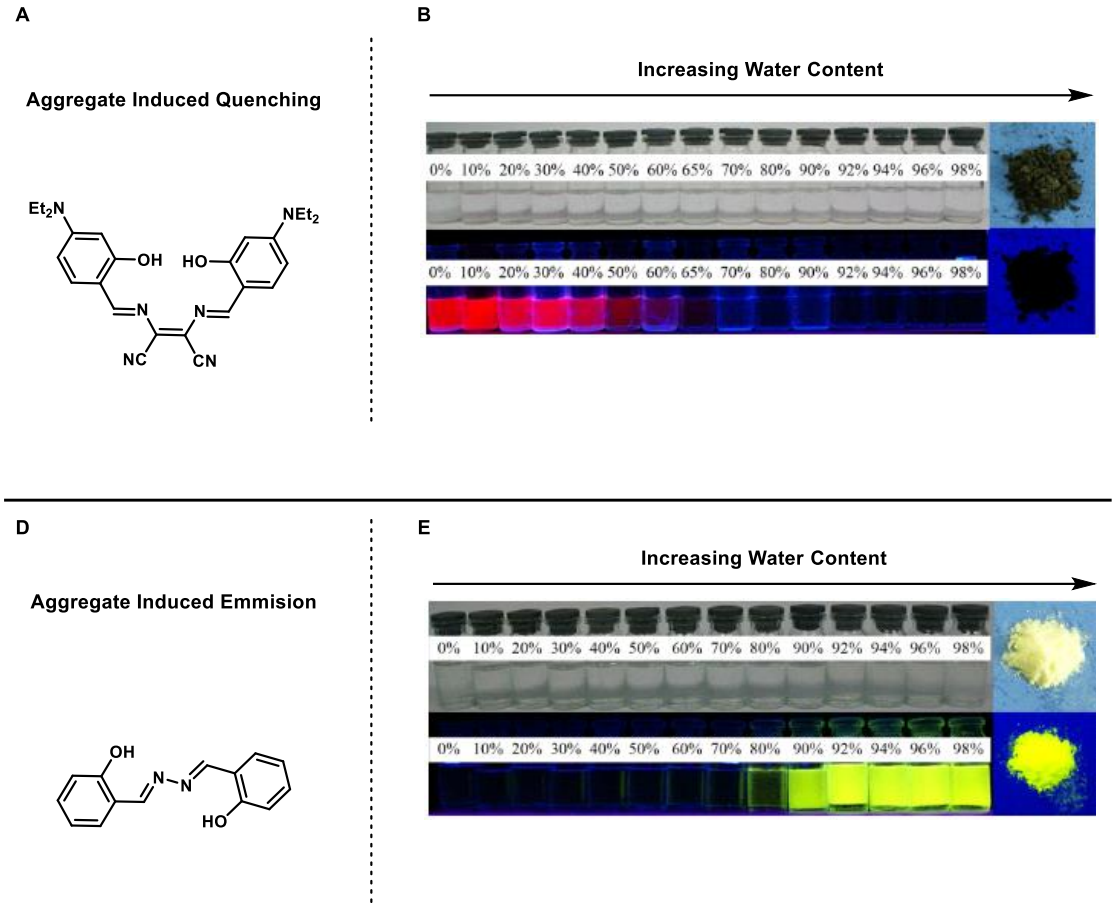

J. Chem. Educ. 2016, 93, 345−350

Figure 19. *Demonstration of aggregated induced emission and quenching. A) Molecule that has aggregate induced quenching. B) increasing water fraction and observation of flu recent quenching at 365nm excitation. D) Molecule that has aggregated induced emission. E) Increase in water fraction leads to aggregation induced emission at 365nm excitation.*

AIE its applications across various spaces with an emphasis on sensing/analytics.[47,48] Currently, the limits of AIE technology are 4 fold: 1) the high molecular weight of the monomeric components, 2) the loss of function at dilute concentrations, 3) the limited emission wavelengths, 4) the inherent hydrophobicity associated with forming the aggregates.[49–51] The current limitations associated with AIE limit potential applications in which either small amounts of material or hydrophilic molecules are needed, however two recently developed polychromic and stimuli responsive AIEs shown in **Figure 20A**

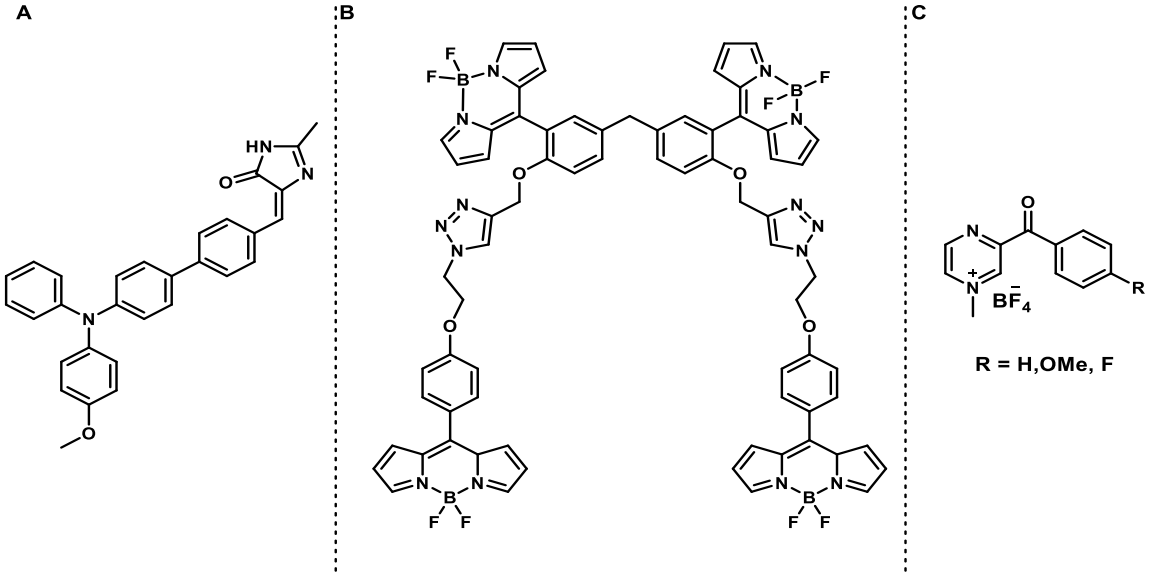

Figure 20*. A) Thermal responsive AIE material. B) Concentration dependent emission. C) Novel small molecule capable of concentration tunable emission.*

(Thermal) and **20B** (Concentration) have illuminated new opportunities in sensing.[52,53] While these two advancements have addressed issues such as hydrophobicity and limited reporting signal, these structures are still not ideal for commercial application due to both a lengthy stepwise synthetic scheme and excessively high molecular weight. Herein we report the photophysical characterization of a series of benzoyl-pyrazinium lumigens (BPL) (**Figure 20C**)

capable of concentration tunable emission in polar media without the addition of water, and the modular synthetic methodology to achieve scalable production as discussed above.

Following synthesis and isolation of the BPL1-3 shown in **Figure 21**, UV-VIS spectroscopy was obtained at: 100mM, 10mM, 1.0mM, and 0.1mM in acetonitrile

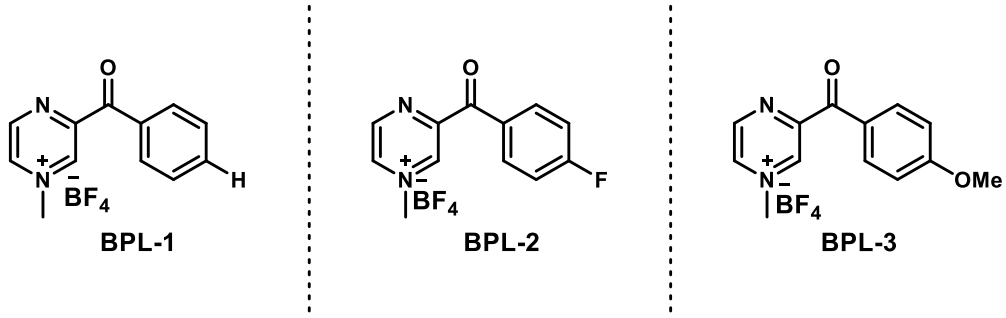

Figure 21. *Structures of BPL1-3*

as shown in **Figure 22**.

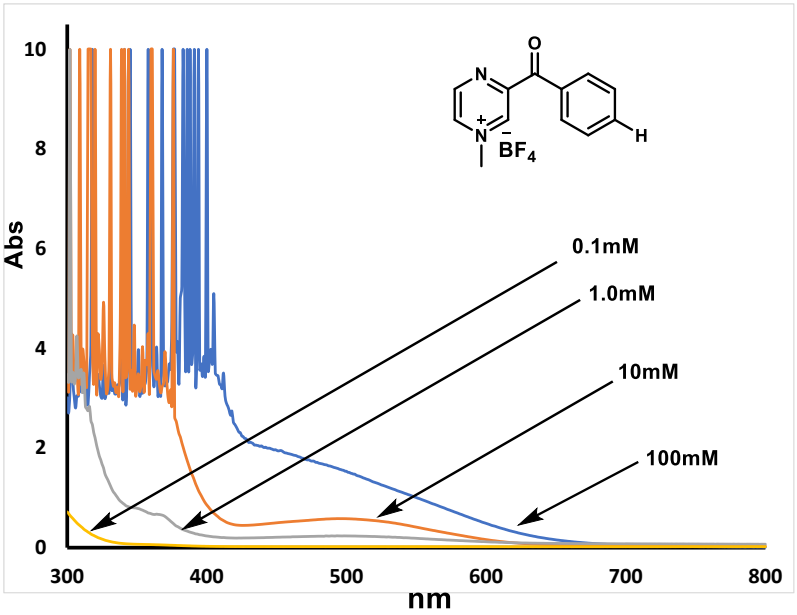

Figure 22. *Concentration dependent UV-Vis spectrum of BPL-1 from 100mM to 0.1mM*

Counterintuitive to foundational understanding of UV-VIS spectroscopy serial dilutions of **BPL1-3** showed significant alterations in the absorption line shape,

rather the pure intensity. To identify any self-screening behavior UV-Vis data of **BPL-1** and **BPL-2** were recollected using a 1mm cuvette instead of the standard 10mm cuvette. The 1mm cuvette caused an observable change in the onset of absorption data for **BPL-1** and **BPL-2** indicating that self-screening was present. (See supporting information). Initially this relationship was attributed to potential instability of the BPL species, however post UVVIS NMR characterization revealed no decomposition had occurred.

Literature precedent of N-alkyl pyridiniums forming AIE complexes through π-π interactions between benzene moieties and the positively charged pyridiniums provided rational for the significant change observed in the titration series in the UV-VIS spectra.[54,55] To investigate the BPLs potential AIE behavior photoluminescence spectroscopy (PL) of **BPL 1-3** at the same conditions used for UV-Vis experiments was performed. The observed broad emission peak of the BPLs collection was obtained through monitoring emission at 90° with no filter and fitting was done omitting the laser peak **Figure 23** shows a concentration dependance on both the center wavelength of the

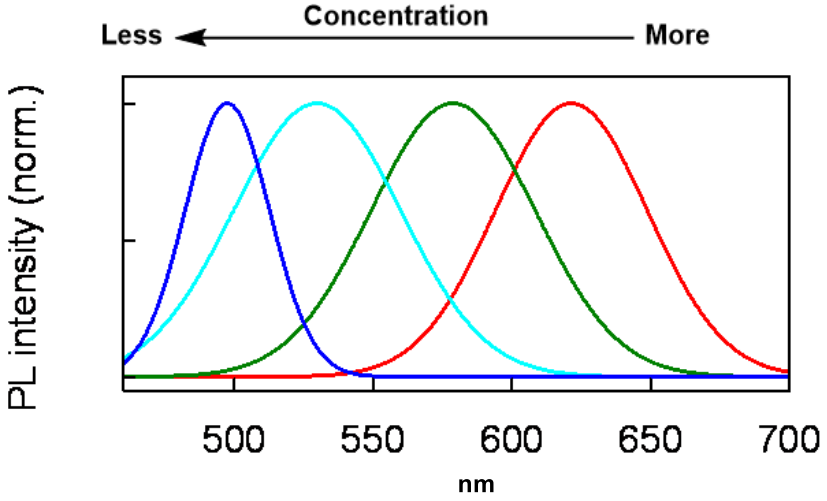

Figure 23. *Concentration dependent photoluminescent spectroscopy of BPL-1 from 100mM to 0.1mM*

emission and full width half maximum (FWHM) with excitation at 430nm for BPL-1 (See supporting information for BPL-2 and BPL-3). An interesting observation was made after inspection of the PL data for all three BPLs. While the emission varies between all BPL species at higher concentrations, they converge as they are diluted to their 0.1mM concentration with a enter wavelengths at approximately 480nm. Interestingly, as samples became more dilute emission was blue shifted and the relative intensity increased compared to the laser peak indicating all three *BPL species can act as chromophores and are not dependent on formation of aggregate species for emission*. Emission of dilute concentrations of AIEs in polar solvents without water is rare, and unprecedented for small molecules. AIE emission in polar solvents is usually demonstrated as a function of the water fraction in a polar solvent (DMSO/MeCN), as the water fraction increases the AIE material is pushed out of the solvent leading to tiny lumisicent aggregate materials through restriction of various non-radiative relaxation pathways.[56] AIE materials in their non-aggregated state are non-emissive due largely in part to either twisted inter molecular charge transfer (TICT) or varying non-radiative pathways of recombination or vibrational relaxation. [53,57,58]

To understand the effect of concentration more fully on electron transfer dynamics time resolved photoluminescent (TRPL) spectroscopy was obtained for all three BPL species using the same spectroscopic conditions as above. TRPL was collected using a Mira-K white light source set to 430nm and pulse rate. All TRPL curves were fitted using a biexponential $I_{pl} = A_1 e^{\frac{-t}{\tau_1}} + A_2 e^{\frac{-t}{\tau_2}}$ and adjusted

R^2> 0.990 were achieved. The results were used to extract average lifetimes using $\tau = (A_1\tau_{1_1}^2 + A_2\tau_2^2)/A_1\tau_1 + A_2\tau_2)$.[44] All BPL samples exhibited similar trends in which in which the more dilute the sample the longer the lifetimes (**Figure 24**), this perplexing result is counterintuitive as when compared with the PL data due the significant blue shift (x> 150nm) that occurs for all BPL samples between 100mM and 0.1mM. As the energy of emission increases (blue shift) one would expect lifetimes to decrease proportionally as well as intensity to decrease as a function of the lower concentration. This data indicates that as

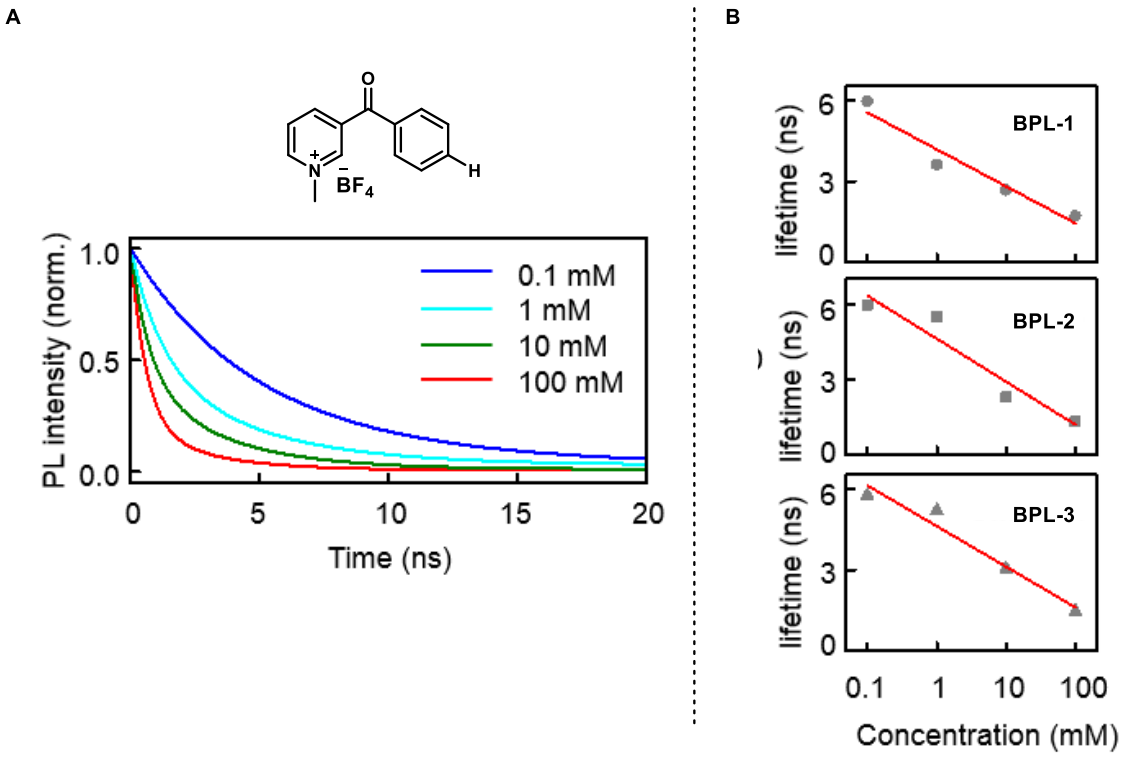

Figure 24. *A) Lifetime curves of BPL-1 at various concentrations. B) Lifetime trends observed for all three BPL species as a function of concentration.*

concentration increases the number of non-radiative decay pathways, leading to the: lower PL intensity, redshift, and shorter lifetimes.[59–61] Due to the well-established ability of pyridiniums to perform intramolecular charge transfer, it is

currently hypothesized that the primary concentration dependent non-radiative decay pathway for the BPLs is through intramolecular charge transfer.[62–64]

To ascertain qualitative evidence of solution aggregation to support both the assertion of AIE type behavior and concentration dependent ITC diffusion-oriented spectroscopy nuclear magnetic resonance (DOSY-NMR). DOSY-NMR provides the ability to determine the (translational) self-diffusion coefficient (SDC) of a substance.[65,66] All three BPL samples were analyzed via DOSY-NMR in deuterated acetone using spectroscopic concentrations with a magnetic gradient of 63g/cm^2. SDCs were extracted by using MNOVA's BAYSIAN transform of 15 H1-NMR spectra to form a pseudo 2D spectra where the cross-peak correlates to SDC. All three BPLs show a significant change in SDCs as a function of concentrations as shown in **Figure 25**. It is observed that as the concentration

increases for both **BPL-2** and **BPL-3** the SDC associated with each BPL becomes larger, while **BPL-1** exhibits the opposite trend. This change in SDC as a function of concentration is a strong indication of aggregate behavior. The

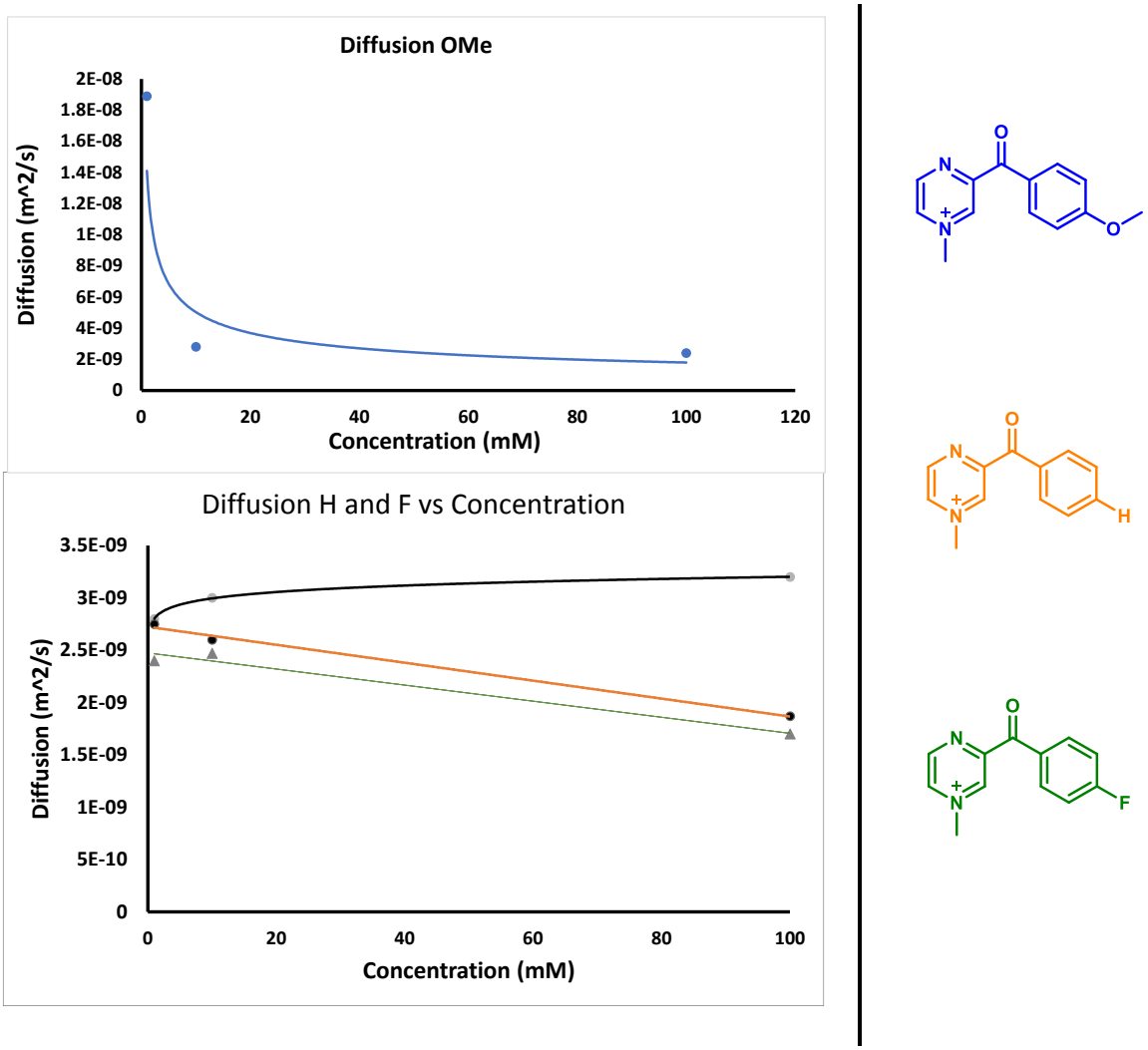

Figure 25. *Self-diffusion coefficients (D) obtained by DOSY NMR of all BPL species at 100mM, 10mM, 1.0mM.*

decrease in SDC as function of concentration indicates **BPL-2** and **BPL-3** form aggregates in more dilute concentrations, while **BPL-1** demonstrates the inverse. This inverse relationship observed with **BPL-1** indicates that the electronic perturbations of the benzoylated arene can significantly impact the aggregate behavior. It is well understood that a pure substance should have a fixed SDC if

both the temperature and viscosity are maintained. It can be inferred that the relationship between increasing concentrations and decreasing SDCs relates to the formation of solution-based aggregate. These aggregates provide support for non-radiative recombination due to ITC observed as decreased PL intensity. While the redshift associated with the emission at higher concentrations is most likely attributed to a complicated CT mechanism within the aggregates in which a non-radiative CT event occurs and either through vibrational or reorganizational the energy level of the excited state decreases prior to radiative recombination. An interesting note is that while the SDCs of all BPLs change as a function of concentration, no significant perturbations to the H^1 spectrum can be observed. This lack of an effect on the H^1 spectrum implies that the aggregation structure/process has a negligible effect on the shielding/de-shielding the individual BPLs. This indicates that the aggregation process, could be significantly affected by the dipole moment of the benzoylated arene. by electronic coordination rather than solubility. While DOSY data provides qualitative evidence of the aggregation behavior altering the emissions, further evidence was desired to support this claim due to the lack of spin transference observed in various 2D NMR experiments (HSQC, COSEY, HMBC). However, when comparing the 100mM and 1mM proton spectra for all three BPLs an increase in relative integrations was observed as a function of decreasing concentration. Increase in signal intensity can only be attributed to increased XY contributions. It is known that changes in T_1 can be attributed to increased non-

covalent interactions.[67,68] This increase in relative integrations indicates an increase T_1, which correlates to the decrease in SDCs observed through DOSY.

Solid State Photoluminescence Data

While BPL solution data shows extreme promise in various application spaces (sensing/biomedical labeling/ devices), to identify the possibility of solid-state devices further experimentation in the solid state is required. Initial PL measurements were taken from thin films drop cast on glass slides at various concentrations of **BPL-1** shown in **Figure 26.** Surprisingly, the broad emission

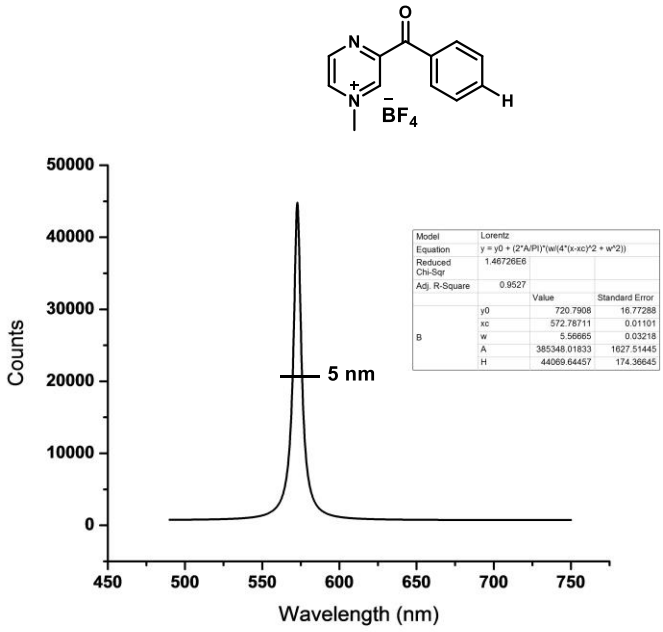

Figure 26. *Solid state PL of a **BPL-1** drop-casted thin film on a glass cover slip demonstrating a 5nm FWHM at room temp.*

peak observed in solution phase was no longer present rather an extremely narrow emission was present. Further experimentation also demonstrated a concentration dependance on the both the center wavelength and absolute intensity. This result is unique due to the narrow FWHM observed in **Figure 26** of 5 nm. Currently, the standard of optical purity for light as of 2021 is X<70nm, with

several purely organic examples failing to meet this standard outside of extreme conditions (temperatures below 12 kelvin). [69] This technology holds significant promise for solid state applications based on this preliminary data.

Conclusion

Herein we have presented a novel Minisci methodology for benzoylation to generate the substituted benzoyl pyrizinium (BPL). BPLs have proven to be highly unique materials that can act as a chromophore in dilute solutions and as concentration increases form solution stable aggregates with tunable emission of over 100nm (650nm-480nm) with the same excitation wavelength. The applications of this technology for sensing are incredibly high as it provides a method for looking not only at the presence of a tagged molecule but also looking at both local and global concentrations a key aspect for analytics employed in the life sciences. Further work is currently under way to ascertain the specific mechanism of electron/hole pair mobility and charge recombination in the aggregate states as well as characterizing the structure of the aggregates.

This work and its continued pursuit was undertaken with the assistance of Imran MD Kahn, Arya Karappilly Rajan, Sayantanni Ghosh, Ryan Baxter

References

(1) Wang, J. Low-Dimensional Semiconductor Materials. **2021**, 1–9. https://doi.org/10.1038/s41467-021-26705-x.

(2) Astruc, D. Electron-Transfer Processes in Dendrimers and Their Implication in Biology, Catalysis, Sensing and Nanotechnology. *Nat. Chem.* **2012**, *4* (4), 255–267. https://doi.org/10.1038/nchem.1304.

(3) Munz, D.; Meyer, K. Charge Frustration in Ligand Design and Functional Group Transfer. *Nat. Rev. Chem.* **2021**, *5* (6), 422–439. https://doi.org/10.1038/s41570-021-00276-3.

(4) Duan, S.; Uragami, C.; Horiuchi, K.; Hino, K.; Wang, X. F.; Sasaki, S. ichi; Tamiaki, H.; Hashimoto, H. Hydroquinone Redox Mediator Enhances the Photovoltaic Performances of Chlorophyll-Based Bio-Inspired Solar Cells. *Commun. Chem.* **2021**, *4* (1), 1–10. https://doi.org/10.1038/s42004-021-00556-5.

(5) Kumar, A.; Hsu, L. H. H.; Kavanagh, P.; Barrière, F.; Lens, P. N. L.; Lapinsonnière, L.; Lienhard, J. H.; Schröder, U.; Jiang, X.; Leech, D. The Ins and Outs of Microorganism-Electrode Electron Transfer Reactions. *Nat. Rev. Chem.* **2017**, *1*, 1–13. https://doi.org/10.1038/s41570-017-0024.

(6) Li, B.; Sougrati, M. T.; Rousse, G.; Morozov, A. V.; Dedryvère, R.; Iadecola, A.; Senyshyn, A.; Zhang, L.; Abakumov, A. M.; Doublet, M. L.; Tarascon, J. M. Correlating Ligand-to-Metal Charge Transfer with Voltage Hysteresis in a

Li-Rich Rock-Salt Compound Exhibiting Anionic Redox. *Nat. Chem.* **2021**, *13* (11), 1070–1080. https://doi.org/10.1038/s41557-021-00775-2.

(7) Wang, S. Emerging Efficient Charge-Transport Landscape Based on Short-Range Order in Conjugated Polymers. *Synth. Met.* **2019**, *251* (March), 104–119. https://doi.org/10.1016/j.synthmet.2019.03.021.

(8) Bates, M.; Lunt, R. R. Organic Salt Photovoltaics. *Sustain. Energy Fuels* **2017**, *1* (5), 955–968. https://doi.org/10.1039/c7se00142h.

(9) Kulkarni, A. P.; Zhu, Y.; Babel, A.; Wu, P. T.; Jenekhe, S. A. New Ambipolar Organic Semiconductors. 2. Effects of Electron Acceptor Strength on Intramolecular Charge Transfer Photophysics, Highly Efficient Electroluminescence, and Field-Effect Charge Transport of Phenoxazine-Based Donor-Acceptor Materials. *Chem. Mater.* **2008**, *20* (13), 4212–4223. https://doi.org/10.1021/cm7022136.

(10) Zampetti, A.; Minotto, A.; Cacialli, F. Near-Infrared (NIR) Organic Light-Emitting Diodes (OLEDs): Challenges and Opportunities. *Adv. Funct. Mater.* **2019**, *29* (21), 1–22. https://doi.org/10.1002/adfm.201807623.

(11) Sentyurin, V. V.; Levitskiy, O. A.; Magdesieva, T. V. Molecular Design of Ambipolar Redox-Active Molecules II: Closed-Shell Systems. *Curr. Opin. Electrochem.* **2020**, *24*, 6–14. https://doi.org/10.1016/j.coelec.2020.05.005.

(12) Hicks, R. G. *Stable Radicals: Fundamentals and Applied Aspects of Odd-Electron Compounds*; 2010. https://doi.org/10.1002/9780470666975.

(13) Antoni, P. W.; Bruckhoff, T.; Hansmann, M. M. Organic Redox Systems Based on Pyridinium-Carbene Hybrids. *J. Am. Chem. Soc.* **2019**, *141* (24), 9701–9711. https://doi.org/10.1021/jacs.9b04249.

(14) Sevov, C. S.; Hickey, D. P.; Cook, M. E.; Robinson, S. G.; Barnett, S.; Minteer, S. D.; Sigman, M. S.; Sanford, M. S. Physical Organic Approach to Persistent, Cyclable, Low-Potential Electrolytes for Flow Battery Applications. *J. Am. Chem. Soc.* **2017**, *139* (8), 2924–2927. https://doi.org/10.1021/jacs.7b00147.

(15) Gomes da Silva, C.; Faria, J. L. Photochemical and Photocatalytic Degradation of an Azo Dye in Aqueous Solution by UV Irradiation. *J. Photochem. Photobiol. A Chem.* **2003**, *155* (1–3), 133–143. https://doi.org/10.1016/s1010-6030(02)00374-x.

(16) Mikhnenko, O. V.; Blom, P. W. M.; Nguyen, T. Q. Exciton Diffusion in Organic Semiconductors. *Energy Environ. Sci.* **2015**, *8* (7), 1867–1888. https://doi.org/10.1039/c5ee00925a.

(17) Zaikowski, L.; Mauro, G.; Bird, M.; Karten, B.; Asaoka, S.; Wu, Q.; Cook, A. R.; Miller, J. R. Charge Transfer Fluorescence and 34 Nm Exciton Diffusion Length in Polymers with Electron Acceptor End Traps. *J. Phys. Chem. B* **2015**, *119* (24), 7231–7241. https://doi.org/10.1021/jp510095p.

(18) Jin, X.; Price, M. B.; Finnegan, J. R.; Boott, C. E.; Richter, J. M.; Rao, A.; Menke, S. M.; Friend, R. H.; Whittell, G. R.; Manners, I. Prepared By Seeded

Growth. *Science (80-.).* **2018**, *360* (May), 897–900.

(19) Gélvez-Rueda, M. C.; Van Gompel, W. T. M.; Herckens, R.; Lutsen, L.; Vanderzande, D.; Grozema, F. C. Inducing Charge Separation in Solid-State Two-Dimensional Hybrid Perovskites through the Incorporation of Organic Charge-Transfer Complexes. *J. Phys. Chem. Lett.* **2020**, *11* (3), 824–830. https://doi.org/10.1021/acs.jpclett.9b03746.

(20) Hill, I. G.; Kahn, A.; Soos, Z. G.; Pascal, R. A. Charge-Separation Energy in Films of π -Conjugated Organic Molecules. *Chem. Phys. Lett.* **2000**, *327* (3–4), 181–188. https://doi.org/10.1016/S0009-2614(00)00882-4.

(21) Leenaers, P. J.; Maufort, A. J. L. A.; Wienk, M. M.; Janssen, R. A. J. Impact of π-Conjugated Linkers on the Effective Exciton Binding Energy of Diketopyrrolopyrrole–Dithienopyrrole Copolymers. *J. Phys. Chem. C* **2020**, acs.jpcc.0c08768. https://doi.org/10.1021/acs.jpcc.0c08768.

(22) Luo, J.; Hu, B.; Hu, M.; Zhao, Y.; Liu, T. L. Status and Prospects of Organic Redox Flow Batteries toward Sustainable Energy Storage. *ACS Energy Lett.* **2019**, *4* (9), 2220–2240. https://doi.org/10.1021/acsenergylett.9b01332.

(23) Gentil, S.; Reynard, D.; Girault, H. H. Aqueous Organic and Redox-Mediated Redox Flow Batteries: A Review. *Curr. Opin. Electrochem.* **2020**, *21*, 7–13. https://doi.org/10.1016/j.coelec.2019.12.006.

(24) Wei, X.; Pan, W.; Duan, W.; Hollas, A.; Yang, Z.; Li, B.; Nie, Z.; Liu, J.; Reed, D.; Wang, W.; Sprenkle, V. Materials and Systems for Organic Redox Flow

Batteries: Status and Challenges. *ACS Energy Lett.* **2017**, *2* (9), 2187–2204. https://doi.org/10.1021/acsenergylett.7b00650.

(25) Sevov, C. S.; Hickey, D. P.; Cook, M. E.; Robinson, S. G.; Barnett, S.; Minteer, S. D.; Sigman, M. S.; Sanford, M. S. Physical Organic Approach to Persistent, Cyclable, Low-Potential Electrolytes for Flow Battery Applications. *J. Am. Chem. Soc.* **2017**, *139* (8), 2924–2927. https://doi.org/10.1021/jacs.7b00147.

(26) Yan, Y.; Vogt, D. B.; Vaid, T. P.; Sigman, M. S.; Sanford, M. Development of High Energy Density Diaminocyclopropenium-Phenothiazine Hybrid Catholytes for Non-Aqueous Redox Flow Batteries. *Angew. Chemie Int. Ed.* **2021**. https://doi.org/10.1002/anie.202111939.

(27) Cabrera, P. J.; Yang, X.; Suttil, J. A.; Hawthorne, K. L.; Brooner, R. E. M.; Sanford, M. S.; Thompson, L. T. Complexes Containing Redox Noninnocent Ligands for Symmetric, Multielectron Transfer Nonaqueous Redox Flow Batteries. *J. Phys. Chem. C* **2015**, *119* (28), 15882–15889. https://doi.org/10.1021/acs.jpcc.5b03582.

(28) Vaid, T. P.; Sanford, M. S. An Organic Super-Electron-Donor as a High Energy Density Negative Electrolyte for Nonaqueous Flow Batteries. *Chem. Commun.* **2019**, *55* (74), 11037–11040. https://doi.org/10.1039/c9cc06080d.

(29) Han, Z.; Vaid, T. P.; Rheingold, A. L. Hexakis(4-(N-

Butylpyridylium))Benzene: A Six-Electron Organic Redox System. *J. Org. Chem.* **2008**, *73* (2), 445–450. https://doi.org/10.1021/jo701944c.

(30) Curphey, T. J. Heterocyclic Diquaternary Salts. *J. Am. Chem. Soc.* **1965**, *87* (9), 2063–2064. https://doi.org/10.1021/ja01087a047.

(31) Sevov, C. S.; Hendriks, K. H.; Sanford, M. S. Low-Potential Pyridinium Anolyte for Aqueous Redox Flow Batteries. *J. Phys. Chem. C* **2017**, *121* (39). https://doi.org/10.1021/acs.jpcc.7b06247.

(32) Qu, X.; Jain, A.; Rajput, N. N.; Cheng, L.; Zhang, Y.; Ong, S. P.; Brafman, M.; Maginn, E.; Curtiss, L. A.; Persson, K. A. The Electrolyte Genome Project: A Big Data Approach in Battery Materials Discovery. *Comput. Mater. Sci.* **2015**, *103*, 56–67. https://doi.org/10.1016/j.commatsci.2015.02.050.

(33) Hammett, L. P. The Effect of Structure upon the Reactions of Organic Compounds. Benzene Derivatives. *J. Am. Chem. Soc.* **1937**, *59* (1), 96–103. https://doi.org/10.1021/ja01280a022.

(34) Hammett, P. Vol. 50. **1933**, *50* (1926), 2666–2673.

(35) Moser, W. R.; Papile, C. J.; Brannon, D. A.; Duwell, R. A.; Weininger, S. J. The Mechanism of Phosphine-Modified Rhodium-Catalyzed Hydroformylation Studied by CIR-FTIR. *J. Mol. Catal.* **1987**, *41* (3), 271–292. https://doi.org/10.1016/0304-5102(87)80106-2.

(36) Pelzer, K. M.; Cheng, L.; Curtiss, L. A. Effects of Functional Groups in Redox-Active Organic Molecules: A High-Throughput Screening Approach.

J. Phys. Chem. C **2017**, *121* (1), 237–245. https://doi.org/10.1021/acs.jpcc.6b11473.

(37) Brethomé, A. V.; Fletcher, S. P.; Paton, R. S. Conformational Effects on Physical-Organic Descriptors: The Case of Sterimol Steric Parameters. *ACS Catal.* **2019**, *9* (3), 2313–2323. https://doi.org/10.1021/acscatal.8b04043.

(38) Charton, M. Steric Effects. I. Esterification and Acid-Catalyzed Hydrolysis of Esters. *J. Am. Chem. Soc.* **1975**, *97* (6), 1552–1556. https://doi.org/10.1021/ja00839a047.

(39) Cheng, L.; Assary, R. S.; Qu, X.; Jain, A.; Ong, S. P.; Rajput, N. N.; Persson, K.; Curtiss, L. A. Accelerating Electrolyte Discovery for Energy Storage with High-Throughput Screening. *J. Phys. Chem. Lett.* **2015**, *6* (2), 283–291. https://doi.org/10.1021/jz502319n.

(40) Minisci, F.; Recupero, F.; Cecchetto, A.; Punta, C.; Gambarotti, C.; Fontana, F.; Pedulli, G. F. Polar Effects in Free-Radical Reactions. A Novel Homolytic Acylation of Heteroaromatic Bases by Aerobic Oxidation of Aldehydes, Catalysed by N-Hydroxyphthalimide and Co Salts. *J. Heterocycl. Chem.* **2003**, *40* (2), 325–328. https://doi.org/10.1002/jhet.5570400220.

(41) Sharma, S.; Kumar, M.; Vishwakarma, R. A.; Verma, M. K.; Singh, P. P. Room Temperature Metal-Catalyzed Oxidative Acylation of Electron-Deficient Heteroarenes with Alkynes, Its Mechanism, and Application Studies. *J. Org. Chem.* **2018**, *83* (20), 12420–12431.

https://doi.org/10.1021/acs.joc.8b01475.

(42) Meng, G.; Shi, S.; Szostak, M. Palladium-Catalyzed Suzuki−Miyaura Cross-Coupling of Amides via Site-Selective N−C Bond Cleavage by Cooperative Catalysis. *ACS Catal.* **2016**, *6* (11), 6–10. https://doi.org/10.1021/acscatal.6b02323.

(43) Galloway, J. D.; Mai, D. N.; Baxter, R. D. Radical Benzylation of Quinones via C-H Abstraction. *J. Org. Chem.* **2019**, *84* (18), 12131–12137. https://doi.org/10.1021/acs.joc.9b01004.

(44) Bartolo, M. D.; Brisbin, R. P.; Ghosh, S.; Baxter, R. D. Impact of Bis (Imino) Pyridine Ligands on Mesoscale Properties of CdSe / ZnS Quantum Dots. **2020**.

(45) Wang, P.; Lindsey, J. S. Riley Oxidation of Heterocyclic Intermediates on Paths to Hydroporphyrins—A Review. *Molecules* **2020**, *25* (8). https://doi.org/10.3390/molecules25081858.

(46) Luo, J.; Xie, Z.; Xie, Z.; Lam, J. W. Y.; Cheng, L.; Chen, H.; Qiu, C.; Kwok, H. S.; Zhan, X.; Liu, Y.; Zhu, D.; Tang, B. Z. Aggregation-Induced Emission of 1-Methyl-1,2,3,4,5-Pentaphenylsilole. *Chem. Commun.* **2001**, *18*, 1740–1741. https://doi.org/10.1039/b105159h.

(47) Hong, Y.; Lam, J. W. Y.; Tang, B. Z. Aggregation-Induced Emission. *Chem. Soc. Rev.* **2011**, *40* (11), 5361–5388. https://doi.org/10.1039/c1cs15113d.

(48) Chen, Y.; Lam, J. W. Y.; Kwok, R. T. K.; Liu, B.; Tang, B. Z. Aggregation-

Induced Emission: Fundamental Understanding and Future Developments. *Mater. Horizons* **2019**, *6* (3), 428–433. https://doi.org/10.1039/c8mh01331d.

(49) Zhu, S. Q.; Liu, Y. L.; Li, H.; Xu, X. H.; Qing, F. L. Direct and Regioselective C-H Oxidative Difluoromethylation of Heteroarenes. *J. Am. Chem. Soc.* **2018**, *140* (37), 11613–11617. https://doi.org/10.1021/jacs.8b08135.

(50) Zhao, Z.; Zhang, H.; Lam, J. W. Y.; Tang, B. Z. Aggregation-Induced Emission: New Vistas at the Aggregate Level. *Angew. Chemie - Int. Ed.* **2020**, *59* (25), 9888–9907. https://doi.org/10.1002/anie.201916729.

(51) He, Z.; Ke, C.; Tang, B. Z. Journey of Aggregation-Induced Emission Research. *ACS Omega* **2018**, *3* (3), 3267–3277. https://doi.org/10.1021/acsomega.8b00062.

(52) Dwivedi, B. K.; Singh, V. D.; Pandey, D. S. Controlling Photophysical Properties of Systems Containing Multiple BODIPY Units Linked by Methylene Bridge. *J. Phys. Chem. C* **2020**, *124* (16), 9056–9067. https://doi.org/10.1021/acs.jpcc.0c00690.

(53) Xue, K.; Wang, C.; Wang, J.; Lv, S.; Hao, B.; Zhu, C.; Tang, B. Z. A Sensitive and Reliable Organic Fluorescent Nanothermometer for Noninvasive Temperature Sensing. *J. Am. Chem. Soc.* **2021**. https://doi.org/10.1021/jacs.1c04597.

(54) Leduskrasts, K.; Suna, E. Aggregation Induced Emission by Pyridinium-Pyridinium Interactions. *RSC Adv.* **2019**, *9* (1), 460–465.

https://doi.org/10.1039/C8RA08771G.

(55) Chen, W.; Elfeky, S. A.; Nonne, Y.; Male, L.; Ahmed, K.; Amiable, C.; Axe, P.; Yamada, S.; James, T. D.; Bull, S. D.; Fossey, J. S. A Pyridinium Cation–π Interaction Sensor for the Fluorescent Detection of Alkyl Halides. *Chem. Commun.* **2011**, *47* (1), 253–255. https://doi.org/10.1039/C0CC01420F.

(56) Zhou, J.; Chang, Z.; Jiang, Y.; He, B.; Du, M.; Lu, P.; Hong, Y.; Kwok, H. S.; Qin, A.; Qiu, H.; Zhao, Z.; Tang, B. Z. From Tetraphenylethene to Tetranaphthylethene: Structural Evolution in AIE Luminogen Continues. *Chem. Commun.* **2013**, *49* (25), 2491–2493. https://doi.org/10.1039/c3cc00010a.

(57) Leung, N. L. C.; Xie, N.; Yuan, W.; Liu, Y.; Wu, Q.; Peng, Q.; Miao, Q.; Lam, J. W. Y.; Tang, B. Z. Restriction of Intramolecular Motions: The General Mechanism behind Aggregation-Induced Emission. *Chem. - A Eur. J.* **2014**, *20* (47), 15349–15353. https://doi.org/10.1002/chem.201403811.

(58) Liu, J.; Meng, Q.; Zhang, X.; Lu, X.; He, P.; Jiang, L.; Dong, H.; Hu, W. Aggregation-Induced Emission Enhancement Based on 11,11,12,12,-Tetracyano-9,10-Anthraquinodimethane. *Chem. Commun.* **2013**, *49* (12), 1199–1201. https://doi.org/10.1039/c2cc38817k.

(59) Rout, Y.; Montanari, C.; Pasciucco, E.; Misra, R.; Carlotti, B. Tuning the Fluorescence and the Intramolecular Charge Transfer of Phenothiazine Dipolar and Quadrupolar Derivatives by Oxygen Functionalization. **2021**.

https://doi.org/10.1021/jacs.1c04173.

(60) Zhu, H.; Li, M.; Hu, J.; Wang, X.; Jie, J.; Guo, Q.; Chen, C.; Xia, A. Ultrafast Investigation of Intramolecular Charge Transfer and Solvation Dynamics of Tetrahydro[5]-Helicene-Based Imide Derivatives. *Sci. Rep.* **2016**, *6* (March), 1–12. https://doi.org/10.1038/srep24313.

(61) Vachova, L.; Novakova, V.; Kopecky, K.; Miletin, M.; Zimcik, P. Effect of Intramolecular Charge Transfer on Fluorescence and Singlet Oxygen Production of Phthalocyanine Analogues. *Dalt. Trans.* **2012**, *41* (38), 11651. https://doi.org/10.1039/c2dt31403g.

(62) Carlotti, B.; Consiglio, G.; Elisei, F.; Fortuna, C. G.; Mazzucato, U.; Spalletti, A. Intramolecular Charge Transfer of Push-Pull Pyridinium Salts in the Triplet Manifold. *J. Phys. Chem. A* **2014**, *118* (36), 7782–7787. https://doi.org/10.1021/jp504963v.

(63) Sasaki, S.; Drummen, G. P. C.; Konishi, G. I. Recent Advances in Twisted Intramolecular Charge Transfer (TICT) Fluorescence and Related Phenomena in Materials Chemistry. *J. Mater. Chem. C* **2016**, *4* (14), 2731–2743. https://doi.org/10.1039/c5tc03933a.

(64) Cesaretti, A.; Bonaccorso, C.; Elisei, F.; Fortuna, C. G.; Mencaroni, L.; Spalletti, A. Photoinduced Intramolecular Charge Transfer and Hyperpolarizability Coefficient in Push-Pull Pyridinium Salts with Increasing Strength of the Acceptor Group. *Chempluschem* **2018**, *83* (11), 1021–1031.

https://doi.org/10.1002/cplu.201800393.

(65) Evans, R. The Interpretation of Small Molecule Diffusion Coefficients: Quantitative Use of Diffusion-Ordered NMR Spectroscopy. *Prog. Nucl. Magn. Reson. Spectrosc.* **2020**, *117*, 33–69. https://doi.org/10.1016/j.pnmrs.2019.11.002.

(66) Šmejkalová, D.; Piccolo, A. Aggregation and Disaggregation of Humic Supramolecular Assemblies by NMR Diffusion Ordered Spectroscopy (DOSY-NMR). *Environ. Sci. Technol.* **2008**, *42* (3), 699–706. https://doi.org/10.1021/es071828p.

(67) Šmejkalová, D.; Piccolo, A. Host-Guest Interactions between 2,4-Dichlorophenol and Humic Substances as Evaluated by 1H NMR Relaxation and Diffusion Ordered Spectroscopy. *Environ. Sci. Technol.* **2008**, *42* (22), 8440–8445. https://doi.org/10.1021/es801809v.

(68) Parenti, F.; Tassinari, F.; Libertini, E.; Lanzi, M.; Mucci, A. π-Stacking Signature in Nmr Solution Spectra of Thiophene-Based Conjugated Polymers. *ACS Omega* **2017**, *2* (9), 5775–5784. https://doi.org/10.1021/acsomega.7b00943.

(69) Ha, J. M.; Hur, S. H.; Pathak, A.; Jeong, J. E.; Woo, H. Y. Recent Advances in Organic Luminescent Materials with Narrowband Emission. *NPG Asia Mater.* **2021**, *13* (1). https://doi.org/10.1038/s41427-021-00318-8.

Synthesis for Chapter 1 & 2

Required Materials

- 2,6 DactylPyridine (CAS: 1129-30-2)
- Aniline Derivatives
- P-toluenesulfonic Acid (CAS: 6192-52-5)
- Toluene (CAS: 108-88-3)
- Methanol (CAS: 67-56-1)

Ligands **A-E** were synthesized through azeotropic distillation of 2,6-diacetylpyridine in toluene with the corresponding aniline. 2,6-diacetylpyridine (3 mmols), the aniline derivative (12 mmol, 20 for ligand **E**), and p-toluenesulfonic acid (0.3 mmol) were added to a flame-dried 250ml round bottom flask. Pre-dried toluene (100 ml) was added to the flame dried 250mL round bottom, and the resulting mixture was refluxed using a Dean-Stark apparatus for 24 hours.

The reaction mixture was cooled to room temperature and aqueous saturated sodium bicarbonate (100 ml) was added. The mixture was transferred to a separatory funnel and the organic layer was extracted. The aqueous layer was washed 3-4 times with dichloromethane and the organic layers were combined, dried with sodium sulfate, and concentrated. The resulting concentrate was dissolved in 15-20 ml of methanol and allowed to sit at room temperature for 24 hours, then placed at –20 Celsius for 12-24 hours. The resulting yellow solid was vacuum filtered and washed with cold methanol, then hexanes.

Crystals were transferred to a 20mL dram vial and put under hi-vacuum for 3-5 hours. 1H-NMR was used to assess purity. If high concentrations of mono condensed species were present, recrystallization in cold methanol was performed if impurities were detected. Single crystals were grown through solvation in hot methanol and allowed to cool over night at room temperature. It should be noted that purification of **G** was carried out differently, and crystallization was carried out in a 70:30 mixture of pre-dried $CHCl_3$: Hexanes. This was done to prevent decomposition of the deactivated imine bonds, that was observed when standard recrystallization in methanol was performed.

Crystallography

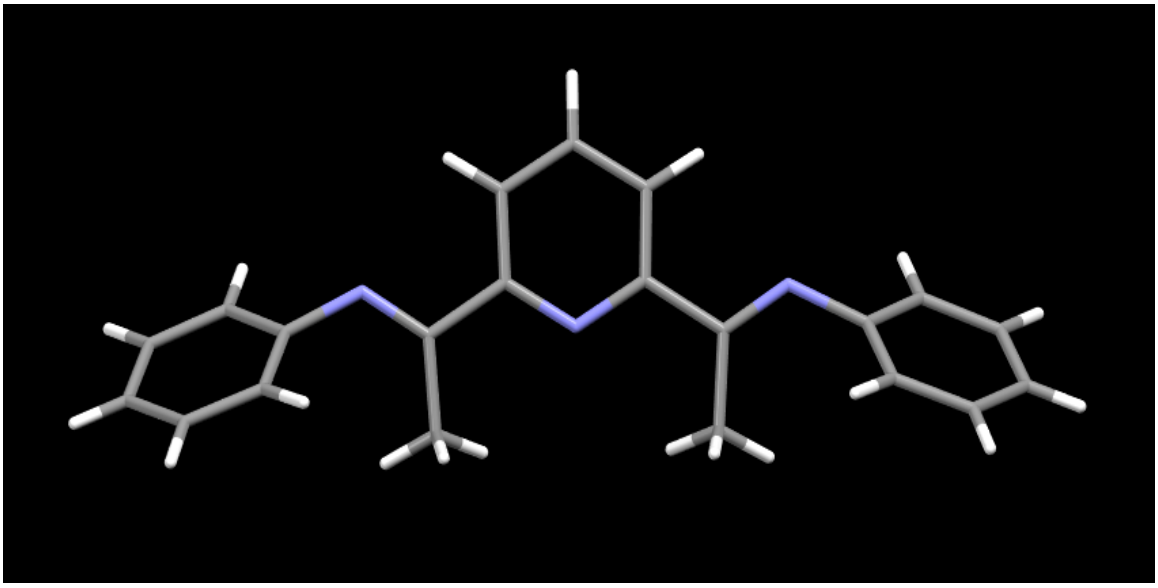

Number	Label	Charge	SybylType	Xfrac + ESD	Yfrac + ESD	Zfrac + ESD
1	C1	0	C.2	0.32014(11)	0.83836(7)	0.48358(7)
2	N1	0	N.2	0.25578(9)	0.76304(6)	0.50489(6)
3	C2	0	C.2	0.45930(11)	0.85477(8)	0.52172(8)
4	H2	0	H	0.5004(14)	0.9108(10)	0.5038(9)
5	C3	0	C.2	0.53473(12)	0.78946(8)	0.58252(8)
6	H3	0	H	0.6323(15)	0.7992(10)	0.6095(9)
7	C4	0	C.2	0.46984(11)	0.71088(8)	0.60394(7)
8	H4	0	H	0.5183(14)	0.6632(10)	0.6457(9)
9	C5	0	C.2	0.32979(11)	0.70126(7)	0.56507(7)
10	C6	0	C.2	0.25441(11)	0.61851(7)	0.58707(7)
11	N6	0	N.2	0.32542(10)	0.55703(6)	0.64024(6)
12	C7	0	C.3	0.10314(12)	0.61490(9)	0.54453(9)
13	H7A	0	H	0.0646(16)	0.5602(11)	0.5658(11)
14	H7B	0	H	0.0818(17)	0.6174(12)	0.4769(12)
15	H7C	0	H	0.0602(18)	0.6716(12)	0.5638(12)
16	C8	0	C.2	0.26649(11)	0.47266(7)	0.66125(7)
17	C9	0	C.2	0.22729(11)	0.46572(8)	0.74392(8)
18	C10	0	C.2	0.18256(12)	0.37954(8)	0.76718(8)
19	H10	0	H	0.1544(14)	0.3744(10)	0.8245(10)
20	C11	0	C.2	0.17651(12)	0.30238(8)	0.71053(8)
21	H11	0	H	0.1460(14)	0.2423(10)	0.7288(10)
22	C12	0	C.2	0.21463(13)	0.31089(8)	0.62869(8)
23	H12	0	H	0.2120(15)	0.2564(10)	0.5877(10)
24	C13	0	C.2	0.26003(12)	0.39569(8)	0.60257(8)
25	C14	0	C.3	0.23280(14)	0.54943(9)	0.80530(9)

26	H14A	0	H	0.3253(17)	0.5767(11)	0.8218(10)
27	H14B	0	H	0.2101(16)	0.5321(10)	0.8639(11)
28	H14C	0	H	0.1682(16)	0.6000(11)	0.7731(11)
29	C15	0	C.3	0.30345(17)	0.40491(10)	0.51459(10)
30	H15A	0	H	0.2477(17)	0.4525(12)	0.4711(12)
31	H15B	0	H	0.2904(18)	0.3460(13)	0.4787(12)
32	H15C	0	H	0.399(2)	0.4246(13)	0.5277(12)
33	C16	0	C.2	0.23511(11)	0.90195(7)	0.41157(7)
34	N16	0	N.2	0.27953(10)	0.98448(7)	0.40688(6)
35	C17	0	C.3	0.10760(13)	0.86130(9)	0.34956(8)
36	H17A	0	H	0.0605(15)	0.9052(10)	0.3027(10)
37	H17B	0	H	0.0461(16)	0.8399(11)	0.3870(11)
38	H17C	0	H	0.1279(17)	0.8041(12)	0.3184(11)
39	C18	0	C.2	0.21195(12)	1.04669(8)	0.33480(8)
40	C19	0	C.2	0.26007(12)	1.05117(8)	0.25537(8)
41	C20	0	C.2	0.20627(14)	1.11934(10)	0.18925(9)
42	H20	0	H	0.2396(16)	1.1219(11)	0.1348(11)
43	C21	0	C.2	0.10737(14)	1.18062(10)	0.20082(9)
44	H21	0	H	0.0713(16)	1.2279(11)	0.1545(11)
45	C22	0	C.2	0.05994(13)	1.17460(9)	0.27917(9)
46	H22	0	H	-0.0114(16)	1.2173(11)	0.2875(10)
47	C23	0	C.2	0.11120(12)	1.10772(8)	0.34744(8)
48	C24	0	C.3	0.36836(15)	0.98466(11)	0.24381(10)
49	H24A	0	H	0.3306(18)	0.9192(13)	0.2297(12)
50	H24B	0	H	0.4446(18)	0.9799(12)	0.3017(12)
51	H24C	0	H	0.4063(17)	1.0046(12)	0.1923(12)
52	C25	0	C.3	0.05940(15)	1.10102(10)	0.43223(9)

53	H25A	0	H	-0.0043(18)	1.1525(13)	0.4347(12)
54	H25B	0	H	0.1341(18)	1.1013(12)	0.4893(12)
55	H25C	0	H	0.0098(18)	1.0420(13)	0.4333(12)
56	C1	0	C.2	0.17986(11)	0.33836(7)	0.01642(7)
57	N1	0	N.2	0.24422(9)	0.26304(6)	-0.00489(6)
58	C2	0	C.2	0.04070(11)	0.35477(8)	-0.02172(8)
59	H2	0	H	-0.0004(14)	0.4108(10)	-0.0038(9)
60	C3	0	C.2	-0.03473(12)	0.28946(8)	-0.08252(8)
61	H3	0	H	-0.1323(15)	0.2992(10)	-0.1095(9)
62	C4	0	C.2	0.03016(11)	0.21088(8)	-0.10394(7)
63	H4	0	H	-0.0183(14)	0.1632(10)	-0.1457(9)
64	C5	0	C.2	0.17021(11)	0.20126(7)	-0.06507(7)
65	C6	0	C.2	0.24559(11)	0.11851(7)	-0.08707(7)
66	N6	0	N.2	0.17458(10)	0.05703(6)	-0.14024(6)
67	C7	0	C.3	0.39686(12)	0.11490(9)	-0.04453(9)
68	H7A	0	H	0.4354(16)	0.0602(11)	-0.0658(11)
69	H7B	0	H	0.4182(17)	0.1174(12)	0.0231(12)
70	H7C	0	H	0.4398(18)	0.1716(12)	-0.0638(12)
71	C8	0	C.2	0.23351(11)	-0.02734(7)	-0.16125(7)
72	C9	0	C.2	0.27271(11)	-0.03428(8)	-0.24392(8)
73	C10	0	C.2	0.31744(12)	-0.12046(8)	-0.26718(8)
74	H10	0	H	0.3456(14)	-0.1256(10)	-0.3245(10)
75	C11	0	C.2	0.32349(12)	-0.19762(8)	-0.21053(8)
76	H11	0	H	0.3540(14)	-0.2577(10)	-0.2288(10)
77	C12	0	C.2	0.28537(13)	-0.18911(8)	-0.12869(8)
78	H12	0	H	0.2880(15)	-0.2436(10)	-0.0877(10)

79	C13	0	C.2	0.23997(12)	-0.10431(8)	-0.10257(8)
80	C14	0	C.3	0.26720(14)	0.04943(9)	-0.30530(9)
81	H14A	0	H	0.1747(17)	0.0767(11)	-0.3218(10)
82	H14B	0	H	0.2899(16)	0.0321(10)	-0.3639(11)
83	H14C	0	H	0.3318(16)	0.1000(11)	-0.2731(11)
84	C15	0	C.3	0.19655(17)	-0.09509(10)	-0.01459(10)
85	H15A	0	H	0.2523(17)	-0.0475(12)	0.0289(12)
86	H15B	0	H	0.2096(18)	-0.1540(13)	0.0213(12)
87	H15C	0	H	0.101(2)	-0.0754(13)	-0.0277(12)
88	C16	0	C.2	0.26489(11)	0.40195(7)	0.08843(7)
89	N16	0	N.2	0.22047(10)	0.48448(7)	0.09312(6)
90	C17	0	C.3	0.39240(13)	0.36130(9)	0.15044(8)
91	H17A	0	H	0.4395(15)	0.4052(10)	0.1973(10)
92	H17B	0	H	0.4539(16)	0.3399(11)	0.1130(11)
93	H17C	0	H	0.3721(17)	0.3041(12)	0.1816(11)
94	C18	0	C.2	0.28805(12)	0.54669(8)	0.16520(8)
95	C19	0	C.2	0.23993(12)	0.55117(8)	0.24463(8)
96	C20	0	C.2	0.29373(14)	0.61934(10)	0.31075(9)
97	H20	0	H	0.2604(16)	0.6219(11)	0.3652(11)
98	C21	0	C.2	0.39263(14)	0.68062(10)	0.29918(9)
99	H21	0	H	0.4287(16)	0.7279(11)	0.3455(11)
100	C22	0	C.2	0.44006(13)	0.67460(9)	0.22083(9)
101	H22	0	H	0.5114(16)	0.7173(11)	0.2125(10)
102	C23	0	C.2	0.38880(12)	0.60772(8)	0.15256(8)
103	C24	0	C.3	0.13164(15)	0.48466(11)	0.25619(10)
104	H24A	0	H	0.1694(18)	0.4192(13)	0.2703(12)

105	H24B	0	H	0.0554(18)	0.4799(12)	0.1983(12)
106	H24C	0	H	0.0937(17)	0.5046(12)	0.3077(12)
107	C25	0	C.3	0.44060(15)	0.60102(10)	0.06777(9)
108	H25A	0	H	0.5043(18)	0.6525(13)	0.0653(12)
109	H25B	0	H	0.3659(18)	0.6013(12)	0.0107(12)
110	H25C	0	H	0.4902(18)	0.5420(13)	0.0667(12)
111	C1	0	C.2	0.67986(11)	0.16164(7)	0.51642(7)
112	N1	0	N.2	0.74422(9)	0.23696(6)	0.49511(6)
113	C2	0	C.2	0.54070(11)	0.14523(8)	0.47828(8)
114	H2	0	H	0.4996(14)	0.0892(10)	0.4962(9)
115	C3	0	C.2	0.46527(12)	0.21054(8)	0.41748(8)
116	H3	0	H	0.3677(15)	0.2008(10)	0.3905(9)
117	C4	0	C.2	0.53016(11)	0.28912(8)	0.39606(7)
118	H4	0	H	0.4817(14)	0.3368(10)	0.3543(9)
119	C5	0	C.2	0.67021(11)	0.29874(7)	0.43493(7)
120	C6	0	C.2	0.74559(11)	0.38149(7)	0.41293(7)
121	N6	0	N.2	0.67458(10)	0.44297(6)	0.35976(6)
122	C7	0	C.3	0.89686(12)	0.38510(9)	0.45547(9)
123	H7A	0	H	0.9354(16)	0.4398(11)	0.4342(11)
124	H7B	0	H	0.9182(17)	0.3826(12)	0.5231(12)
125	H7C	0	H	0.9398(18)	0.3284(12)	0.4362(12)
126	C8	0	C.2	0.73351(11)	0.52734(7)	0.33875(7)
127	C9	0	C.2	0.77271(11)	0.53428(8)	0.25608(8)
128	C10	0	C.2	0.81744(12)	0.62046(8)	0.23282(8)
129	H10	0	H	0.8456(14)	0.6256(10)	0.1755(10)
130	C11	0	C.2	0.82349(12)	0.69762(8)	0.28947(8)
131	H11	0	H	0.8540(14)	0.7577(10)	0.2712(10)

132	C12	0	C.2	0.78537(13)	0.68911(8)	0.37131(8)
133	H12	0	H	0.7880(15)	0.7436(10)	0.4123(10)
134	C13	0	C.2	0.73997(12)	0.60431(8)	0.39743(8)
135	C14	0	C.3	0.76720(14)	0.45057(9)	0.19470(9)
136	H14A	0	H	0.6747(17)	0.4233(11)	0.1782(10)
137	H14B	0	H	0.7899(16)	0.4679(10)	0.1361(11)
138	H14C	0	H	0.8318(16)	0.4000(11)	0.2269(11)
139	C15	0	C.3	0.69655(17)	0.59509(10)	0.48541(10)
140	H15A	0	H	0.7523(17)	0.5475(12)	0.5289(12)
141	H15B	0	H	0.7096(18)	0.6540(13)	0.5213(12)
142	H15C	0	H	0.601(2)	0.5754(13)	0.4723(12)
143	C16	0	C.2	0.76489(11)	0.09805(7)	0.58843(7)
144	N16	0	N.2	0.72047(10)	0.01552(7)	0.59312(6)
145	C17	0	C.3	0.89240(13)	0.13870(9)	0.65044(8)
146	H17A	0	H	0.9395(15)	0.0948(10)	0.6973(10)
147	H17B	0	H	0.9539(16)	0.1601(11)	0.6130(11)
148	H17C	0	H	0.8721(17)	0.1959(12)	0.6816(11)
149	C18	0	C.2	0.78805(12)	-0.04669(8)	0.66520(8)
150	C19	0	C.2	0.73993(12)	-0.05117(8)	0.74463(8)
151	C20	0	C.2	0.79373(14)	-0.11934(10)	0.81075(9)
152	H20	0	H	0.7604(16)	-0.1219(11)	0.8652(11)
153	C21	0	C.2	0.89263(14)	-0.18062(10)	0.79918(9)
154	H21	0	H	0.9287(16)	-0.2279(11)	0.8455(11)
155	C22	0	C.2	0.94006(13)	-0.17460(9)	0.72083(9)
156	H22	0	H	1.0114(16)	-0.2173(11)	0.7125(10)
157	C23	0	C.2	0.88880(12)	-0.10772(8)	0.65256(8)

158	C24	0	C.3	0.63164(15)	0.01534(11)	0.75619(10)
159	H24A	0	H	0.6694(18)	0.0808(13)	0.7703(12)
160	H24B	0	H	0.5554(18)	0.0201(12)	0.6983(12)
161	H24C	0	H	0.5937(17)	-0.0046(12)	0.8077(12)
162	C25	0	C.3	0.94060(15)	-0.10102(10)	0.56777(9)
163	H25A	0	H	1.0043(18)	-0.1525(13)	0.5653(12)
164	H25B	0	H	0.8659(18)	-0.1013(12)	0.5107(12)
165	H25C	0	H	0.9902(18)	-0.0420(13)	0.5667(12)
166	C1	0	C.2	0.82014(11)	0.66164(7)	0.98358(7)
167	N1	0	N.2	0.75578(9)	0.73696(6)	1.00489(6)
168	C2	0	C.2	0.95930(11)	0.64523(8)	1.02172(8)
169	H2	0	H	1.0004(14)	0.5892(10)	1.0038(9)
170	C3	0	C.2	1.03473(12)	0.71054(8)	1.08252(8)
171	H3	0	H	1.1323(15)	0.7008(10)	1.1095(9)
172	C4	0	C.2	0.96984(11)	0.78912(8)	1.10394(7)
173	H4	0	H	1.0183(14)	0.8368(10)	1.1457(9)
174	C5	0	C.2	0.82979(11)	0.79874(7)	1.06507(7)
175	C6	0	C.2	0.75441(11)	0.88149(7)	1.08707(7)
176	N6	0	N.2	0.82542(10)	0.94297(6)	1.14024(6)
177	C7	0	C.3	0.60314(12)	0.88510(9)	1.04453(9)
178	H7A	0	H	0.5646(16)	0.9398(11)	1.0658(11)
179	H7B	0	H	0.5818(17)	0.8826(12)	0.9769(12)
180	H7C	0	H	0.5602(18)	0.8284(12)	1.0638(12)
181	C8	0	C.2	0.76649(11)	1.02734(7)	1.16125(7)
182	C9	0	C.2	0.72729(11)	1.03428(8)	1.24392(8)
183	C10	0	C.2	0.68256(12)	1.12046(8)	1.26718(8)

184	H10	0	H	0.6544(14)	1.1256(10)	1.3245(10)
185	C11	0	C.2	0.67651(12)	1.19762(8)	1.21053(8)
186	H11	0	H	0.6460(14)	1.2577(10)	1.2288(10)
187	C12	0	C.2	0.71463(13)	1.18911(8)	1.12869(8)
188	H12	0	H	0.7120(15)	1.2436(10)	1.0877(10)
189	C13	0	C.2	0.76003(12)	1.10431(8)	1.10257(8)
190	C14	0	C.3	0.73280(14)	0.95057(9)	1.30530(9)
191	H14A	0	H	0.8253(17)	0.9233(11)	1.3218(10)
192	H14B	0	H	0.7101(16)	0.9679(10)	1.3639(11)
193	H14C	0	H	0.6682(16)	0.9000(11)	1.2731(11)
194	C15	0	C.3	0.80345(17)	1.09509(10)	1.01459(10)
195	H15A	0	H	0.7477(17)	1.0475(12)	0.9711(12)
196	H15B	0	H	0.7904(18)	1.1540(13)	0.9787(12)
197	H15C	0	H	0.899(2)	1.0754(13)	1.0277(12)
198	C16	0	C.2	0.73511(11)	0.59805(7)	0.91157(7)
199	N16	0	N.2	0.77953(10)	0.51552(7)	0.90688(6)
200	C17	0	C.3	0.60760(13)	0.63870(9)	0.84956(8)
201	H17A	0	H	0.5605(15)	0.5948(10)	0.8027(10)
202	H17B	0	H	0.5461(16)	0.6601(11)	0.8870(11)
203	H17C	0	H	0.6279(17)	0.6959(12)	0.8184(11)
204	C18	0	C.2	0.71195(12)	0.45331(8)	0.83480(8)
205	C19	0	C.2	0.76007(12)	0.44883(8)	0.75537(8)
206	C20	0	C.2	0.70627(14)	0.38066(10)	0.68925(9)
207	H20	0	H	0.7396(16)	0.3781(11)	0.6348(11)
208	C21	0	C.2	0.60737(14)	0.31938(10)	0.70082(9)
209	H21	0	H	0.5713(16)	0.2721(11)	0.6545(11)
210	C22	0	C.2	0.55994(13)	0.32540(9)	0.77917(9)

211	H22	0	H	0.4886(16)	0.2827(11)	0.7875(10)
212	C23	0	C.2	0.61120(12)	0.39228(8)	0.84744(8)
213	C24	0	C.3	0.86836(15)	0.51534(11)	0.74381(10)
214	H24A	0	H	0.8306(18)	0.5808(13)	0.7297(12)
215	H24B	0	H	0.9446(18)	0.5201(12)	0.8017(12)
216	H24C	0	H	0.9063(17)	0.4954(12)	0.6923(12)
217	C25	0	C.3	0.55940(15)	0.39898(10)	0.93223(9)
218	H25A	0	H	0.4957(18)	0.3475(13)	0.9347(12)
219	H25B	0	H	0.6341(18)	0.3987(12)	0.9893(12)
220	H25C	0	H	0.5098(18)	0.4580(13)	0.9333(12)

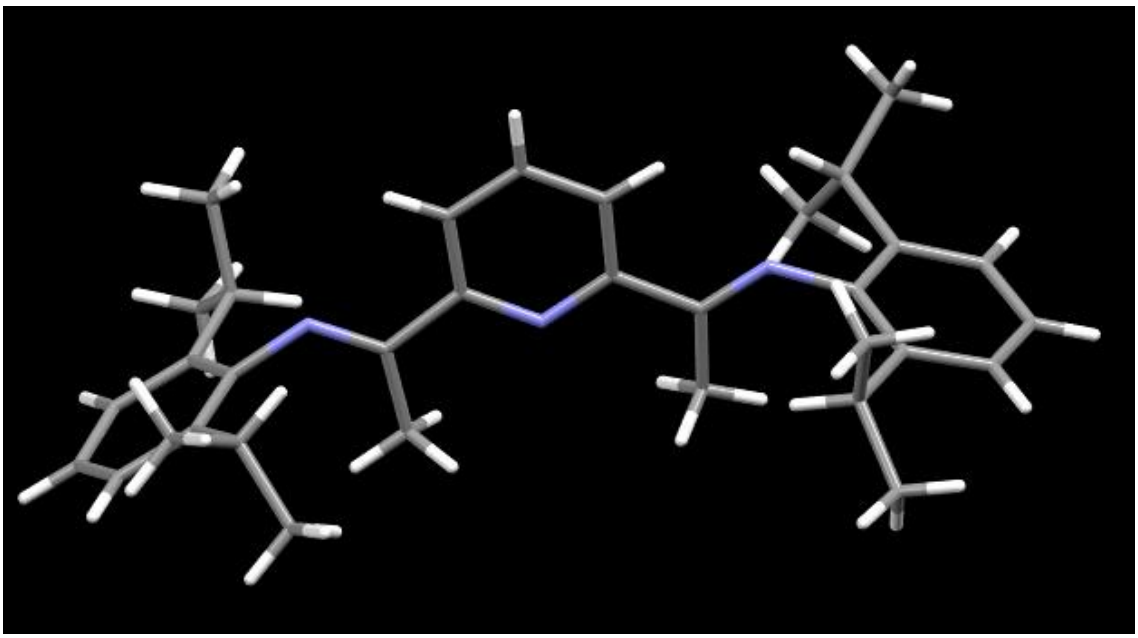

Number	Label	Charge	SybylType	Xfrac + ESD	Yfrac + ESD	Zfrac + ESD	Symm. op.

1	C1	0	C.2	0.21032(6)	0.43629(4)	0.22297(10)	x,y,z
2	N1	0	N.2	0.25300(5)	0.49104(4)	0.23847(9)	x,y,z
3	C2	0	C.2	0.24056(7)	0.38696(5)	0.13930(11)	x,y,z
4	H2	0	H	0.2069(8)	0.3483(6)	0.1322(14)	x,y,z
5	C3	0	C.2	0.31682(7)	0.39512(5)	0.06680(12)	x,y,z
6	H3	0	H	0.3388(8)	0.3614(6)	0.0076(14)	x,y,z
7	C4	0	C.2	0.36088(6)	0.45179(5)	0.08025(11)	x,y,z
8	H4	0	H	0.4142(8)	0.4591(5)	0.0334(13)	x,y,z
9	C5	0	C.2	0.32722(6)	0.49813(4)	0.16879(10)	x,y,z
10	C6	0	C.2	0.12674(6)	0.43083(4)	0.29976(11)	x,y,z
11	N6	0	N.2	0.08686(5)	0.37851(4)	0.28829(9)	x,y,z
12	C7	0	C.3	0.09693(8)	0.48715(5)	0.38164(15)	x,y,z
13	H7A	0	H	0.0378(11)	0.4815(7)	0.4122(18)	x,y,z
14	H7B	0	H	0.0966(10)	0.5246(8)	0.3188(19)	x,y,z
15	H7C	0	H	0.1389(12)	0.4953(8)	0.468(2)	x,y,z
16	C8	0	C.2	0.00577(7)	0.36772(5)	0.35305(12)	x,y,z

17	C9	0	C.2	0.00637(7)	0.34515(5)	0.50068(12)	x,y,z
18	C10	0	C.2	-0.07438(8)	0.32884(5)	0.55416(14)	x,y,z
19	H10	0	H	-0.0732(9)	0.3119(6)	0.6576(16)	x,y,z
20	C11	0	C.2	-0.15252(8)	0.33561(6)	0.46632(16)	x,y,z
21	H11	0	H	-0.2083(10)	0.3245(7)	0.5069(17)	x,y,z
22	C12	0	C.2	-0.15177(8)	0.35826(6)	0.32191(17)	x,y,z
23	H12	0	H	-0.2095(10)	0.3639(7)	0.2578(17)	x,y,z
24	C13	0	C.2	-0.07311(7)	0.37410(5)	0.26187(14)	x,y,z
25	C14	0	C.3	0.0922(3)	0.33901(18)	0.5977(5)	x,y,z
26	H14	0	H	0.1322(12)	0.3716(9)	0.564(2)	x,y,z
27	C15	0	C.3	0.0792(2)	0.34929(15)	0.7639(3)	x,y,z
28	H15A	0	H	0.049211	0.389319	0.776415	x,y,z
29	H15B	0	H	0.136769	0.349906	0.821452	x,y,z
30	H15C	0	H	0.04338	0.315236	0.800167	x,y,z
31	C16	0	C.3	0.13195(17)	0.27555(12)	0.5710(3)	x,y,z

32	H16A	0	H	0.090918	0.242724	0.597251	x,y,z
33	H16B	0	H	0.187576	0.271187	0.633193	x,y,z
34	H16C	0	H	0.143124	0.271584	0.465043	x,y,z
35	C17	0	C.3	-0.0692(4)	0.3946(2)	0.0995(5)	x,y,z
36	H17	0	H	-0.0121(17)	0.3856(11)	0.065(3)	x,y,z
37	C18	0	C.3	-0.0905(3)	0.4635(2)	0.0799(5)	x,y,z
38	H18A	0	H	-0.083(2)	0.4802(16)	-0.023(4)	x,y,z
39	H18B	0	H	-0.045(2)	0.4885(14)	0.153(4)	x,y,z
40	H18C	0	H	-0.156(3)	0.473(2)	0.136(5)	x,y,z
41	C19	0	C.3	-0.12616(13)	0.35842(9)	-0.01066(19)	x,y,z
42	H19A	0	H	-0.1083(15)	0.3141(12)	-0.004(3)	x,y,z
43	H19B	0	H	-0.1204(11)	0.3753(8)	-0.114(2)	x,y,z
44	H19C	0	H	-0.1890(14)	0.3601(9)	0.013(2)	x,y,z
45	C20	0	C.2	0.37432(6)	0.55899(4)	0.19603(11)	x,y,z
46	N20	0	N.2	0.44622(5)	0.56674(4)	0.13379(9)	x,y,z
47	C21	0	C.3	0.33373(8)	0.60497(5)	0.29702(14)	x,y,z

48	H21A	0	H	0.3709(10)	0.6408(8)	0.3160(17)	x,y,z
49	H21B	0	H	0.3223(10)	0.5847(7)	0.3925(18)	x,y,z
50	H21C	0	H	0.2767(11)	0.6177(7)	0.2533(18)	x,y,z
51	C22	0	C.2	0.49578(7)	0.62294(4)	0.15442(11)	x,y,z
52	C23	0	C.2	0.47515(7)	0.67446(5)	0.05977(12)	x,y,z
53	C24	0	C.2	0.52866(8)	0.72742(5)	0.07763(14)	x,y,z
54	H24	0	H	0.5151(9)	0.7639(7)	0.0122(16)	x,y,z
55	C25	0	C.2	0.59946(9)	0.72949(5)	0.18484(14)	x,y,z
56	H25	0	H	0.6358(9)	0.7671(7)	0.1962(16)	x,y,z
57	C26	0	C.2	0.61936(8)	0.67805(5)	0.27475(13)	x,y,z
58	H26	0	H	0.6697(9)	0.6786(6)	0.3479(16)	x,y,z
59	C27	0	C.2	0.56904(7)	0.62339(5)	0.25979(11)	x,y,z
60	C28	0	C.3	0.39843(7)	0.67032(5)	-0.05932(13)	x,y,z
61	H28	0	H	0.3496(9)	0.6491(6)	-0.0143(15)	x,y,z
62	C29	0	C.3	0.36476(10)	0.73411(6)	-0.11519(17)	x,y,z

63	H29A	0	H	0.3514(10)	0.7621(7)	-0.0290(18)	x,y,z
64	H29B	0	H	0.3083(11)	0.7290(7)	-0.1824(19)	x,y,z
65	H29C	0	H	0.4093(10)	0.7553(7)	-0.1719(18)	x,y,z
66	C30	0	C.3	0.42323(8)	0.63024(6)	-0.19142(14)	x,y,z
67	H30A	0	H	0.4732(9)	0.6493(6)	-0.2391(16)	x,y,z
68	H30B	0	H	0.3727(9)	0.6261(6)	-0.2717(16)	x,y,z
69	H30C	0	H	0.4409(9)	0.5869(7)	-0.1588(15)	x,y,z
70	C31	0	C.3	0.59140(7)	0.56635(5)	0.35640(12)	x,y,z
71	H31	0	H	0.5582(8)	0.5305(6)	0.3093(13)	x,y,z
72	C32	0	C.3	0.56008(9)	0.57509(7)	0.51325(14)	x,y,z
73	H32A	0	H	0.5933(11)	0.6098(8)	0.5638(18)	x,y,z
74	H32B	0	H	0.5701(10)	0.5356(8)	0.5738(18)	x,y,z
75	H32C	0	H	0.4958(10)	0.5854(7)	0.5092(17)	x,y,z

76	C33	0	C.3	0.68933(9)	0.54988(7)	0.36577(16)	x,y,z
77	H33A	0	H	0.7118(11)	0.5455(8)	0.265(2)	x,y,z
78	H33B	0	H	0.7002(10)	0.5091(8)	0.4231(18)	x,y,z
79	H33C	0	H	0.7247(11)	0.5838(8)	0.4203(19)	x,y,z
80	C14B	0	C.3	0.0923(7)	0.3322(4)	0.5958(12)	x,y,z
81	H14B	0	H	0.140874	0.345141	0.533299	x,y,z
82	C15B	0	C.3	0.1021(4)	0.3731(3)	0.7369(7)	x,y,z
83	H15D	0	H	0.05514	0.362926	0.801728	x,y,z
84	H15E	0	H	0.097812	0.417366	0.708235	x,y,z
85	H15F	0	H	0.159577	0.365255	0.791018	x,y,z
86	C16B	0	C.3	0.1092(5)	0.2636(3)	0.6352(9)	x,y,z
87	H16D	0	H	0.112249	0.239282	0.54297	x,y,z
88	H16E	0	H	0.061061	0.247683	0.691098	x,y,z
89	H16F	0	H	0.165075	0.259777	0.696939	x,y,z
90	C17B	0	C.3	-0.0799(6)	0.4048(3)	0.1063(7)	x,y,z
91	H17B	0	H	-0.012(2)	0.4184(17)	0.091(4)	x,y,z
92	C18B	0	C.3	-0.1279(5)	0.4673(3)	0.1102(8)	x,y,z
93	H18D	0	H	-0.130(3)	0.4878(18)	0.009(5)	x,y,z
94	H18E	0	H	-0.105(3)	0.500(2)	0.192(5)	x,y,z
95	H18F	0	H	-0.187(3)	0.455(2)	0.126(6)	x,y,z

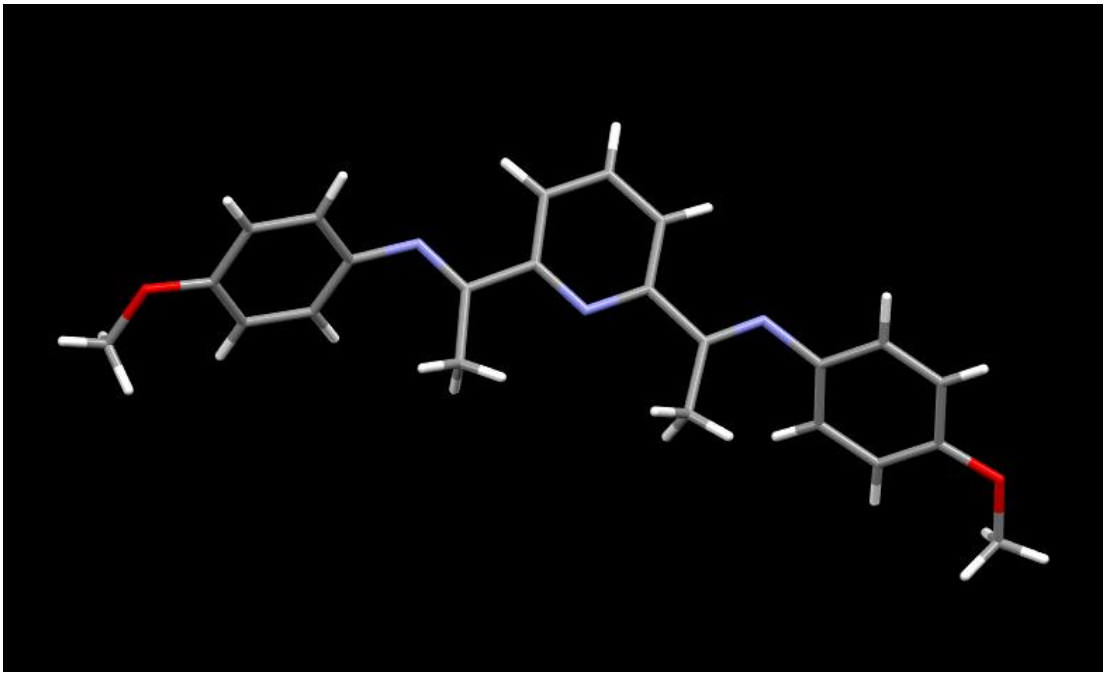

Number	Label	Charge	SybylType	Xfrac + ESD	Yfrac + ESD	Zfrac + ESD	Symm. op.
1	C1	0	C.2	0.528604	0.256456	0.418669	x,y,z
2	N1	0	N.2	0.5	0.24466	0.516507	x,y,z
3	C2	0	C.2	0.529542	0.279544	0.220956	x,y,z
4	H2	0	H	0.551086	0.286618	0.155805	x,y,z
5	C3	0	C.2	0.5	0.290678	0.121849	x,y,z
6	H3	0	H	0.5	0.311444	-0.01327	x,y,z
7	C4	0	C.2	0.560268	0.24361	0.530327	x,y,z
8	N4	0	N.2	0.587108	0.255291	0.433532	x,y,z

9	C5	0	C.3	0.557663	0.214875	0.740633	x,y,z
10	H5A	0	H	0.553622	0.33309	0.797622	x,y,z
11	H5B	0	H	0.577238	0.153128	0.787948	x,y,z
12	H5C	0	H	0.538879	0.136195	0.767157	x,y,z
13	C6	0	C.2	0.618812	0.25272	0.520893	x,y,z
14	C7	0	C.2	0.627854	0.380453	0.664077	x,y,z
15	H7	0	H	0.61172	0.471952	0.708869	x,y,z
16	C8	0	C.2	0.660214	0.38166	0.736178	x,y,z
17	H8	0	H	0.665229	0.474597	0.825269	x,y,z
18	C9	0	C.2	0.683427	0.252747	0.664867	x,y,z
19	O9	0	O.3	0.715655	0.239179	0.726981	x,y,z
20	C10	0	C.2	0.674806	0.126345	0.51698	x,y,z
21	H10	0	H	0.690847	0.040736	0.467793	x,y,z
22	C11	0	C.2	0.642896	0.127797	0.443526	x,y,z
23	H11	0	H	0.637345	0.043044	0.329754	x,y,z
24	C12	0	C.3	0.725023	0.364233	0.879724	x,y,z

25	H12A	0	H	0.711247	0.341482	0.996226	x,y,z
26	H12B	0	H	0.723061	0.499331	0.840131	x,y,z
27	H12C	0	H	0.747725	0.334256	0.903476	x,y,z
28	C1	0	C.2	0.471396	0.256456	0.418669	1-x,y,z
29	C2	0	C.2	0.470458	0.279544	0.220956	1-x,y,z
30	H2	0	H	0.448914	0.286618	0.155805	1-x,y,z
31	C4	0	C.2	0.439732	0.24361	0.530327	1-x,y,z
32	N4	0	N.2	0.412892	0.255291	0.433532	1-x,y,z
33	C5	0	C.3	0.442337	0.214875	0.740633	1-x,y,z
34	H5A	0	H	0.446378	0.33309	0.797622	1-x,y,z
35	H5B	0	H	0.422762	0.153128	0.787948	1-x,y,z
36	H5C	0	H	0.461121	0.136195	0.767157	1-x,y,z
37	C6	0	C.2	0.381188	0.25272	0.520893	1-x,y,z
38	C7	0	C.2	0.372146	0.380453	0.664077	1-x,y,z
39	H7	0	H	0.38828	0.471952	0.708869	1-x,y,z
40	C8	0	C.2	0.339786	0.38166	0.736178	1-x,y,z

41	H8	0	H	0.334771	0.474597	0.825269	1-x,y,z
42	C9	0	C.2	0.316573	0.252747	0.664867	1-x,y,z
43	O9	0	O.3	0.284345	0.239179	0.726981	1-x,y,z
44	C10	0	C.2	0.325194	0.126345	0.51698	1-x,y,z
45	H10	0	H	0.309153	0.040736	0.467793	1-x,y,z
46	C11	0	C.2	0.357104	0.127797	0.443526	1-x,y,z
47	H11	0	H	0.362655	0.043044	0.329754	1-x,y,z
48	C12	0	C.3	0.274977	0.364233	0.879724	1-x,y,z
49	H12A	0	H	0.288753	0.341482	0.996226	1-x,y,z
50	H12B	0	H	0.276939	0.499331	0.840131	1-x,y,z
51	H12C	0	H	0.252275	0.334256	0.903476	1-x,y,z

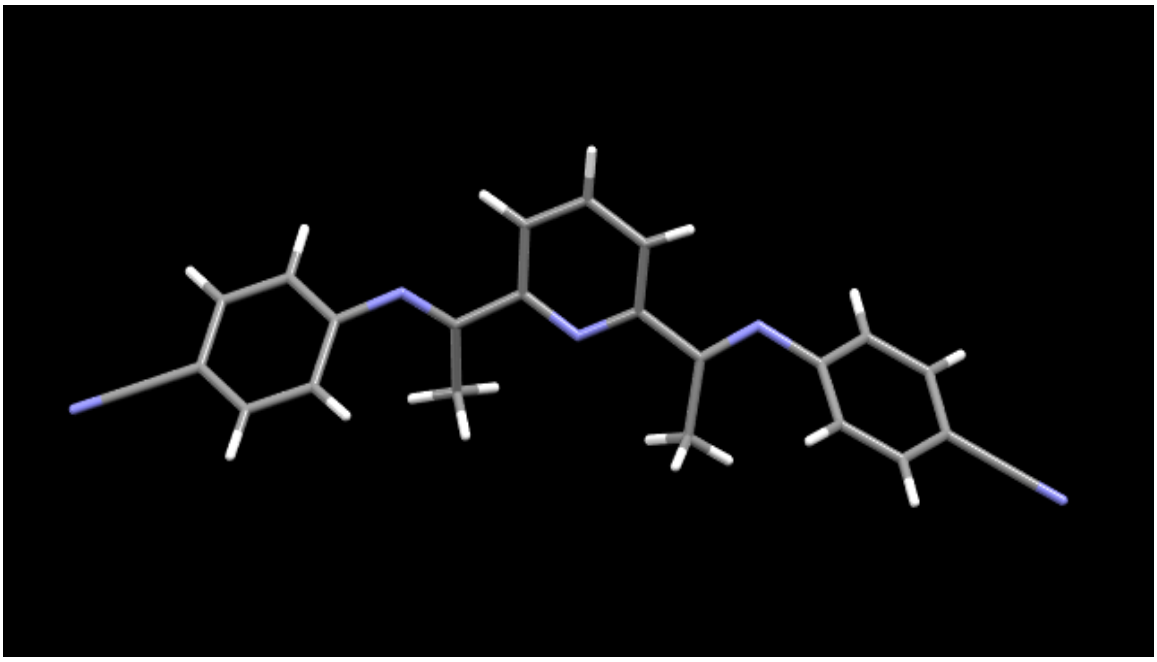

Number	Label	Charge	SybylType	Xfrac + ESD	Yfrac + ESD	Zfrac + ESD	Symm. op.
1	C1	0	C.2	0.581185	0.404259	0.687269	x,y,z
2	N1	0	N.2	0.480974	0.336999	0.753903	x,y,z
3	C2	0	C.2	0.622099	0.553174	0.666789	x,y,z
4	H2	0	H	0.693034	0.593944	0.617246	x,y,z
5	C3	0	C.2	0.560959	0.636995	0.720119	x,y,z
6	H3	0	H	0.592786	0.743633	0.709817	x,y,z
7	C4	0	C.2	0.458884	0.56916	0.789956	x,y,z
8	H4	0	H	0.413747	0.624691	0.828211	x,y,z

9	C5	0	C.2	0.420251	0.418699	0.803401	x,y,z
10	C6	0	C.2	0.652331	0.312748	0.63647	x,y,z
11	N6	0	N.2	0.779118	0.386879	0.601438	x,y,z
12	C7	0	C.3	0.570096	0.145685	0.633807	x,y,z
13	H7A	0	H	0.638406	0.096403	0.62083	x,y,z
14	H7B	0	H	0.467366	0.105724	0.569095	x,y,z
15	H7C	0	H	0.540855	0.122016	0.706277	x,y,z
16	C8	0	C.2	0.854798	0.314149	0.548485	x,y,z
17	C9	0	C.2	0.772381	0.216106	0.444549	x,y,z
18	H9	0	H	0.658441	0.19502	0.407382	x,y,z
19	C10	0	C.2	0.852643	0.149608	0.394179	x,y,z
20	H10	0	H	0.792362	0.079552	0.322621	x,y,z
21	C11	0	C.2	1.01698	0.182371	0.446672	x,y,z
22	C12	0	C.2	1.10172	0.284713	0.548413	x,y,z
23	H12	0	H	1.21627	0.307033	0.582772	x,y,z
24	C13	0	C.2	1.02128	0.350911	0.598362	x,y,z

25	H13	0	H	1.08053	0.422753	0.668343	x,y,z
26	C14	0	C.1	1.10047	0.111832	0.395641	x,y,z
27	N14	0	N.1	1.16818	0.056311	0.355717	x,y,z
28	C15	0	C.2	0.300578	0.338026	0.870725	x,y,z
29	N15	0	N.2	0.216913	0.405572	0.895449	x,y,z
30	C16	0	C.3	0.28613	0.185907	0.900306	x,y,z
31	H16A	0	H	0.23031	0.156882	0.961648	x,y,z
32	H16B	0	H	0.395212	0.18357	0.922063	x,y,z
33	H16C	0	H	0.219907	0.113493	0.831399	x,y,z
34	C17	0	C.2	0.089706	0.336743	0.948889	x,y,z
35	C18	0	C.2	0.10405	0.399005	1.05966	x,y,z
36	H18	0	H	0.204546	0.486696	1.10031	x,y,z
37	C19	0	C.2	-0.024052	0.340758	1.11075	x,y,z
38	H19	0	H	-0.013596	0.382582	1.18858	x,y,z
39	C20	0	C.2	-0.170256	0.22161	1.04914	x,y,z

40	C21	0	C.2	-0.186138	0.159504	0.937498	x,y,z
41	H21	0	H	-0.288153	0.076453	0.895705	x,y,z
42	C22	0	C.2	-0.056371	0.216668	0.887891	x,y,z
43	H22	0	H	-0.065195	0.175494	0.809769	x,y,z
44	C23	0	C.1	-0.306683	0.163078	1.09932	x,y,z
45	N23	0	N.1	-0.415077	0.116664	1.13999	x,y,z
46	C1	0	C.2	0.418815	0.595741	0.312731	1-x,1-y,1-z
47	N1	0	N.2	0.519026	0.663001	0.246097	1-x,1-y,1-z
48	C2	0	C.2	0.377901	0.446826	0.333211	1-x,1-y,1-z
49	H2	0	H	0.306966	0.406056	0.382754	1-x,1-y,1-z
50	C3	0	C.2	0.439041	0.363005	0.279881	1-x,1-y,1-z
51	H3	0	H	0.407214	0.256367	0.290183	1-x,1-y,1-z
52	C4	0	C.2	0.541116	0.43084	0.210044	1-x,1-y,1-z
53	H4	0	H	0.586253	0.375309	0.171789	1-x,1-y,1-z

54	C5	0	C.2	0.579749	0.581301	0.196599	1-x,1-y,1-z
55	C6	0	C.2	0.347669	0.687252	0.36353	1-x,1-y,1-z
56	N6	0	N.2	0.220882	0.613121	0.398562	1-x,1-y,1-z
57	C7	0	C.3	0.429904	0.854315	0.366193	1-x,1-y,1-z
58	H7A	0	H	0.361594	0.903597	0.37917	1-x,1-y,1-z
59	H7B	0	H	0.532634	0.894276	0.430905	1-x,1-y,1-z
60	H7C	0	H	0.459145	0.877984	0.293723	1-x,1-y,1-z
61	C8	0	C.2	0.145202	0.685851	0.451515	1-x,1-y,1-z
62	C9	0	C.2	0.227619	0.783894	0.555451	1-x,1-y,1-z
63	H9	0	H	0.341559	0.80498	0.592618	1-x,1-y,1-z
64	C10	0	C.2	0.147357	0.850392	0.605821	1-x,1-y,1-z
65	H10	0	H	0.207638	0.920448	0.677379	1-x,1-y,1-z
66	C11	0	C.2	-0.01698	0.817629	0.553328	1-x,1-y,1-z
67	C12	0	C.2	-0.101719	0.715287	0.451587	Unknown
68	H12	0	H	-0.216275	0.692967	0.417228	Unknown

69	C13	0	C.2	-0.021279	0.649089	0.401638	Unknown
70	H13	0	H	-0.080534	0.577247	0.331657	Unknown
71	C14	0	C.1	-0.100465	0.888168	0.604359	Unknown
72	N14	0	N.1	-0.168182	0.943689	0.644283	Unknown
73	C15	0	C.2	0.699422	0.661974	0.129275	1-x,1-y,1-z
74	N15	0	N.2	0.783087	0.594428	0.104551	1-x,1-y,1-z
75	C16	0	C.3	0.71387	0.814093	0.099694	1-x,1-y,1-z
76	H16A	0	H	0.76969	0.843118	0.038352	1-x,1-y,1-z
77	H16B	0	H	0.604788	0.81643	0.077937	1-x,1-y,1-z
78	H16C	0	H	0.780093	0.886507	0.168601	1-x,1-y,1-z
79	C17	0	C.2	0.910294	0.663257	0.051111	1-x,1-y,1-z
80	C18	0	C.2	0.89595	0.600995	-0.059659	Unknown
81	H18	0	H	0.795454	0.513304	-0.10031	1-x,1-y,1-z
82	C19	0	C.2	1.02405	0.659242	-0.110747	Unknown

83	H19	0	H	1.0136	0.617418	-0.188583	Unknown
84	C20	0	C.2	1.17026	0.77839	-0.04914	Unknown
85	C21	0	C.2	1.18614	0.840496	0.062502	Unknown
86	H21	0	H	1.28815	0.923547	0.104295	Unknown
87	C22	0	C.2	1.05637	0.783332	0.112109	Unknown
88	H22	0	H	1.0652	0.824506	0.190231	Unknown
89	C23	0	C.1	1.30668	0.836922	-0.099322	Unknown
90	N23	0	N.1	1.41508	0.883336	-0.139989	Unknown

Calculation of Torsional Angles from Crystal Structures

Calculations of torsional angles are depicted below. L_n and R_n are arbitrarily assigned sides of the molecule in solid state when viewed using Mercury viewing software. "*n* either the torsional angle <1234 or <1235. In the case where R series is blank, the left side (as assigned here) is isotropic, and no distinguishable differences were noted from the crystal lattice.

Summation of Torsional angles	**R**	**Ome**	**H**	**CN(L)**	**Me(o)**	**iPr(o)**
	L1	-54.49	-59.49	-123.39	88.3	-89.5
	L2	132.28	126.3	61.24	-97.3	96.8
	R1			117.08	94.5	-86.3
	R2			-69.22	-92.1	99.4
	Total from "0"	77.79	66.81	-14.29	-6.6	20.4

Reversibility Measurements Calculations

All electrochemical measurements were carried out using an IKA ElectraSyn2.0. Electrolyte solution was made immediately prior to measurement using acetonitrile pre-dried over 4 angstrom molecular sieves. Molecular sieves were activated in a 500mL flame dried round bottom flask under high vacuum while on a heating mantle for 24 hours. Acetonitrile was also degassed through a series of freeze/pump/thaws using a hi-vacuum line (approx. -20 psi).

A 0.1M solution of tetrabutylammounium tetrafluoroborate was used for cyclic voltammetry measurements. A 3mm glassy carbon working electrode, a platinum counter and a silver/silver chloride in saturated aqueous potassium chloride (Ag/AgCl) reference was used for the 3-electrode cell.

ElectraSyn2.0 was set to perform cyclic voltammetry in an anodic sweep direction for 6 segments (yielded 2-3 complete cycles) from -1.3V to 1V vs Ag/AgCl with a sweep rate of 80 mV/s. Vessel was sparged with N_2 from a Schlenk line with a calcium chloride drying tube in place. Background scans were collected of solvent electrolyte solution prior to the addition of a specific ligand. Following background scans enough ligand was added to bring the solution concentration to 1.0 mM, and vessel was capped and sonicated in a water bath until homogenized (varying degrees of color change was observed, and solution would transition from colorless to varied shades of yellow).

Calculations of Ia/Ic of Bis(imino)pyridines

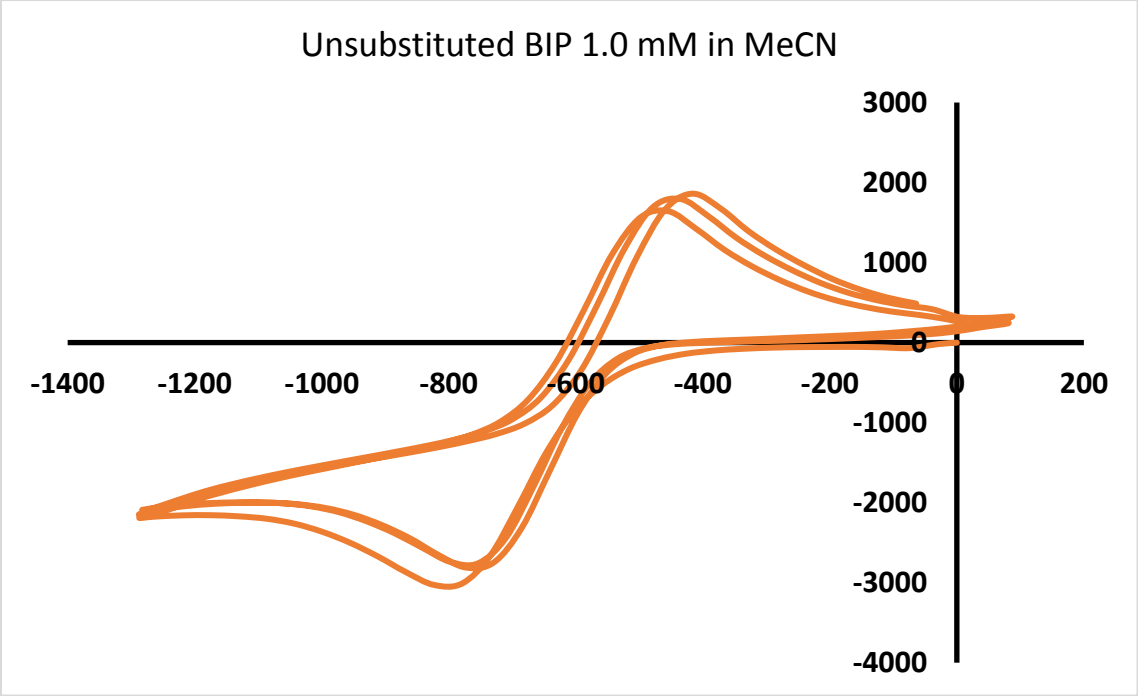

Calculations for Ligand A

Cycle	Ia	Ic	Unadjusted Ia/Ic	std
1	1641	3029	0.541762958	0.066298
2	1794	2759	0.650235593	
3	1861	2811	0.662041978	

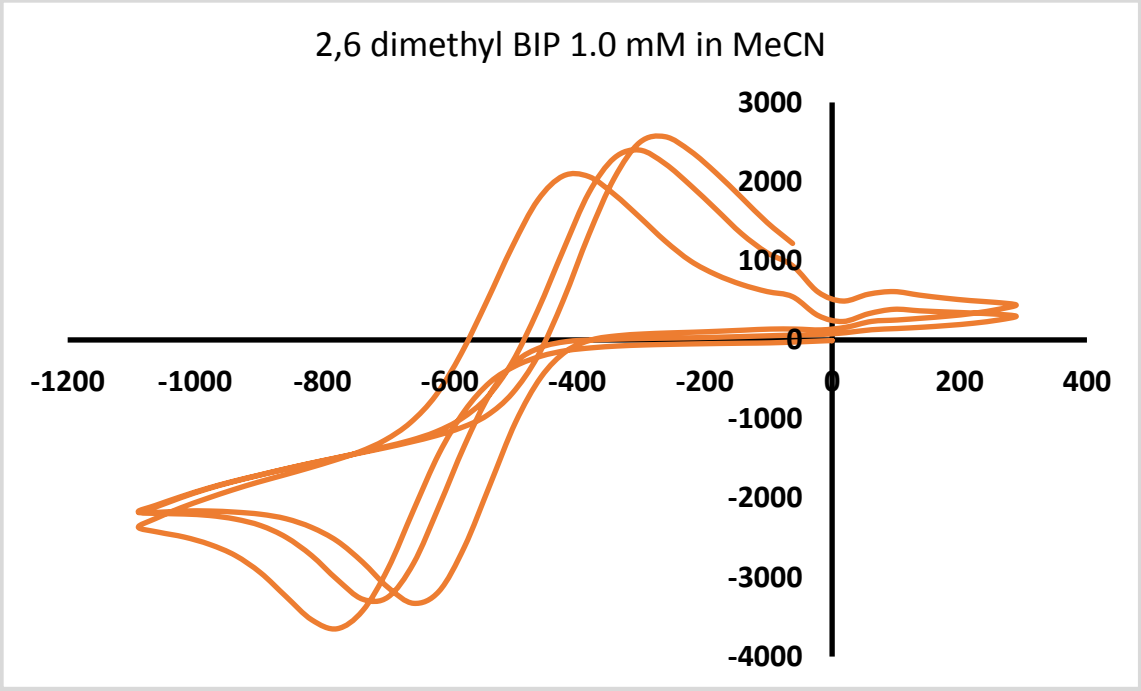

Calculations for Ligand B

Cycle	Ic	Ia	Ia/Ic	std
1	2072	3648	0.567982	0.107987
2	2398	3275	0.732214	
3	2567	3327	0.771566	

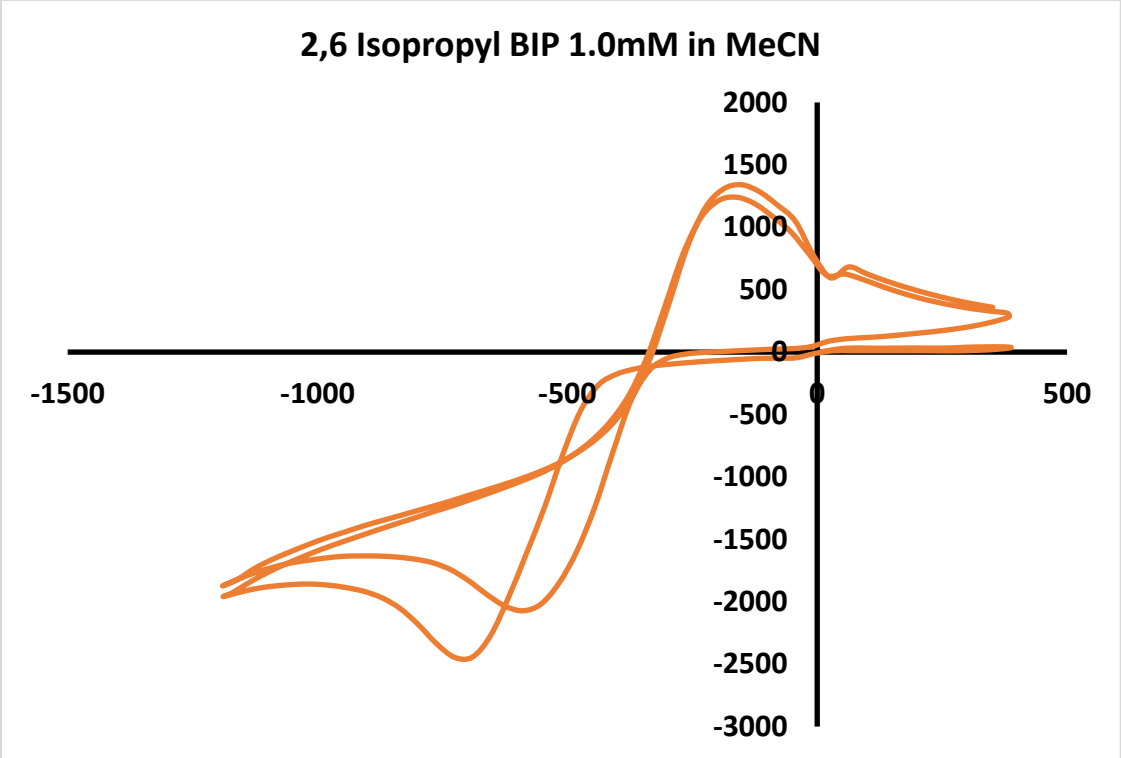

Calculations for Ligand C

cy	Ia	Ic	Ia/Ic	std
1	1240	2445	0.507157	0.153389
2	1341	1852	0.724082	

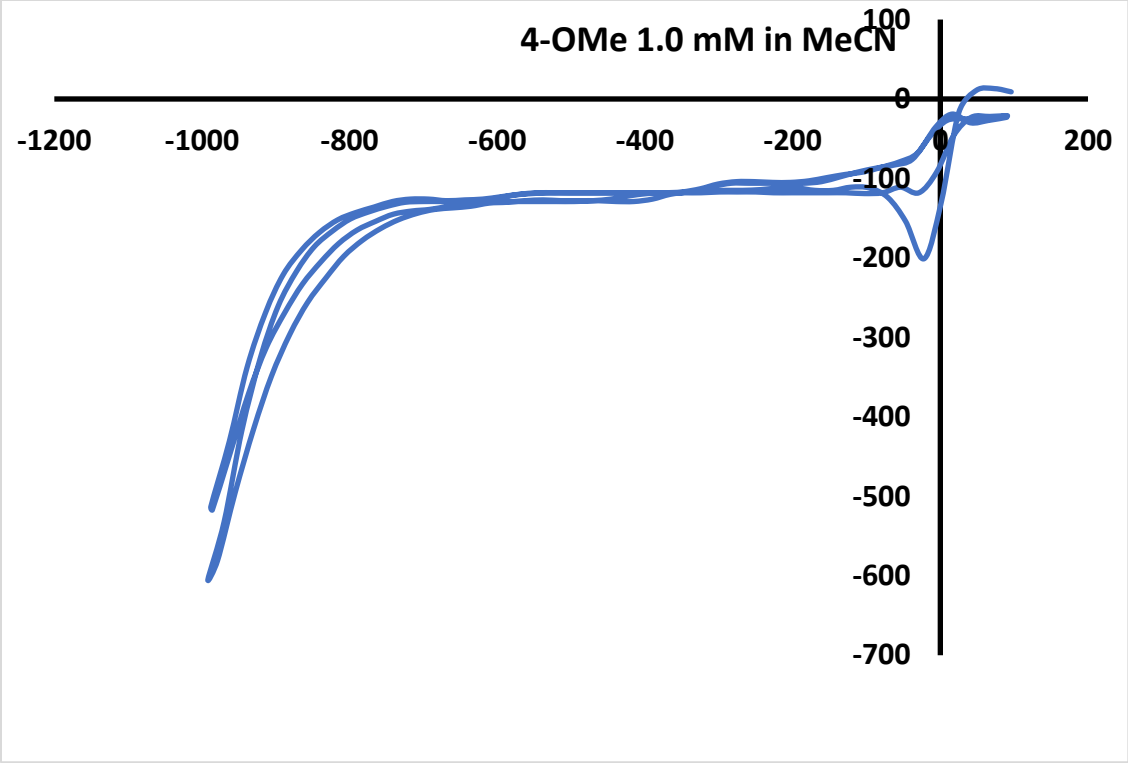

Calculations for Ligand D

cy	Ia	Ic	Ia/Ic	
1	21	201	0.104478	0.105896
2	30	118	0.254237	

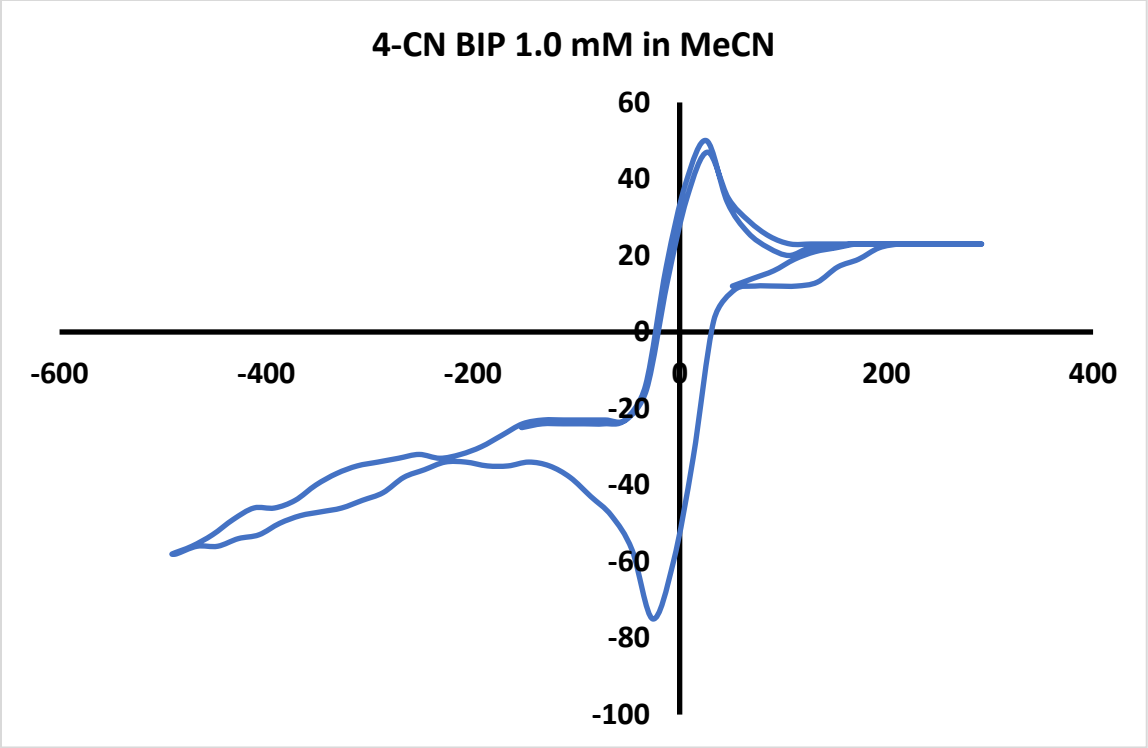

Calculations for Ligand E

Cy	Ia	Ic	Ia/Ic	std
1	50	68	0.735294118	0.076811
2	47	75	0.626666667	

Full Computational Results

All calculations were done using development version of the Gaussian suite of electronic structure theory.[1] The B3LYP functional was used and the unrestricted formalism was employed for all open-shell species.[2] The 6-311G(d) basis set was used on all atoms.[3] Geometry optimizations were carried out using standard methods and all nature of all potential energy surface stationary points was confirmed by second-derivative calculations.[4] In all cases, the stability of the calculated Kohn-Sham determinants has been verified.[5,6] To account for dispersion corrections, the empirical GD3 model has been used.[7] In order to provide a compact orbital description of the electron attachment process, the natural ionization orbital model was used.[8] The model computes the difference in density matrices between the initial and the final states. Then the resulting *difference density matrix* is then used to compute a set of orbitals, referred to as the *natural ionization orbitals,* which provide a representation of the attachment/detachment process in the occupation number basis. In addition, the computed eigenvalues of these orbitals reflect their respective occupation change numbers.

1. M. J. Frisch, G. W. Trucks, H. B. Schlegel, G. E. Scuseria, M. A. Robb, J. R. Cheeseman, G. Scalmani, V. Barone, B. Mennucci, G. A. Petersson, H. Nakatsuji, M. Caricato, X. Li, H. P. Hratchian, A. F. Izmaylov, J. Bloino, B. Janesko, F. Lipparini, G. Zheng, J. L. Sonnenberg, W. Liang, M. Hada, M. Ehara, K. Toyota, R. Fukuda, J. Hasegawa, M. Ishida, T. Nakajima, Y. Honda, O. Kitao, H. Nakai, T. Vreven, J. A. Montgomery, Jr., J. E. Peralta, F. Ogliaro, M. Bearpark, J. J. Heyd, E. Brothers, K. N. Kudin, V. N. Staroverov, T. Keith, R. Kobayashi, J. Normand, K. Raghavachari, A. Rendell, J. C. Burant, S. S. Iyengar, J. Tomasi, M. Cossi, N. Rega, J. M. Millam, M. Klene, J. E. Knox, J. B. Cross, V. Bakken, C. Adamo, J. Jaramillo, R. Gomperts, R. E. Stratmann, O. Yazyev, A. J. Austin, R. Cammi, C. Pomelli, J. W. Ochter- ski, R. L. Martin, K. Morokuma, V. G. Zakrzewski, G. A. Voth, P. Salvador, J. J. Dannenberg, S. Dapprich, P. V. Parandekar, N. J. Mayhall, A. D. Daniels, O. Farkas, J. B. Foresman, J. V. Ortiz, J. Cioslowski, D. J. Fox, gaussian Development Version, Revision I.03+, Gaussian, Inc., Wallingford CT, 2014.
2. A. D. Becke, “Density-functional thermochemistry. III. The role of exact exchange,” *J. Chem. Phys.*, **98**(1993) 5648-52
3. K. Raghavachari, J. S. Binkley, R. Seeger, and J. A. Pople, “Self-Consistent Molecular Orbital Methods. 20. Basis set for correlated wave-functions,” *J. Chem. Phys.*, **72** (1980) 650-54

4. H. P. Hratchian, H. B. Schlegel, Finding minima, transition states, and following reaction pathways on ab initio potential energy surfaces, in: Theory and applications of computational chemistry, Elsevier, 2005, pp. 195–249

5. R.Bauernschmitt,R.Ahlrichs,Stabilityanalysisforsolutionsoftheclosedshellkohn–sham equation, The Journal of chemical physics 104 (22) (1996) 9047–9052.

6. R. Seeger, J. A. Pople, Self-consistent molecular orbital methods. xviii. constraints and stability in hartree–fock theory, The Journal of Chemical Physics 66 (7) (1977) 3045–3050.

7. Ehrlich, S., Moellmann, J., Reckien, W., Bredow, T., & Grimme, S. (2011). System-Dependent Dispersion Coefficients for the DFT-D3 Treatment of Adsorption Processes on Ionic Surfaces. ChemPhysChem, 12(17), 3414-3420.

8. L. M. Thompson, H. Harb, H. P. Hratchian, Natural ionization orbitals for interpreting electron detachment processes, The Journal of chemical physics 144 (20) (2016) 204117.

Natural Ionization Orbitals

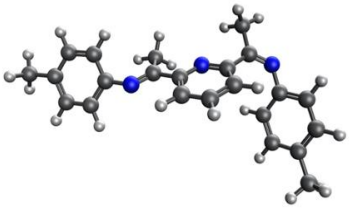
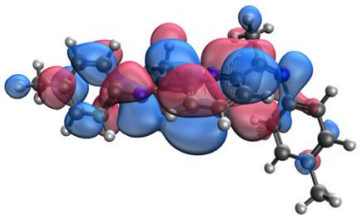
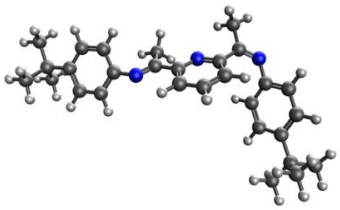
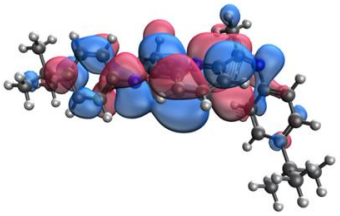
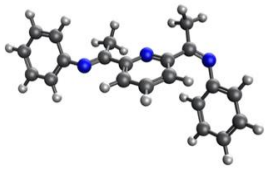
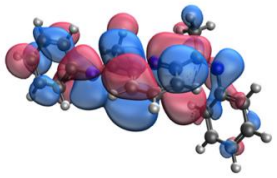
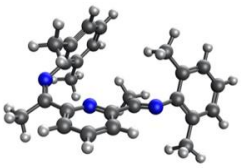
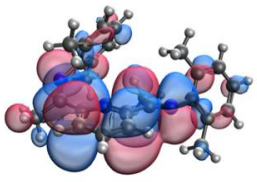

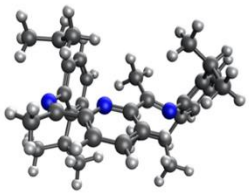

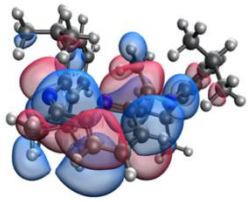

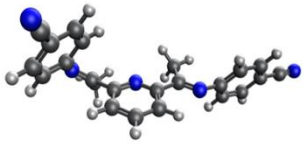

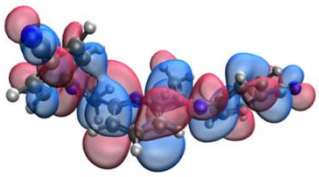

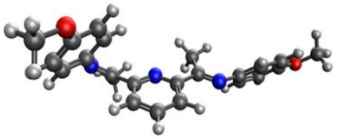

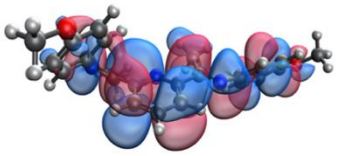

P-Character Vs Ia/Ic

In order to determine if any of the structural modifications of the ligands significantly affected the total amount of p-character %p character was determined. This value is representative of the total amount conjugation available to the molecule and is predicated on the conservation of the atomic orbitals in the assembly of the larger molecular orbital system. Population analysis was performed to inspect the %p character of each natural ionization orbital. As viewed below when compared to torsional angles no observable affect is exhibited of the % p-character on the torsional angles with all ligands. In addition, we have shown that, in all cases, the detached/attached electron is associated with a predominantly p-type orbital.

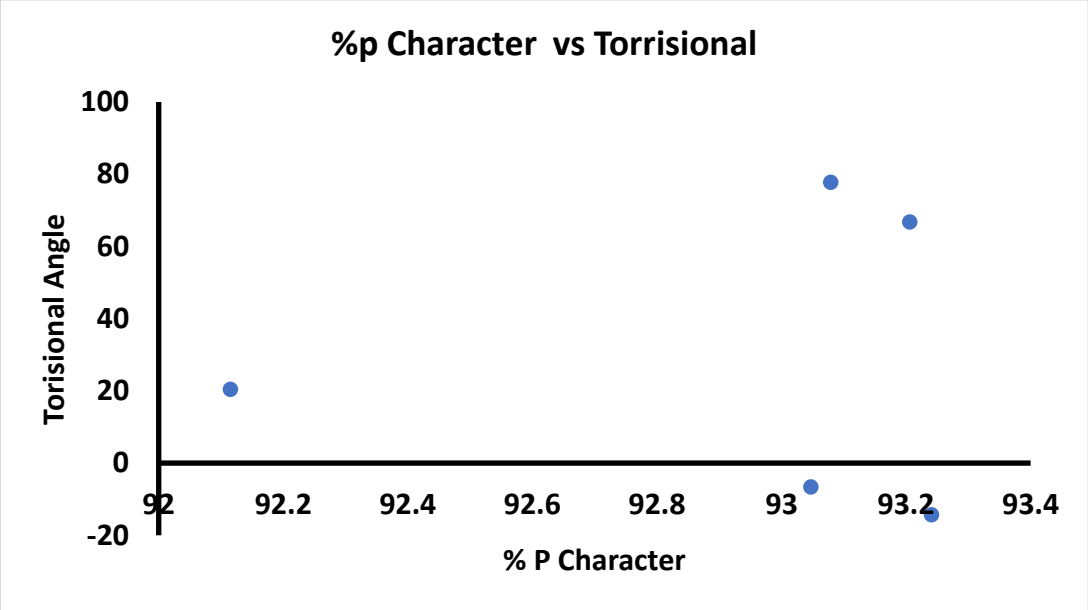

Geometries and SCF Energies of all structures

SI info for A

SCF Energy = -1054.82846784 Hartree

0 1

C -0.48939614 0.39145160 0.60257393

C -0.15483603 -0.39897308 1.70973730

C 1.14102618 -0.34116438 2.20458146

C 2.06854544 0.48698225 1.58034803

C 1.65204452 1.24187970 0.48055733

N 0.39847523 1.20462676 0.01340170

H 1.42825587 -0.93578257 3.06468199

H -0.90833761 -1.03106288 2.15984232

H 3.09044960 0.54821481 1.93216281

C 2.58928837 2.18909291 -0.21815502

C -1.87400897 0.37995857 0.02970468

C 4.31554267 0.60541538 -0.51720710

C 5.53448524 0.40940261 0.14405181

C 3.71525173 -0.48798285 -1.15640364

C 6.10890053 -0.85629278 0.20184211

H 6.01379091 1.25555520 0.62556475

C 4.31130512 -1.74481265 -1.10978558

H 2.78028721 -0.34565099 -1.68791511

C 5.51236944 -1.95780859 -0.42457057

H 7.04357157 -0.98885123 0.73947182

H 3.82684064 -2.57742775 -1.61211623

C -4.09072291 -0.41975807 0.25518244

C -4.91522230 0.71422532 0.22035941

C -4.66952899 -1.67398588 0.01291664

C -6.27272875 0.59114919 -0.06432584

H -4.48999537 1.68901948 0.43379539

C -6.02082795 -1.78027382 -0.29613940

H -4.04274130 -2.55860765 0.05741630

C -6.85142465 -0.65275044 -0.33634552

H -6.89110820 1.48418427 -0.08020849

H -6.44117853 -2.76095043 -0.50065283

N -2.73499960 -0.36161830 0.61994386

N 3.77833102 1.90833898 -0.59303218

C 2.05371841 3.57455848 -0.45374816

H 1.14844095 3.52423434 -1.06369583

H 1.76773050 4.04254736 0.49373291

H 2.80107942 4.18994583 -0.95328116

C -2.10826379 1.22352986 -1.19885677

H -3.05803776 0.98316989 -1.67299064

H -2.10800655 2.28618624 -0.94066336

H -1.29465929 1.07990513 -1.91048355

C -8.32728527 -0.78459698 -0.62267912

H -8.52711266 -1.58702691 -1.33722432

H -8.88720711 -1.01871638 0.28948002

H -8.74233372 0.14064317 -1.02910645

C 6.16635773 -3.31774926 -0.39562355

H 6.89270684 -3.42480886 -1.20886014

H 6.70492647 -3.48410965 0.54065936

H 5.43245310 -4.11902497 -0.50989248

SI info for B

SCF Energy = -1290.77584121 Hartree

0 1

C -0.27925614 0.92337411 0.65497678

C 0.13762518 0.22969927 1.79835272

C 1.43622871 0.41279356 2.25397238

C 2.28532068 1.26553964 1.55578144

C 1.78993687 1.91730006 0.42303939

N 0.53225678 1.76024018 -0.00666573

H 1.78597872 -0.10373276 3.14094320

H -0.55687080 -0.42599947 2.30602281

H 3.30698598 1.42336464 1.87672044

C 2.63948795 2.88287281 -0.35810578

C -1.67220737 0.77718049 0.12256724

C 4.47047845 1.41268520 -0.59089917

C 5.70437322 1.34419603 0.06908943

C 3.95333225 0.24140927 -1.15315293

C 6.36516000 0.12991148 0.20139615

H 6.12827997 2.25012807 0.49008387

C 4.63778083 -0.96704074 -1.03193626

H 3.01013471 0.27941598 -1.68808728

C 5.85214232 -1.05974117 -0.34314642

H 7.30768967 0.11628863 0.73814086
H 4.19543512 -1.84511276 -1.48553412
C -3.81315858 -0.17715632 0.44509895
C -4.72855625 0.88046524 0.40351160
C -4.29839984 -1.47960931 0.25578516
C -6.08170749 0.64191625 0.16384468
H -4.38118381 1.89310281 0.57923777
C -5.64330529 -1.70028800 -0.00733122
H -3.60464700 -2.31234946 0.30829394
C -6.57430098 -0.64841506 -0.05798082
H -6.74915872 1.49439261 0.14962372
H -5.97271515 -2.72155429 -0.16574817
N -2.45833716 0.00156378 0.77034626
N 3.83877551 2.66506190 -0.74222832
C 1.99844886 4.20698413 -0.67029911
H 1.09082803 4.05184641 -1.25866507
H 1.69224113 4.71262384 0.25112100
H 2.69069742 4.84207050 -1.22188647
C -2.00076677 1.53932751 -1.13689042
H -2.95290542 1.22327319 -1.55867551
H -2.04790425 2.61280252 -0.93417772
H -1.20804866 1.40029001 -1.87284775
C -8.05546650 -0.94661837 -0.33698642
C 6.62424240 -2.37727150 -0.17350919
C -8.91717139 0.32749198 -0.34754949
H -9.95892408 0.06634008 -0.55117350
H -8.89086965 0.84565832 0.61495998

H -8.59721944 1.02970051 -1.12225881

C -8.18983818 -1.62977441 -1.71636064

H -7.63815910 -2.57163769 -1.76012814

H -9.23978039 -1.85033825 -1.93179623

H -7.80997661 -0.98134338 -2.51096692

C 5.90620554 -3.56594070 -0.83486269

H 4.91555133 -3.73473346 -0.40384035

H 5.78992840 -3.42386065 -1.91276610

H 6.48923148 -4.47845350 -0.68523135

C 6.78142444 -2.68810033 1.33191310

H 7.32894144 -3.62502225 1.47300445

H 7.33053547 -1.90196187 1.85522183

H 5.80422198 -2.79109642 1.81222421

C 8.02300117 -2.24214810 -0.81552579

H 8.58696687 -3.17291867 -0.70094416

H 7.94146571 -2.02487829 -1.88431202

H 8.60748805 -1.44239129 -0.35490646

C -8.60592206 -1.89059198 0.75535239

H -8.52523805 -1.43072505 1.74437088

H -9.66120636 -2.11326903 0.57019042

H -8.06745175 -2.84068678 0.78275112

SI info for C

SCF Energy = -976.172963823 Hartree

0 1

C -0.59561073 0.18462737 0.56478657

C -0.30965122 -0.68422761 1.62563464

C 0.98351239 -0.71964286 2.12941440

C 1.95583110 0.09509435 1.55783987

C 1.58594264 0.93135944 0.50109963

N 0.33545268 0.98462624 0.02734725

H 1.23423784 -1.37535943 2.95580849

H -1.09707362 -1.30262299 2.03484929

H 2.97627586 0.08533835 1.91882301

C 2.57467906 1.86611026 -0.14098550

C -1.97498957 0.27570166 -0.01419111

C 4.22060772 0.21425862 -0.51520148

C 5.40968879 -0.07860596 0.16638894

C 3.58254215 -0.80107196 -1.24327773

C 5.92401983 -1.37227692 0.15609942

H 5.91224619 0.71441308 0.71015772

C 4.11409754 -2.08787030 -1.26563902

H 2.67370208 -0.57105428 -1.78895266

C 5.28038281 -2.38357358 -0.55948115

H 6.83581464 -1.58938885 0.70322594

H 3.61071467 -2.86343885 -1.83402990

H 5.68945209 -3.38810819 -0.57479461

C -4.22566650 -0.43468395 0.13534049

C -5.00717598 0.72542001 0.25017929

C -4.83587090 -1.62839770 -0.27754686

C -6.36546475 0.69061216 -0.05718154

H -4.54537355 1.64413421 0.59565155

C -6.18839220 -1.64955448 -0.60502059

H -4.23487276 -2.52911402 -0.34453687

C -6.96146973 -0.49219432 -0.49421812

H -6.95804073 1.59449889 0.04173790

H -6.64297429 -2.57687497 -0.93862447

H -8.01837733 -0.51494404 -0.73729139

N -2.87385936 -0.46391190 0.51768979

N 3.74973204 1.54373273 -0.52554301

C 2.11354175 3.28788540 -0.30533768

H 1.21235369 3.31765727 -0.92259488

H 1.84414177 3.71886120 0.66424712

H 2.89623862 3.88897515 -0.76657232

C -2.16206943 1.21308624 -1.18066684

H -3.13803977 1.08558581 -1.64469781

H -2.06146091 2.25207811 -0.85552797

H -1.37915068 1.04589886 -1.92155005

SI info for D

SCF Energy = -1133.49109106 Hartree

0 1

C 0.11391387 -1.52335707 -0.13924134

C 0.08645132 -2.58362791 -1.05503686

C 1.28485834 -3.19325667 -1.39708404
C 2.47179746 -2.71617963 -0.84351616
C 2.40972144 -1.63254872 0.03724193
N 1.24982761 -1.07118606 0.39889275
H 1.30092478 -4.02649176 -2.09077644
H -0.85772974 -2.90638902 -1.47327298
H 3.42027542 -3.16602264 -1.10860090
C 3.65551117 -1.00485971 0.59583492
C -1.13505647 -0.80582894 0.26702193
C 2.90374885 1.22195027 0.25093846
C 2.80939192 1.53309185 -1.11882079
C 2.17412851 1.94867957 1.21175498
C 1.94915832 2.56422845 -1.50899336
C 1.32690820 2.96861328 0.78032758
C 1.20488337 3.27738833 -0.57400165
H 1.86445581 2.80707311 -2.56444431
H 0.74685421 3.51938533 1.51537822
H 0.54041796 4.07253044 -0.89576339
C -3.38248400 -0.29679535 -0.21753174
C -4.44349746 -0.99968370 0.38435444
C -3.54560446 1.02968837 -0.66378479
C -5.66868844 -0.34977594 0.54557205
C -4.79091357 1.63948366 -0.49064450
C -5.84783826 0.96225536 0.11259853
H -6.49089171 -0.88156686 1.01575804
H -4.92934590 2.66102857 -0.83303432
H -6.80783107 1.45218563 0.23934680

N -2.16979701 -0.97665402 -0.46183198
N 3.83000598 0.25398340 0.70259436
C 4.75398425 -1.93220876 1.04444780
H 5.18336975 -2.47183682 0.19471293
H 5.54734560 -1.36226301 1.52620642
H 4.36935469 -2.68548210 1.73785122
C -1.04633723 0.07628380 1.48303179
H -2.01984167 0.48863153 1.74376700
H -0.65057914 -0.48848369 2.33009080
H -0.34243164 0.89042673 1.30150856
C 3.61053897 0.76630509 -2.14180986
H 3.22894547 -0.25121444 -2.27493054
H 3.57904447 1.25895909 -3.11530731
H 4.65769924 0.67091429 -1.84058513
C 2.27032309 1.56161281 2.66193173
H 3.30979440 1.54695726 3.00375930
H 1.70519665 2.24506569 3.29859565
H 1.87638225 0.55070730 2.80865225
C -4.23415994 -2.41802063 0.84977132
H -3.85773520 -3.04810566 0.03787859
H -3.49107459 -2.47144845 1.65206055
H -5.16213380 -2.85541340 1.22257717
C -2.39973715 1.76357456 -1.31565615
H -1.60323165 1.99675462 -0.60200815
H -1.93959759 1.16306241 -2.10581491
H -2.73390556 2.70595824 -1.75342829

SI info for E

SCF Energy = -1448.07758793 Hartree

0 1

C 0.21421082 -1.21816939 0.98682563

C 0.52805743 -1.97502998 2.12489755

C -0.51295473 -2.51609463 2.86257745

C -1.82568269 -2.26734879 2.46747814

C -2.05276180 -1.47938004 1.33204794

N -1.04217887 -0.99265658 0.60145794

H -0.31190733 -3.12040880 3.74010624

H 1.56205304 -2.12461636 2.40441132

H -2.64444849 -2.67296599 3.04547471

C -3.44885707 -1.10055049 0.92560776

C 1.29018414 -0.59195329 0.15466320

C -2.94597600 0.61762471 -0.70860451

C -2.53364470 1.88216101 -0.22231856

C -2.71385183 0.25418217 -2.05860737

C -1.81607622 2.71853857 -1.08382166

C -2.00323047 1.13953740 -2.87207226

C -1.53826905 2.36098022 -2.39726560

H -1.47457424 3.67900332 -0.70948207

H -1.80831865 0.85742672 -3.90294915

H -0.97733097 3.02809897 -3.04361189

C 3.51625300 0.16228116 0.03643120

C 4.44518413 -0.62906899 -0.67994798

C 3.70779306 1.55762567 0.17973019

C 5.50734343 0.01734190 -1.32078680

C 4.78992127 2.14563921 -0.48400265

C 5.67740264 1.39485985 -1.24590409

H 6.21841559 -0.57977207 -1.88438896

H 4.93855316 3.21769738 -0.39188036

H 6.50748176 1.87458077 -1.75433725

N 2.43493753 -0.45716507 0.70301275

N -3.77026402 -0.20720677 0.07743049

C -4.58533806 -1.82196223 1.61310786

H -4.61913118 -1.58108852 2.68002748

H -5.52866489 -1.51915994 1.16322723

H -4.48069784 -2.90714353 1.52764256

C 0.91143594 -0.17195447 -1.23753283

H 1.74302425 0.31119834 -1.74675484

H 0.59965967 -1.04631540 -1.81394041

H 0.05383909 0.49706518 -1.21569801

C -2.86555657 2.42720301 1.16696040

C -3.21799491 -1.04152917 -2.69200215

C 4.39578178 -2.15509111 -0.74734224

C 2.83313810 2.46176352 1.05020126

C 1.42696134 2.72723808 0.48452098

H 1.45908513 2.97869398 -0.57805304

H 0.76355142 1.87204113 0.60244701

H 0.96390728 3.56545413 1.01404551

C 2.75964577 2.00382756 2.51737476

H 2.22982208 1.05558571 2.61578475

H 3.76018122 1.87640408 2.94024518

H 2.23248370 2.75216923 3.11715159

C 4.53084301 -2.80245940 0.64206257

H 5.43600583 -2.45775673 1.14950967

H 3.67658368 -2.55969840 1.27560147

H 4.58807978 -3.89141272 0.55041071

C 3.19535972 -2.73877991 -1.51394131

H 2.27619881 -2.69900835 -0.92904021

H 3.02376961 -2.21018350 -2.45479033

H 3.38382693 -3.79066062 -1.74848388

C -2.16287867 1.71587754 2.33705588

H -2.22955665 2.33423912 3.23749711

H -2.62150645 0.75564899 2.57185179

H -1.10652409 1.54011127 2.12476131

C -4.38020000 2.53695127 1.41723181

H -4.86597210 3.11969496 0.62948356

H -4.85394810 1.55464018 1.44780947

H -4.57082903 3.03595918 2.37251653

C -4.75387666 -1.14473709 -2.70485180

H -5.06885642 -2.03211066 -3.26297753

H -5.15797696 -1.21666995 -1.69442224

H -5.20024119 -0.26902060 -3.18470090

C -2.57955487 -2.32199407 -2.12479356

H -1.49457910 -2.22785915 -2.05251651

H -2.95706797 -2.56519181 -1.13172614

H -2.80734823 -3.16961114 -2.77875095

H 3.34532560 3.43031252 1.05462356

H 5.28668167 -2.44539588 -1.31486782

H -2.90445255 -0.98821065 -3.74071136

H -2.47892693 3.45225568 1.16627162

SI info for F

SCF Energy = -1160.72223777 Hartree

0 1

C 0.45204057 -0.50802008 0.61346218

C 0.08195036 0.24919439 1.73208370

C -1.21948595 0.14734884 2.20413513

C -2.11593394 -0.68699170 1.54338805

C -1.66355300 -1.40289256 0.43152190

N -0.40353844 -1.32624445 -0.01168589

H -1.53507637 0.71143693 3.07440541

H 0.81136463 0.88946020 2.20974577

H -3.13864842 -0.78527634 1.88362006

C -2.56465656 -2.34291997 -0.32002610

C 1.84384860 -0.45256680 0.06402524

C -4.35079852 -0.81270322 -0.54484141

C -5.54631000 -0.68987270 0.18167232

C -3.82919595 0.31374612 -1.20409061

C -6.18317511 0.53562112 0.28440418

H -5.95748361 -1.56506769 0.67128578

C -4.47179663 1.53794324 -1.11799747

H -2.91798541 0.21580794 -1.78255155

H -7.09596112 0.62554220 0.86156412

H -4.06089567 2.40219995 -1.62660863

C 4.02476875 0.41157377 0.32593583

C 4.91174473 -0.66500809 0.49762538

C 4.52577889 1.65078407 -0.10643794

C 6.26317352 -0.51167409 0.23087139

H 4.53038519 -1.61606228 0.85086276

C 5.87263053 1.80348763 -0.39037021

H 3.84298761 2.48452425 -0.22152561

C 6.75510851 0.72273994 -0.22217200

H 6.93987586 -1.34732415 0.36593622

H 6.24859192 2.75892517 -0.73713694

N 2.67653551 0.30627045 0.66997656

N -3.76169809 -2.07467781 -0.67843091

C -1.98764451 -3.69159024 -0.64159901

H -1.08320828 -3.57229203 -1.24269788

H -1.68860285 -4.20740191 0.27617673

H -2.71408005 -4.29730272 -1.18144855

C 2.13021927 -1.28081655 -1.16098262

H 3.12160305 -1.07808622 -1.56140240

H 2.05486994 -2.34491357 -0.92315987

H 1.37949346 -1.08381947 -1.92770601

C -5.65052521 1.66252851 -0.36486416

C -6.30892942 2.92397425 -0.26749138

C 8.14448879 0.88134068 -0.50342631

N -6.84208681 3.94723548 -0.18711717

N 9.27082843 1.01002922 -0.73250198

SI info for G

SCF Energy = -1205.28546934 Hartree

0 1

C -0.43243366 0.60940487 0.62074171

C -0.08020745 -0.17055388 1.73040571

C 1.21900803 -0.09740485 2.21396663

C 2.13317769 0.73669565 1.57792704

C 1.69996981 1.48143940 0.47778332

N 0.44326175 1.42837130 0.02027908

H 1.51900975 -0.68462942 3.07485746

H -0.82391245 -0.80670117 2.19081495

H 3.15767648 0.81026599 1.92001834

C 2.62264527 2.43830984 -0.22705186

C -1.82136060 0.58020929 0.06017465

C 4.35888201 0.87069665 -0.55619251

C 5.61477603 0.69069938 0.02795607

C 3.73148030 -0.24066847 -1.14478645

C 6.21628042 -0.56673785 0.07967717

H 6.11966694 1.54731169 0.46195490

C 4.33318472 -1.48901178 -1.11930590

H 2.76931737 -0.11589932 -1.62928990

C 5.57541638 -1.66873414 -0.49626098
H 7.18118842 -0.66694929 0.55939138
H 3.85351030 -2.34678219 -1.57805025
C -4.02943745 -0.24326989 0.32582038
C -4.85733107 0.88553094 0.18467876
C -4.61871218 -1.50877745 0.22644376
C -6.21328883 0.74405688 -0.06750867
H -4.43567567 1.87733328 0.30172495
C -5.97447784 -1.65976936 -0.05713889
H -3.99672444 -2.38697487 0.36334253
C -6.78446492 -0.52795443 -0.20448324
H -6.85423060 1.61360622 -0.16396240
H -6.38410948 -2.65755534 -0.14546706
N -2.66875984 -0.16560145 0.66706637
N 3.81125666 2.17176828 -0.61548883
C 2.07312416 3.82126915 -0.44651747
H 1.16444647 3.76880986 -1.05143774
H 1.78886429 4.27878202 0.50668702
H 2.81167636 4.44767930 -0.94557344
C -2.07253778 1.40762949 -1.17669770
H -2.99826106 1.11532876 -1.66975405
H -2.13621639 2.47052455 -0.92620832
H -1.23808003 1.30410008 -1.87022070
O 6.07405815 -2.93896101 -0.51606558
O -8.12257989 -0.55546090 -0.46450596
C 7.34036196 -3.17920208 0.09368448
H 7.32086044 -2.94245110 1.16231905

H 7.53571727 -4.24163842 -0.03640375

H 8.13375736 -2.60246802 -0.39236965

C -8.76178650 -1.82319636 -0.60159281

H -9.80845703 -1.60694461 -0.80510065

H -8.34073661 -2.39452305 -1.43486822

H -8.68503453 -2.41058266 0.31883226

Structures of Anions and SCF Energies:

SI info for A

SCF Energy = -1054.91562082 Hartree

-1 2

C -0.51889861 0.35595367 0.52794049

C -0.18932419 -0.44275272 1.67361020

C 1.06922179 -0.37697537 2.22014654

C 2.03820207 0.47566617 1.65008850

C 1.64633731 1.23238309 0.54055815

N 0.42834774 1.20432610 -0.00179848

H 1.32014740 -0.97998158 3.08880775

H -0.95322446 -1.08820390 2.08775264

H 3.04403581 0.54329294 2.04448879

C 2.61028279 2.19897127 -0.09091565

C -1.81528717 0.31046232 -0.07833767

C 4.33790847 0.62577701 -0.43452152

C 5.54826520 0.38438006 0.22715582

C 3.74581386 -0.42748908 -1.14691030

C 6.12316521 -0.88352416 0.21178480
H 6.02265027 1.19787272 0.76695091
C 4.34033751 -1.68473818 -1.17266485
H 2.81244265 -0.25151178 -1.67106653
C 5.53510819 -1.94239865 -0.48966949
H 7.05174829 -1.04999257 0.75106927
H 3.86006260 -2.48483181 -1.72962351
C -4.06302175 -0.49354504 0.15005163
C -4.82269661 0.68504991 -0.09100616
C -4.80901367 -1.70267845 0.20572120
C -6.20025628 0.63827370 -0.28311923
H -4.32386174 1.64749335 -0.08268158
C -6.18037005 -1.73360920 0.00159663
H -4.26588606 -2.62022932 0.41515048
C -6.91582036 -0.56498494 -0.25639435
H -6.73675425 1.57017297 -0.45168680
H -6.69946844 -2.68900192 0.04696842
N -2.72137813 -0.54432808 0.42208645
N 3.81027431 1.93332749 -0.45073712
C 2.09999407 3.60250596 -0.27795545
H 1.20036389 3.58707938 -0.89737116
H 1.80845088 4.03440501 0.68527322
H 2.86056359 4.23021355 -0.74263117
C -2.03626469 1.15090067 -1.32274501
H -2.89367745 0.79045989 -1.89356431
H -2.21307047 2.21084746 -1.10018529
H -1.15014228 1.12031883 -1.96028366

C -8.40373937 -0.61288241 -0.50812951

H -8.63476121 -0.90255320 -1.54086166

H -8.90149598 -1.33928370 0.14188245

H -8.87220894 0.36015934 -0.33648657

C 6.18643494 -3.30331685 -0.54320118

H 6.85620803 -3.39000270 -1.40619681

H 6.78490049 -3.49796906 0.35021667

H 5.44399793 -4.10060498 -0.63127909

SI info for B

SCF Energy = -1290.86308581 Hartree

-1 2

C -0.30862336 0.86923037 0.57332467

C 0.09427134 0.17729229 1.76437782

C 1.34914258 0.37783108 2.28629820

C 2.24270574 1.26224495 1.64639164

C 1.78225014 1.90822496 0.49391347

N 0.56483515 1.74913944 -0.02639730

H 1.65508272 -0.14405886 3.18916444

H -0.61133956 -0.49693050 2.23243863

H 3.24393273 1.43400350 2.02034479

C 2.66128839 2.89838604 -0.21966179

C -1.60368044 0.68453661 -0.00986689

C 4.50039278 1.44146008 -0.47293250

C 5.72809195 1.33946293 0.19476649

C 3.99535873 0.29749273 -1.10031966

C 6.39436470 0.12253982 0.26858715

H 6.14484614 2.22344691 0.66719123

C 4.68290272 -0.91311140 -1.03630746

H 3.05310332 0.35980755 -1.63453167

C 5.89259291 -1.03840947 -0.34307230

H 7.33248935 0.08456977 0.81236504

H 4.24693263 -1.76831381 -1.53777430

C -3.77875438 -0.27997666 0.30172617

C -4.63864365 0.80003719 -0.03250360

C -4.42227643 -1.53696837 0.46832117

C -6.00967456 0.62184077 -0.20717845

H -4.22726195 1.79931393 -0.11732797

C -5.78447799 -1.69969213 0.28058610

H -3.80419991 -2.38630884 0.74688314

C -6.62920528 -0.62734812 -0.07029702

H -6.60054018 1.49787001 -0.45189885

H -6.20405010 -2.69299911 0.41395943

N -2.43686039 -0.19973164 0.56080172

N 3.87425838 2.69983283 -0.57918100

C 2.04078233 4.24117754 -0.49602943

H 1.12340463 4.10977962 -1.07401908

H 1.75141934 4.72646859 0.44231330

H 2.73542986 4.88365747 -1.03739862

C -1.89960475 1.41929985 -1.30448224

H -2.71324862 0.93895442 -1.85095781

H -2.18531044 2.46747613 -1.14916021

H -1.01049339 1.43928483 -1.93772384

C -8.13464849 -0.85813505 -0.26664670

C 6.66966239 -2.36004720 -0.23827877

C -8.88021400 0.43308718 -0.64555064

H -9.94490377 0.22222464 -0.78049838

H -8.79214877 1.19689115 0.13213458

H -8.50700005 0.85781931 -1.58167227

C -8.36067142 -1.88814047 -1.39664739

H -7.88864674 -2.84726423 -1.17030698

H -9.42998349 -2.07147388 -1.54597020

H -7.94399830 -1.52583673 -2.34103780

C 5.96148767 -3.51500293 -0.96680884

H 4.96860230 -3.71006286 -0.55239602

H 5.85142682 -3.31607075 -2.03637456

H 6.54738957 -4.43206925 -0.86202255

C 6.81917803 -2.75135636 1.24904509

H 7.36970456 -3.69256942 1.34345572

H 7.36165251 -1.99221218 1.81731132

H 5.83942971 -2.88332595 1.71693005

C 8.07220375 -2.18626187 -0.86248689

H 8.64001111 -3.11939216 -0.79346531

H 7.99699042 -1.91285686 -1.91886191

H 8.64955316 -1.40923195 -0.35614192

C -8.75542215 -1.40171935 1.04020838

H -8.62143116 -0.68885902 1.85911745

H -9.82916962 -1.57751268 0.91571160

H -8.29798220 -2.34675322 1.34280087

SI info for C

SCF Energy = -976.25949377 Hartree

-1 2
C -0.77865428 -0.12713460 0.37125663
C -0.46853200 -1.31868521 1.05465325
C 0.87373662 -1.52111975 1.41377182
C 1.83170149 -0.59383123 1.06997312
C 1.45337729 0.58478255 0.33946075
N 0.13093109 0.78533511 0.03247887
H 1.15680460 -2.40852671 1.97402619
H -1.24650443 -2.02756878 1.30129354
H 2.86108540 -0.73712855 1.36738788
C 2.37447916 1.62212739 -0.03168567
C -2.19291226 0.18686844 -0.00661696
C 4.48424546 0.46463296 -0.15025469
C 5.76740561 0.41475961 0.45709764
C 4.14509963 -0.63017760 -0.99556475
C 6.62986464 -0.65644821 0.26132882
H 6.05781572 1.24742758 1.09188000
C 5.02085187 -1.68998601 -1.19539663
H 3.18388246 -0.61975257 -1.49837011
C 6.26937314 -1.72743696 -0.56510434

H 7.59786440 -0.65712650 0.75620655

H 4.72570631 -2.50293869 -1.85469609

H 6.94548274 -2.56200586 -0.72057618

C -4.46366833 -0.47071366 0.05208081

C -5.18434300 0.53630056 0.71481075

C -5.15799464 -1.35529879 -0.78823862

C -6.55952157 0.65946447 0.52928052

H -4.65681042 1.21046908 1.38148716

C -6.52910707 -1.21466010 -0.98360549

H -4.60578806 -2.14522558 -1.28686018

C -7.23934239 -0.20888907 -0.32513872

H -7.10042821 1.44210730 1.05221345

H -7.04684458 -1.89899564 -1.64850412

H -8.30969641 -0.10847117 -0.47066629

N -3.09570598 -0.67876825 0.28317997

N 3.71405580 1.58446748 0.02569861

C 1.78930618 2.96347035 -0.42684366

H 1.36724863 2.93778094 -1.43942245

H 0.97690270 3.28212794 0.23319298

H 2.58165580 3.71461248 -0.41431468

C -2.44285040 1.49608257 -0.71844374

H -3.45046164 1.54529083 -1.12832596

H -2.30601243 2.33546904 -0.03123731

H -1.71195986 1.63056827 -1.51514158

SI info for D

SCF Energy = -1133.57264205 Hartree

-1 2

C -0.04355265 -1.30934994 -0.30541518

C -0.09019556 -2.38539093 -1.25938891

C 1.05096767 -3.08554014 -1.55712846

C 2.27094147 -2.74949732 -0.92293955

C 2.24405308 -1.67568237 -0.01542288

N 1.15335662 -0.98268398 0.29522758

H 1.02144705 -3.89955079 -2.27711897

H -1.03818696 -2.62354968 -1.72559240

H 3.18564843 -3.28309589 -1.14738857

C 3.51200269 -1.24044369 0.66188475

C -1.20325799 -0.55211214 0.04325426

C 3.18265902 1.08915706 0.32076139

C 3.32541879 1.45469725 -1.03233684

C 2.47110783 1.90979156 1.21708797

C 2.73422043 2.64341765 -1.47037397

C 1.89483309 3.08648926 0.74071735

C 2.01946407 3.45940252 -0.59734416

H 2.83733422 2.92917773 -2.51382212

H 1.32974784 3.71228051 1.42625771

H 1.56690226 4.37921517 -0.95435388

C -3.56690459 -0.24408813 -0.20352340

C -4.18677675 -0.54182701 1.04309247

C -4.27527431 0.55747741 -1.14172452

C -5.45475280 -0.02596982 1.32294705

C -5.53736952 1.05530437 -0.82095069

C -6.13437883 0.77759609 0.40941563

H -5.92214115 -0.26897473 2.27475228

H -6.06027279 1.67651821 -1.54458940

H -7.11900356 1.16941763 0.64578991

N -2.35682699 -0.79247903 -0.58615960

N 3.87788239 -0.02790901 0.82854775

C 4.41878260 -2.32696133 1.18592294

H 4.84072306 -2.91263158 0.36354889

H 5.23897592 -1.88929313 1.75486084

H 3.86453363 -3.02655049 1.81814563

C -1.02947587 0.55772408 1.06138235

H -1.95837629 1.11291758 1.20130727

H -0.71059587 0.17062986 2.03463903

H -0.24485830 1.25207078 0.75063236

C 4.10089101 0.57617290 -1.98256947

H 3.60378467 -0.38683966 -2.13618161

H 4.21631280 1.05411354 -2.95754594

H 5.09853098 0.35131285 -1.59185934

C 2.29454047 1.46162086 2.64120394

H 3.25844371 1.26808728 3.12311929

H 1.75316908 2.20241343 3.23362146

H 1.73385025 0.52256459 2.66066104

C -3.50864314 -1.45866042 2.03117129

H -3.05168480 -2.31164500 1.52122533

H -2.70278106 -0.95953327 2.57783956

H -4.21997182 -1.83723274 2.76950670

C -3.63494306 0.86585543 -2.47135592

H -2.68817154 1.40113480 -2.34575917

H -3.39076664 -0.05209276 -3.01559077

H -4.28962000 1.47554075 -3.09962008

SI info for E

SCF Energy = -1448.16031744 Hartree

-1 2

C 0.23282135 1.16651049 1.06680761

C 0.57887919 1.99955385 2.15296687

C -0.48803754 2.58793084 2.86582731

C -1.78937199 2.31625898 2.51471538

C -2.06731190 1.41973757 1.41740481

N -1.01358373 0.89519947 0.70576160

H -0.28101721 3.25920054 3.69591261

H 1.61436549 2.17890322 2.40619445

H -2.59845982 2.77327223 3.07175931

C -3.39987467 1.03390237 1.06184796

C 1.29525677 0.52052725 0.23460040

C -3.00508777 -0.58934638 -0.72385130

C -2.78883943 -0.16271824 -2.06818255

C -2.59191637 -1.90419286 -0.35267900

C -2.10865519 -1.00059736 -2.95518605

C -1.91049910 -2.69504902 -1.28249474

C -1.64904218 -2.25822165 -2.57736324

H -1.93411248 -0.65315669 -3.97115959

H -1.58266724 -3.68727366 -0.98072494

H -1.11349073 -2.88990243 -3.27965883

C 3.54580891 -0.14850230 0.02063094

C 3.80758826 -1.53216792 0.18466358

C 4.41374146 0.65801783 -0.75717674

C 4.88151567 -2.09327515 -0.51470544

C 5.47094527 0.03950748 -1.43262362

C 5.70179078 -1.32819129 -1.33583682

H 5.07798352 -3.15622310 -0.40433976

H 6.13052939 0.65101284 -2.04220488

H 6.52643388 -1.78698739 -1.87206198

N 2.47899313 0.44843009 0.72016838

N -3.78656074 0.17831685 0.12915090

C -4.54309768 1.65836689 1.84269679

H -4.53936858 2.75360992 1.78799109

H -5.49095024 1.30166833 1.43988930

H -4.50803389 1.39801774 2.90812913

C 0.88412610 0.02290193 -1.12658507

H 1.67148620 -0.56599126 -1.59489980

H -0.03447944 -0.55540204 -1.06399839

H 0.65683270 0.87687965 -1.77069997

C -3.28608661 1.17578629 -2.61152019

C -2.90172372 -2.54158392 1.00200452

C 3.01468490 -2.44928778 1.11714733

C 4.30374743 2.17950102 -0.85429994
C 3.04538937 2.70228052 -1.56964700
H 2.85077793 2.15146584 -2.49331136
H 2.15971428 2.63207775 -0.93832590
H 3.17896016 3.75718440 -1.82879239
C 4.47934341 2.86306793 0.51332882
H 3.65862245 2.60901432 1.18509019
H 5.41560085 2.55665059 0.98853623
H 4.50079205 3.95107404 0.39497137
C 3.00097102 -1.95854171 2.57544313
H 4.01782138 -1.79198234 2.94284497
H 2.44962344 -1.02312232 2.67522513
H 2.52789853 -2.70627796 3.21985252
C 1.59126656 -2.77669828 0.63322135
H 0.91392290 -1.93270011 0.75220887
H 1.58055003 -3.06719113 -0.42027313
H 1.18080188 -3.60752173 1.21581431
C -2.60093574 2.40133369 -1.98374895
H -2.91808789 3.31457106 -2.50025591
H -2.84457898 2.50120493 -0.92696884
H -1.51351332 2.32841413 -2.06391717
C -4.81877191 1.30799680 -2.56059482
H -5.29881142 0.47873613 -3.09008417
H -5.17158599 1.29927334 -1.52947521
H -5.14051289 2.24105592 -3.03616630
C -4.41316892 -2.64873354 1.27192536
H -4.59963793 -3.18668437 2.20786682

H -4.86232389 -1.65792112 1.34235334

H -4.91665016 -3.19210041 0.46600690

C -2.17372014 -1.90797997 2.19873391

H -1.10375263 -1.81086739 2.00476998

H -2.55661553 -0.91360217 2.42253183

H -2.30393372 -2.53455804 3.08845746

H 5.15462802 2.48990506 -1.47126623

H 3.56189076 -3.39894535 1.11528260

H -2.52727989 -3.57052617 0.93065513

H -3.01172637 1.18355399 -3.67414848

SI info for F

SCF Energy = -1160.82165597 Hartree

-1 2

C 0.68618811 -0.09813698 0.47461588

C 0.31249867 0.96040243 1.31774495

C -1.03167593 1.02886908 1.70795723

C -1.93398520 0.09660915 1.24107267

C -1.49123890 -0.93801177 0.35786485

N -0.16947440 -1.01223566 0.01664992

H -1.36199729 1.81137591 2.38482147

H 1.04762307 1.67760007 1.65610675

H -2.96717358 0.13242571 1.55789833

C -2.35109165 -1.97673050 -0.14473921

C 2.10911176 -0.26604592 0.04278485
C -4.53440927 -0.97459900 -0.13226218
C -5.85407455 -1.11224124 0.40207062
C -4.25400877 0.25961546 -0.80799836
C -6.79036508 -0.10848116 0.31062711
H -6.09911273 -2.04528191 0.89979292
C -5.19653400 1.25691742 -0.91391205
H -3.27904094 0.39543521 -1.26115684
H -7.77620364 -0.24806595 0.74300806
H -4.95173226 2.17268172 -1.44367069
C 4.33029871 0.52443851 0.19659445
C 5.13407721 -0.47865268 0.76876997
C 4.94279364 1.53327266 -0.56813016
C 6.50569674 -0.48155523 0.57289041
H 4.66821798 -1.24832728 1.37334296
C 6.31127150 1.52649571 -0.77859459
H 4.32640426 2.31527833 -0.99642392
C 7.10801749 0.51851237 -0.20804623
H 7.11463781 -1.26036957 1.01735300
H 6.77082927 2.30185330 -1.38059334
N 2.96433458 0.59660907 0.45355951
N -3.69144796 -2.02509638 -0.04801564
C -1.69717734 -3.20898267 -0.72865660
H -1.30156496 -3.01397942 -1.73332591
H -0.85089754 -3.56083864 -0.13142145
H -2.44006450 -4.00449337 -0.80944221
C 2.42480646 -1.43372311 -0.85892501

H 3.44401277 -1.38706526 -1.23919076

H 2.29330836 -2.37342825 -0.31660771

H 1.72190352 -1.46220923 -1.69161757

C -6.48469004 1.10917844 -0.34686901

C -7.44460912 2.14206125 -0.44817790

C 8.51851042 0.51506459 -0.41568361

N -8.23425839 2.99039834 -0.53328883

N 9.66290121 0.51200289 -0.58531374

SI info for G

SCF Energy = -1205.36885839 Hartree

-1 2

C -0.67730173 0.11545226 0.40297009

C -0.29259941 -1.02991359 1.13225872

C 1.06278323 -1.13937893 1.48319332

C 1.96502991 -0.17508864 1.09290530

C 1.51387790 0.94877289 0.31445208

N 0.17892173 1.05759017 0.01352130

H 1.40084875 -1.98482419 2.07746610

H -1.02683528 -1.76936916 1.41947914

H 3.00194045 -0.24643832 1.38970239

C 2.36453438 2.02665561 -0.10812658

C -2.11089377 0.34401202 0.04206049

C 4.54509911 1.00129440 -0.16616116

C 5.81477275 1.06144829 0.44985845

C 4.28799500 -0.16086926 -0.94509672

C 6.75509866 0.03741668 0.33570222

H 6.05317749 1.94447397 1.03589444

C 5.22389829 -1.17507203 -1.07265282

H 3.33680541 -0.24496979 -1.45921026

C 6.46471126 -1.09814371 -0.42705062

H 7.70668799 0.14213854 0.84322826

H 5.01104086 -2.05138439 -1.67827568

C -4.35059057 -0.41232741 0.22278765

C -5.08921503 0.69425253 0.68183169

C -5.05729116 -1.47615349 -0.35049862

C -6.46982791 0.73436052 0.55285878

H -4.57172849 1.51769743 1.16133904

C -6.44231758 -1.43391003 -0.50699763

H -4.50534105 -2.34820242 -0.68561843

C -7.16065443 -0.32327124 -0.05175046

H -7.03755976 1.58443854 0.91603153

H -6.94329534 -2.27349907 -0.97154646

N -2.96529381 -0.54311309 0.41249382

N 3.70188588 2.08699648 -0.07269840

C 1.68606475 3.30840317 -0.55256400

H 1.27051795 3.21656840 -1.56406864

H 0.85110279 3.59268707 0.09451103

H 2.42374442 4.11315052 -0.56797314

C -2.43521596 1.59345766 -0.74636886

H -3.40393087 1.51327730 -1.23910306

H -2.45954704 2.46953105 -0.09141312

H -1.65548753 1.78134629 -1.48230395

O 7.31256809 -2.16902554 -0.61120537

O -8.51705233 -0.18008896 -0.13789283

C 8.58410831 -2.12460253 0.02008925

H 8.49272102 -2.06731821 1.11089044

H 9.08725818 -3.05238839 -0.24809073

H 9.18184630 -1.27618783 -0.33265964

C -9.27131215 -1.23344939 -0.73149535

H -10.31030952 -0.91187881 -0.69621980

H -8.97846465 -1.39794631 -1.77357534

H -9.16243844 -2.16837588 -0.17214693

Supporting Information for for Chapter 4

Kinetic Protocol for Determining Rate of Enhancement in Methyl Orange Decomposition Experiments.

Kinetic Experiments

All kinetic experiments were performed as a series of independent reactions with various exposure times. All experimental reactions consisted of a 15mL aliquot from a fresh made bulk solution consisting of a 1:15 dilution of stock methyl orange (MO) solution with a concentration of 1% W:V. Kinetic experiments begin by placing the desired substrate (TiO_2 blanket, Al patterned) into the bottom of a with a 15mL aliquot from the diluted bulk solution into 6" borosilicate petri dish (catalytic side face up). Following substrate placement, a 15mL aliquot of the diluted bulk solution was measured using a 15mL volumetric flask and carefully poured into the petri dish. The addition of dilute MO solution must be done slowly and with care as rapid addition of solution cause substrate to lift off from the surface of the petri dish and float.

Once addition of MO solution was accomplished and substrate remained submerged, petri dish was capped with the borosilicate top and covered in tinfoil. The reaction was allowed to equilibrate under the tinfoil covering for 10 minutes and transferred to the IntelliRay-600 UV shutter flood light set to 35% power with no temperature input for UV exposure. Exposure time was set in seconds (**Table S1**) on the display the door to the UV chamber was shut to allow UV exposure. Following the UV exposure reaction vessel was left in the UV chamber for an additional 2-3 minutes prior to removal. Following removal of the reaction from the UV chamber, the cap was removed, ***and a micro-pipette was used to transfer all liquid from reaction vessel to a clean 15mL volumetric flask***. Evaporative loss was assessed by volume loss and compensated for by addition of proportional milli-Q deionized water (DI).

Post volumetric normalization the flask was capped and inverted four time (4x) to ensure the homogeneity of the reaction solution.

One hundred (100) microliters were transferred into a cuvette followed by 900 microliters of DI water (1:10 dilution of post UV exposed solution) for use in a Perkin Elmer 950 UV-Vis spectrophotometer with attached 60mm integrating sphere for concentration assessment. Four (4) samples were taken from each reaction (time point) for establishment of standard deviation.

Table S1

Minutes

0
1
3
5
7
14
x

x= any additional time points decided upon later

S2

Equations for Mapping Kinetic Data

Following collection of the UV-Vis data analysis was conducted via calculating absorption [A] from percent transdamission. Absorption values at **469nm** was compared to an externally generated calibration curve to ascertain methyl orange concentration. Equations were mapped to the concentration/time as shown in **Figure S1A**, equations for polynomial fitting are displayed in **Table 1**. Following curve fitting of the concentration/time plots, the slope was found by calculating the first derivative and using the slope as a proxy for k, which can be found in **Figure S1B** and **Table 2.**

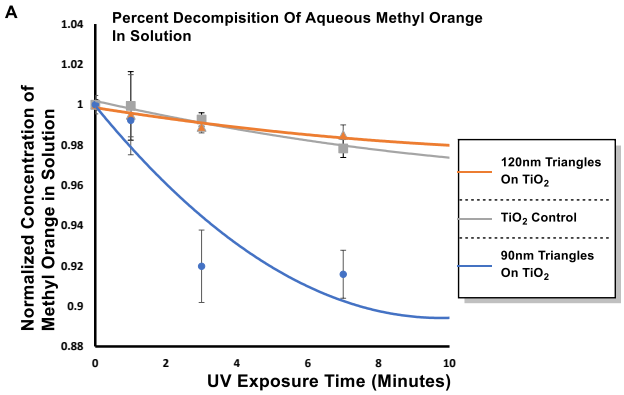

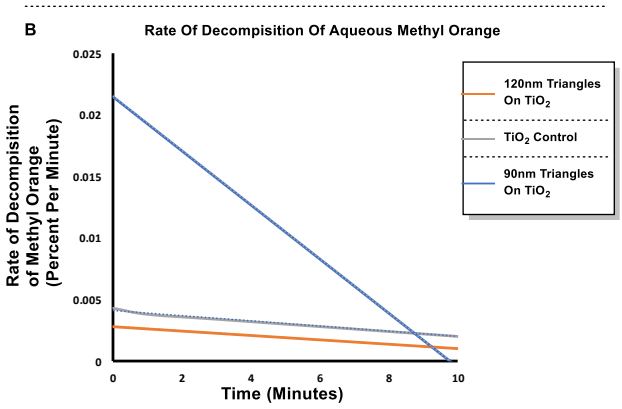

Figure S2

Table 1

Experiment	Graphics Analysis
Methyl Orange Control	$y = - 0.0003x + 1.0005$
TiO_2	$y = 0.0001x^2 – 0.004x + 1.0018$
TiO_2 Off Tuned	$y = 9E\text{-}05x^2 – 0.0028x + 0.9985$
TiO_2 Tuned	$y = 0.0011x^2 – 0.0215x + 0.9994$

S3

Table 2

Experiment	Maximum Rate of Decomposition (percent decomposition $minute^{-1}$)
Methyl Orange Control	N/A
TiO_2	0.0002
TiO_2 Off Tuned	0.0002
TiO_2 Tuned	0.0022

S4

Spectrum of UV-Lamp from Manufacturer

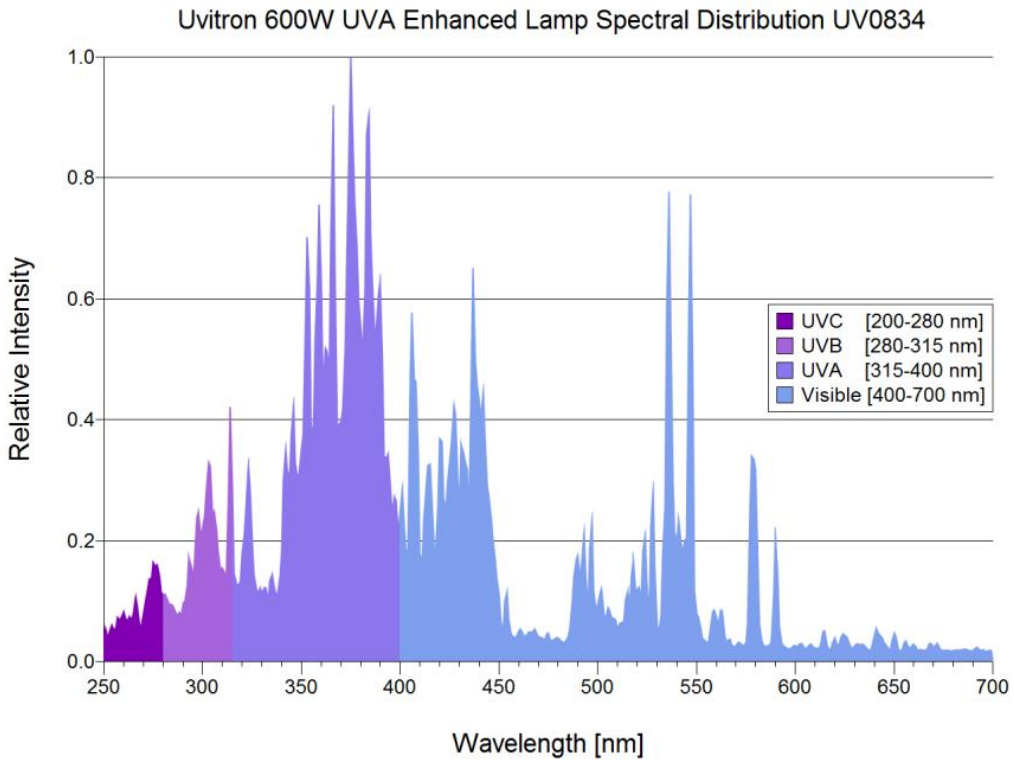

S5

Methodology

Chips were imaged with SEM before and after UV exposure to determine the average feature size and gap size. For each measurement, the feature and gap sizes on three identical chips were imaged and measured on two different locations on the chip. While some defects are present on the chips, only the triangular features were accounted for when collecting the measurements across the different samples. The two areas measured on each chip varied from one to another. However, the locations pertained to clusters of defect-free features where most of the activity will occur. Ultimately, the resulting measurements show a clear dimensional distinction between the two feature sizes before and after UV exposure.

120 nm Al- Feature Before UV Exposure

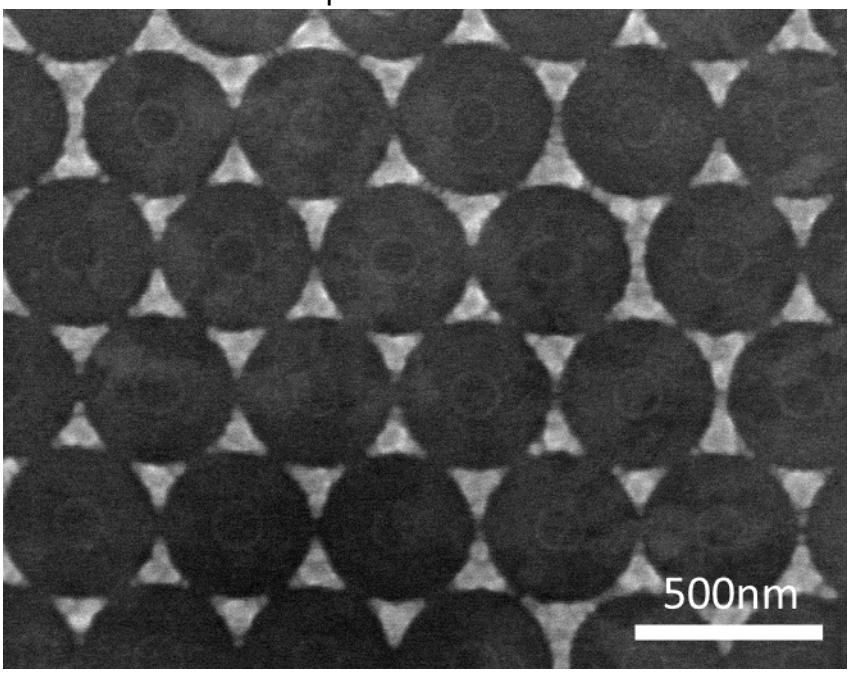

S6

120 nm Al- Feature After UV Exposure

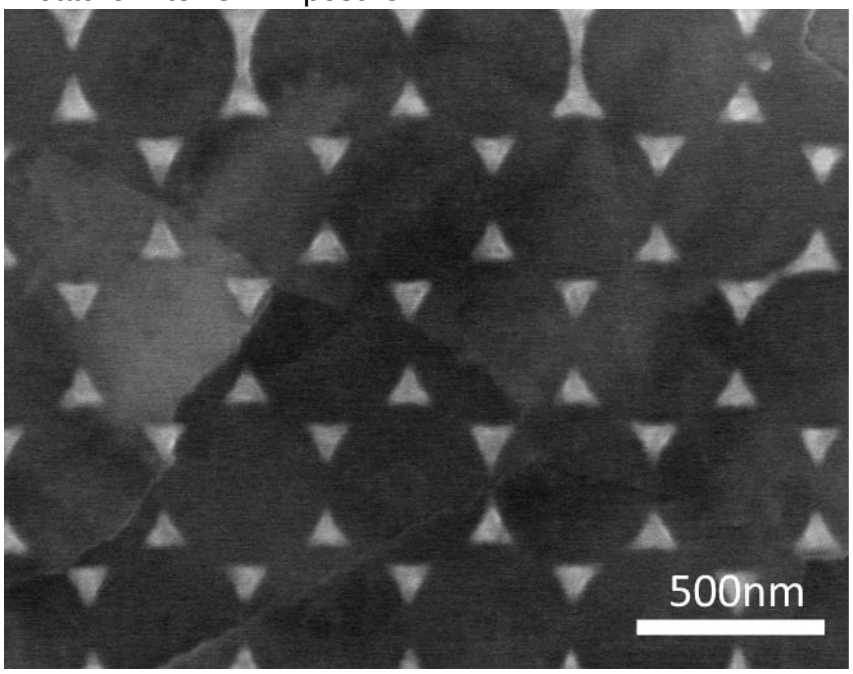

S7

90nm Al Feature Before UV Exposure

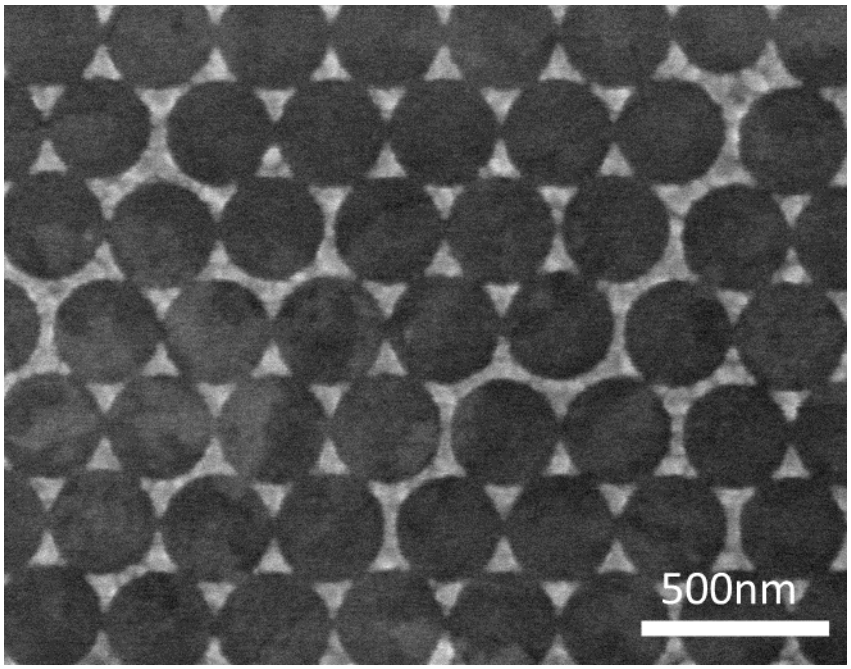

90nm Al Features After UV Exposure

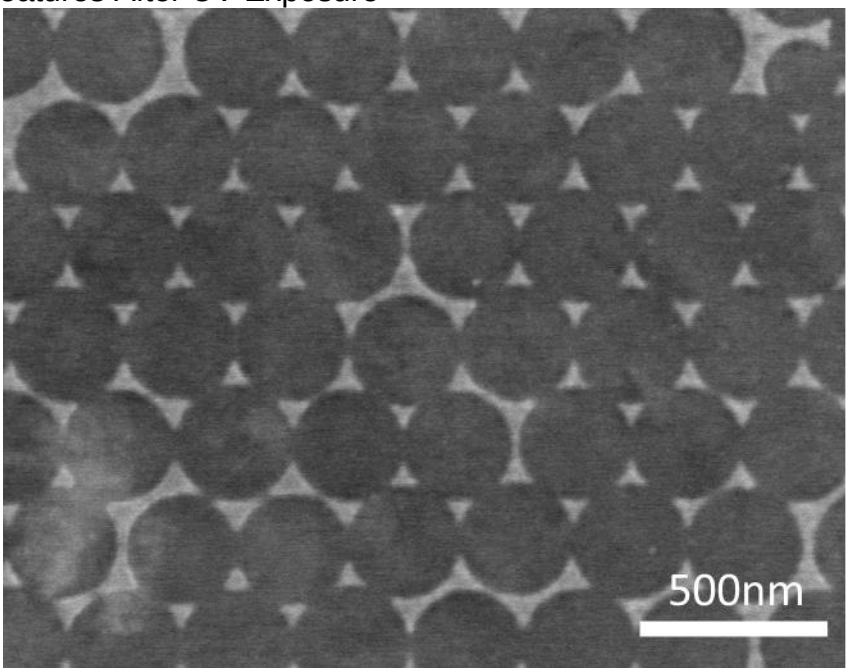

S8

Average Feature Size (nm)	*Feature Size (nm)		**Gap (nm)	
	Pre-UV	Post-UV	Pre-UV	Post-UV
120	120.3 ± 7.0	94.2 ± 6.7	60.2 ± 6.0	101.7 ± 12.0
90	90.4 ± 5.0	63.3 ± 5.1	39.8 ± 4.1	73.0 ± 7.1

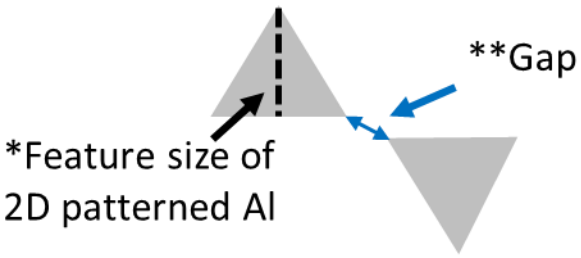
**Gap
*Feature size of
2D patterned Al

S8

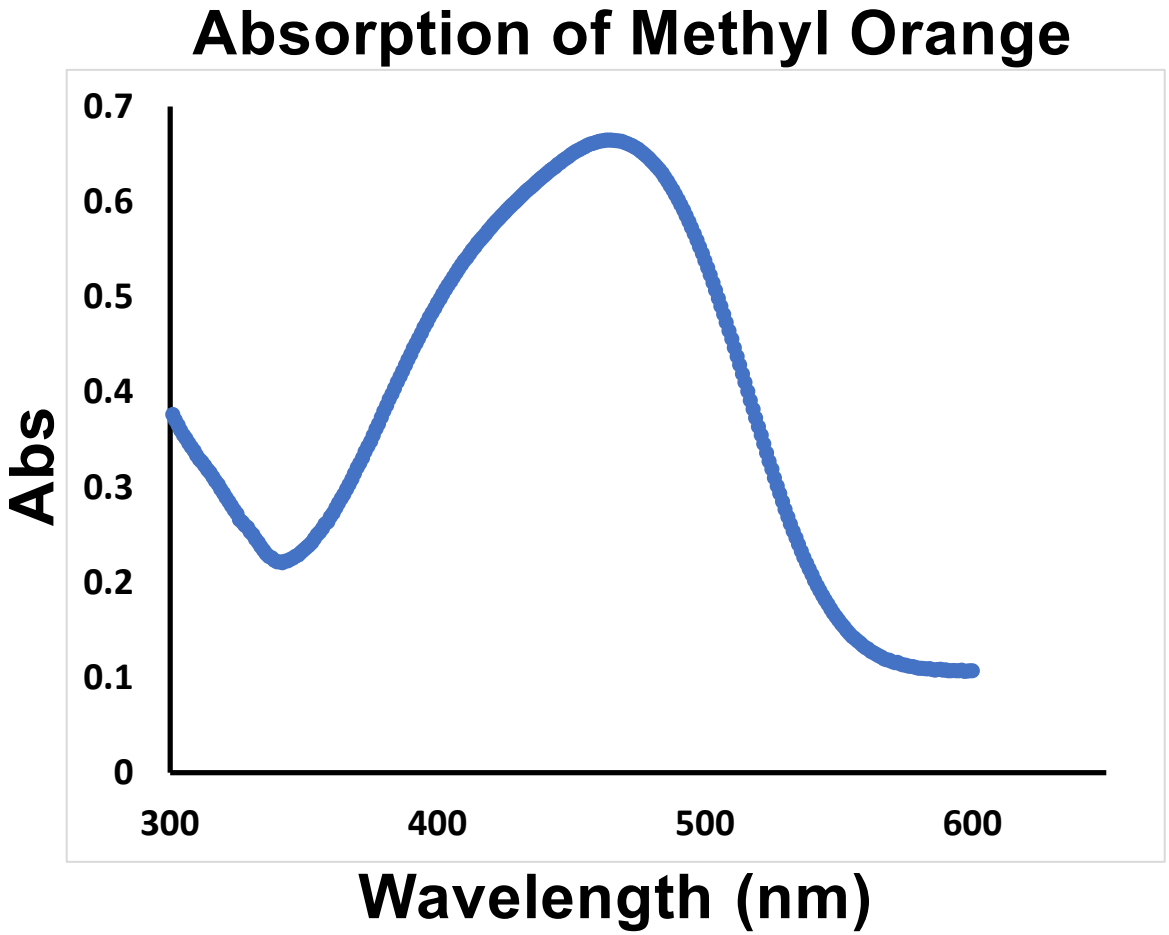
Absorption of Methyl Orange
Abs
0.7
0.6
0.5
0.4
0.3
0.2
0.1
0
300
400
500
600
Wavelength (nm)

S9

Energy diagram of the Fermi level of Al and the approximations of the conduction band (CB) and valence band of TiO_2.[1–3]

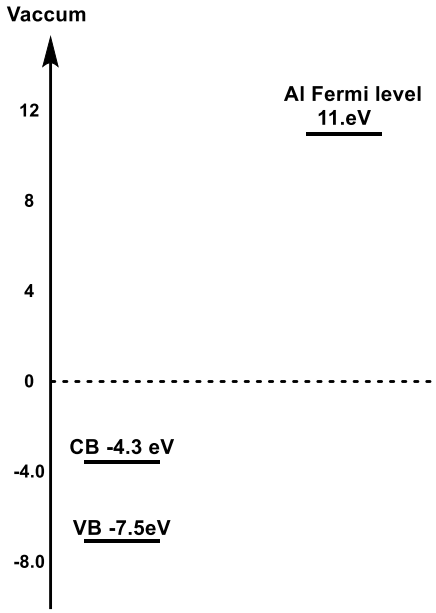

(1) Gai, Y.; Li, J.; Li, S. S.; Xia, J. B.; Wei, S. H. Design of Narrow-Gap TiO2: A Passivated Codoping Approach for Enhanced Photoelectrochemical Activity. *Phys. Rev. Lett.* **2009**, *102* (3), 23–26.

(2) Serpone, N.; Emeline, A. V.; Horikoshi, S.; Kuznetsov, V. N.; Ryabchuk, V. K. On the Genesis of Heterogeneous Photocatalysis: A Brief Historical Perspective in the Period 1910 to the Mid-1980s. *Photochem. Photobiol. Sci.* **2012**, *11* (7), 1121–1150.

(3) Ashcroft, N. W. The Fermi Surface of Aluminium. *Philos. Mag.* **1963**, *8* (96), 2055–2083..

Supporting for Chapter 5

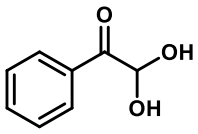

NMR (500MHz, $CD_3(CO)CD_3$): ^1H: 8.17 (d, J= Hz, 2H), 7.67-7.70 (t, J= Hz, 1H), 7.55 -7.58 (t, J= Hz, 2H), 5.95-5.99 (t, J+ Hz, 1H), 5.70-5.72 (d, J= Hz, 2H)

^{13}C (500MHz, $CD_3(CO)CD_3$: 195.73, 133.67,133.63, 129.50, 128.53, 88.05

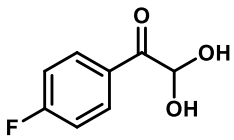

NMR (500MHz, $CD_3(CO)CD_3$): ^1H: 8.26-8.28 (t, J= 5.67Hz, 2H), 7.33-7.30 (t, J=8.80 Hz, 1H), 5.98 -5.94 (t, J= 7.82Hz, 2H), 5.82-5.80 (d, J= 7.98Hz, 1H)

^{13}C (500MHz, $CD_3(CO)CD_3$: 194.45, 164.86, 164.86, 132.61,132.53,115.62,115.44,88.39

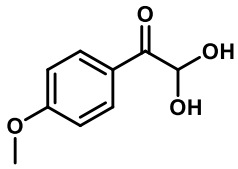

NMR (500MHz, $CD_3(CO)CD_3$): ^1H: 8.14-8.16 (d, J= 8.98Hz, 2H,) 7.06-7.08 (d, J= 8.97 Hz, 2H), 5.90 (s, 1H), 5.74 (bs, 2H), 3.94 (s, 3H)

^{13}C (500MHz, $CD_3(CO)CD_3$: 194.30, 164.11, 131.93, 126.25, 113.79, 88.72, 55.13

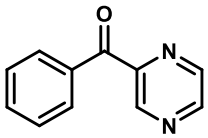

NMR (500MHz, $CDCl_3$): ^1H: 9.25 (s, 1H), 8.78 (d, J= 2.31Hz, 1H), 8.68 (s, 1H), 8.07 (d, J= 7.31 Hz, 2H), 7.64-7.65 (t, J = 7.41Hz, 1H), 7.49-7.53 (t, J= 7.70Hz, 2H),

^{13}C (500MHz, $CDCl_3$): 192.24, 149.91, 146.79, 146.09, 142.91, 135.48, 133.55, 130.86, 128.37

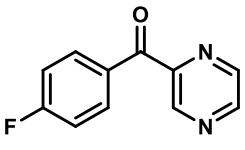

NMR (500MHz, $CDCl_3$): ^1H: 9.17 (s,1H), 8.87 (d, J= 2.28, 1H), 8.75 (s, 1H), 8.22-8.24 (m, 2H), 7.30-7.33 (t, J=8.69Hz, 2H)

^{13}C (500MHz, $CDCl_3$): 190.20,164.65 (d, J=253Hz), 149.83, 147.24, 145.63,

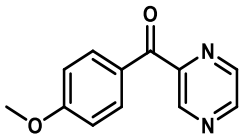

NMR (500MHz, $CDCl_3$): ^1H: 9.12 (s,1H), 8.85 (d, J=2.47Hz, 1H), 8.76 (m, 1H), 8.15(d, J= 8.96Hz, 2H), 7.10 (d, J=8.95Hz,2H), 3.94 (s, 3H)

^{13}C (500MHz, $CDCl_3$): 190.19, 164.09, 150.81, 146.76, 145.44, 142.95, 133.28,128.47, 113.59, 55.15

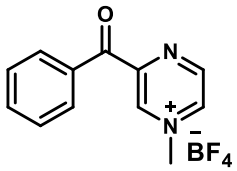

NMR (500MHz, CD_3CN): ^1H: 9.45(s,1H), 9.32 (s, 1H), 8.99 (s, 1H), 8.07 (d, J= 7.74, 2H), 7.77 (t, J = 7.36, 1H), 7.60 (t, J=7.64, 2H), 4.48 (s, 3H)

^{13}C (500MHz, CD_3CN): 188.80, 155.02, 149.17, 139.24-139.39 (m), 138.86-139.01 (m), 134.69, 134.02, 131.02, 128.74, 49.68

Hi-res MS found: 199.0795

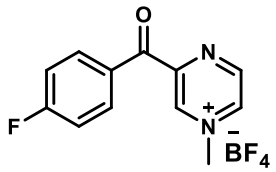

NMR (500MHz, CD_3CN): ^1H: 9.76 (s, 1H), 9.61 (s,1H), 9.40 (d, J= 3.40Hz), 8.13-8.16 (m, 2H), 7.45-7.49 (t, J= 8.86 Hz), 4.51 (s, 3H)

^{13}C (500MHz, CD_3CN): 188.06, 166.14 (d, J= 254.54Hz), 154.31, 149.13, 140.12(m), 134.57 (d, J= 9.85Hz), 131.13 (d, J= 2.76 Hz),116 (d, J= 22.18Hz), 44.94

Hi-res MS found: 217.0696

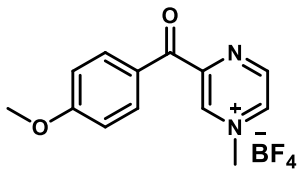

NMR (500MHz, CD_3CN): ^1H: 9.40 (s, 1H), 9.17 (s, 1H), 8.84 (d, J= 3.25Hz, 1H), 8.04 (d, J=11.91Hz, 2H), 7.04 (d, J=11.91Hz, 2H), 4.46 (s, 3H), 3.87 (s,3H)

^{13}C (500MHz, CD_3CN): 187.53, 166.04, 157.00, 150.17,140.06-140.25 (m), 139.67-139.85 (m), 134.83,127.60, 115.24, 56.71, 50.50

Hi-res MS found: 229.0893

RPB-3-45_RECRYSTALIZATION_PROTON_01
RPB-3-45_RECRYSTALIZATION

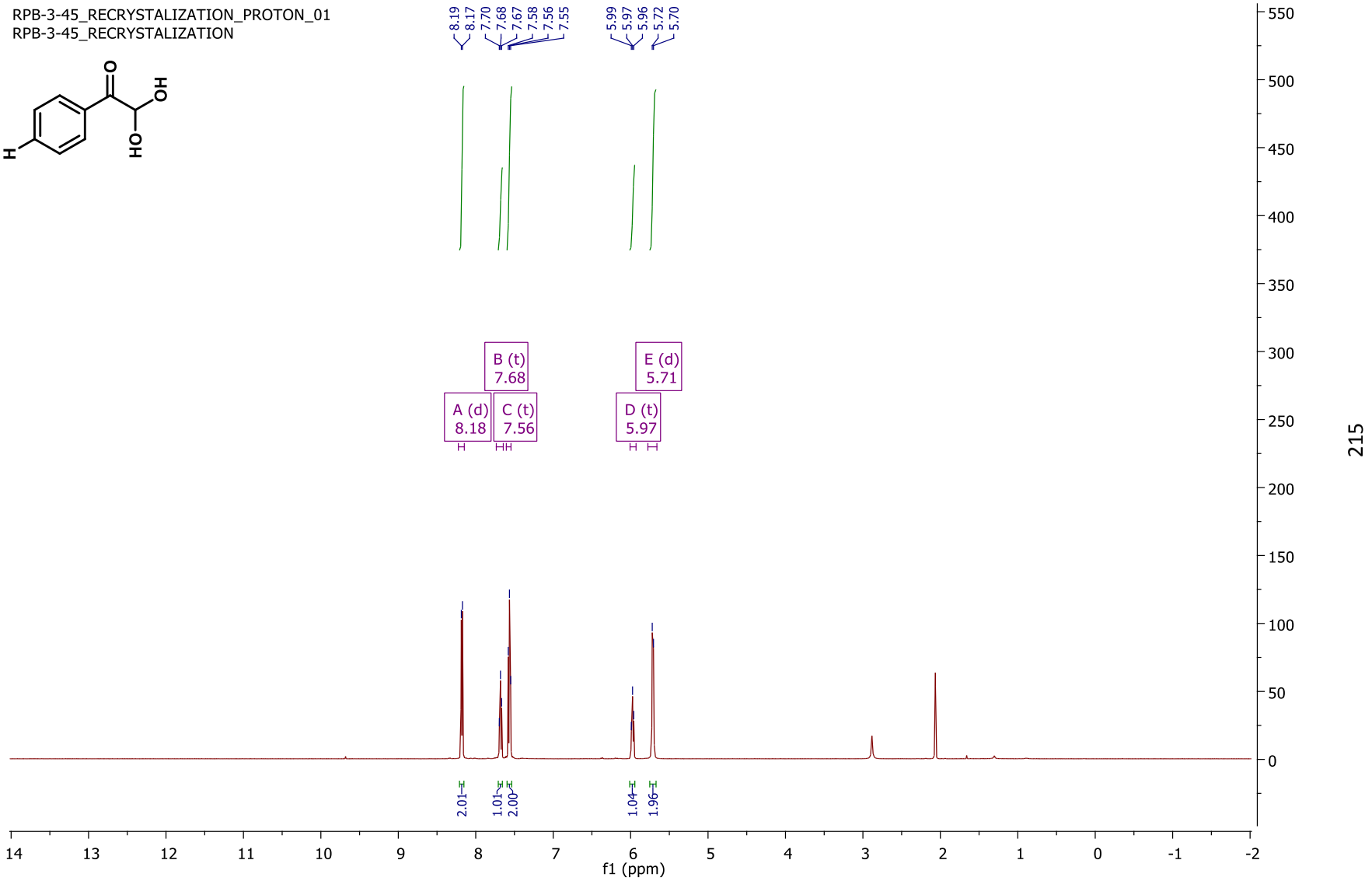

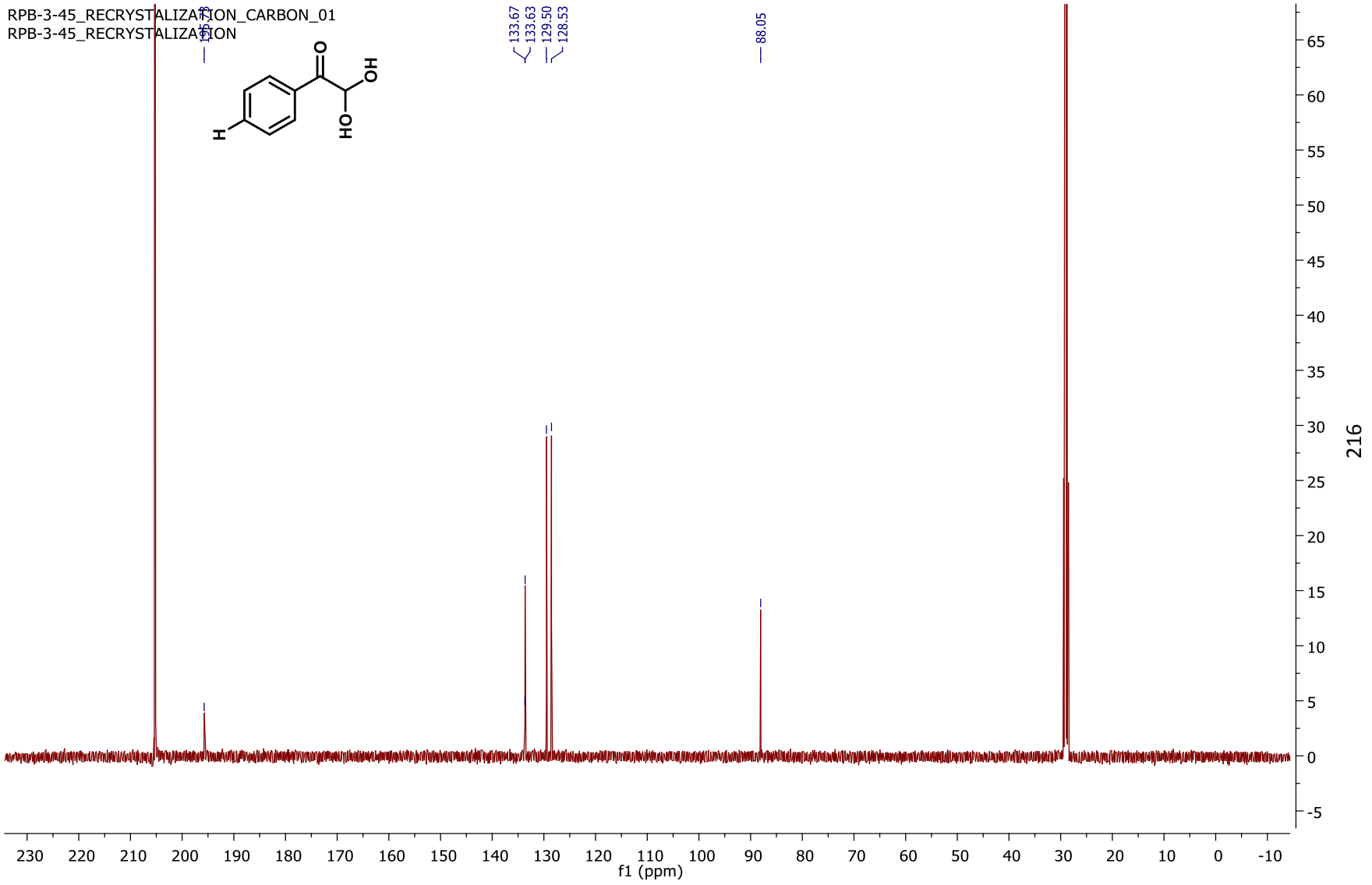
RPB-3-45_RECRYSTALIZATION_CARBON_01
RPB-3-45_RECRYSTALIZATION
133.67
133.63
129.50
128.53
88.05
O
OH
HO
H
216
f1 (ppm)

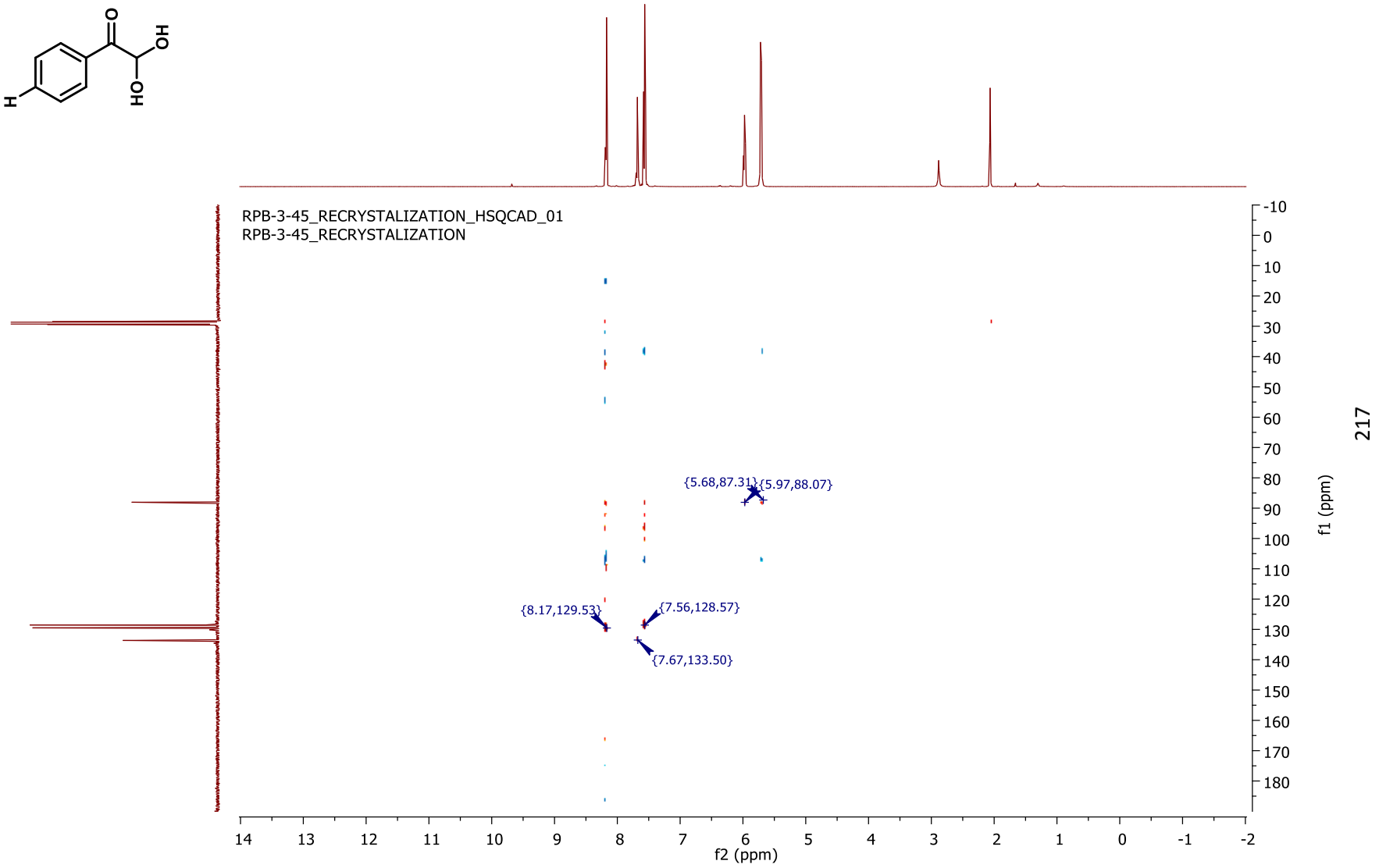
RPB-3-45_RECRYSTALIZATION_HSQCAD_01
RPB-3-45_RECRYSTALIZATION
{5.68,87.31}
{5.97,88.07}
{8.17,129.53}
{7.56,128.57}
{7.67,133.50}
f2 (ppm)
f1 (ppm)
217

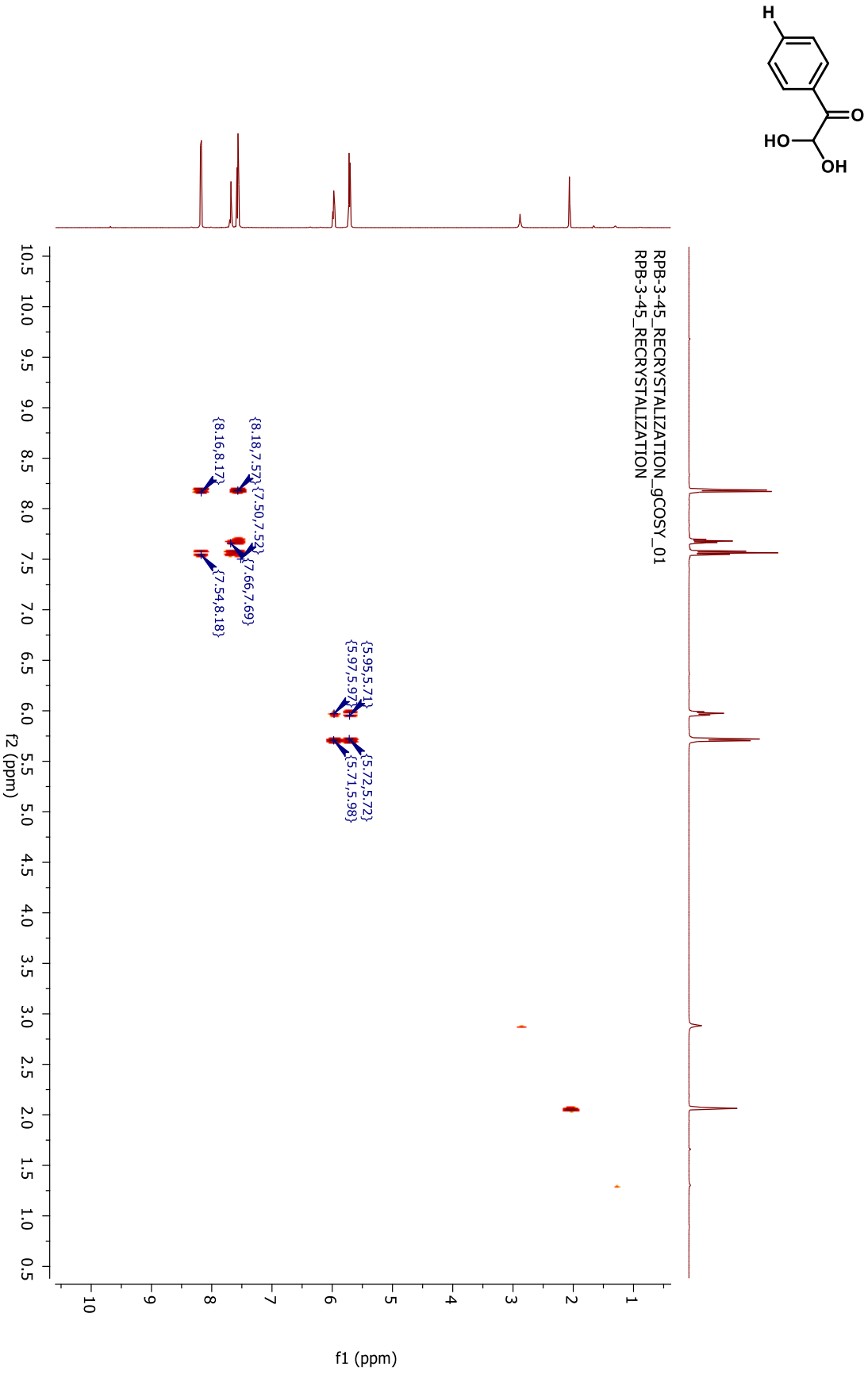
RPB-3-45_RECRYSTALIZATION_gCOSY_01
RPB-3-45_RECRYSTALIZATION
{8.16,8.17}
{8.18,7.57}
{7.50,7.52}
{7.54,8.18}
{7.66,7.69}
{5.95,5.71}
{5.97,5.97}
{5.72,5.72}
{5.71,5.98}
f2 (ppm)
f1 (ppm)
HO
OH
O
H

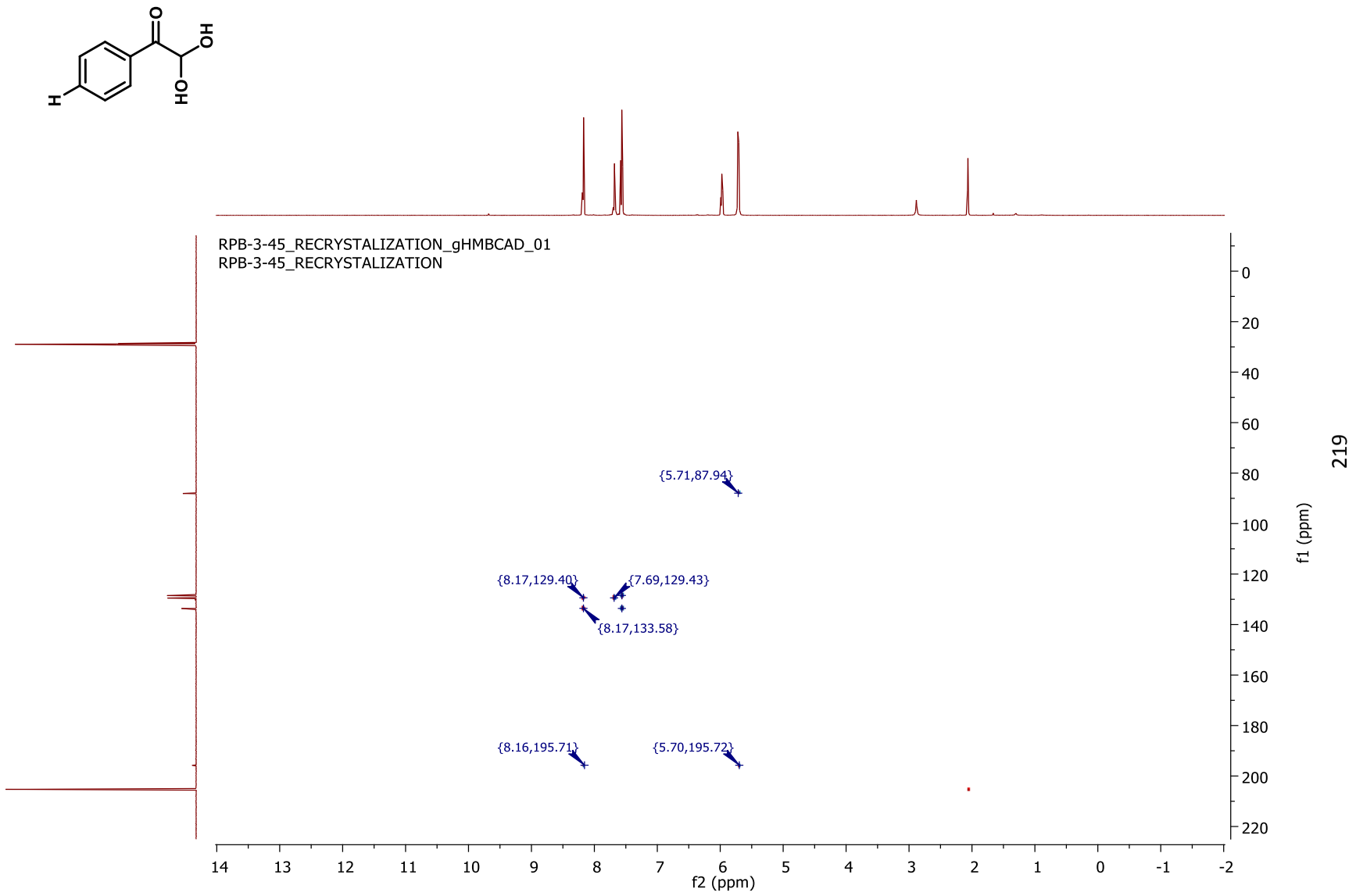
RPB-3-45_RECRYSTALIZATION_gHMBCAD_01
RPB-3-45_RECRYSTALIZATION
{5.71,87.94}
{8.17,129.40}
{7.69,129.43}
{8.17,133.58}
{8.16,195.71}
{5.70,195.72}
f2 (ppm)
f1 (ppm)
219

RPB-3-75_MORE_CONCENTRATED_PROTON_01
RPB-3-75_MORE_CONCENTRATED

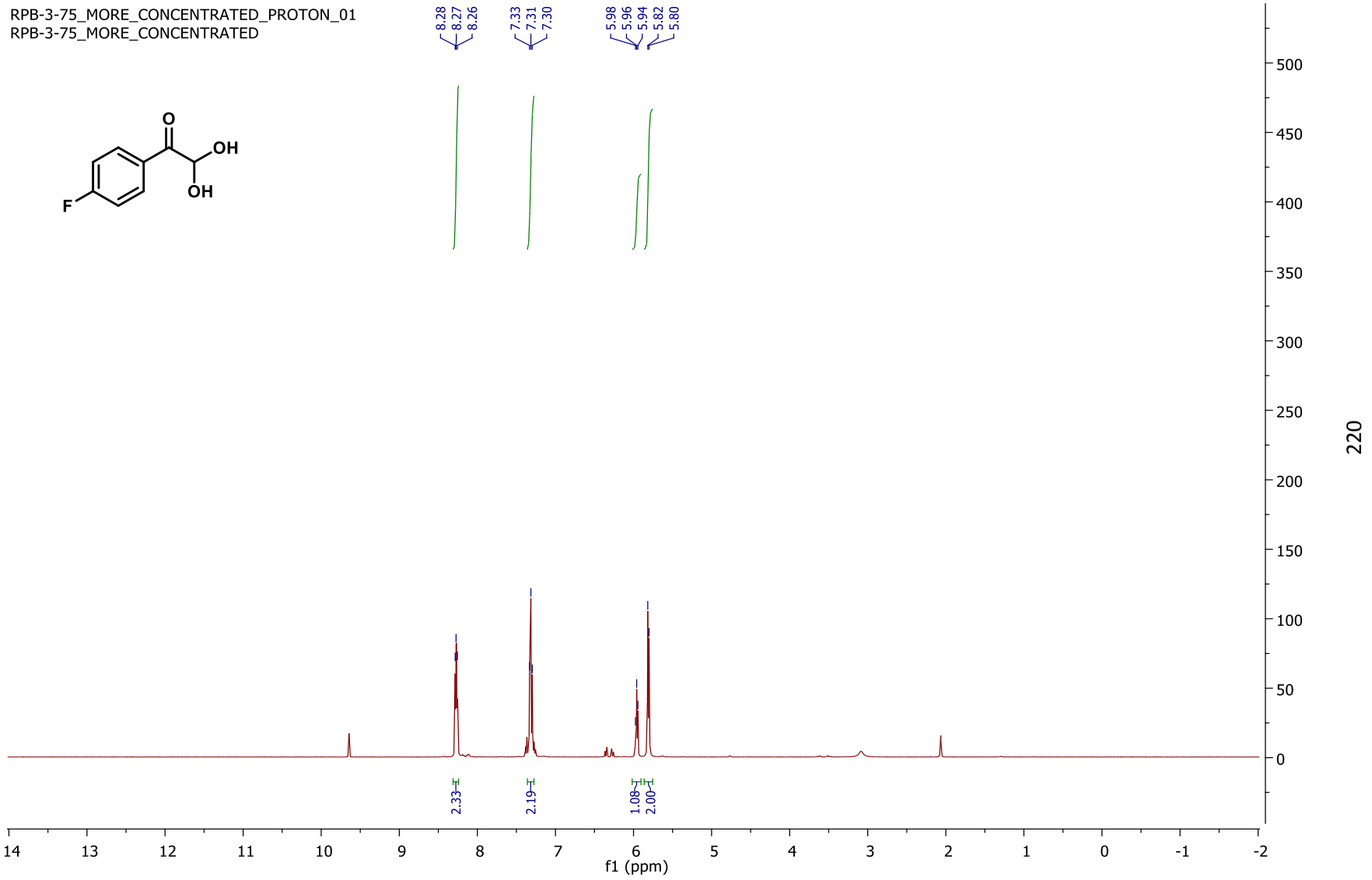

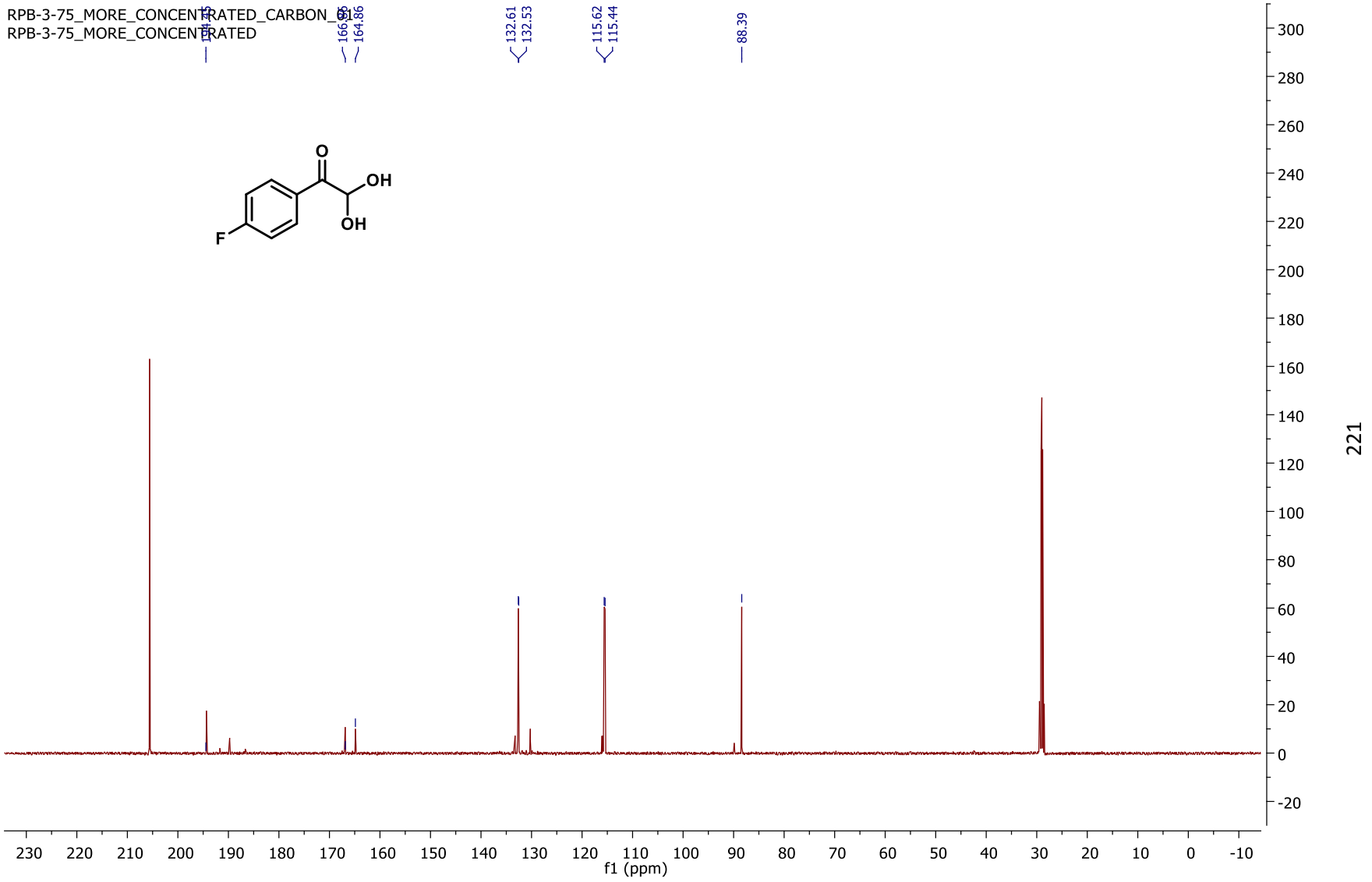
RPB-3-75_MORE_CONCENTRATED_CARBON_01
RPB-3-75_MORE_CONCENTRATED
164.86
132.61
132.53
115.62
115.44
88.39
O
OH
OH
F
f1 (ppm)
221

rpb-3-75_crystals_washed_with_water_and_hivaced_24_hrs_FLUORINE_01
rpb-3-75_crystals_washed_with_water_and_hivaced_24_hrs

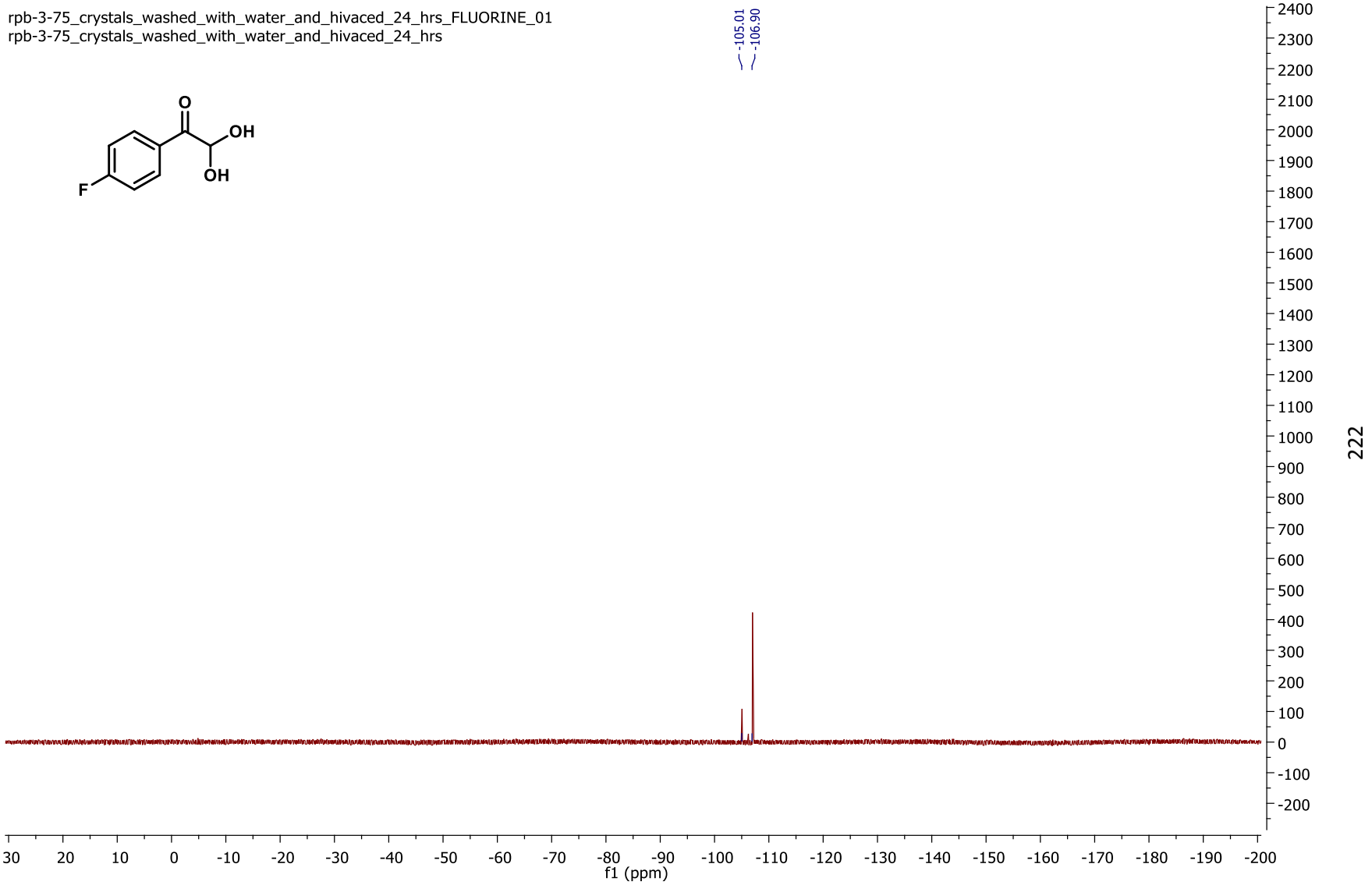

222

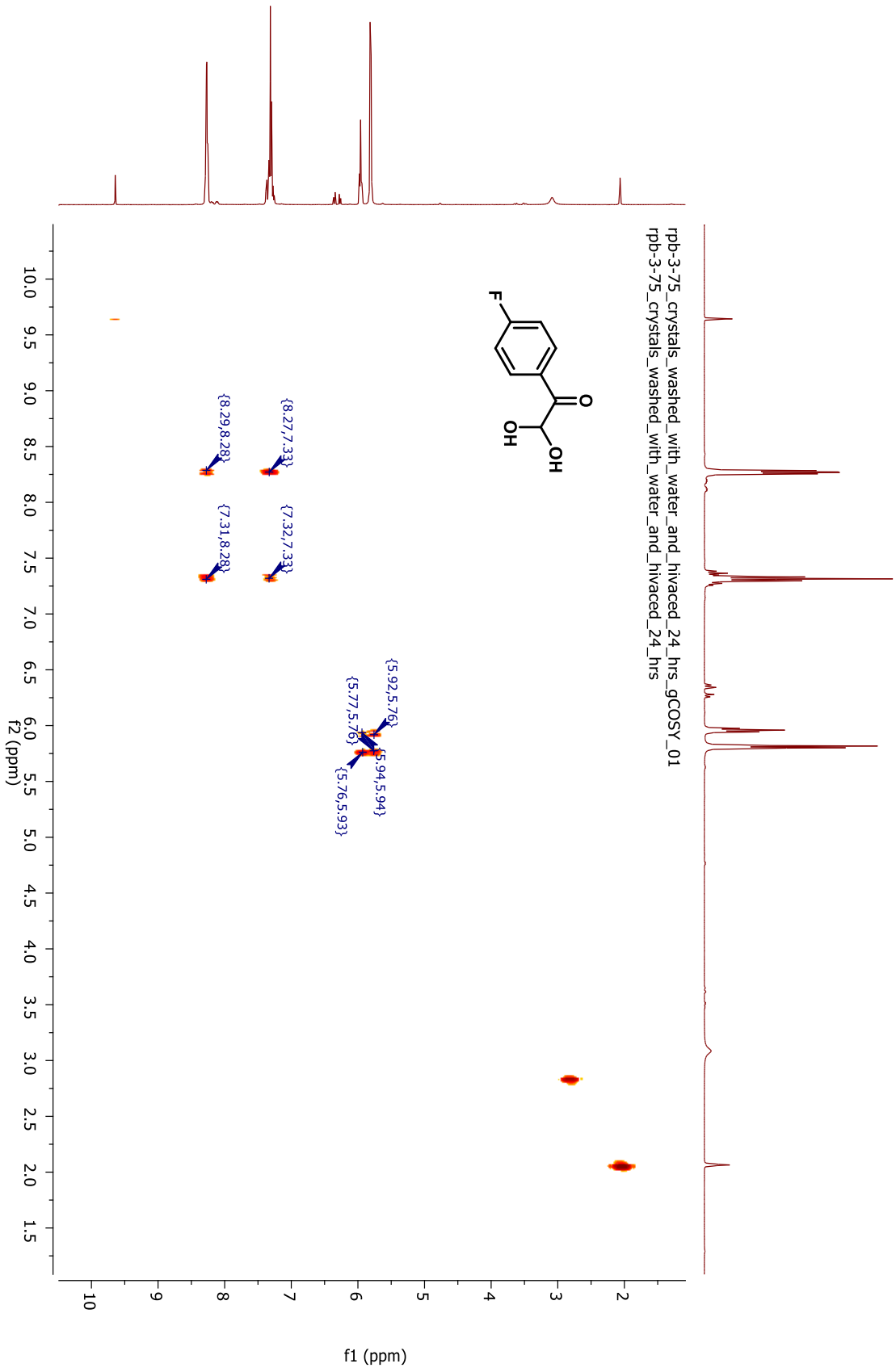
rpb-3-75_crystals_washed_with_water_and_hivaced_24_hrs_gCOSY_01
rpb-3-75_crystals_washed_with_water_and_hivaced_24_hrs
F
O
OH
OH
{8.29,8.28}
{8.27,7.33}
{7.31,8.28}
{7.32,7.33}
{5.92,5.76}
{5.77,5.76}
{5.94,5.94}
{5.76,5.93}
f2 (ppm)
f1 (ppm)

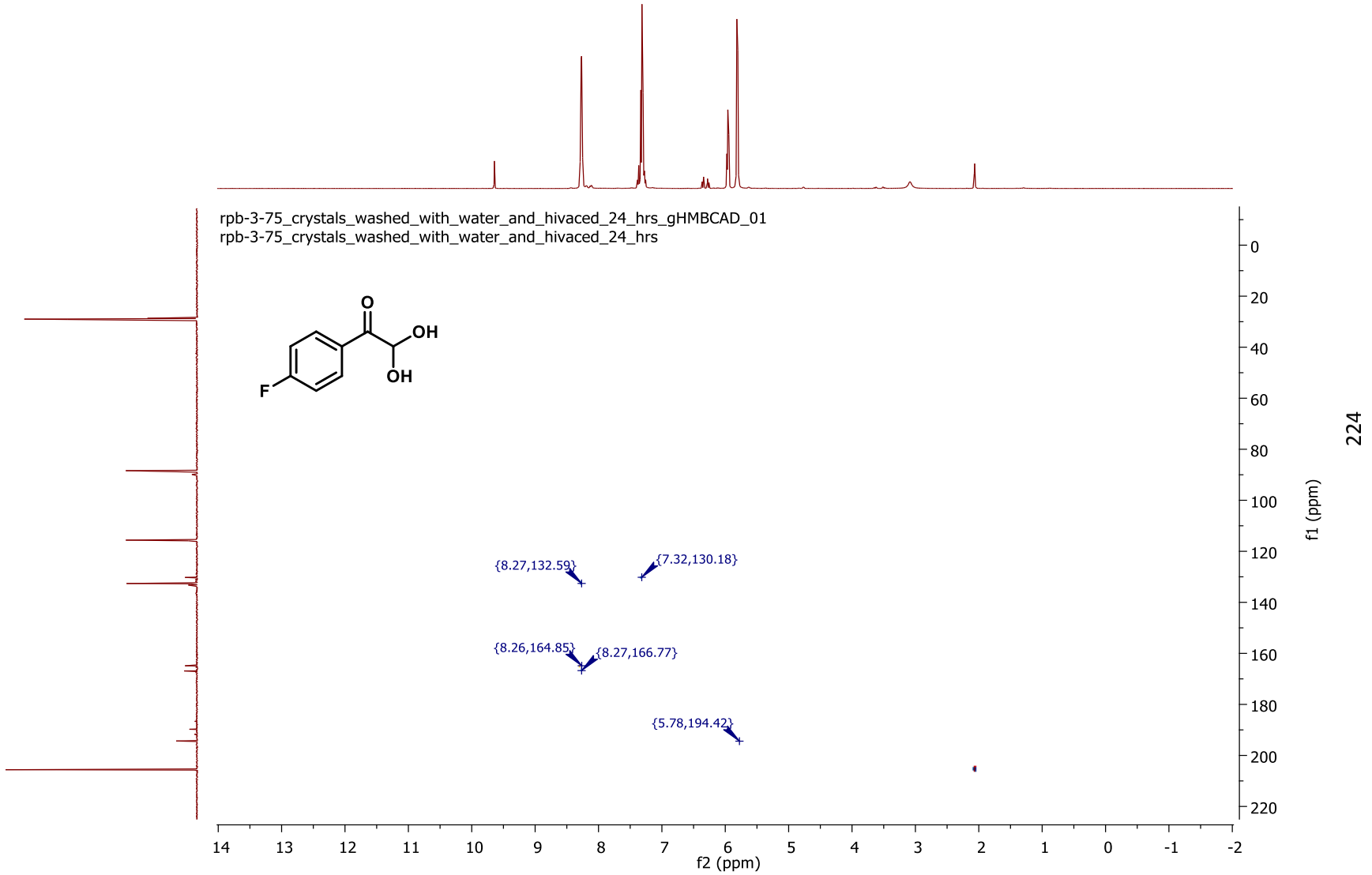
rpb-3-75_crystals_washed_with_water_and_hivaced_24_hrs_gHMBCAD_01
rpb-3-75_crystals_washed_with_water_and_hivaced_24_hrs
O
OH
OH
F
{8.27,132.59}
{7.32,130.18}
{8.26,164.85}
{8.27,166.77}
{5.78,194.42}
14 13 12 11 10 9 8 7 6 5 4 3 2 1 0 -1 -2
f2 (ppm)
0 20 40 60 80 100 120 140 160 180 200 220
f1 (ppm)
224

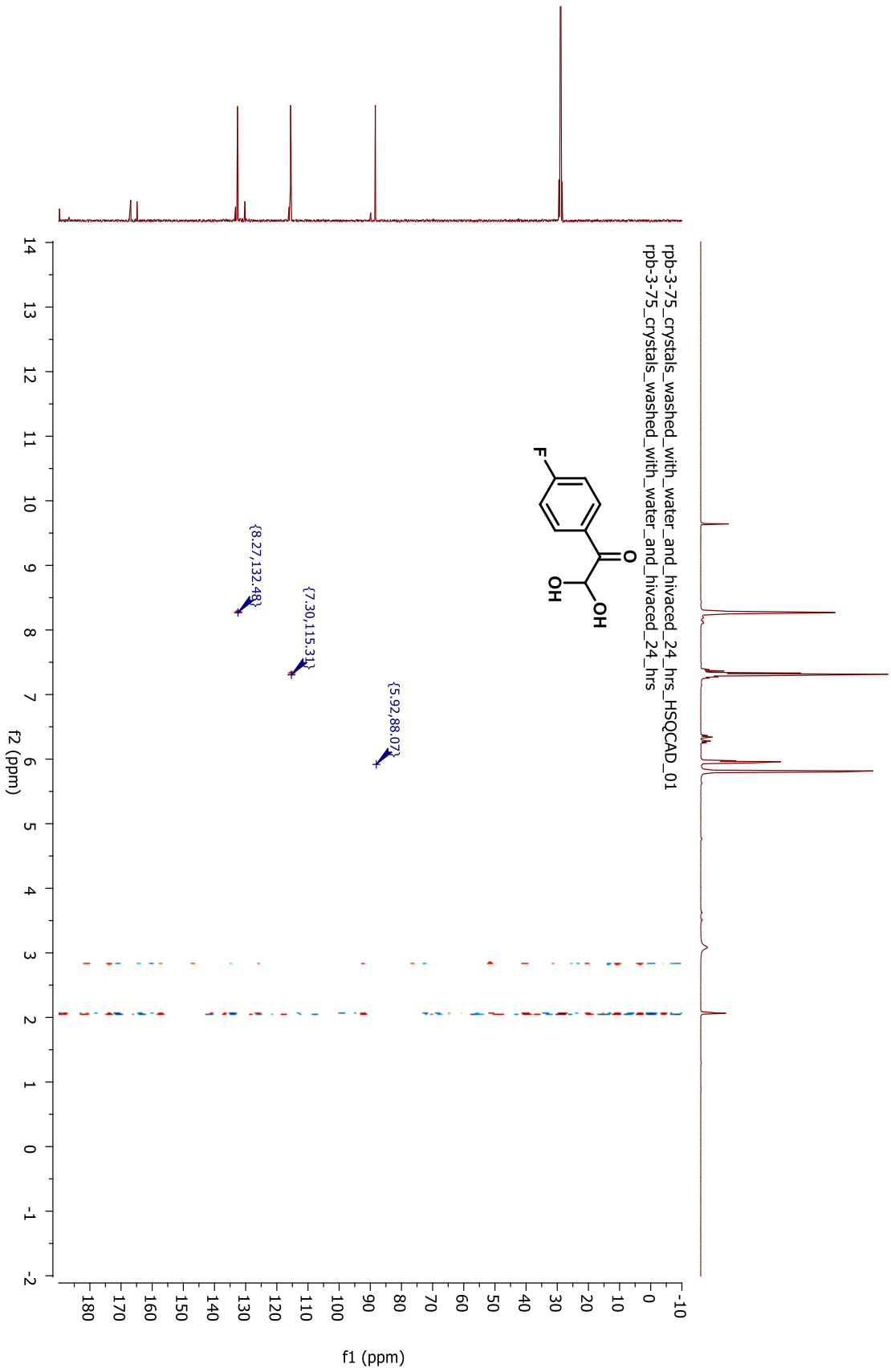
rpb-3-75_crystals_washed_with_water_and_hivaced_24_hrs_HSQCAD_01
rpb-3-75_crystals_washed_with_water_and_hivaced_24_hrs
F
O
OH
OH
{8.27,132.48}
{7.30,115.31}
{5.92,88.07}
f2 (ppm)
f1 (ppm)

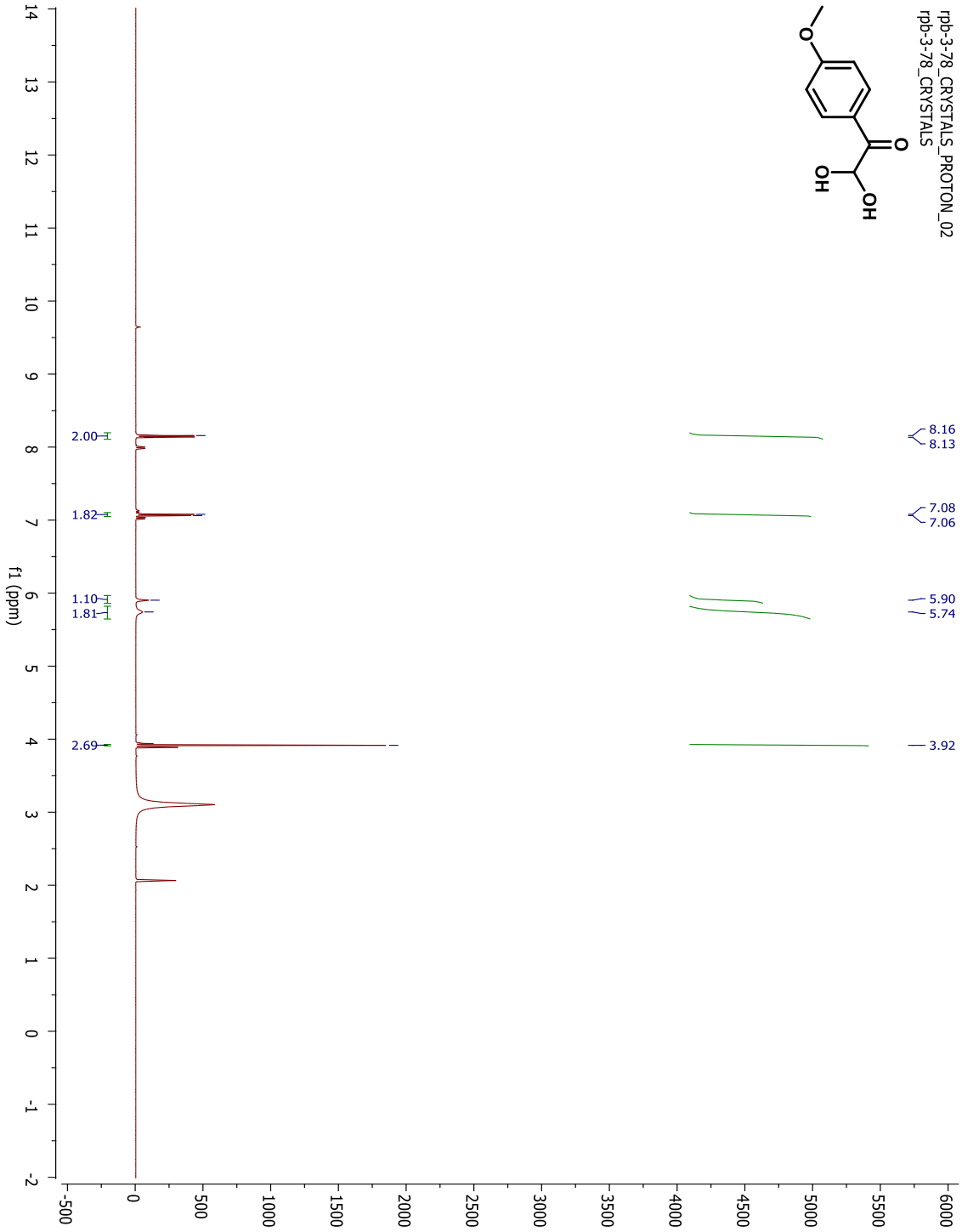
rpb-3-78_CRYSTALS_PROTON_02
rpb-3-78_CRYSTALS
O
O
OH
OH
f1 (ppm)
2.00
1.82
1.10
1.81
2.69
8.16
8.13
7.08
7.06
5.90
5.74
3.92

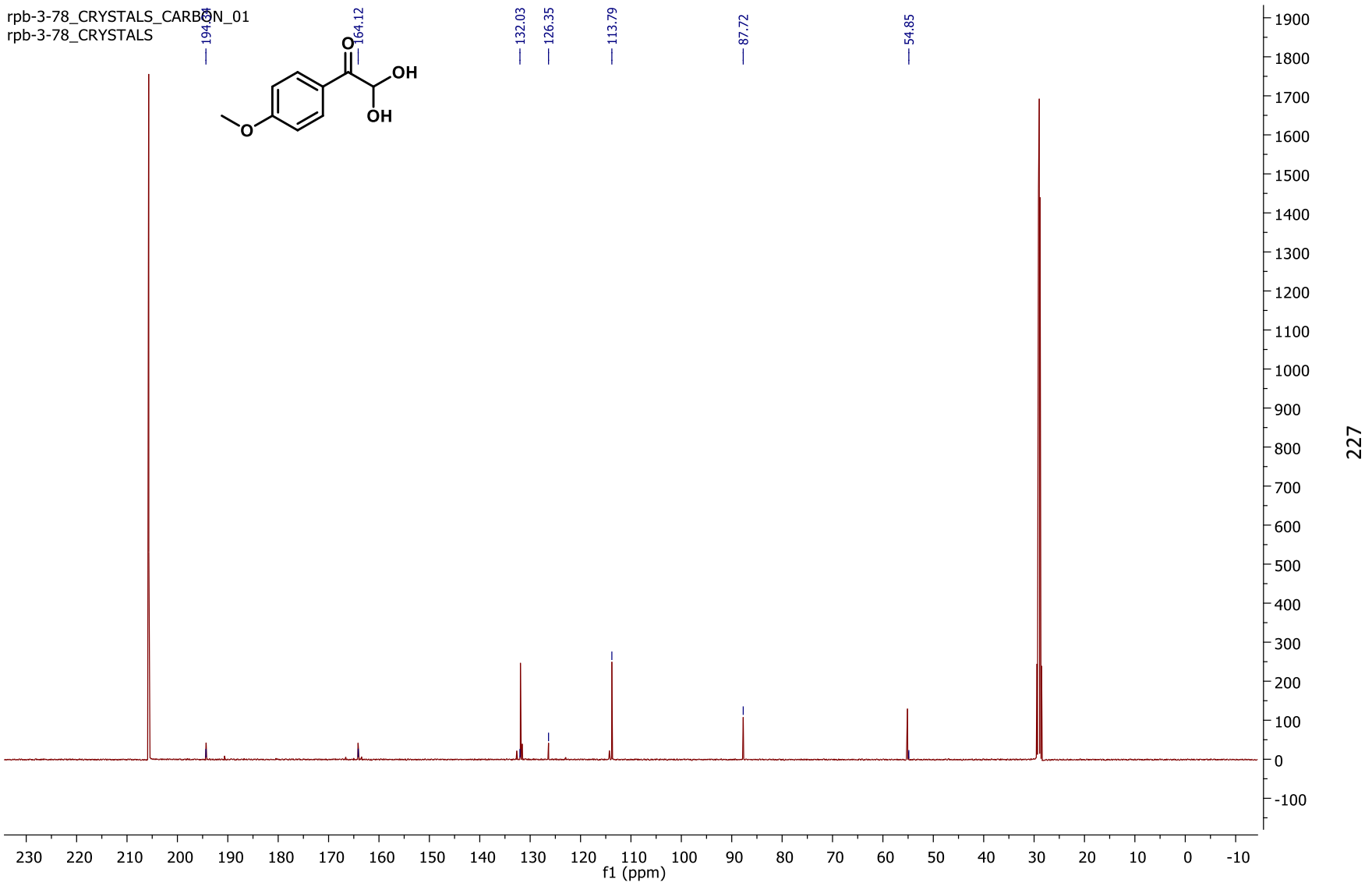
rpb-3-78_CRYSTALS_CARBON_01
rpb-3-78_CRYSTALS
194.04
164.12
132.03
126.35
113.79
87.72
54.85
O
OH
OH
O
227
f1 (ppm)

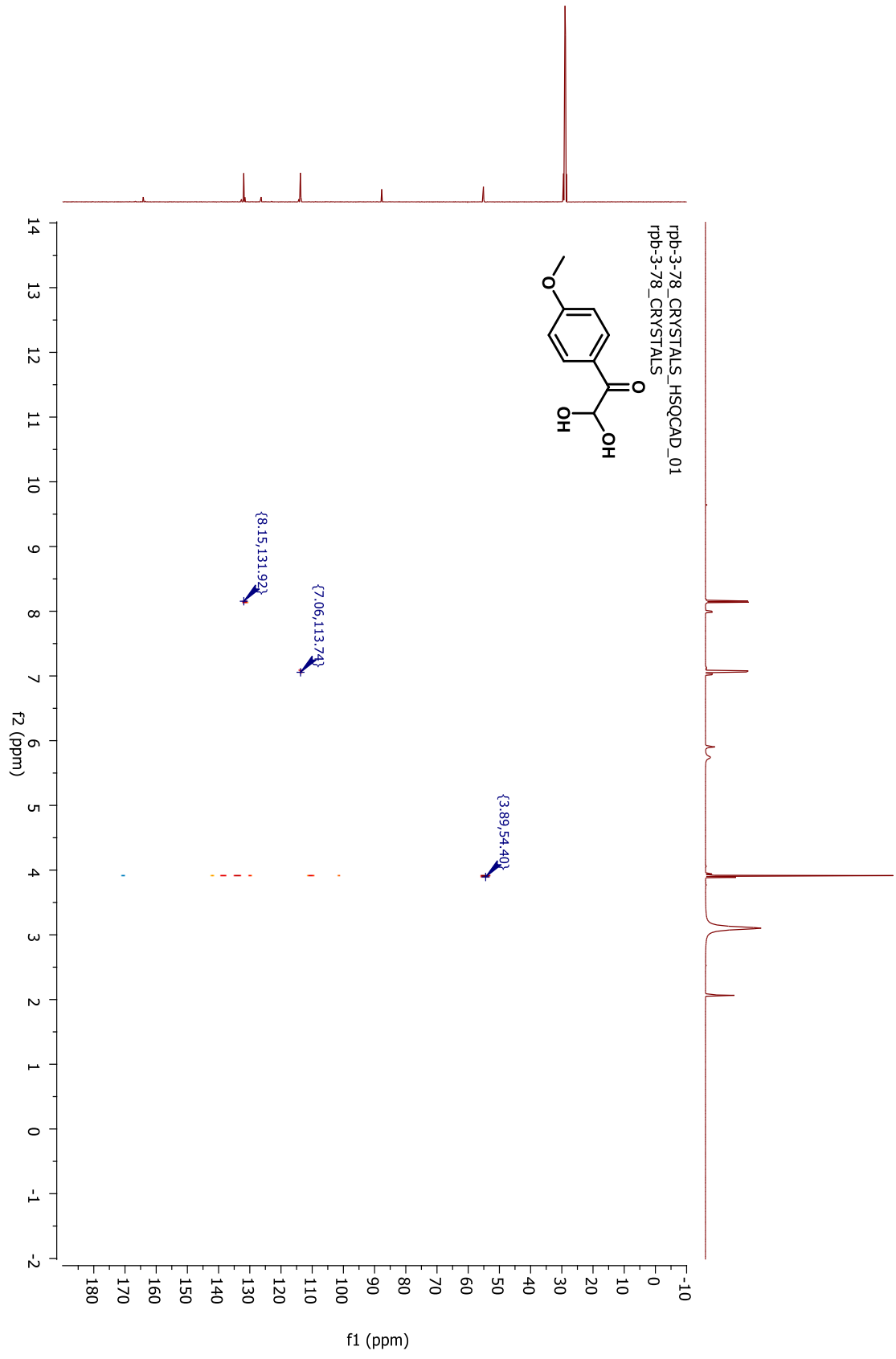
rpb-3-78_CRYSTALS_HSQCAD_01
rpb-3-78_CRYSTALS
O
OH
OH
{8.15,131.92}
{7.06,113.74}
{3.89,54.40}
f2 (ppm)
f1 (ppm)

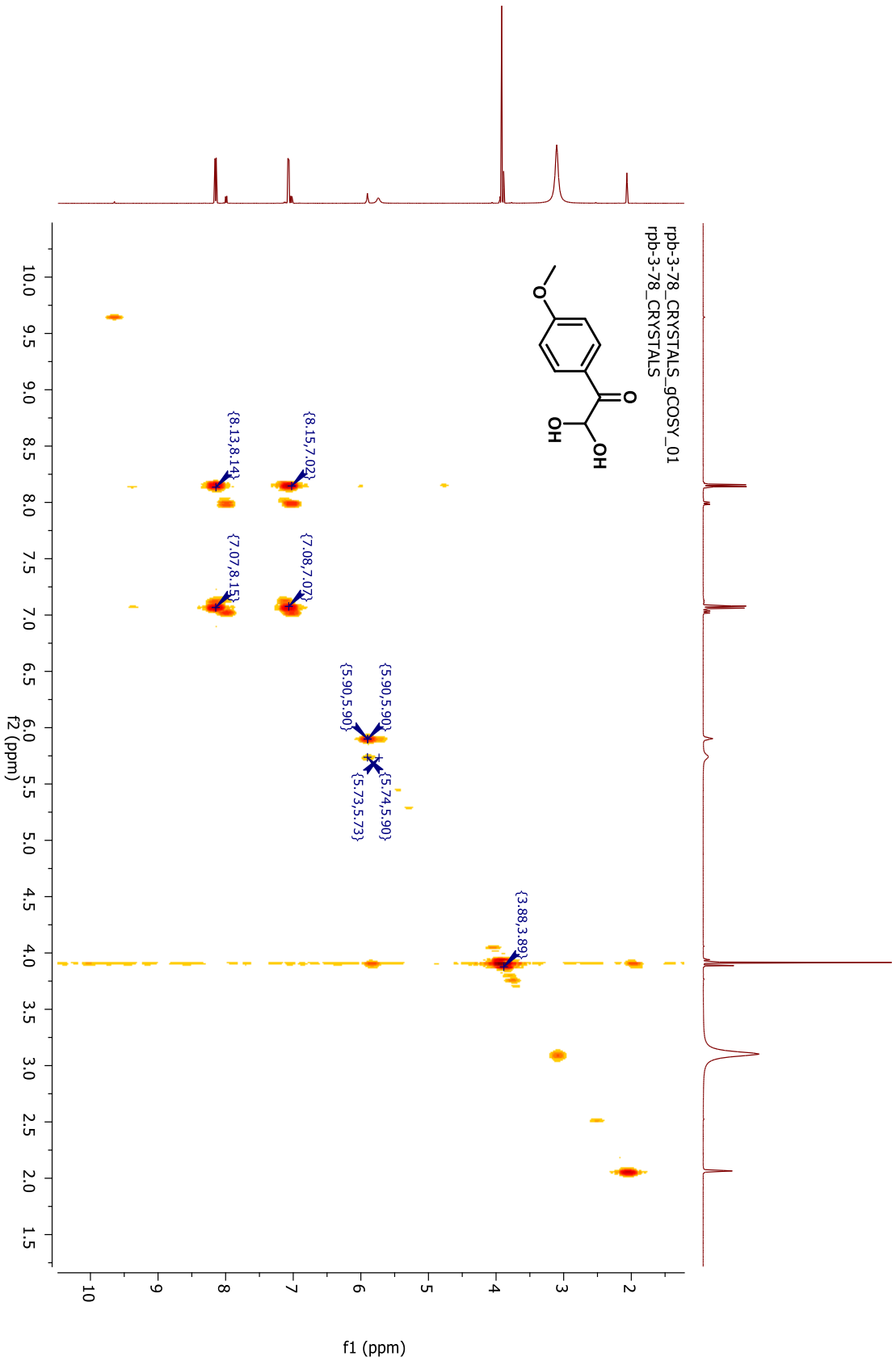
rpb-3-78_CRYSTALS_gCOSY_01
rpb-3-78_CRYSTALS
O
OH
OH
{8.13,8.14}
{8.15,7.02}
{7.07,8.15}
{7.08,7.07}
{5.90,5.90}
{5.90,5.90}
{5.74,5.90}
{5.73,5.73}
{3.88,3.89}
f2 (ppm)
f1 (ppm)

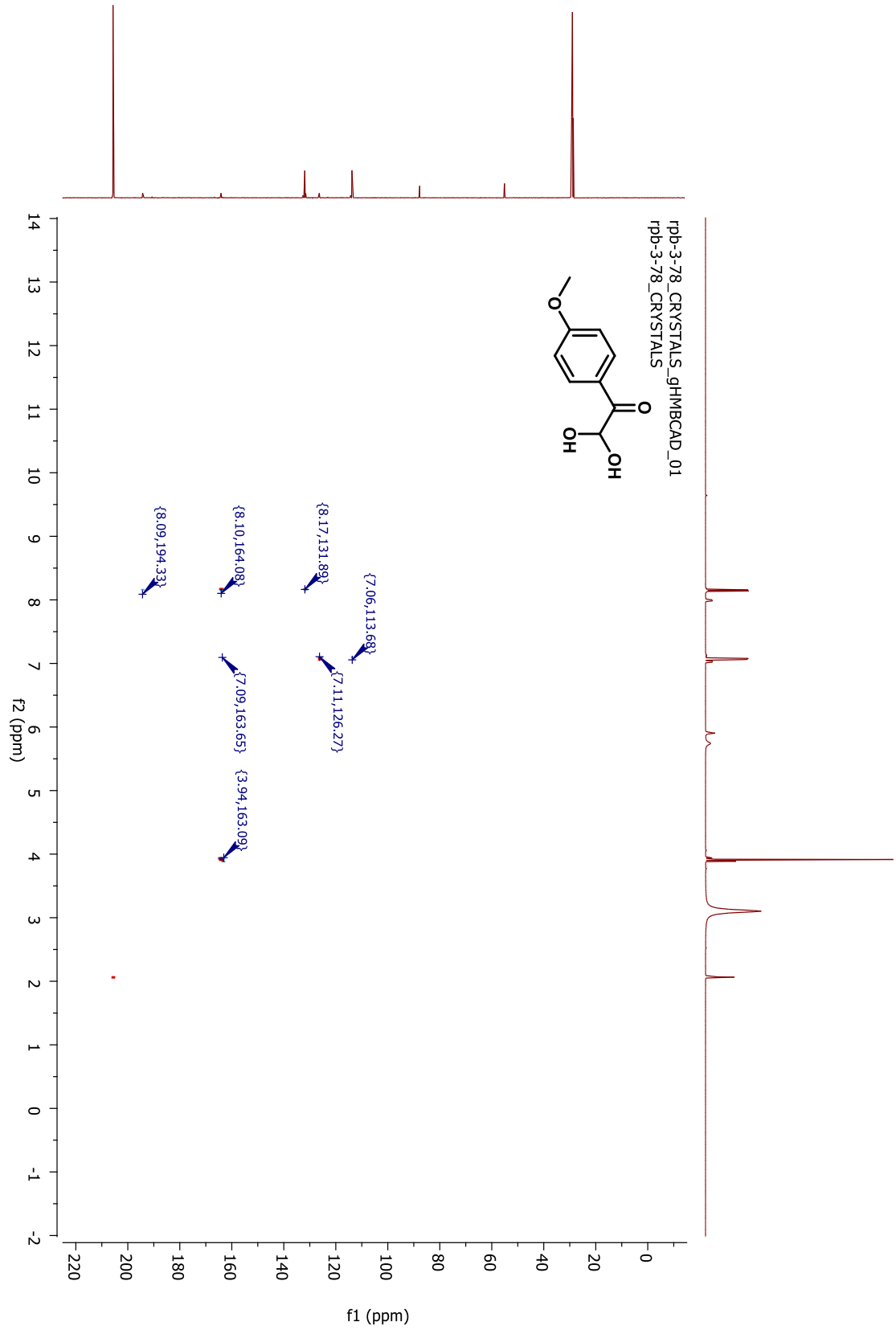
rpb-3-78_CRYSTALS_gHMBCAD_01
rpb-3-78_CRYSTALS
O
OH
OH
{8.09,194.33}
{8.10,164.08}
{8.17,131.89}
{7.06,113.68}
{7.09,163.65}
{7.11,126.27}
{3.94,163.09}
f2 (ppm)
f1 (ppm)

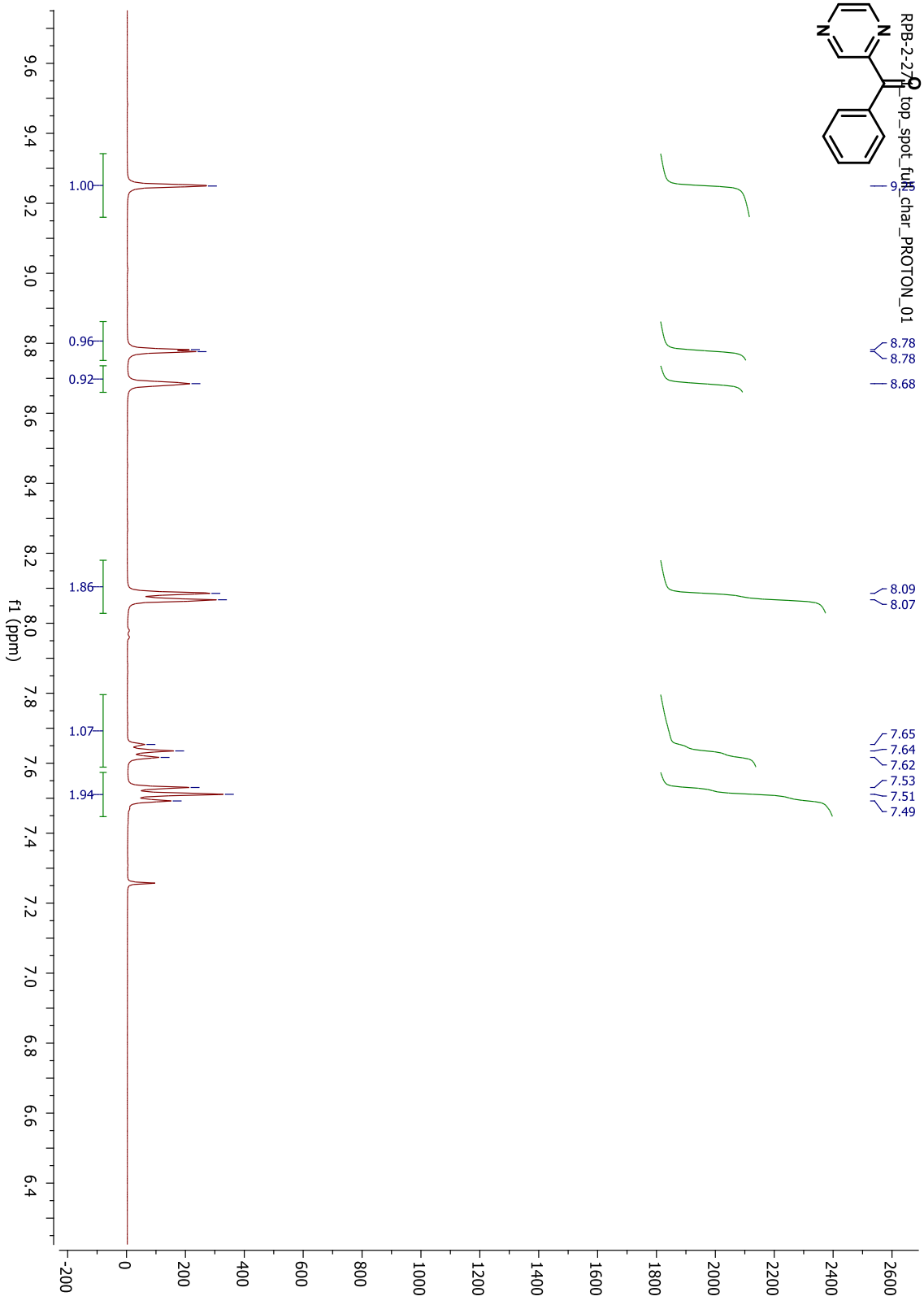
RPB-2-27_top_spot_fun_char_PROTON_01
f1 (ppm)
1.00
0.96
0.92
1.86
1.07
1.94
9.15
8.78
8.78
8.68
8.09
8.07
7.65
7.64
7.62
7.53
7.51
7.49

RPB-2-271_top_spot_full_char_CARBON_01

192.24
149.91
146.79
146.09
142.91
135.48
133.55
130.86
128.37

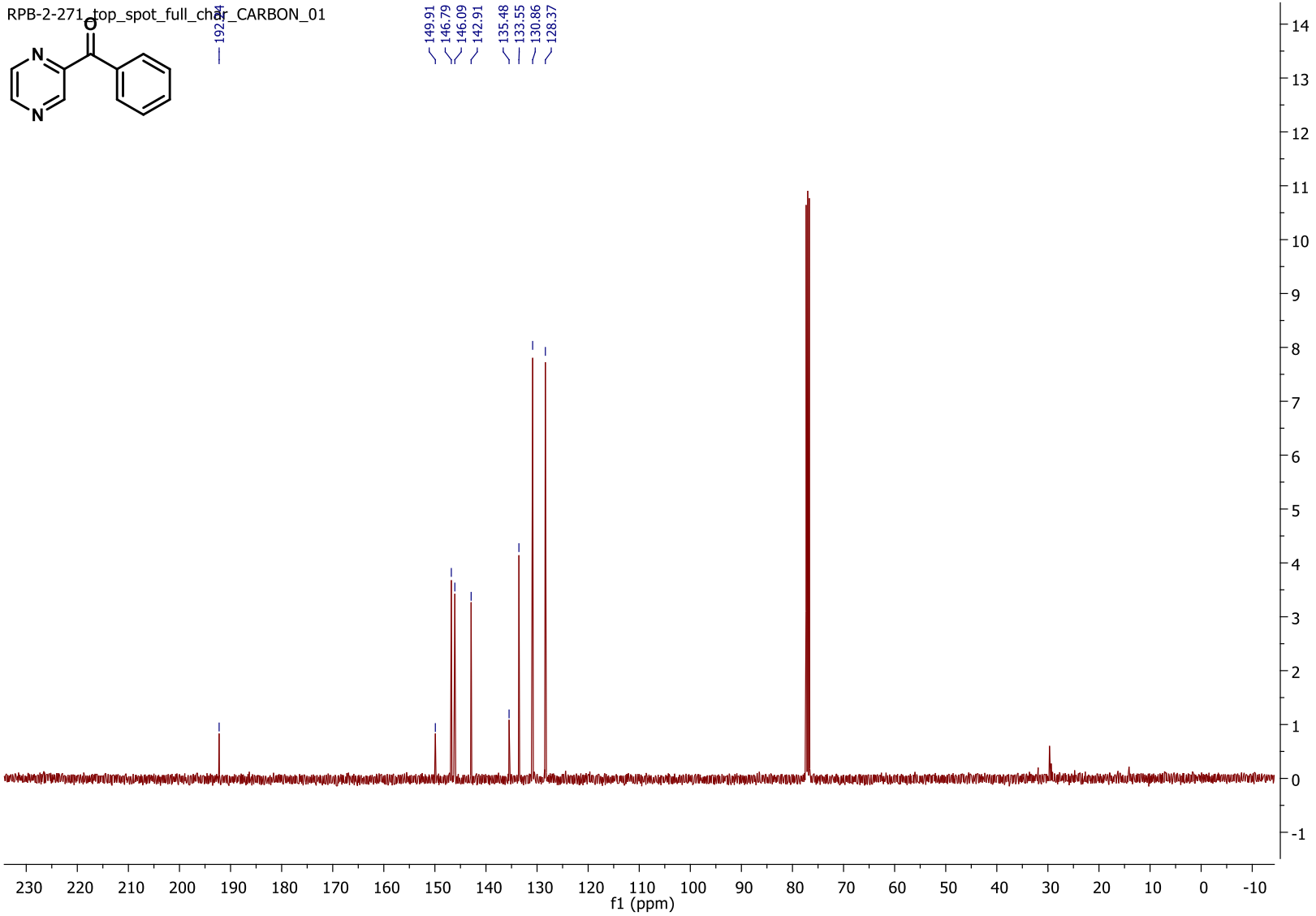

232

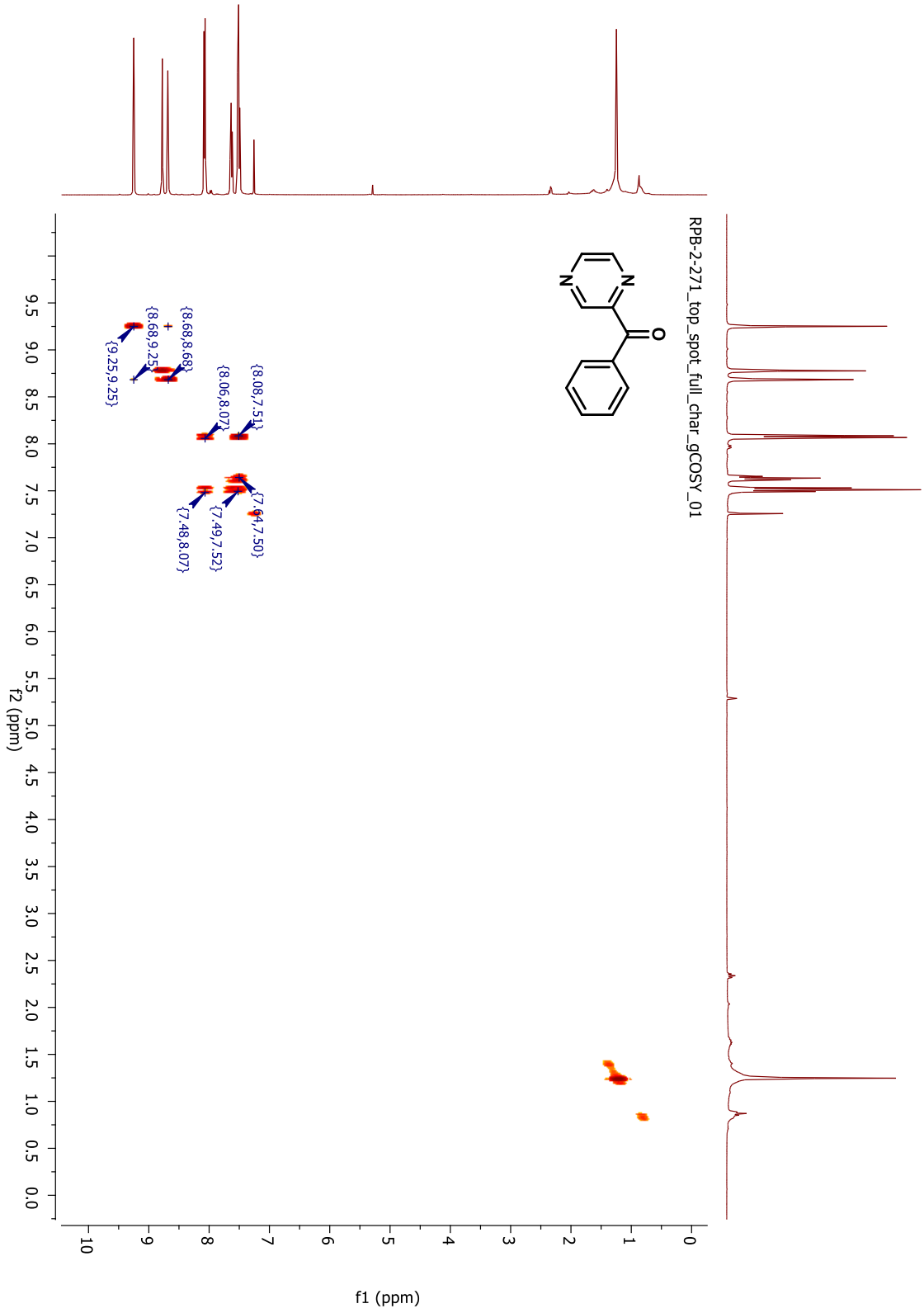
RPB-2-271_top_spot_full_char_gCOSY_01
{9.25,9.25}
{8.68,9.25}
{8.68,8.68}
{8.06,8.07}
{8.08,7.51}
{7.48,8.07}
{7.49,7.52}
{7.64,7.50}
f2 (ppm)
f1 (ppm)

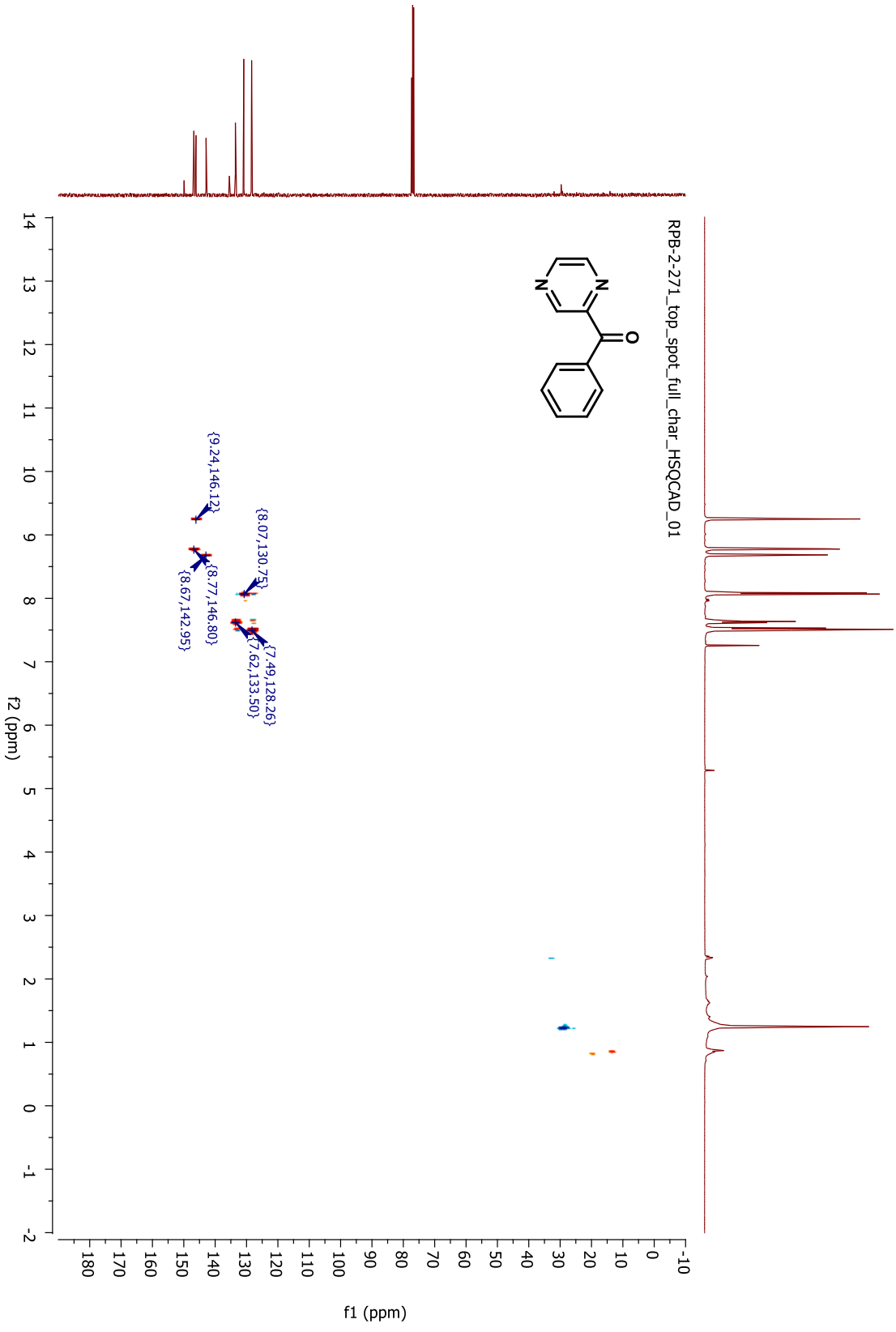
RPB-2-271_top_spot_full_char_HSQCAD_01
{9.24,146.12}
{8.77,146.80}
{8.67,142.95}
{8.07,130.75}
{7.62,133.50}
{7.49,128.26}
f1 (ppm)
f2 (ppm)

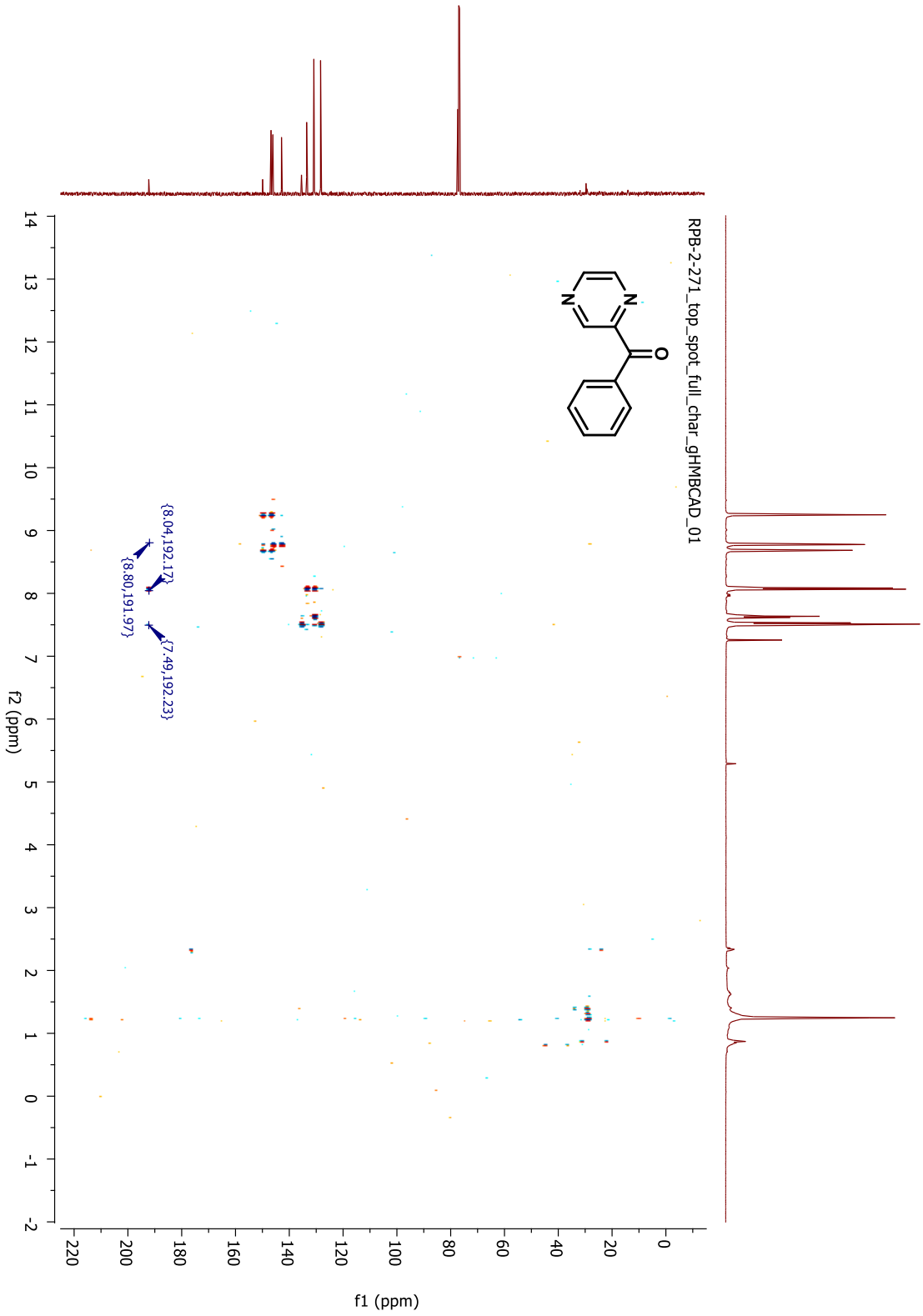
RPB-2-271_top_spot_full_char_gHMBCAD_01
{8.04,192.17}
{8.80,191.97}
{7.49,192.23}
f2 (ppm)
f1 (ppm)

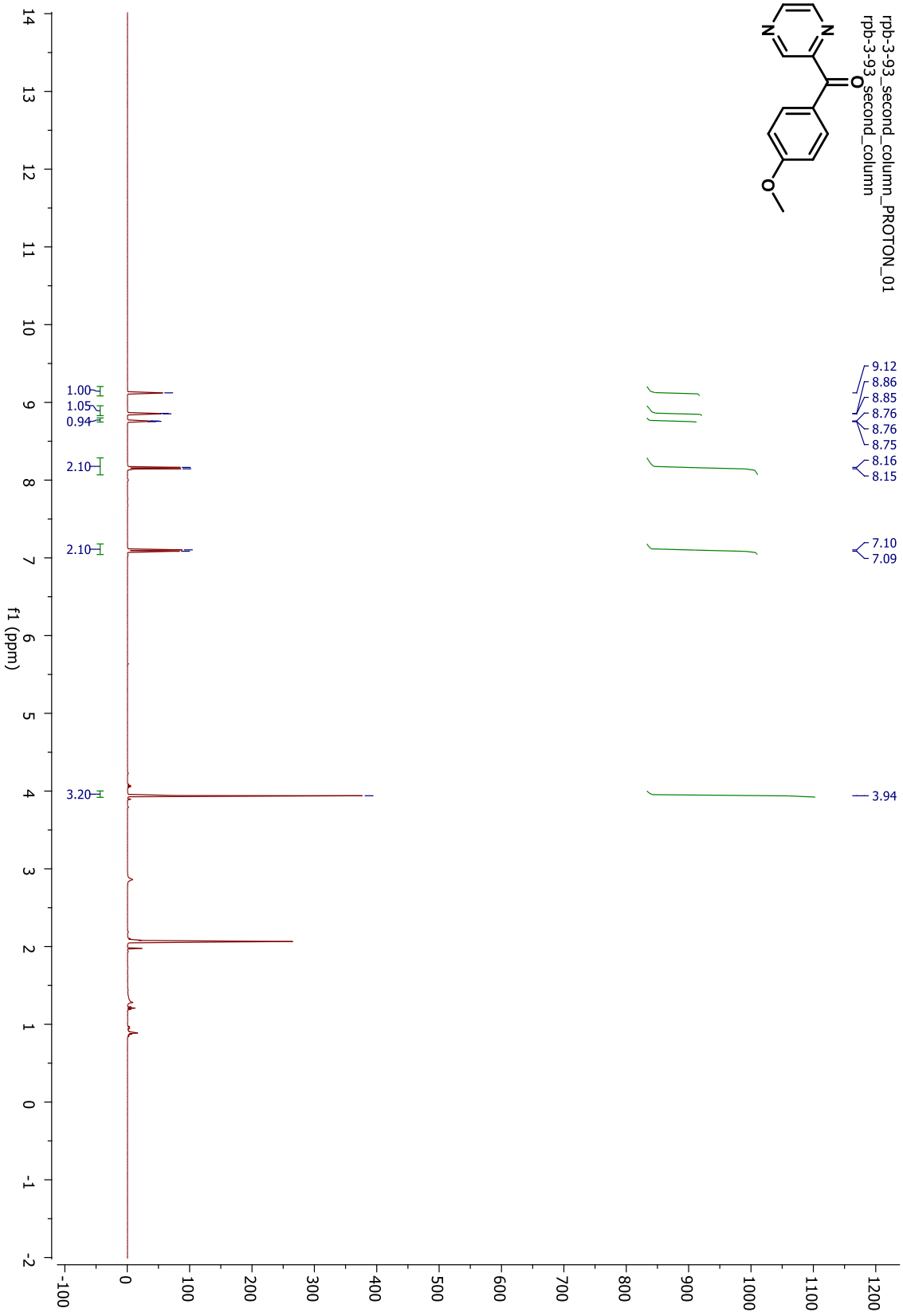
rpb-3-93_second_column_PROTON_01
rpb-3-93_second_column
O
N
N
O
9.12
8.86
8.85
8.76
8.76
8.75
8.16
8.15
7.10
7.09
3.94
1.00
1.05
0.94
2.10
2.10
3.20
f1 (ppm)

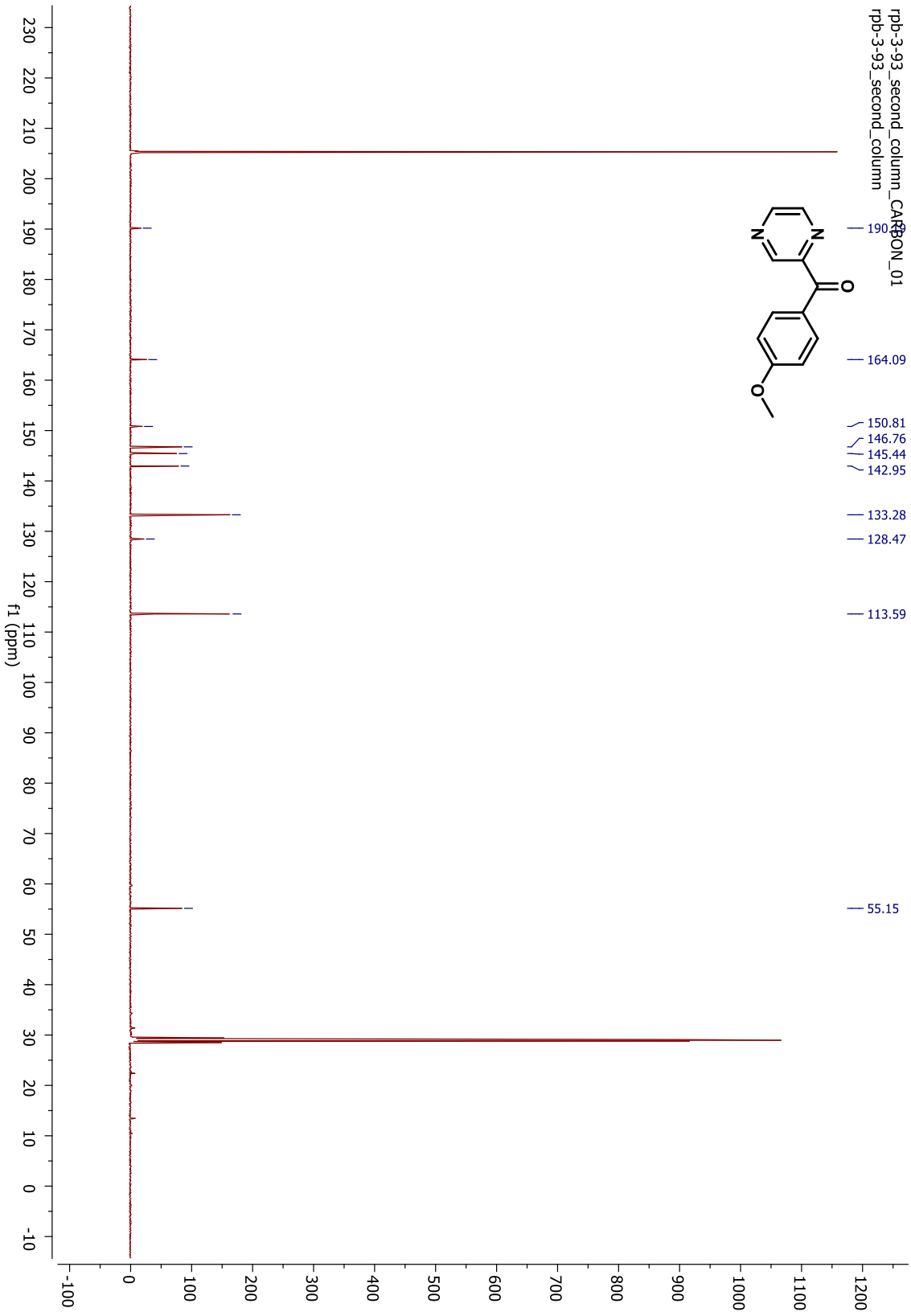
rpb-3-93_second_column_CARBON_01
rpb-3-93_second_column
190.79
164.09
150.81
146.76
145.44
142.95
133.28
128.47
113.59
55.15
f1 (ppm)

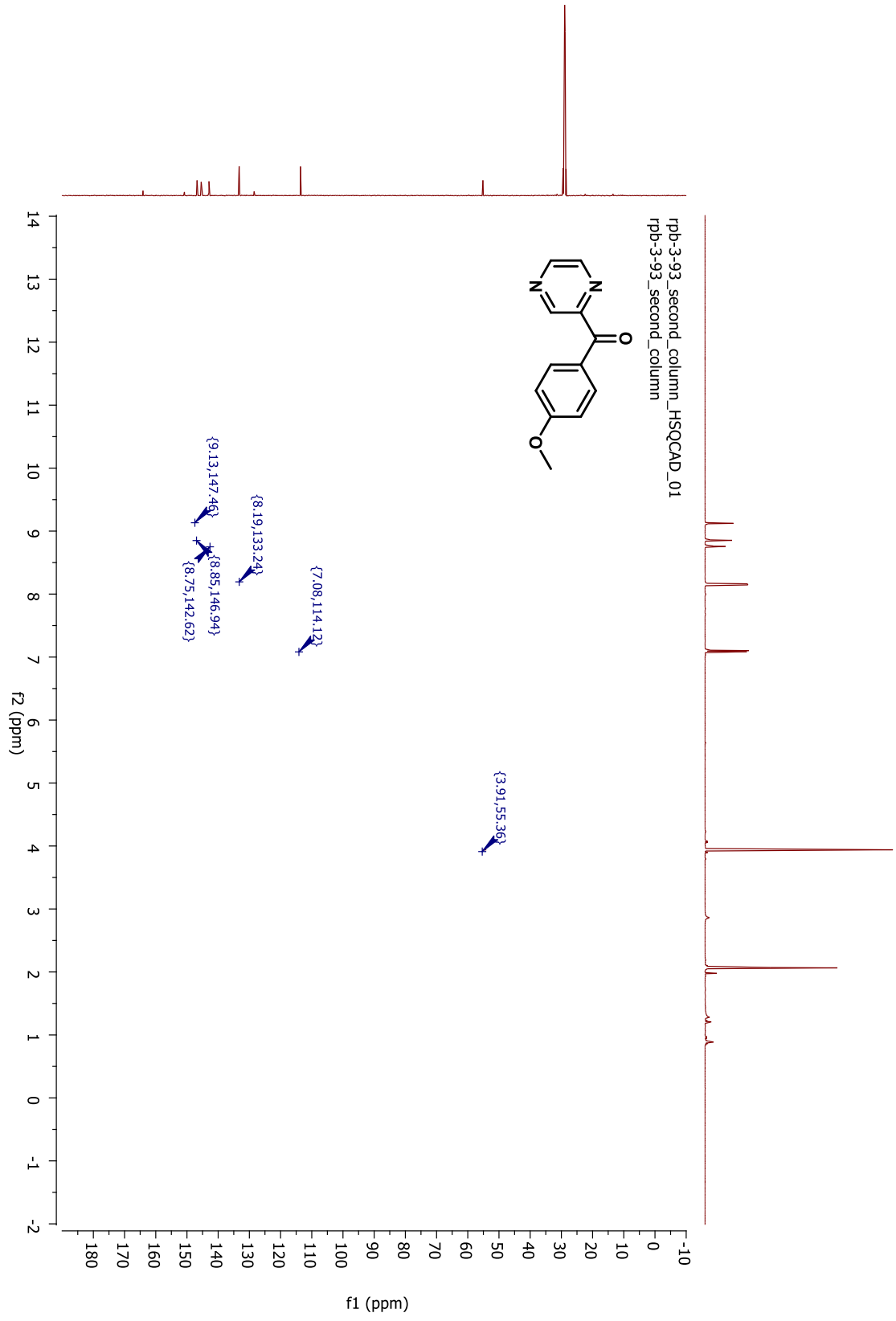
rpb-3-93_second_column_HSQCAD_01
rpb-3-93_second_column
{9.13,147.46}
{8.85,146.94}
{8.75,142.62}
{8.19,133.24}
{7.08,114.12}
{3.91,55.36}
f2 (ppm)
f1 (ppm)

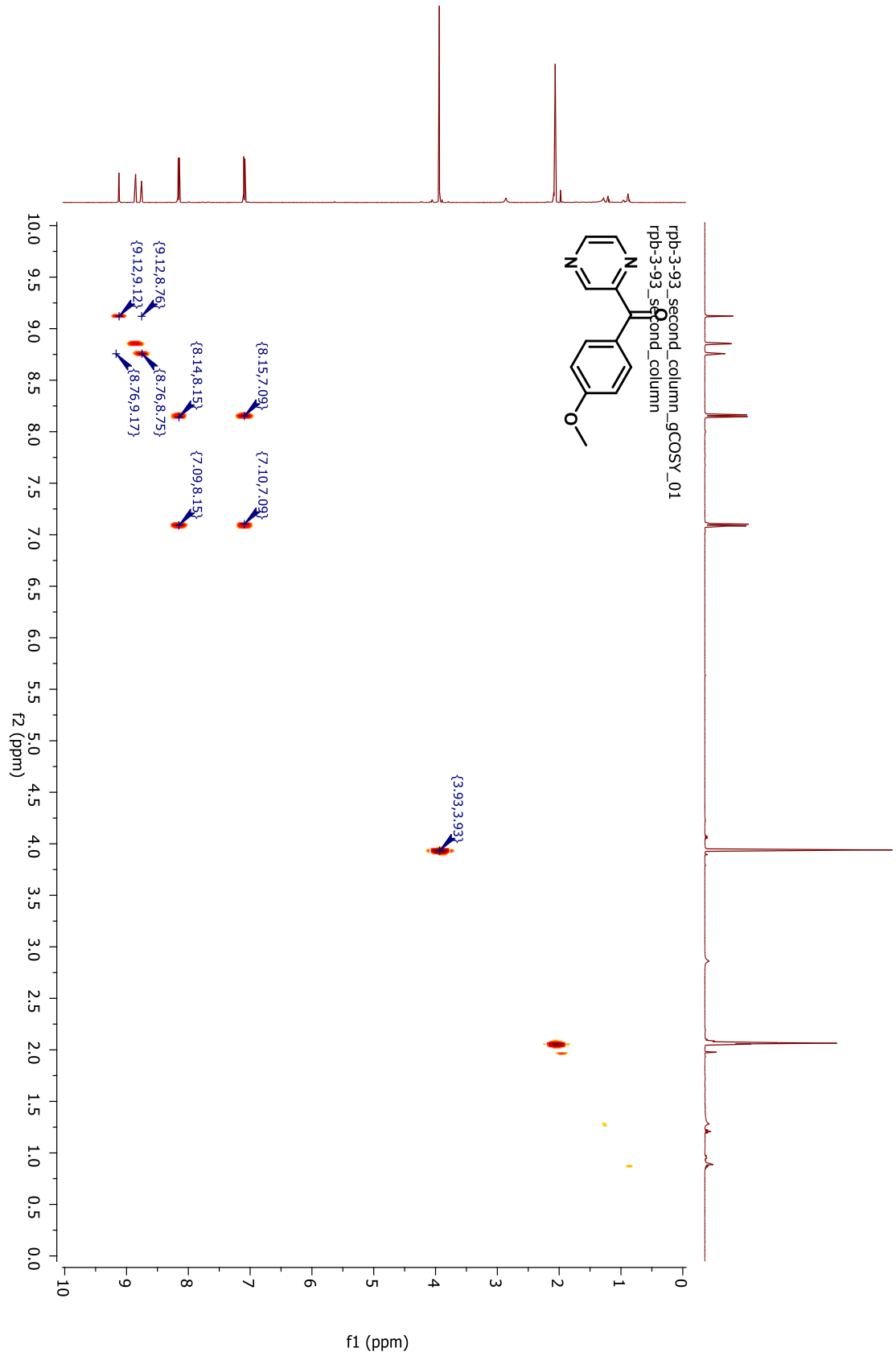
rpb-3-93_second_column_gCOSY_01
rpb-3-93_second_column
{9.12,8.76}
{9.12,9.12}
{8.76,8.75}
{8.76,9.17}
{8.14,8.15}
{8.15,7.09}
{7.09,8.15}
{7.10,7.09}
{3.93,3.93}
f2 (ppm)
f1 (ppm)

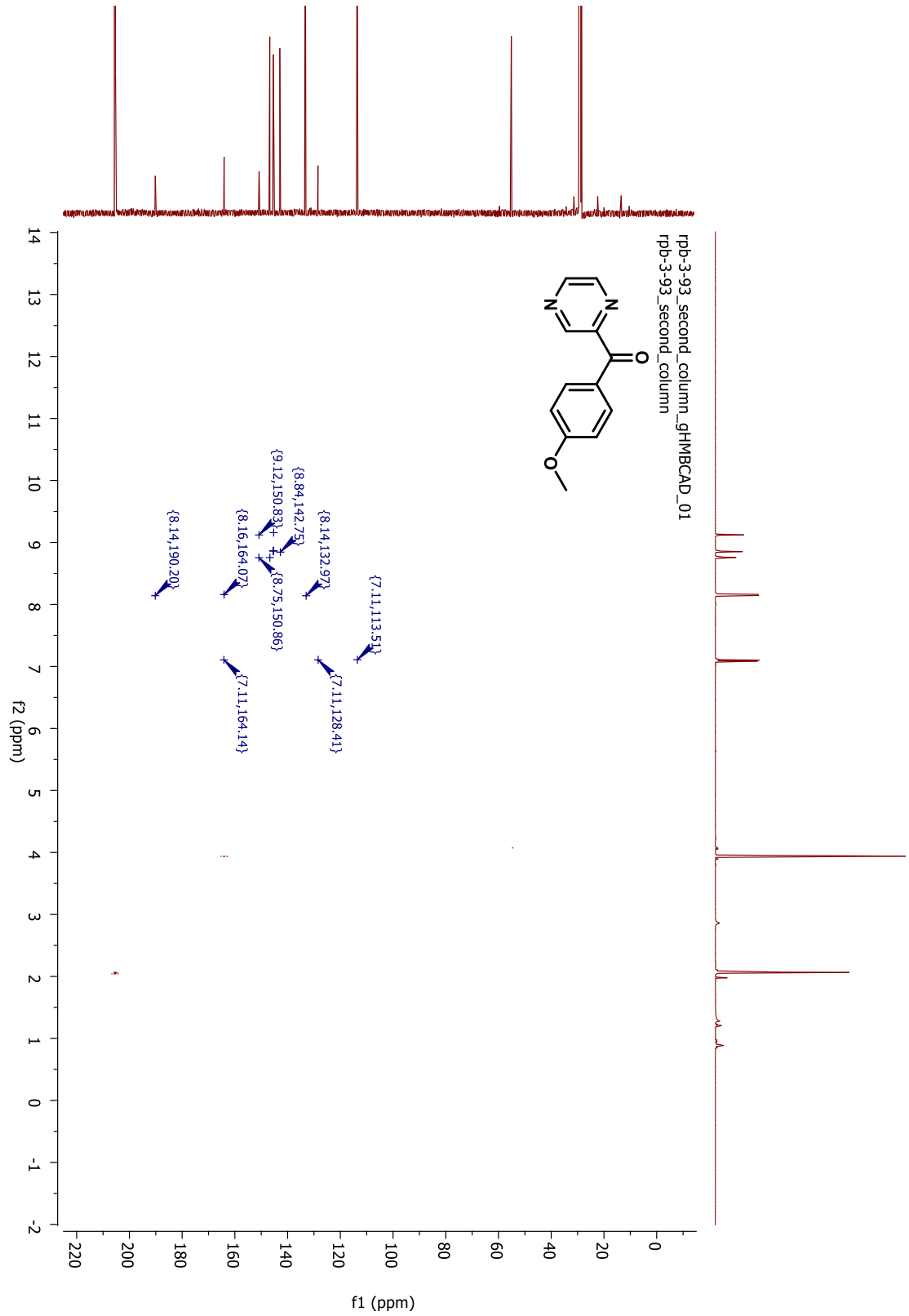
rpb-3-93_second_column_gHMBCAD_01
rpb-3-93_second_column
{8.14,190.20}
{8.16,164.07}
{9.12,150.83}
{8.84,142.75}
{8.75,150.86}
{8.14,132.97}
{7.11,113.51}
{7.11,164.14}
{7.11,128.41}
f2 (ppm)
f1 (ppm)

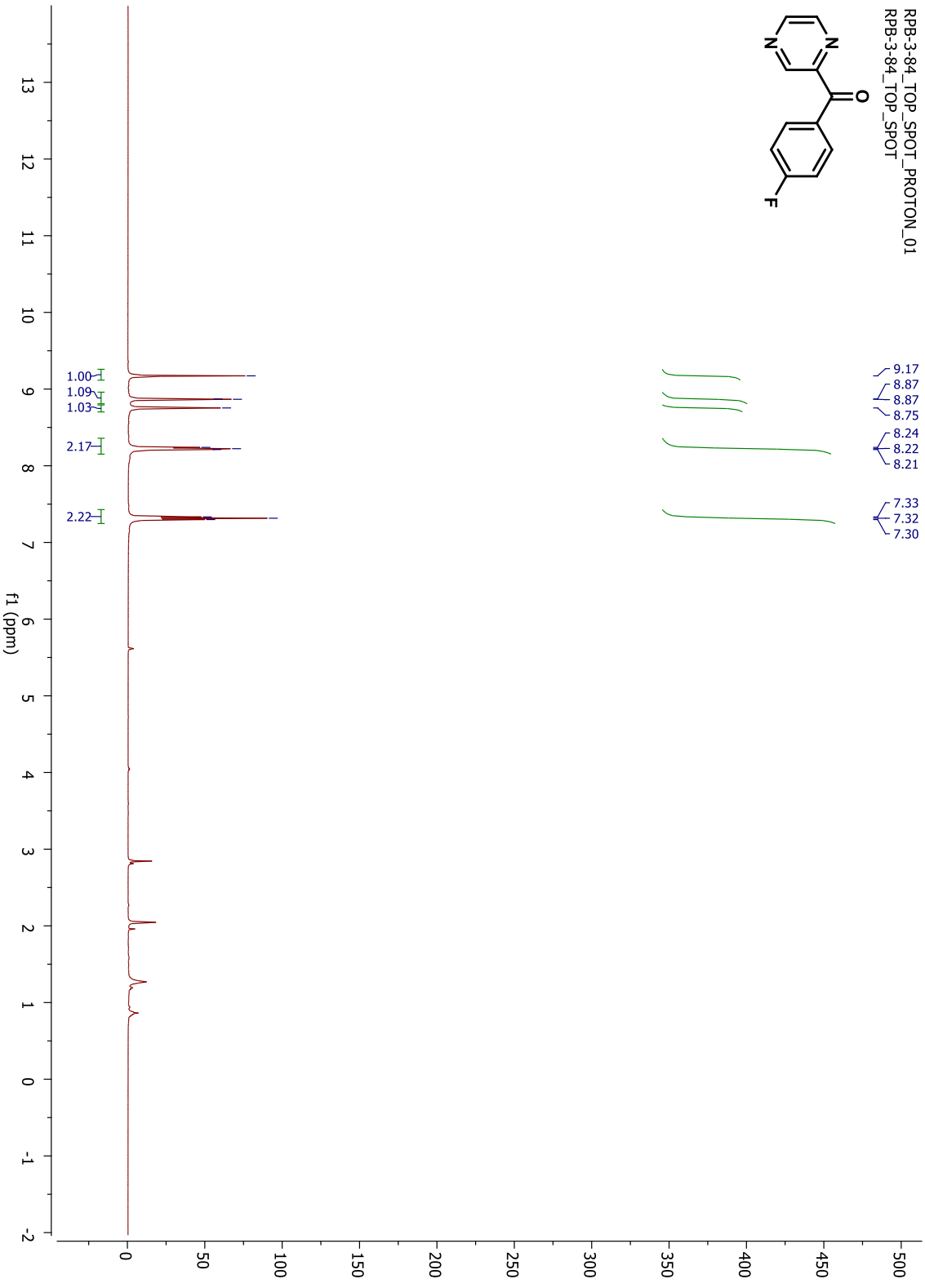
RPB-3-84_TOP_SPOT_PROTON_01
RPB-3-84_TOP_SPOT
O
N
N
F
9.17
8.87
8.87
8.75
8.24
8.22
8.21
7.33
7.32
7.30
1.00
1.09
1.03
2.17
2.22
f1 (ppm)

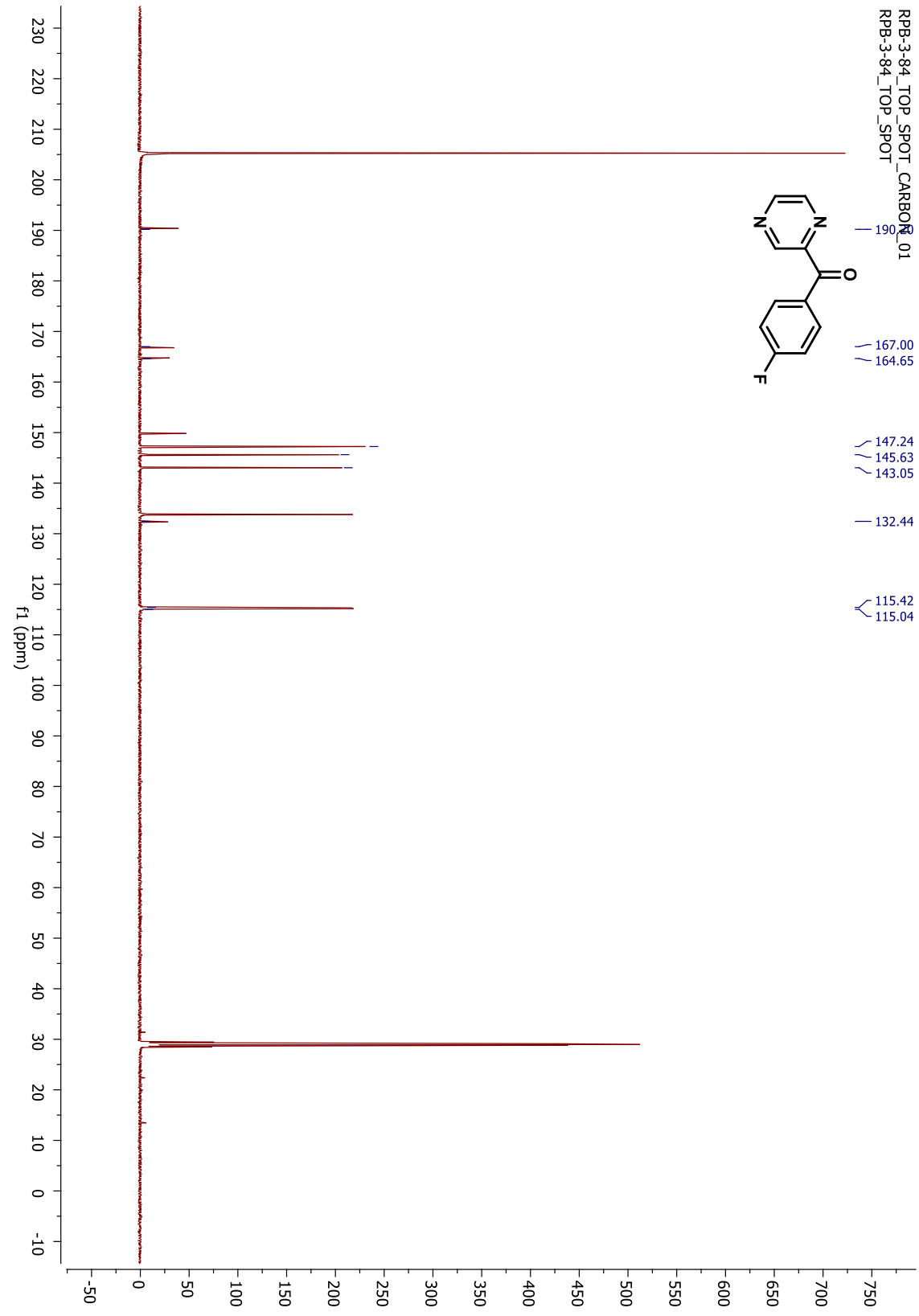
RPB-3-84_TOP_SPOT_CARBON_01
RPB-3-84_TOP_SPOT
190.42
167.00
164.65
147.24
145.63
143.05
132.44
115.42
115.04
f1 (ppm)

C

RPB-3-84_TOP_SPOT_FLUORINE_01
RPB-3-84_TOP_SPOT

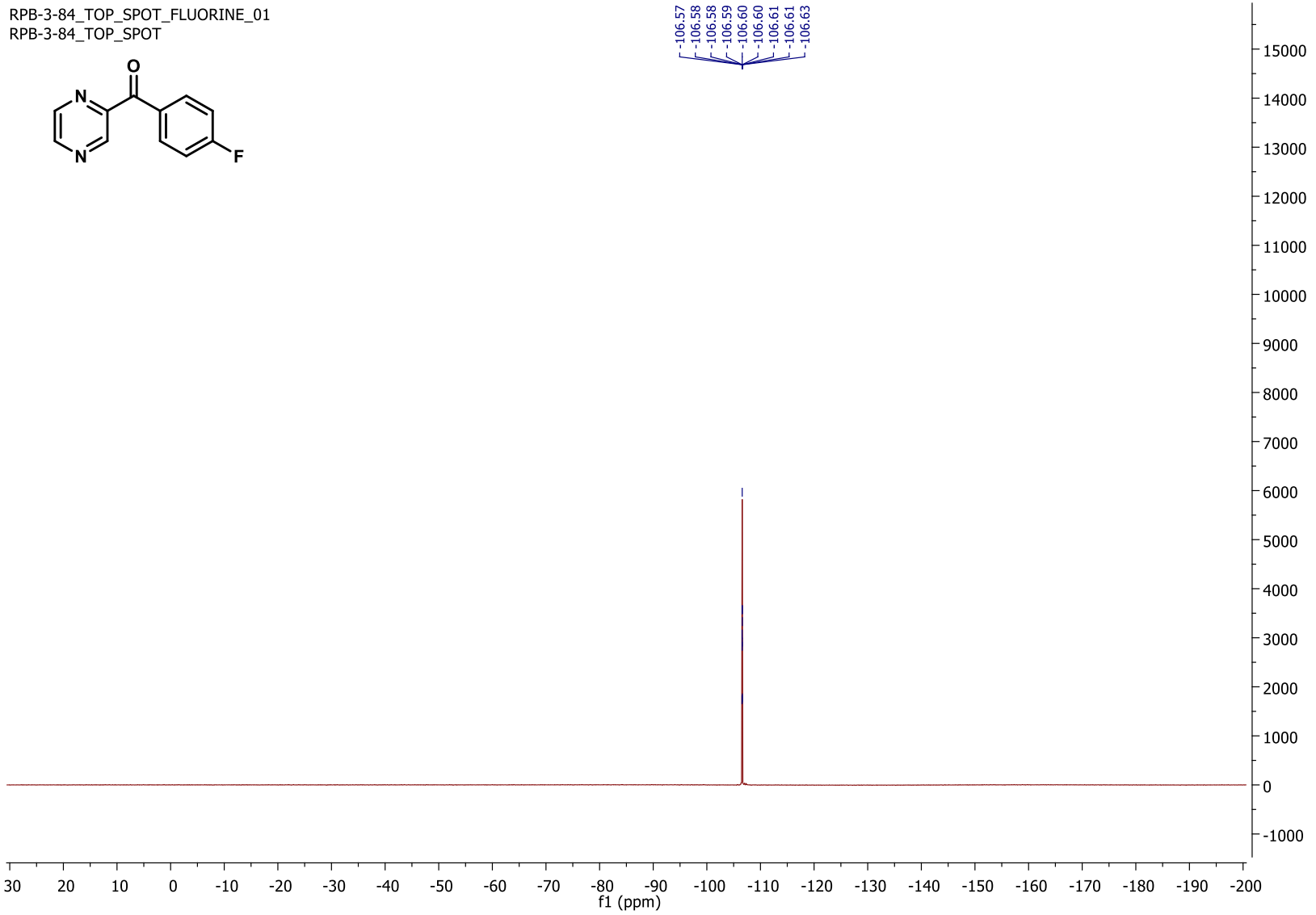

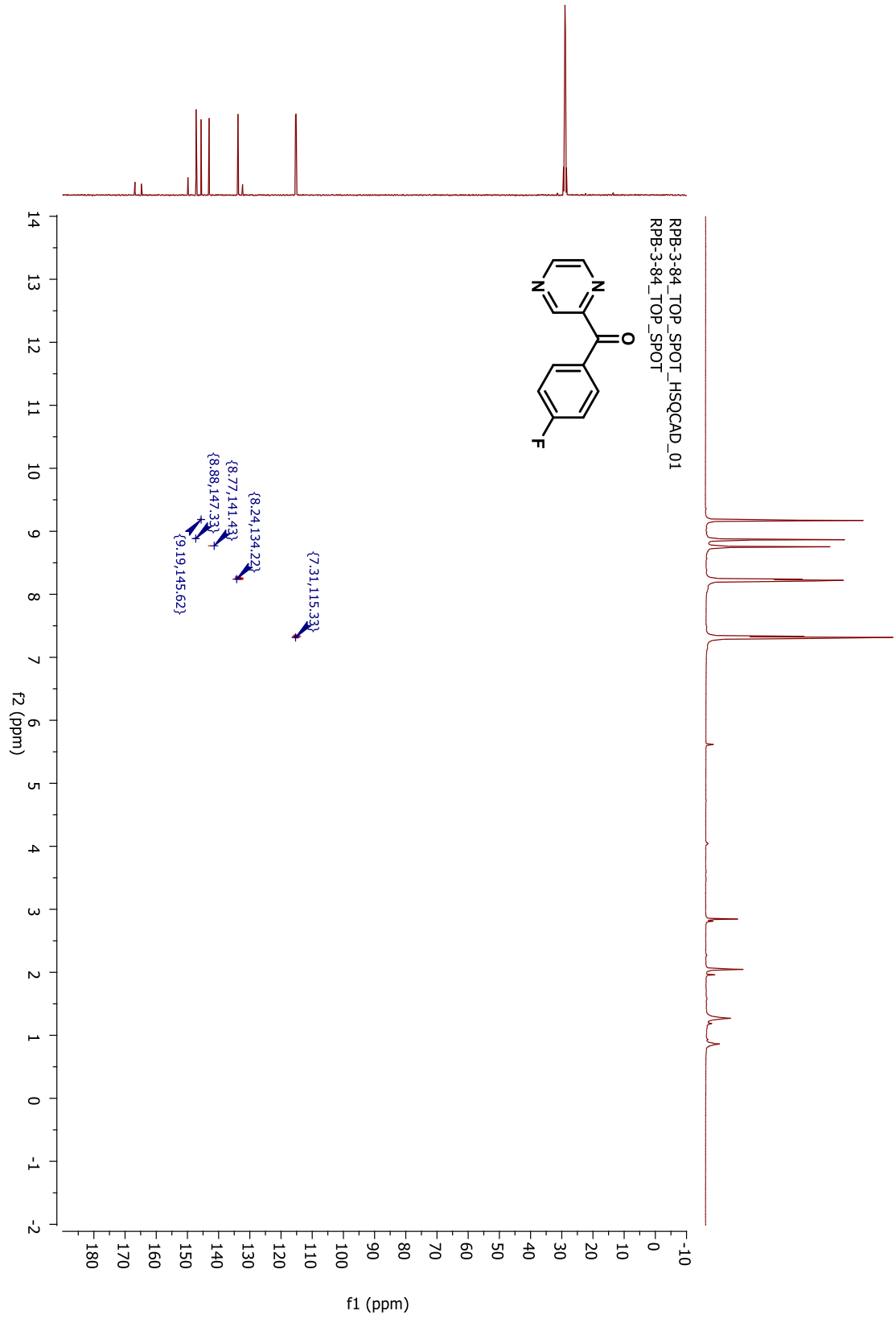
RPB-3-84_TOP_SPOT_HSQCAD_01
RPB-3-84_TOP_SPOT
N
N
O
F
{7.31,115.33}
{8.24,134.22}
{8.77,141.43}
{8.88,147.33}
{9.19,145.62}
f1 (ppm)
f2 (ppm)

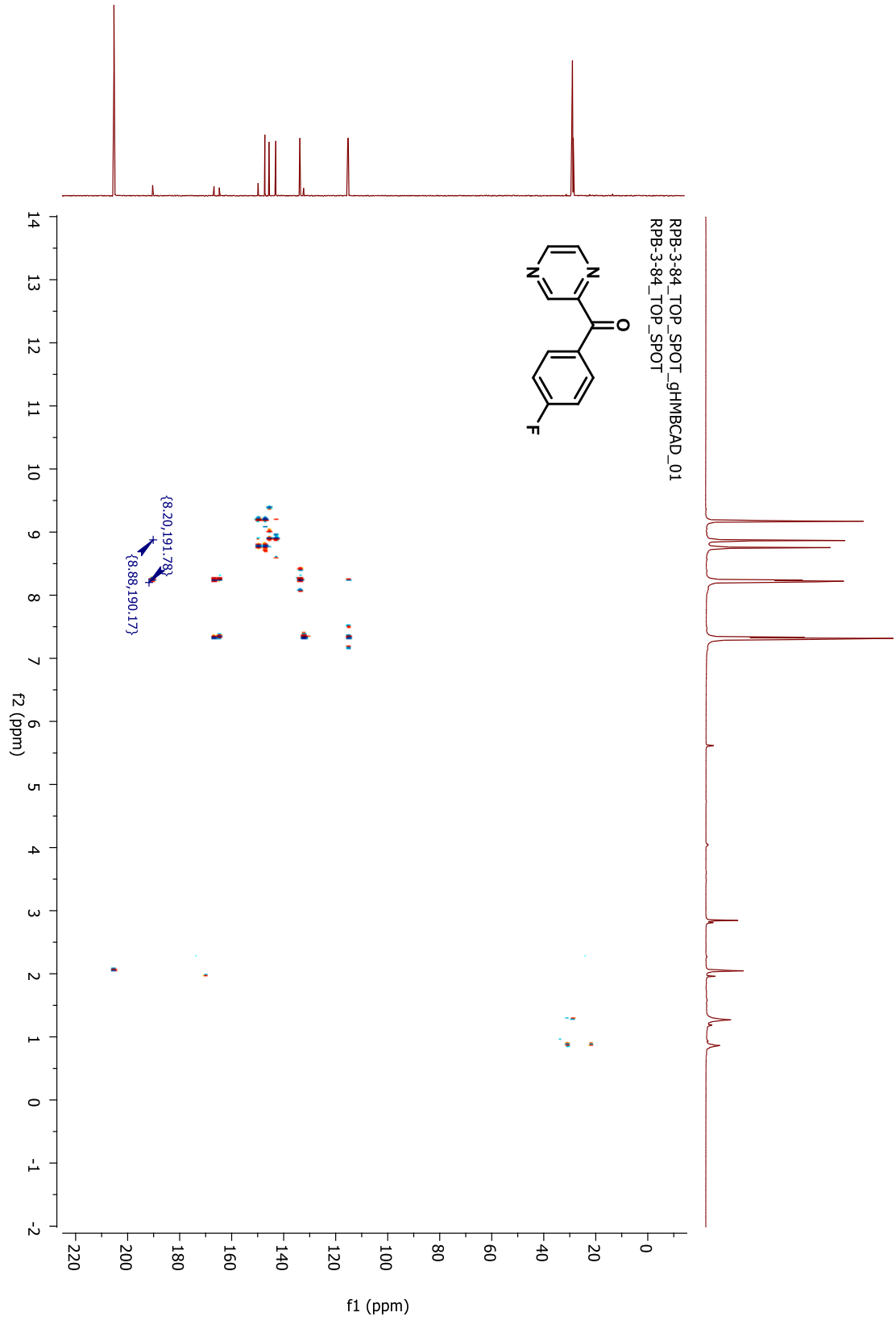
RPB-3-84_TOP_SPOT_gHMBCAD_01
RPB-3-84_TOP_SPOT
{8.20,191.78}
{8.88,190.17}
f1 (ppm)
f2 (ppm)

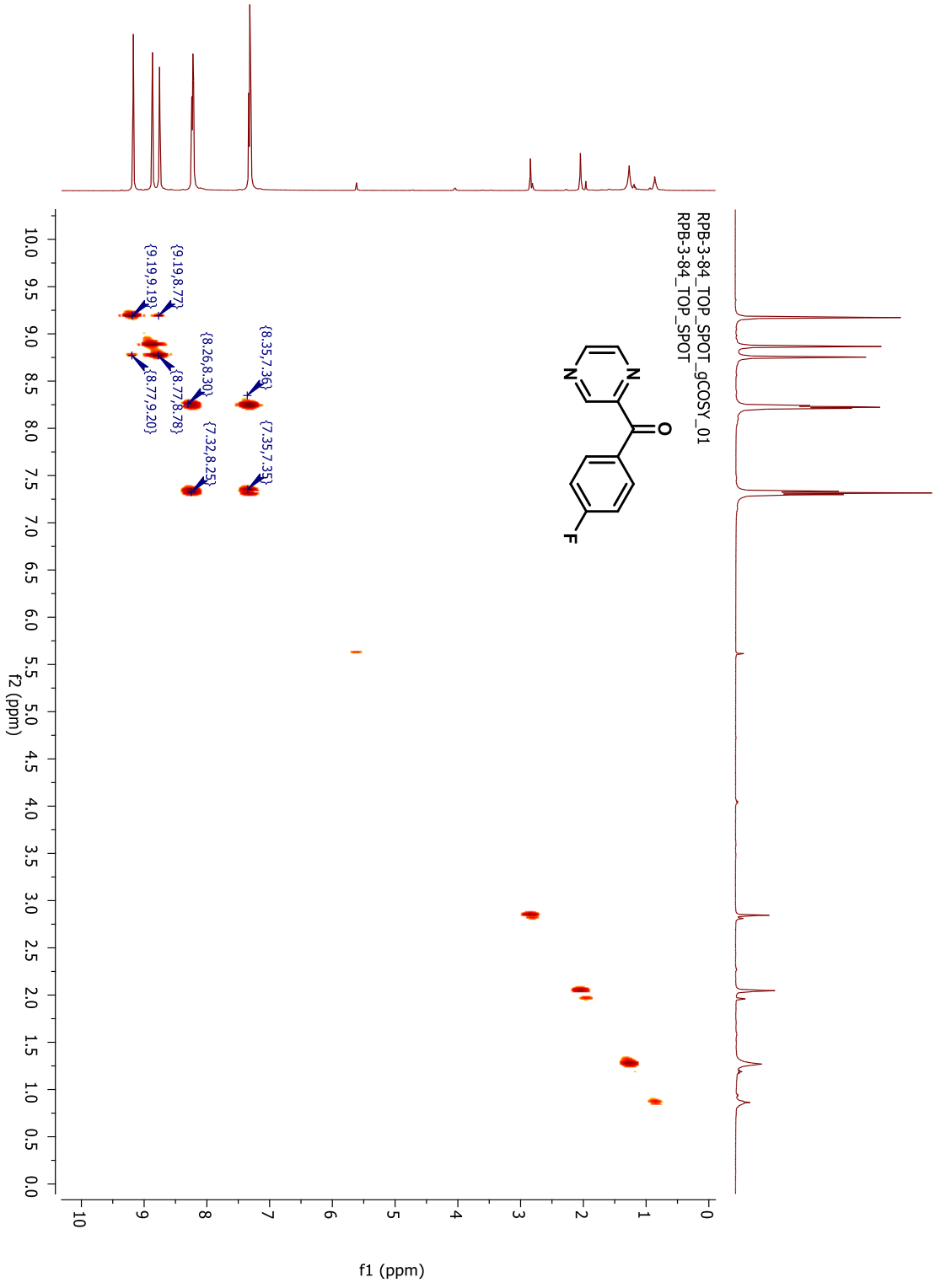
RPB-3-84_TOP_SPOT_gCOSY_01
RPB-3-84_TOP_SPOT
{9.19,9.19}
{9.19,8.77}
{8.77,9.20}
{8.77,8.78}
{8.26,8.30}
{7.32,8.25}
{8.35,7.36}
{7.35,7.35}
N
N
O
F
f2 (ppm)
f1 (ppm)

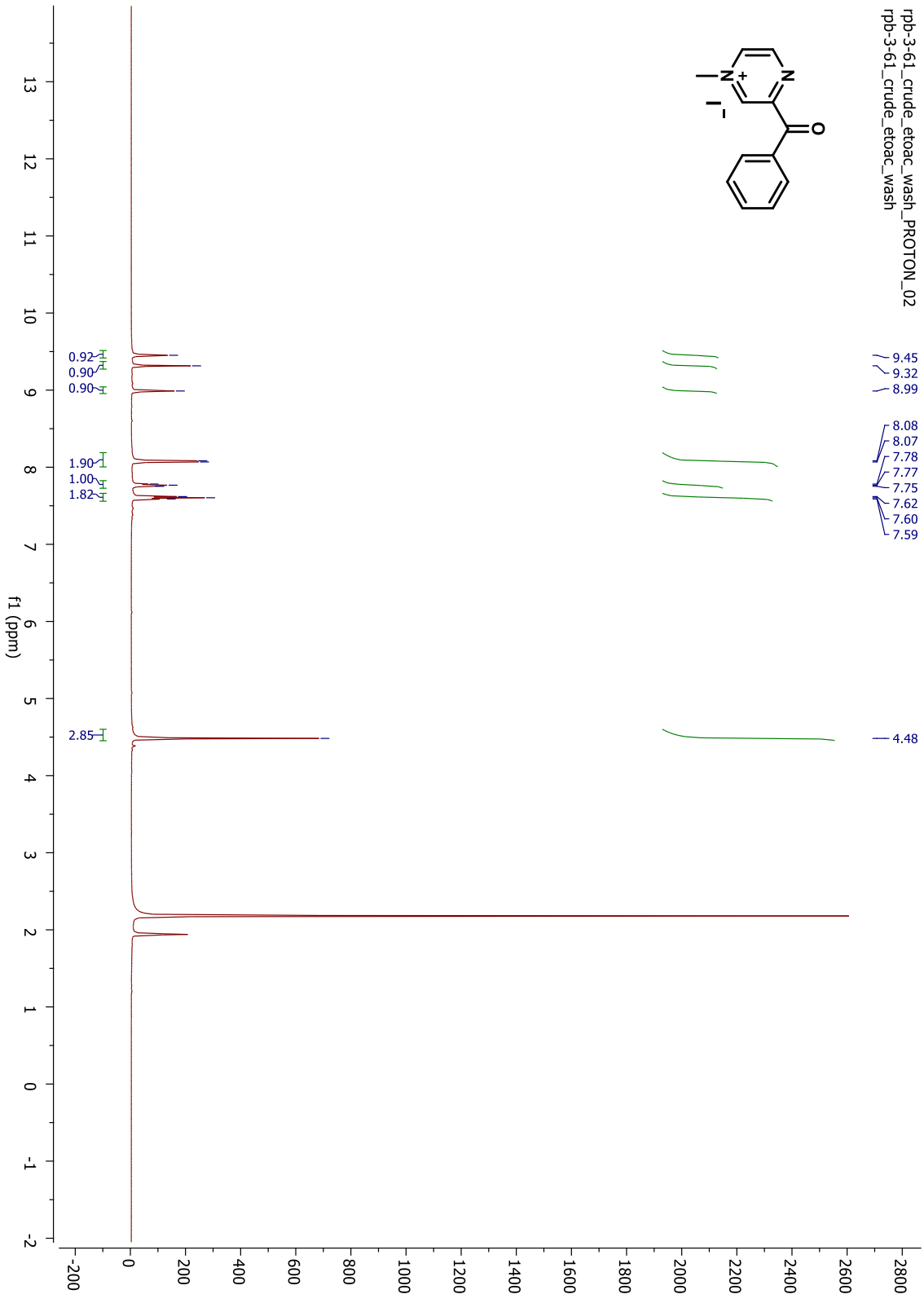
rpb-3-61_crude_etoac_wash_PROTON_02
rpb-3-61_crude_etoac_wash
f1 (ppm)
0.92
0.90
0.90
1.90
1.00
1.82
2.85
9.45
9.32
8.99
8.08
8.07
7.78
7.77
7.75
7.62
7.60
7.59
4.48

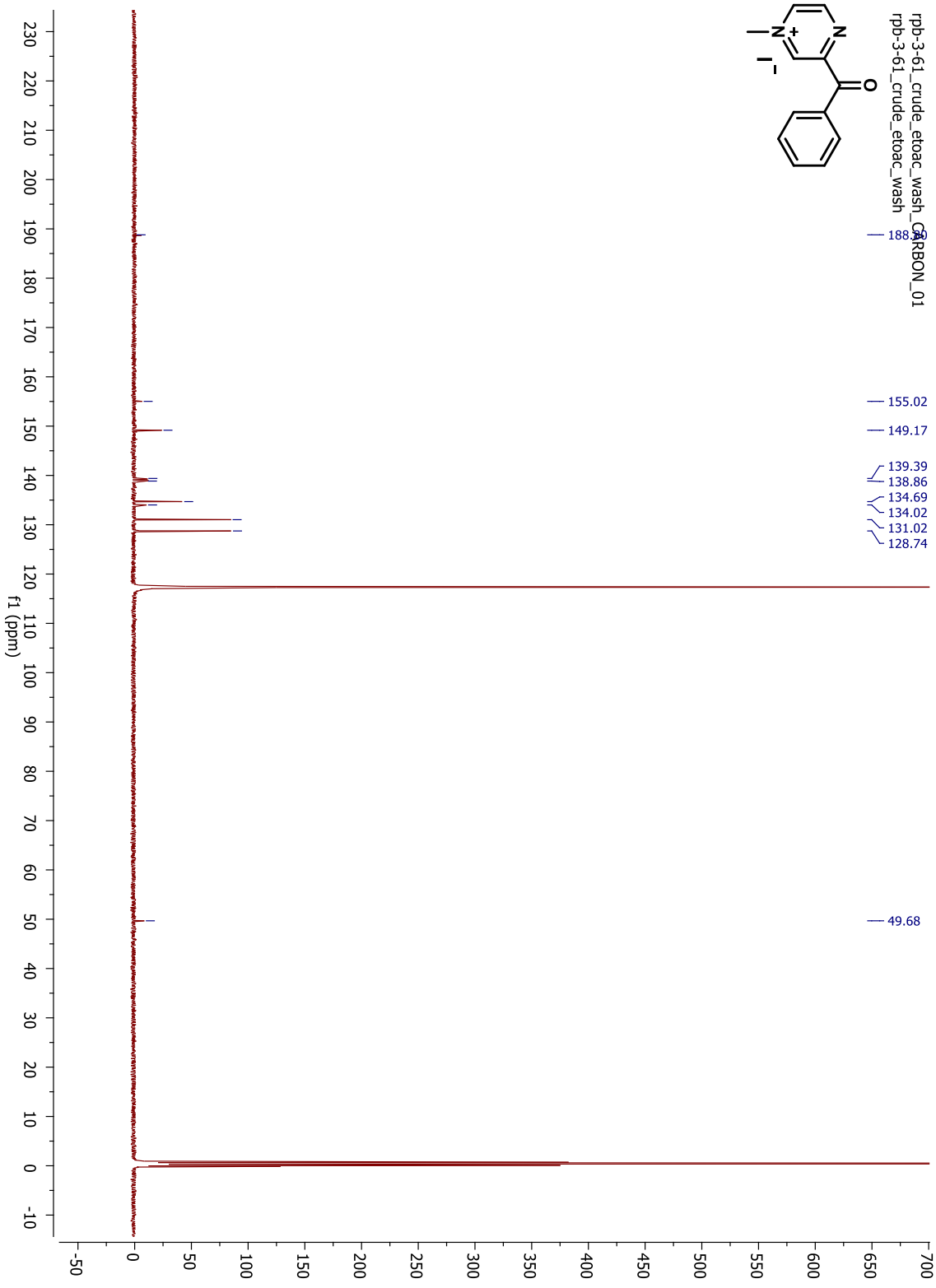
rpb-3-61_crude_etoac_wash_CARBON_01
rpb-3-61_crude_etoac_wash
188.30
155.02
149.17
139.39
138.86
134.69
134.02
131.02
128.74
49.68
f1 (ppm)

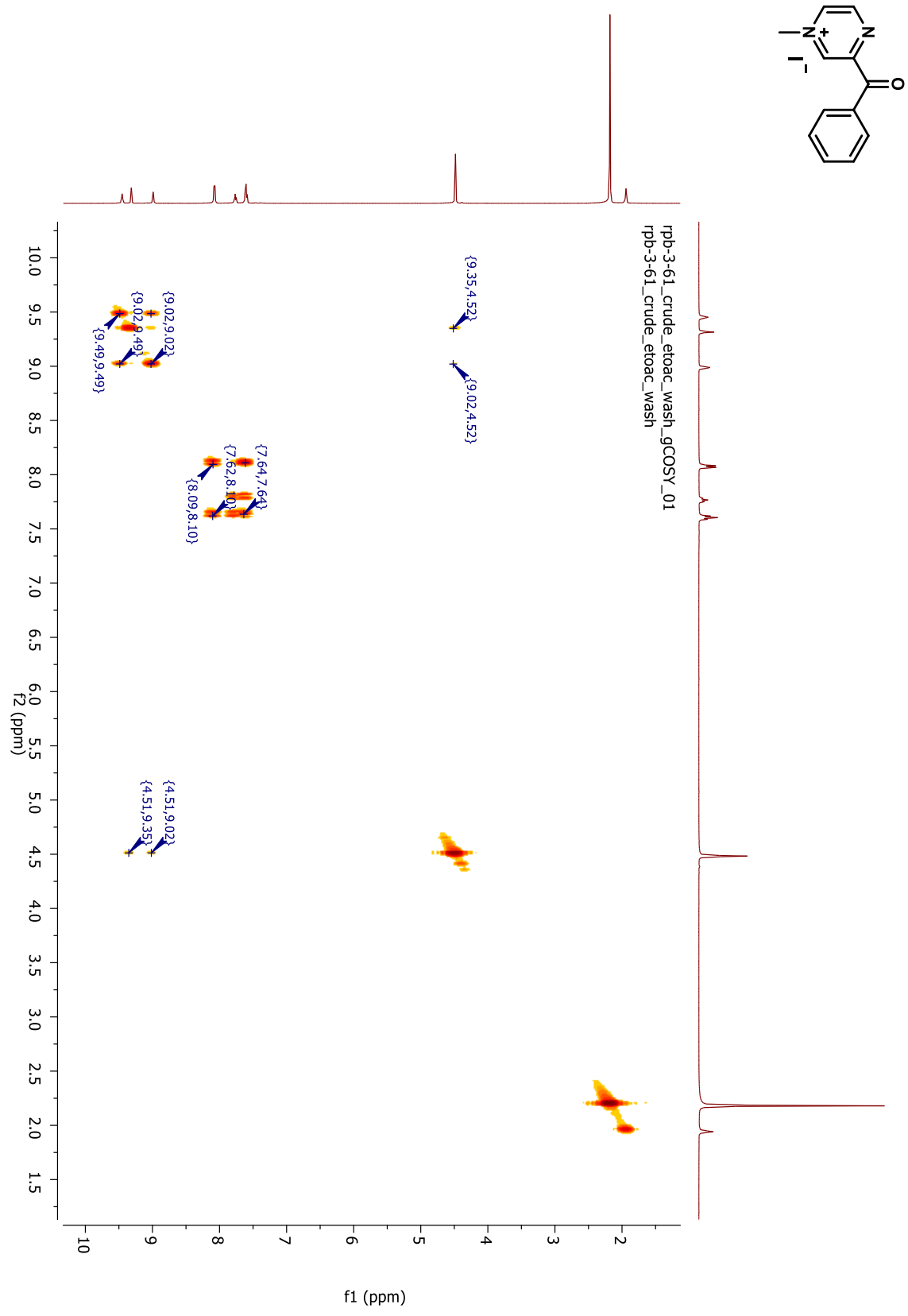
rpb-3-61_crude_etoac_wash_gCOSY_01
rpb-3-61_crude_etoac_wash
{9.35,4.52}
{9.02,4.52}
{9.02,9.02}
{9.02,9.49}
{9.49,9.49}
{7.64,7.64}
{7.62,8.10}
{8.09,8.10}
{4.51,9.02}
{4.51,9.35}
f2 (ppm)
f1 (ppm)

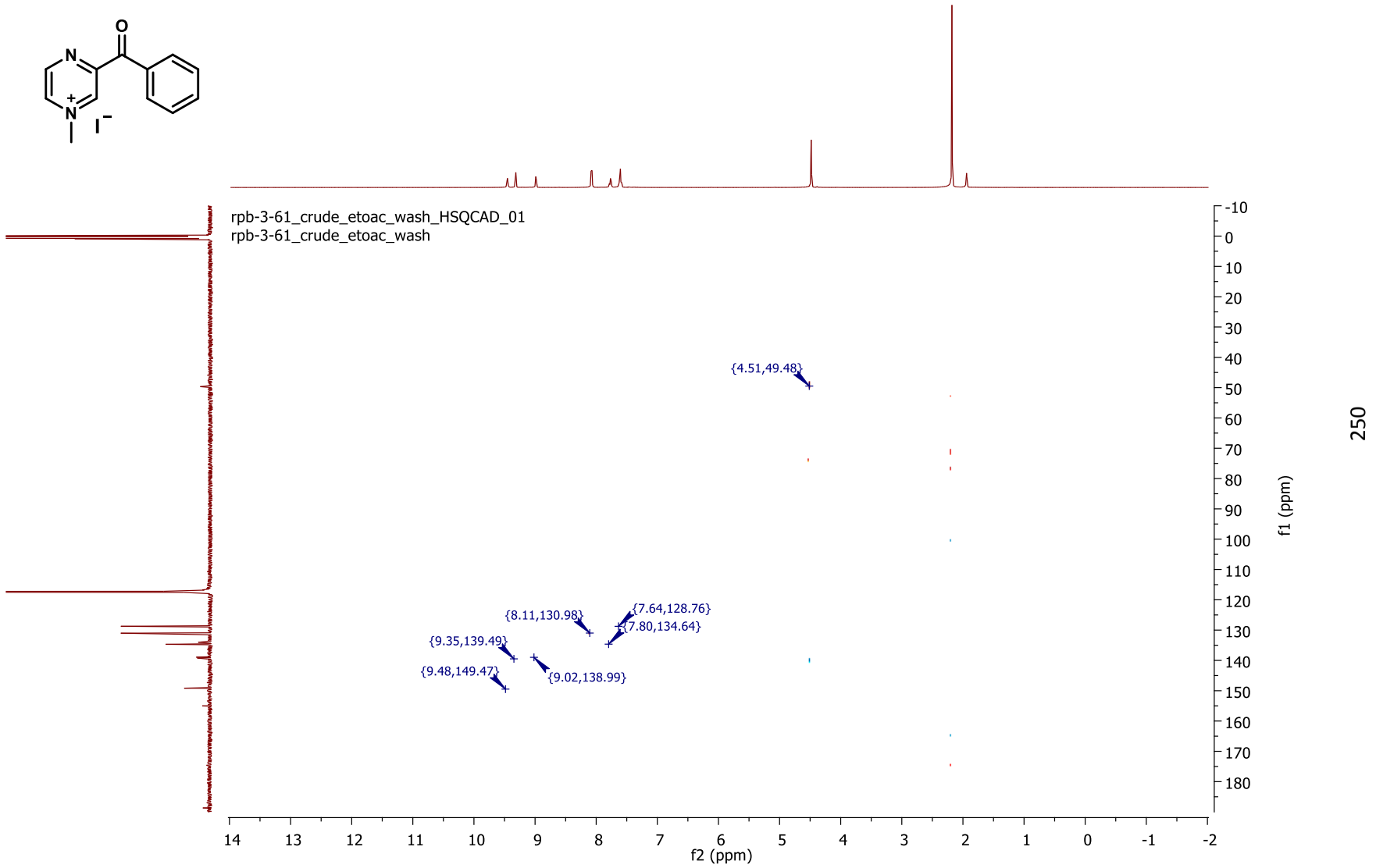
rpb-3-61_crude_etoac_wash_HSQCAD_01
rpb-3-61_crude_etoac_wash
{4.51,49.48}
{8.11,130.98}
{7.64,128.76}
{7.80,134.64}
{9.35,139.49}
{9.48,149.47}
{9.02,138.99}
f2 (ppm)
f1 (ppm)
250

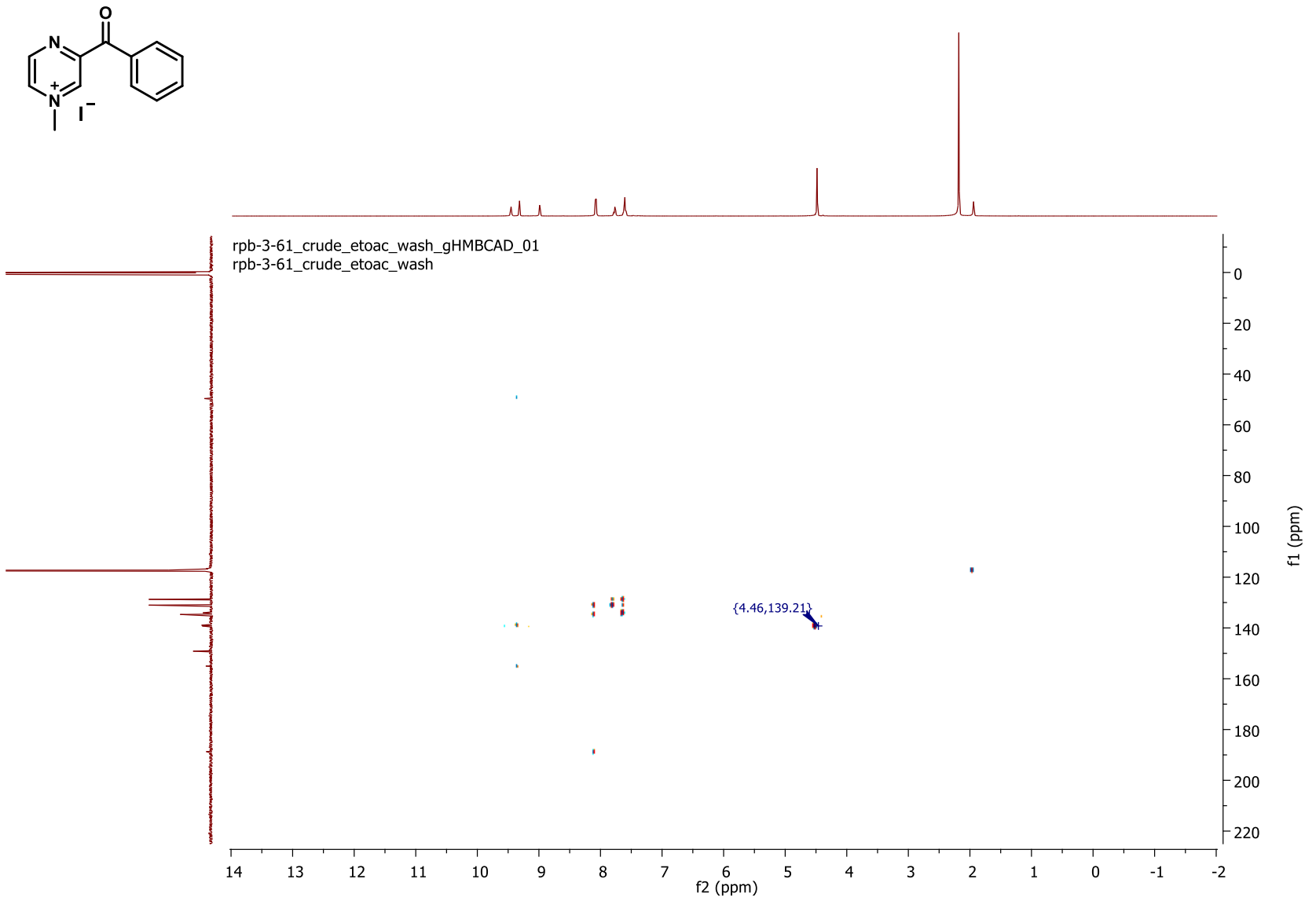
rpb-3-61_crude_etoac_wash_gHMBCAD_01
rpb-3-61_crude_etoac_wash
{4.46,139.21}
f2 (ppm)
f1 (ppm)

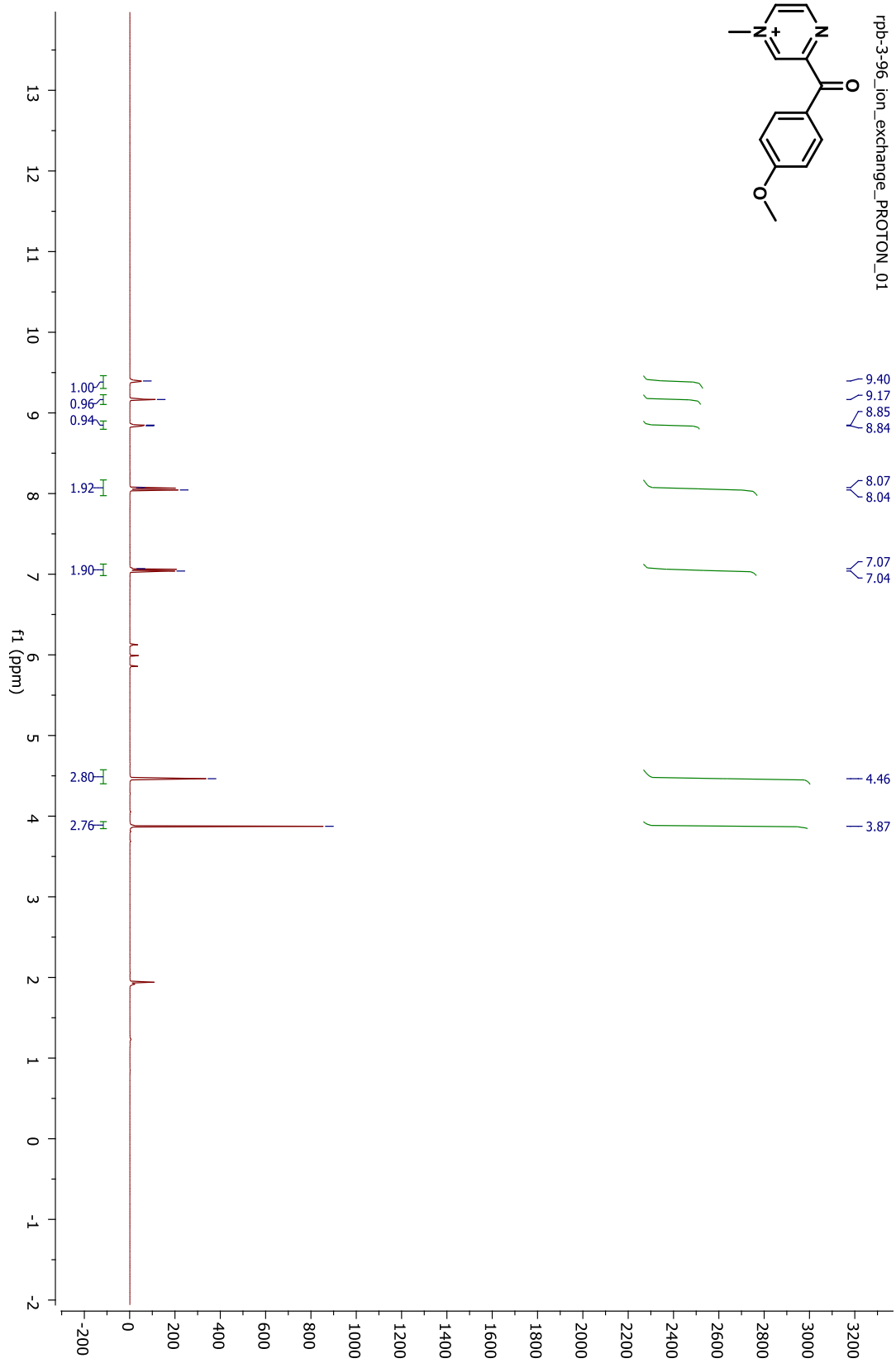
rpb-3-96_ion_exchange_PROTON_01
f1 (ppm)
1.00
0.96
0.94
1.92
1.90
2.80
2.76
9.40
9.17
8.85
8.84
8.07
8.04
7.07
7.04
4.46
3.87

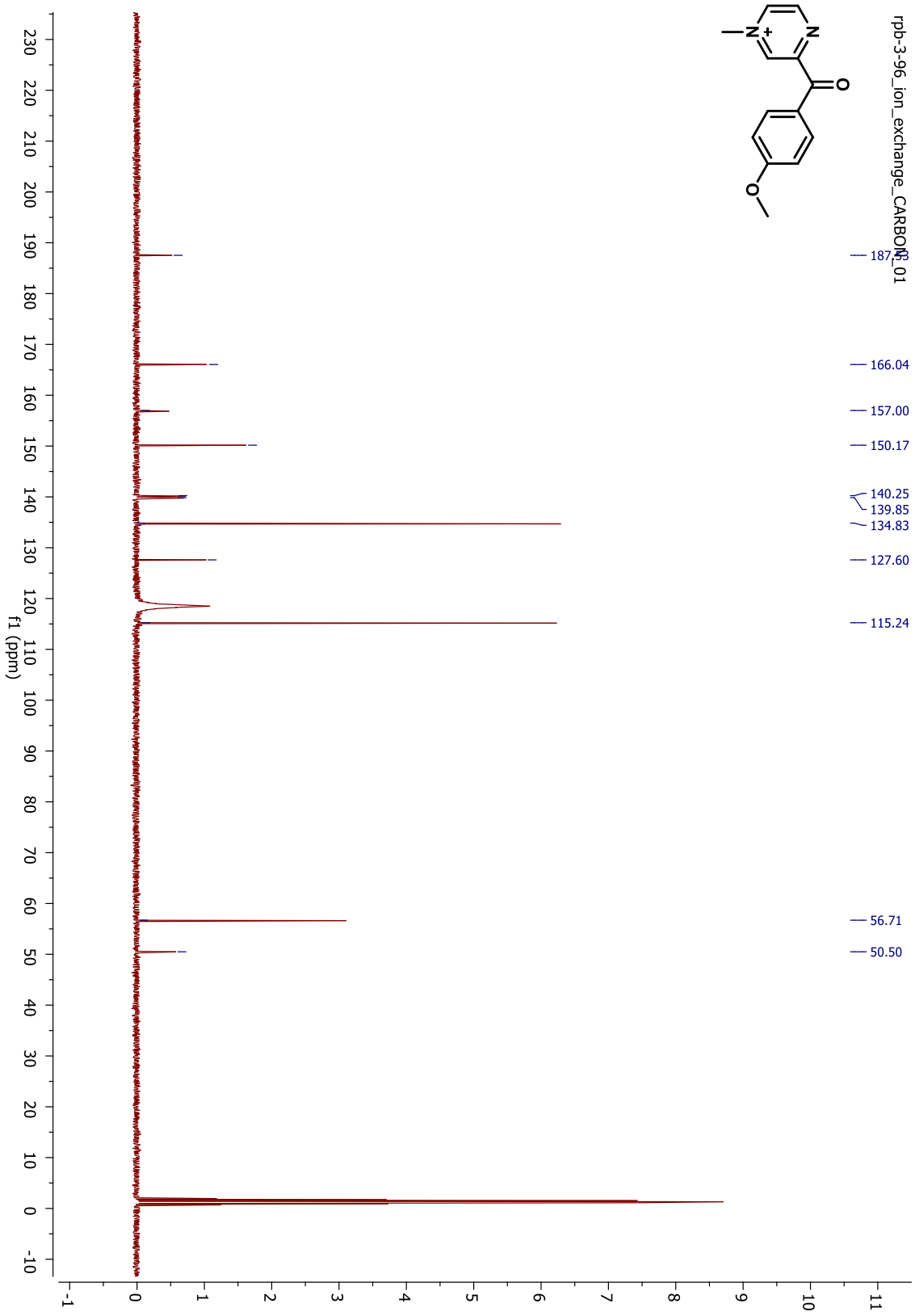
rpb-3-96_ion_exchange_CARBON_01
187.33
166.04
157.00
150.17
140.25
139.85
134.83
127.60
115.24
56.71
50.50
f1 (ppm)

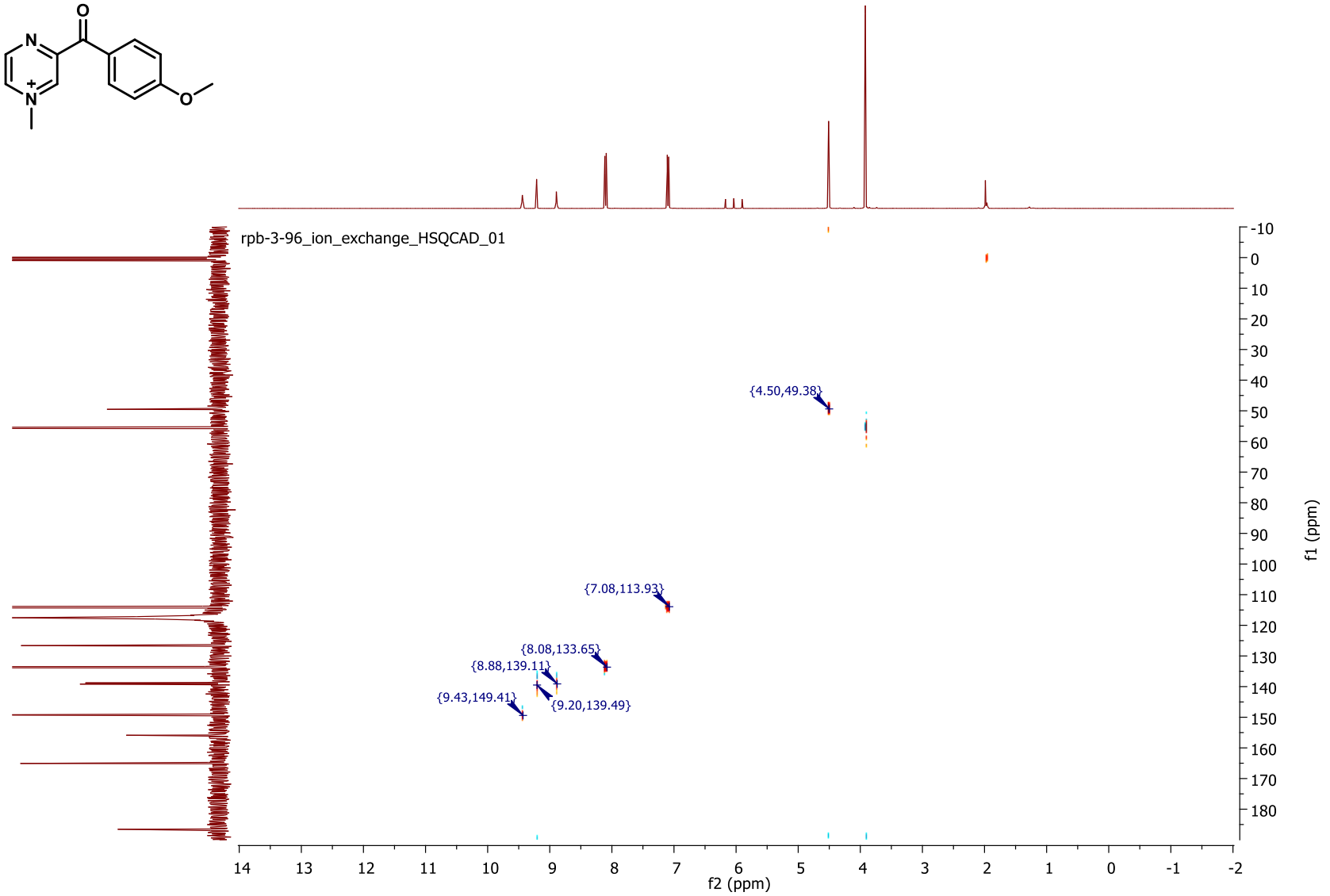
rpb-3-96_ion_exchange_HSQCAD_01
{4.50,49.38}
{7.08,113.93}
{8.08,133.65}
{8.88,139.11}
{9.43,149.41}
{9.20,139.49}
f2 (ppm)
f1 (ppm)

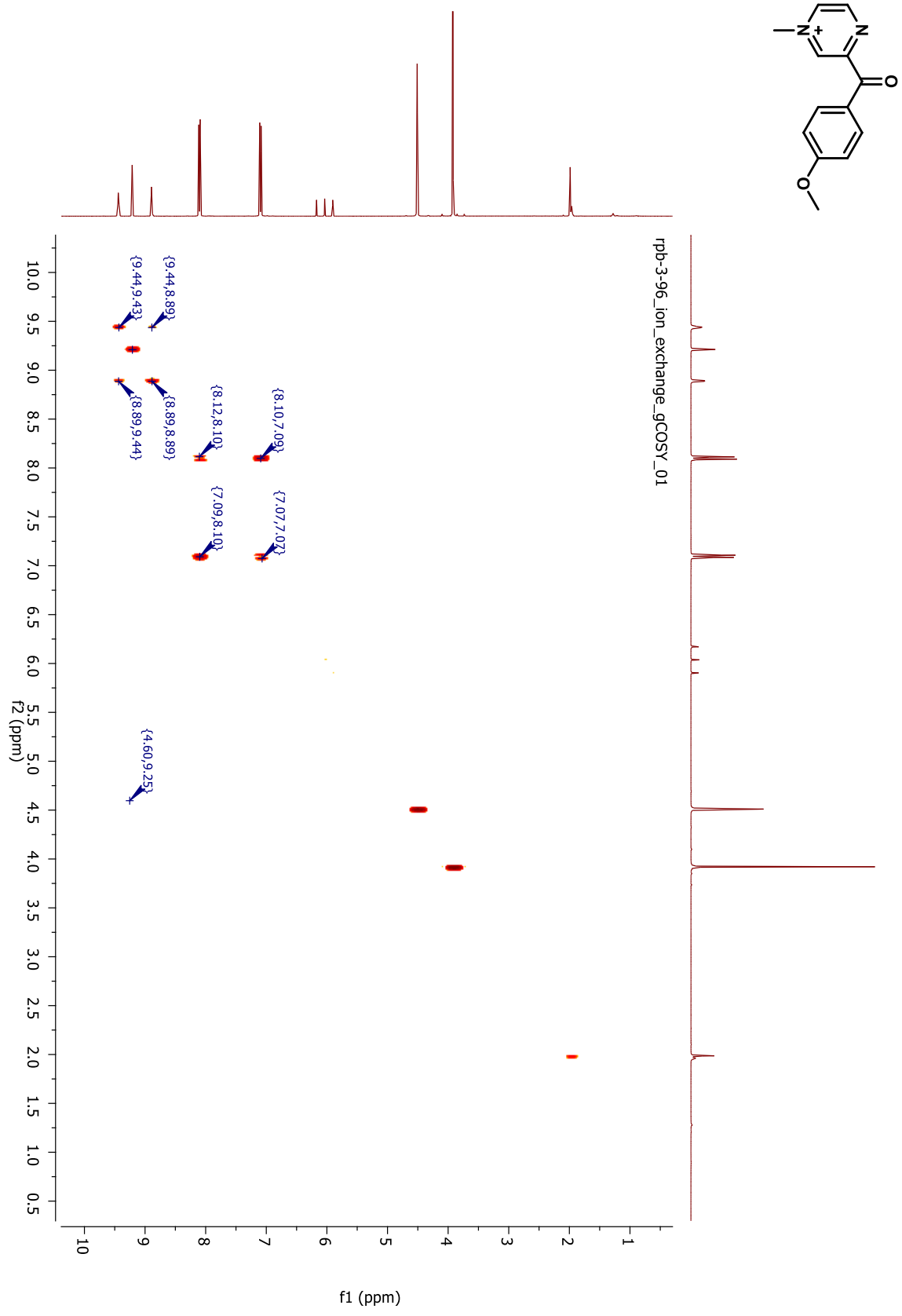
rpb-3-96_ion_exchange_gCOSY_01
{9.44,9.43}
{9.44,8.89}
{8.89,9.44}
{8.89,8.89}
{8.12,8.10}
{8.10,7.09}
{7.09,8.10}
{7.07,7.07}
{4.60,9.25}
f2 (ppm)
f1 (ppm)

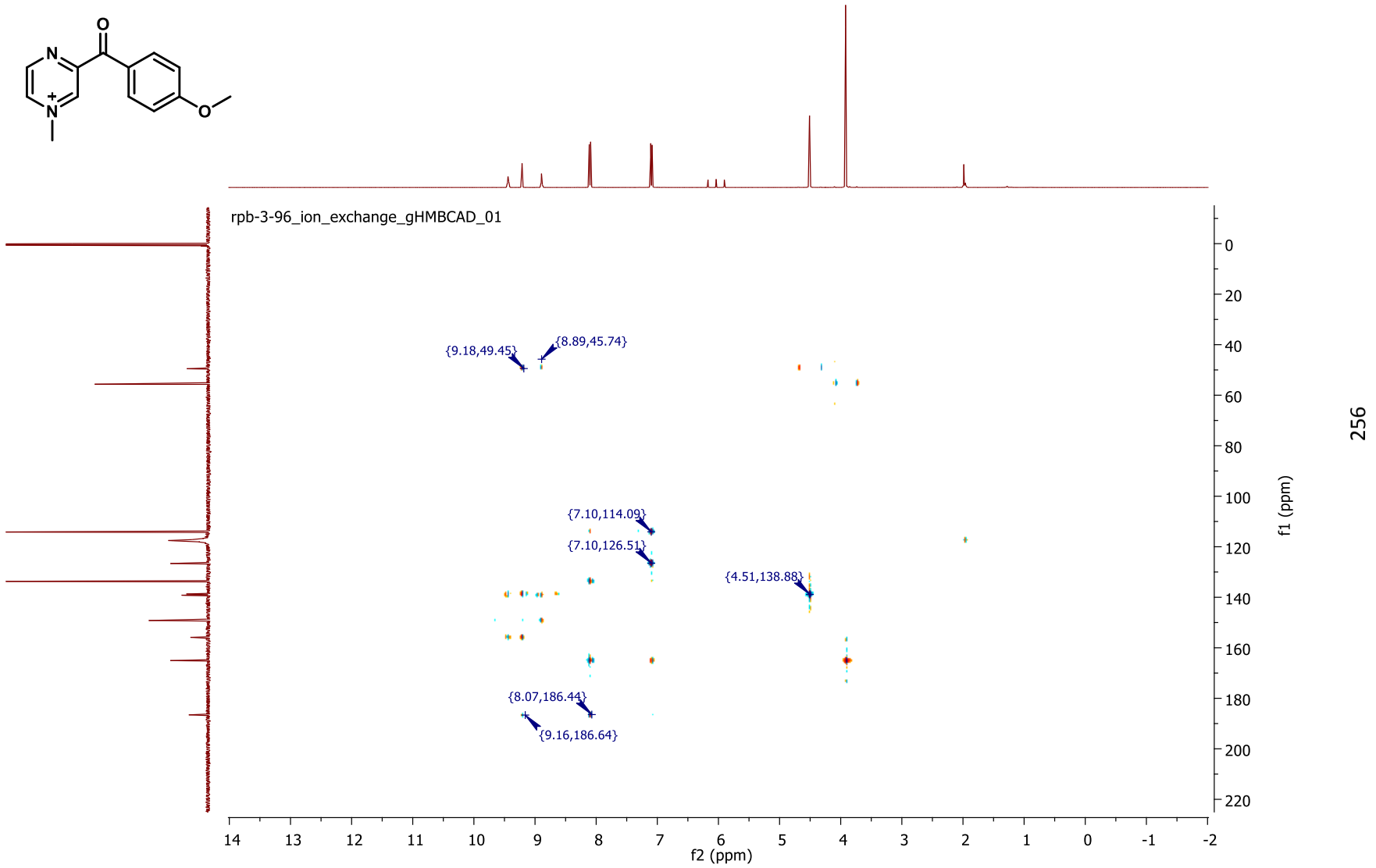
rpb-3-96_ion_exchange_gHMBCAD_01
{9.18,49.45}
{8.89,45.74}
{7.10,114.09}
{7.10,126.51}
{4.51,138.88}
{8.07,186.44}
{9.16,186.64}
f2 (ppm)
f1 (ppm)
256

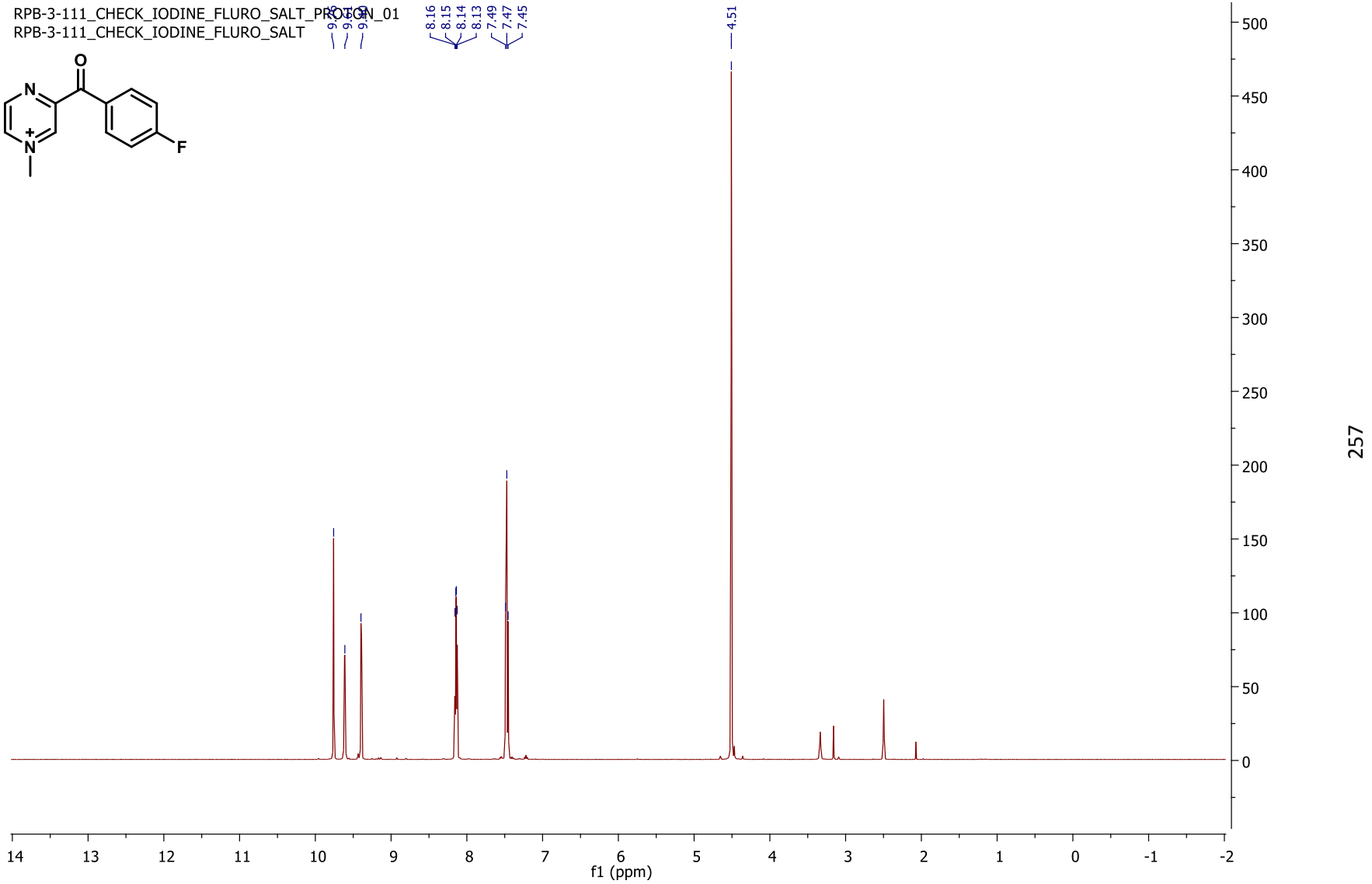
RPB-3-111_CHECK_IODINE_FLURO_SALT_PROTON_01
RPB-3-111_CHECK_IODINE_FLURO_SALT
9.76
9.61
9.44
8.16
8.15
8.14
8.13
7.49
7.47
7.45
4.51
O
N
N
F
500
450
400
350
300
250
200
150
100
50
0
14
13
12
11
10
9
8
7
6
5
4
3
2
1
0
-1
-2
f1 (ppm)

257

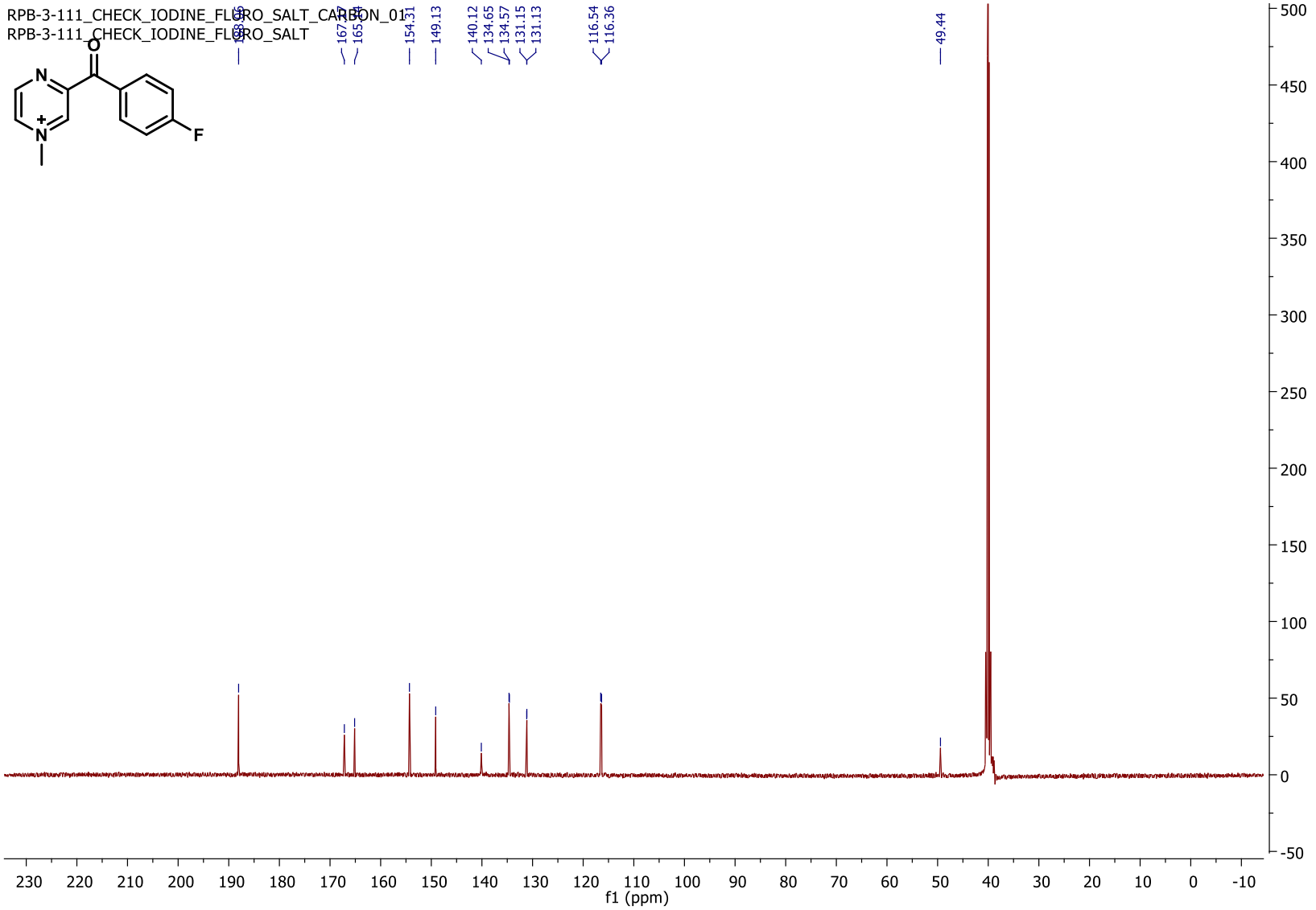
RPB-3-111_CHECK_IODINE_FLORO_SALT_CARBON_01
RPB-3-111_CHECK_IODINE_FLORO_SALT
189.66
167.23
165.58
154.31
149.13
140.12
134.65
134.57
131.15
131.13
116.54
116.36
49.44
O
N
N
F
f1 (ppm)

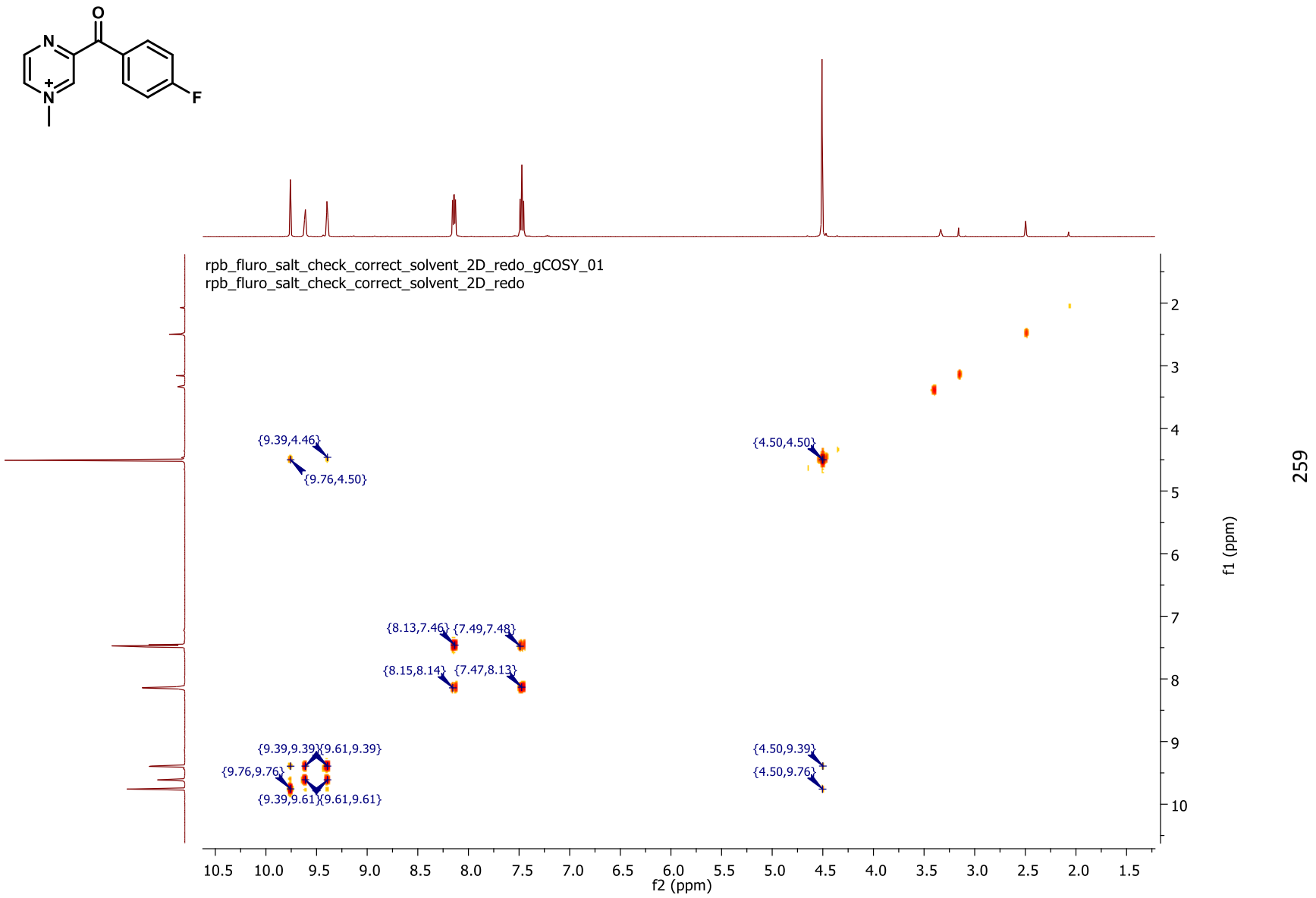
rpb_fluro_salt_check_correct_solvent_2D_redo_gCOSY_01
rpb_fluro_salt_check_correct_solvent_2D_redo
{9.39,4.46}
{9.76,4.50}
{4.50,4.50}
{8.13,7.46}
{7.49,7.48}
{8.15,8.14}
{7.47,8.13}
{9.39,9.39}
{9.61,9.39}
{9.76,9.76}
{9.39,9.61}
{9.61,9.61}
{4.50,9.39}
{4.50,9.76}
f2 (ppm)
f1 (ppm)

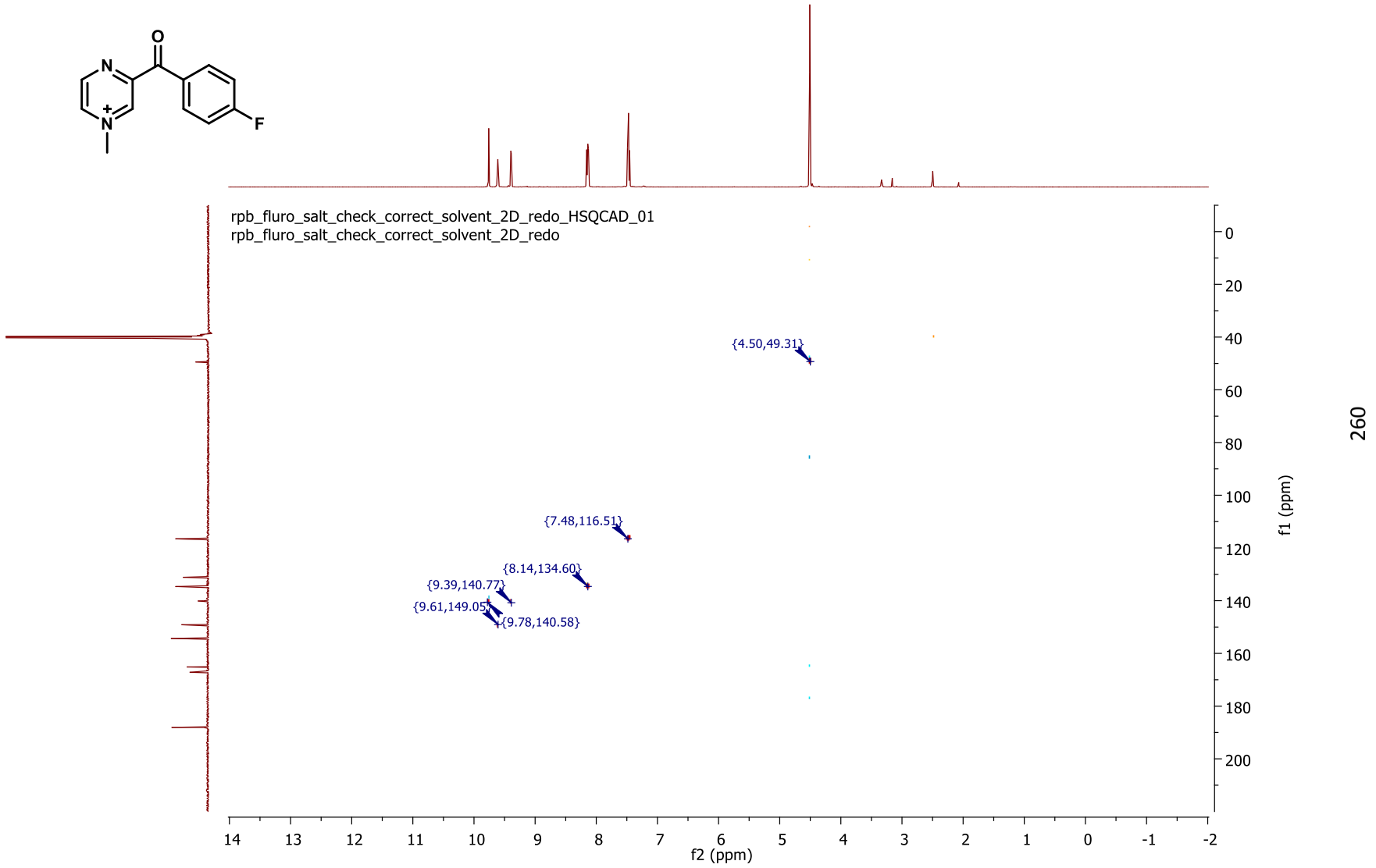
rpb_fluro_salt_check_correct_solvent_2D_redo_HSQCAD_01
rpb_fluro_salt_check_correct_solvent_2D_redo
{4.50,49.31}
{7.48,116.51}
{8.14,134.60}
{9.39,140.77}
{9.61,149.05}
{9.78,140.58}
f2 (ppm)
f1 (ppm)

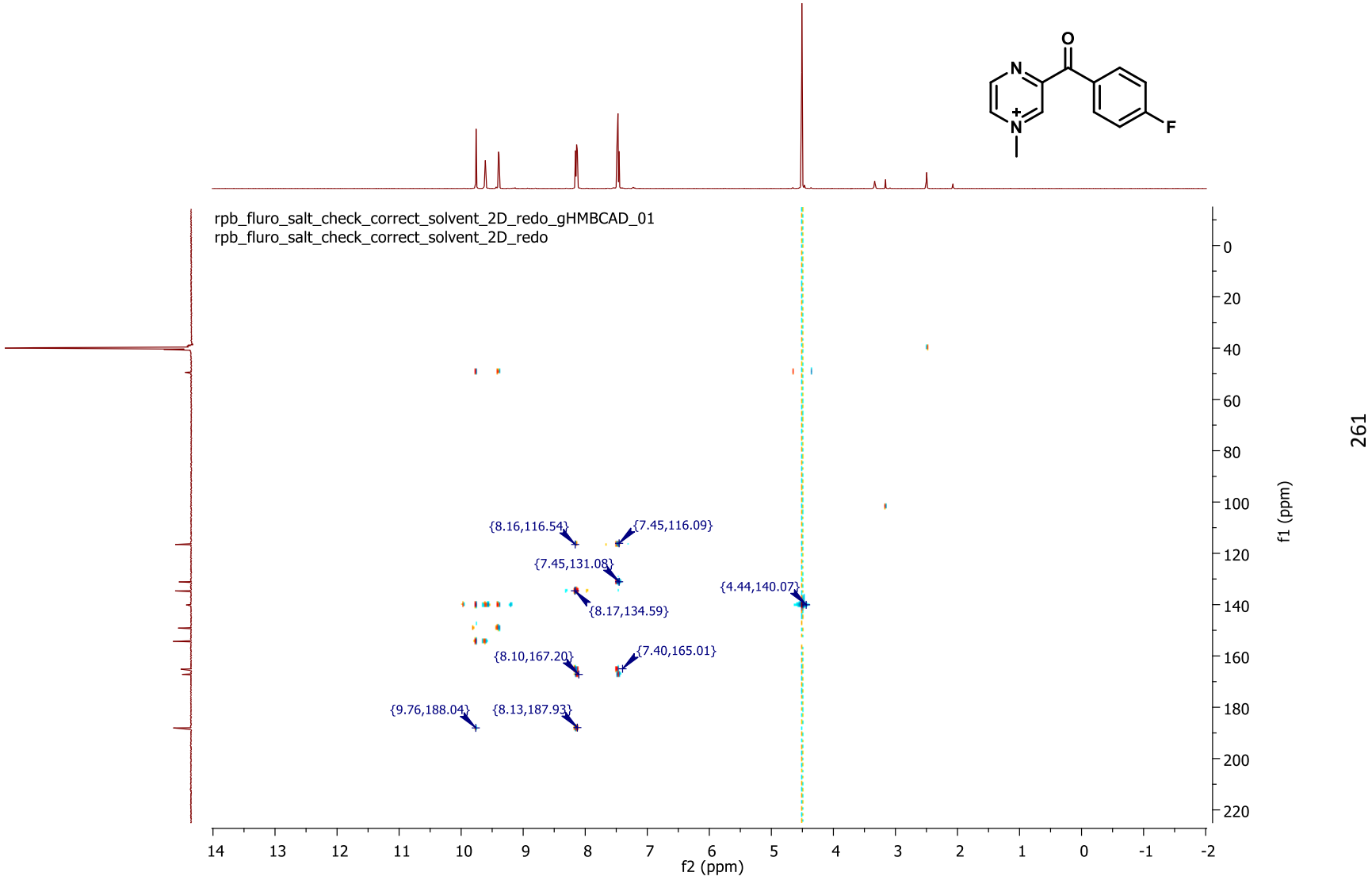
rpb_fluro_salt_check_correct_solvent_2D_redo_gHMBCAD_01
rpb_fluro_salt_check_correct_solvent_2D_redo
{8.16,116.54}
{7.45,116.09}
{7.45,131.08}
{8.17,134.59}
{4.44,140.07}
{8.10,167.20}
{7.40,165.01}
{9.76,188.04}
{8.13,187.93}
f2 (ppm)
f1 (ppm)
O
N
N
F

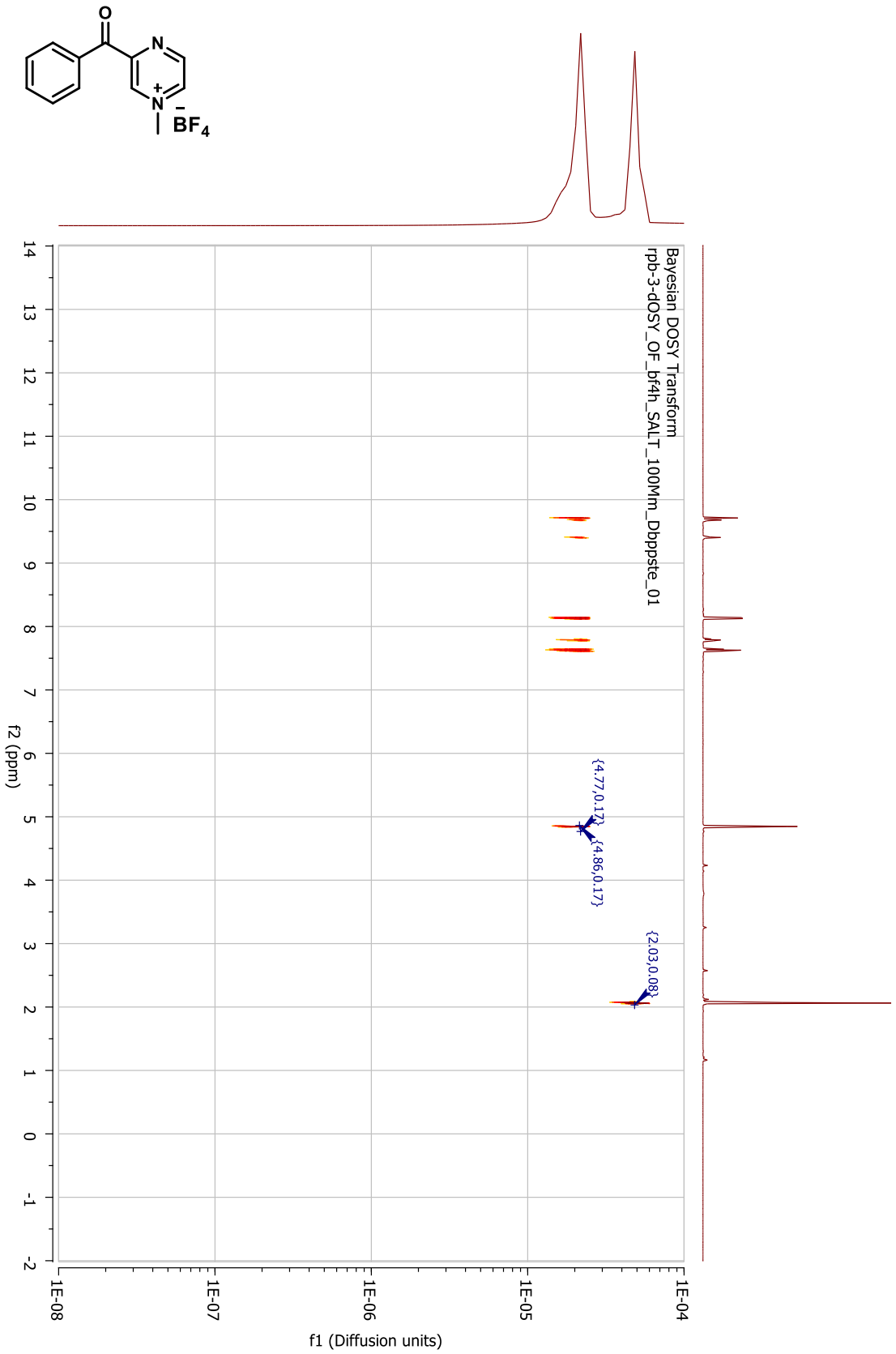
Bayesian DOSY Transform
rpb-3-dOSY_OF_bf4h_SALT_100Mm_Dbppste_01
{4.77,0.17}
{4.86,0.17}
{2.03,0.08}
f2 (ppm)
f1 (Diffusion units)
1E-08
1E-07
1E-06
1E-05
1E-04
14
13
12
11
10
9
8
7
6
5
4
3
2
1
0
-1
-2
O
N
N
BF4

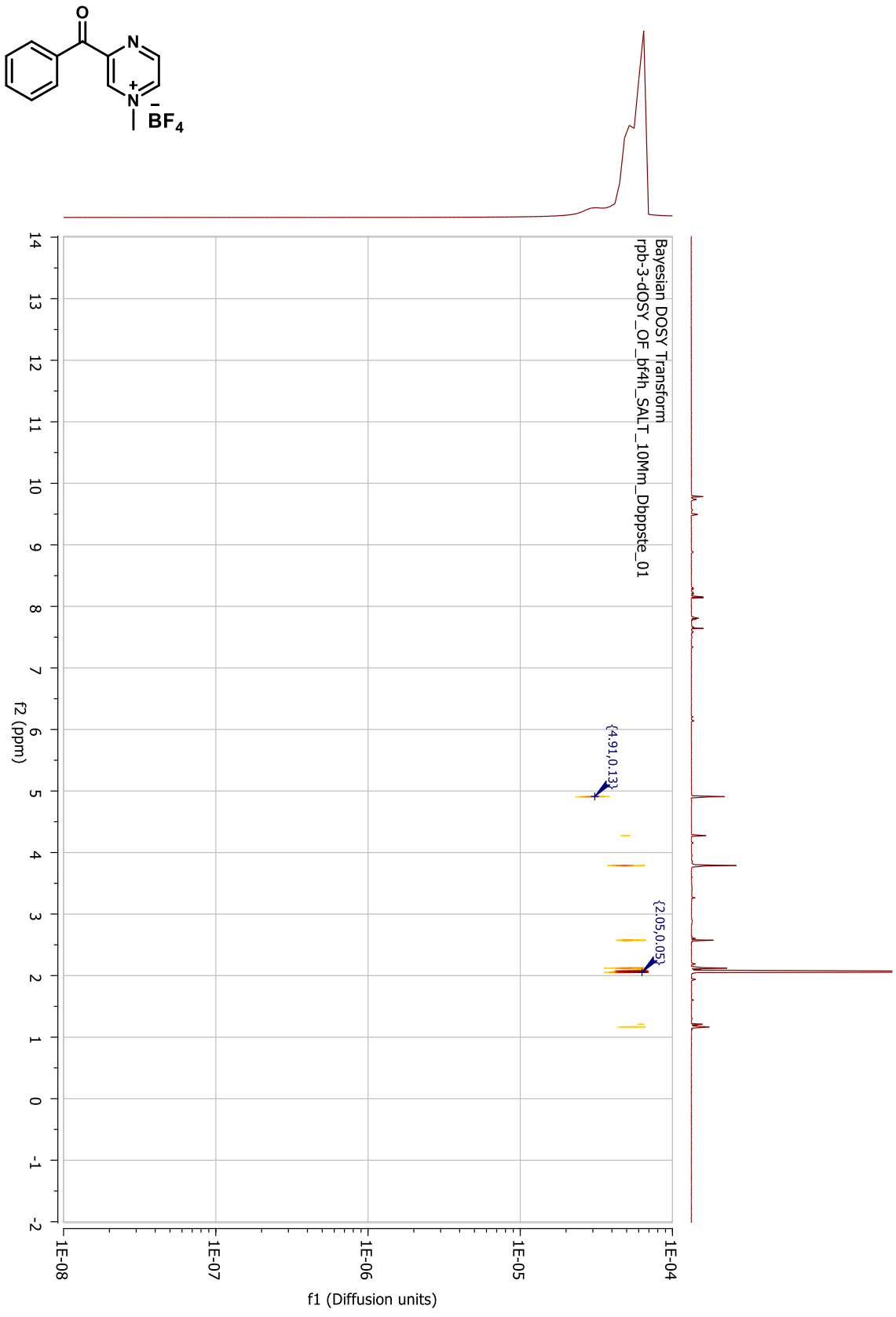
Bayesian DOSY Transform
rpb-3-dOSY_OF_bf4h_SALT_10Mm_Dbppste_01
{4.91,0.13}
{2.05,0.05}
f2 (ppm)
f1 (Diffusion units)
1E-08
1E-07
1E-06
1E-05
1E-04
14
13
12
11
10
9
8
7
6
5
4
3
2
1
0
-1
-2
O
N
N
BF4

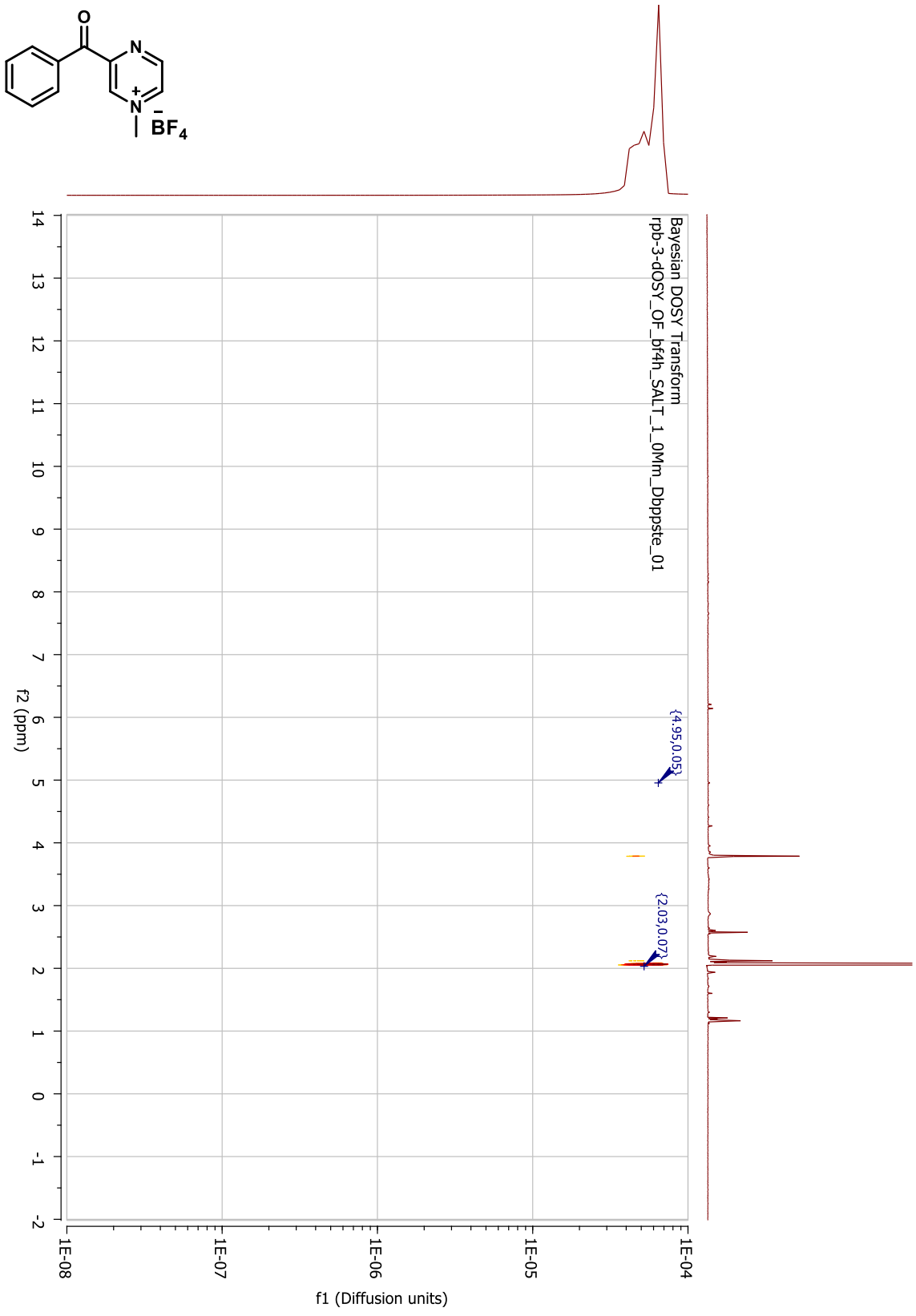
O
N
N
BF4
Bayesian DOSY Transform
rpb-3-dOSY_OF_bf4h_SALT_1_0Mm_Dbppste_01
{4.95,0.05}
{2.03,0.07}
f2 (ppm)
f1 (Diffusion units)
1E-08
1E-07
1E-06
1E-05
1E-04

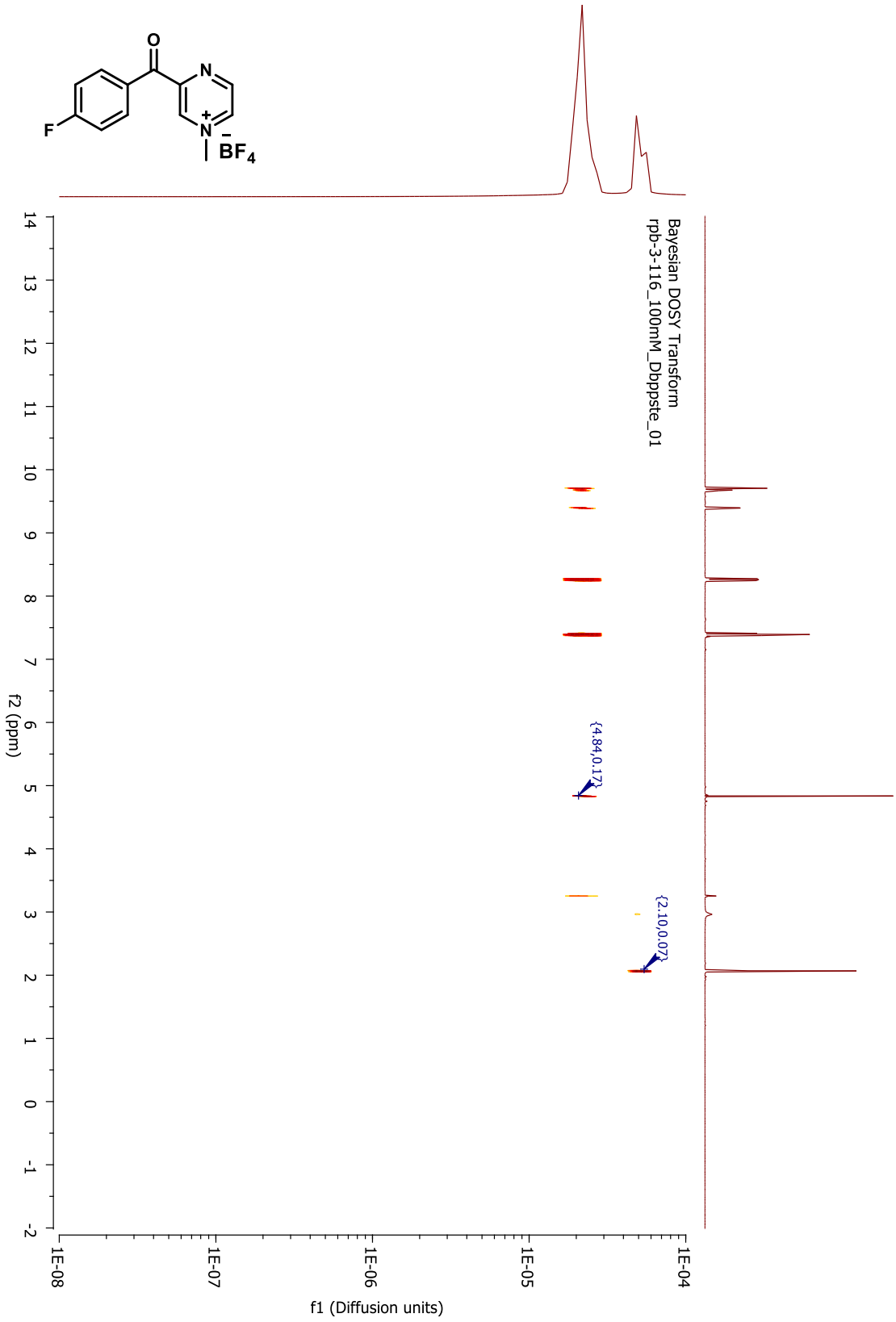
Bayesian DOSY Transform
rpb-3-116_100mM_Dbppste_01
{4.84,0.17}
{2.10,0.07}
f2 (ppm)
f1 (Diffusion units)
1E-04
1E-05
1E-06
1E-07
1E-08
14
13
12
11
10
9
8
7
6
5
4
3
2
1
0
-1
-2
O
N
F
BF4

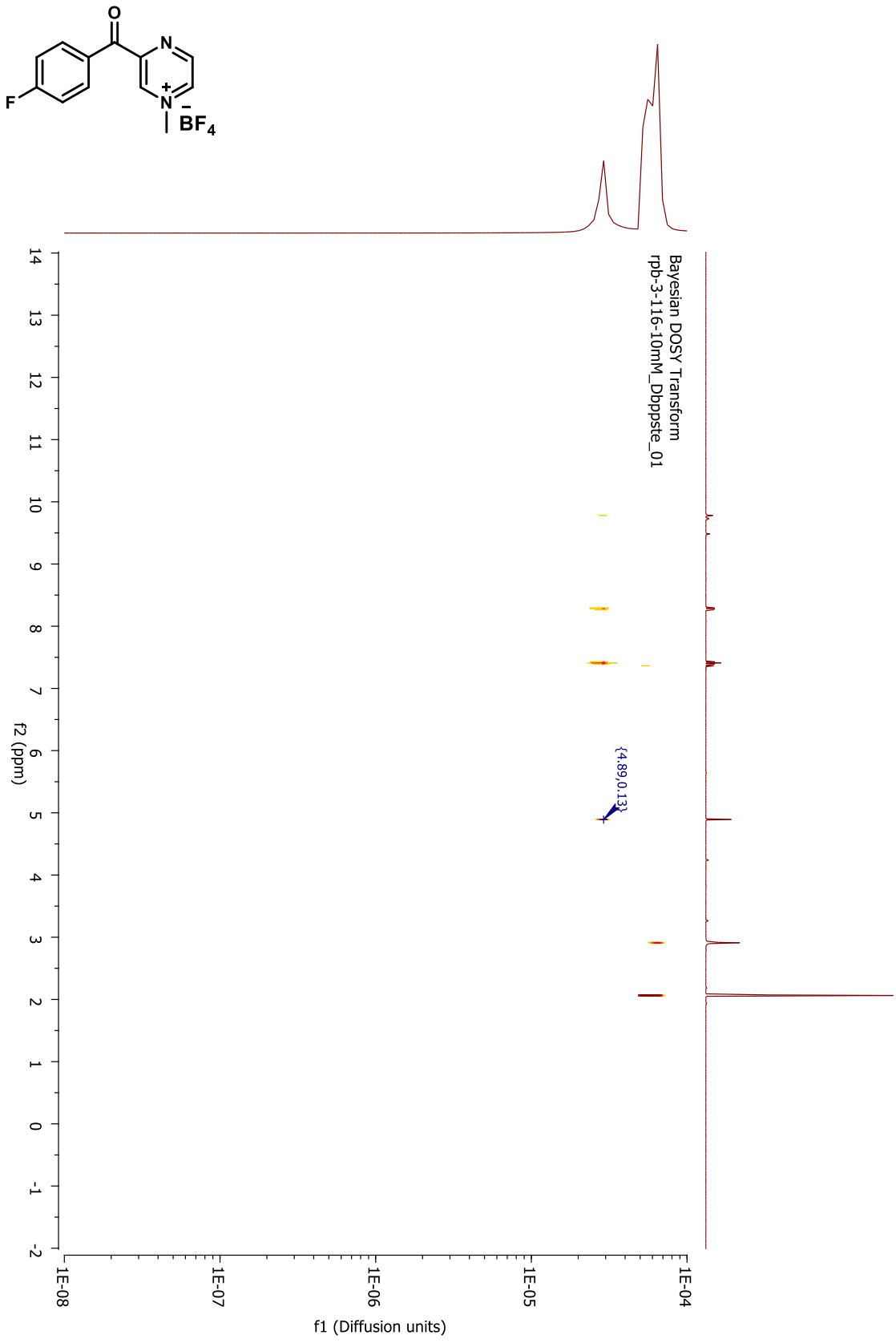
O
N
F
N
BF4
Bayesian DOSY Transform
rpb-3-116-10mM_Dbppste_01
{4.89,0.13}
f2 (ppm)
14
13
12
11
10
9
8
7
6
5
4
3
2
1
0
-1
-2
1E-08
1E-07
1E-06
1E-05
1E-04
f1 (Diffusion units)

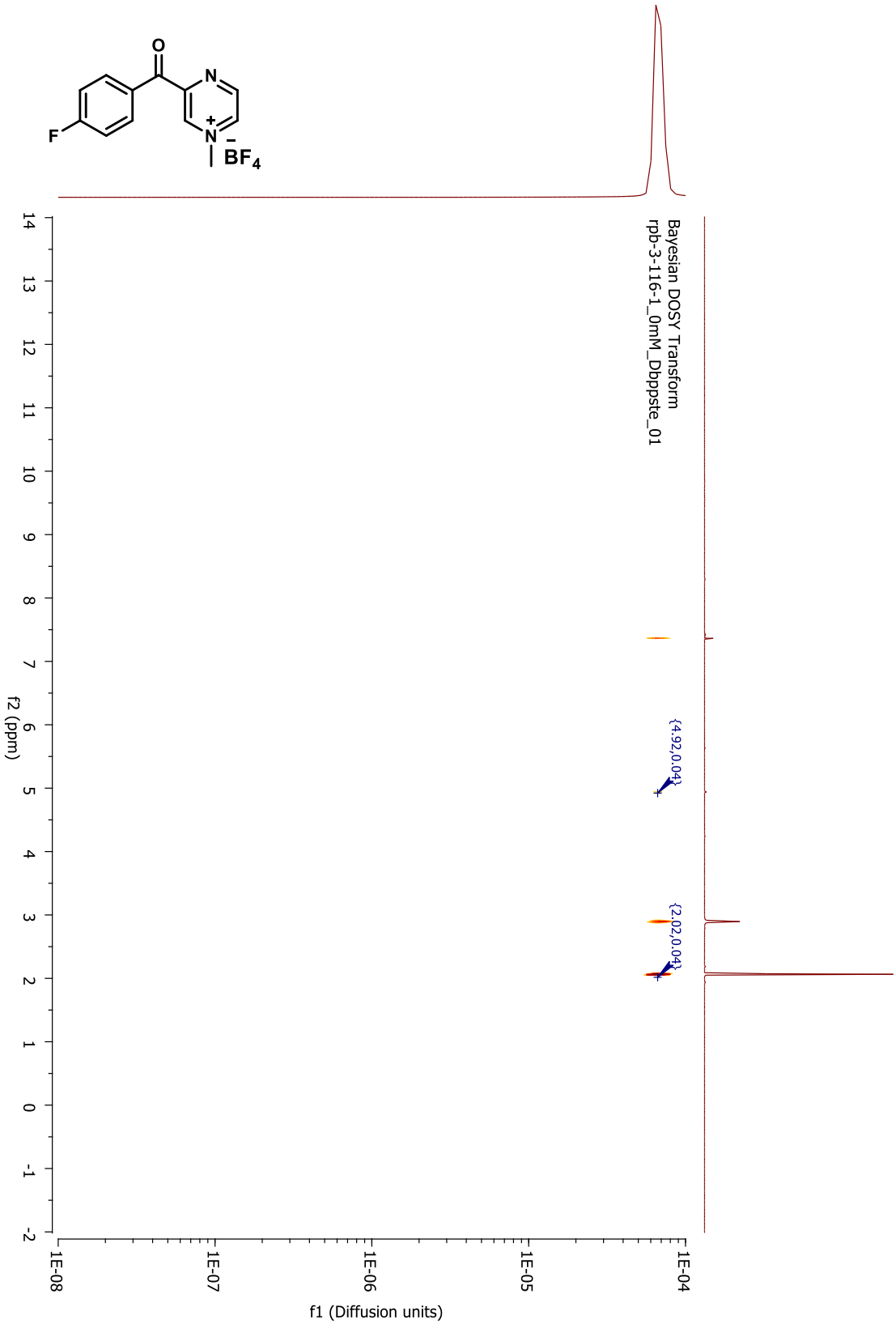
Bayesian DOSY Transform
rpb-3-116-1_0mM_Dbppste_01
{4.92,0.04}
{2.02,0.04}
f2 (ppm)
f1 (Diffusion units)
1E-04
1E-05
1E-06
1E-07
1E-08
14
13
12
11
10
9
8
7
6
5
4
3
2
1
0
-1
-2
O
N
F
BF4

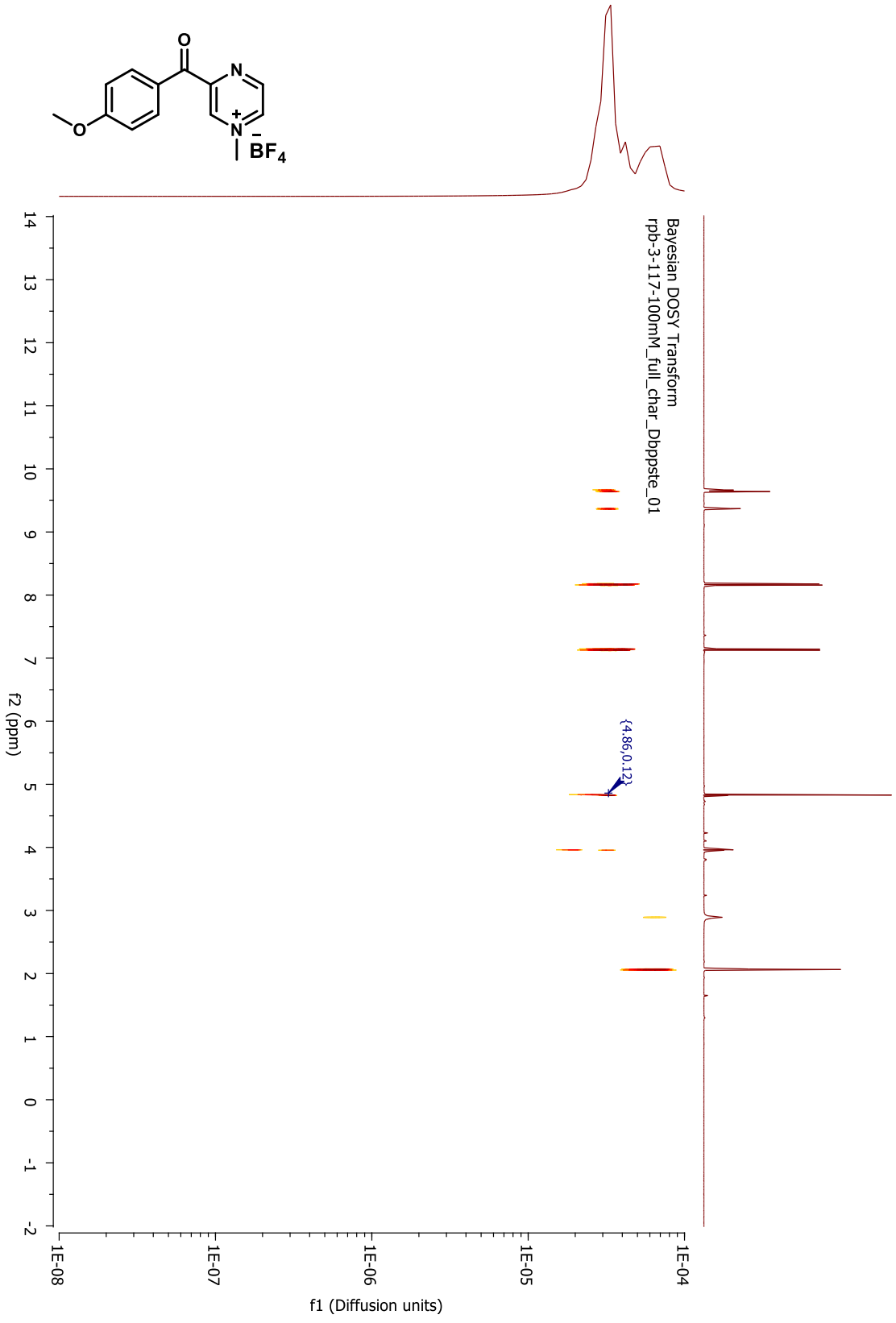
Bayesian DOSY Transform
rpb-3-117-100mM_full_char_Dbppste_01
{4.86,0.12}
f2 (ppm)
f1 (Diffusion units)
1E-08
1E-07
1E-06
1E-05
1E-04
14
13
12
11
10
9
8
7
6
5
4
3
2
1
0
-1
-2
O
N
+
N
−
BF4
O

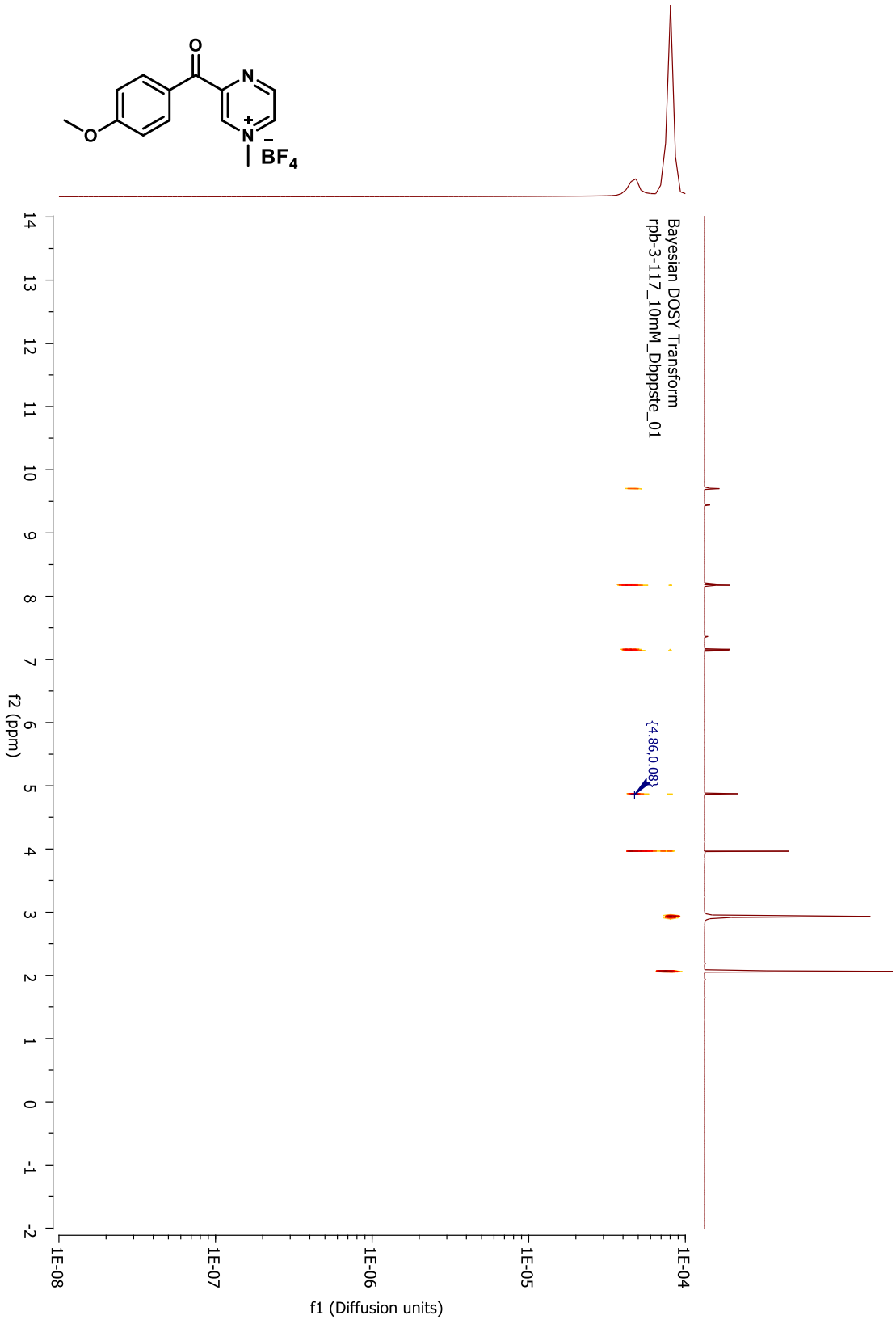
Bayesian DOSY Transform
rpb-3-117_10mM_Dbppste_01
{4.86,0.08}
f2 (ppm)
f1 (Diffusion units)
1E-04
1E-05
1E-06
1E-07
1E-08
14
13
12
11
10
9
8
7
6
5
4
3
2
1
0
-1
-2
O
N
O
N
BF4